

DISSERTATION

STRUCTURAL AND SUPERCONDUCTING PROPERTIES OF SPUTTER-DEPOSITED NIOBIUM FILMS FOR APPLICATIONS IN RF ACCELERATING CAVITIES

ausgeführt am europäischen Kernforschungszentrum in Genf (CERN)
zum Zwecke der Erlangung des akademischen Grades eines Doktors der
Technischen Wissenschaften

eingereicht an der Technischen Universität
Technisch-Naturwissenschaftliche Fakultät
Atominstitut der Österreichischen Universitäten

von

Dipl. Ing. Michael Alexander Peck
5, Rue de la Prairie
F-01630 St. Genis-Pouilly
Matr. Nr. 8727052
geb. am 5. Juni 1968 in Wien

Genf, im September 1999

Abstract

The present work presents the results of a systematic study of superconducting and structural properties of niobium films sputter deposited onto the inner walls of radiofrequency copper resonators. The measured superconducting quantities include the surface resistance, the critical temperature, the penetration depth and the upper and lower critical fields. In addition to films grown with different discharge gases (Xe, Kr, Ar, Ne and Ar-Ne mixtures) and to films grown on substrates prepared under different conditions, the study also includes massive niobium cavities. The surface resistance is analysed in terms of its dependence on the temperature and on the rf field amplitude and, when possible, compared to theoretical predictions. In general, good agreement with BCS theory is observed. All experimental results are presented in the form of a simple, but adequate parameterisation. The residual resistance is observed to be essentially uncorrelated with the other variables, but strongly dependent on the macroscopic defect density of the copper substrate. Several mechanisms, leading to the generation of a non-zero residual resistance in niobium films are discussed. Electrochemical polishing of the copper resonators before sputter deposition of niobium gives reliably low values of the residual resistance. These values are entirely comparable with those obtained on bulk resonators, defeating any argumentation against the applicability of film cavities for particle accelerators. By comparing the relative merits of the bulk and film technologies, the latter should be preferred in future large-scale applications using superconducting cavities.

Knowledge about the film structure is necessary, when discussing the differences of the superconducting properties observed between different types of films. Therefore, niobium films cut from different sites of 1.5GHz resonators, and films, deposited under different conditions on small copper samples are analysed by X-ray diffraction. The films are characterised by measuring the resistivity, the lattice parameter, the texture, the stress and the microstrain. The strong dependence of these properties, especially of the resistivity and the film strain, on the amount of implanted noble gas is evidenced, and the effect of sputter cleaning before deposition is evaluated. It is found that stresses and microstrains of niobium films deposited on oxidised copper are considerably higher than those of films grown on sputter cleaned copper. The dependence of stress on the nature of the substrate can be interpreted by a combined consideration of growth and misfit stresses. The critical temperature is found to be higher than the nominal value of 9.3K of bulk niobium and is observed to depend on the amount of macrostresses present in the material. Films, which had been removed from their substrates, release their elastic stresses and show a transition temperature close to that of the bulk material. The residual resistivity is shown to be determined by the grain size and the presence of microstrains representing crystal imperfections, such as dislocations and embedded noble gas atoms. The mean free path is calculated for different films from the experimentally determined residual resistivity ratio and from measured values of the penetration depth. Excellent agreement between both sets of data is obtained. The upper critical field of the films is independent of the amount of stresses present in their interior and found to take values similar to those measured on bulk niobium with a comparable mean free path.

Acknowledgments

This research has been carried out at CERN, the European Laboratory for Particle Physics, and has mainly been funded by the CERN Austrian Doctoral Student Program. For the opportunity to realise this work, I have first to thank:

Cristoforo Benvenuti, the leader of the Surface and Material group of the EST Division at CERN, who proposed and constantly supported the research;
Prof. Harald W. Weber, who supervised the thesis at the Technical University of Vienna, and who provided a great amount of valuable advice.

Many people at CERN have contributed in an important way to the realisation of this work. I would like to express my gratitude in particular to:

Pierre Darriulat, for his encouragement and his essential contribution to the success of this work;
Sergio Calatroni, the leader of the Thin Film laboratory for many helpful comments, suggestions and techniques;
Stefano Sgobba, for his suggestions about the characterisation of the films.

I am also indebted to:

Jean Cavé for his help in the construction and maintenance of the electropolishing system;
Stefan Bauer and Serge Forel for their work on the chemical treatment of the substrates;
Paolo Chiggiato for performing the thermal desorption experiments;
Mauro Taborrelli for the XPS analysis;
Massimo Marino for countless useful discussions and his important help in several occasions;
Ayatollah Karimi of the EPFL for providing valuable information about the indentation measurements;
Victor Buntar and Prof. Franz Sauerzopf of the TU Vienna for their help in the interpretation of the critical field measurements.

I would further like to express my gratitude to many other members of the Surface and Material group of the EST division and especially to Roberto Russo, Anne-Marie Valente, René Matet, A. van't Hof, V. Arbet-Engels and Paule Henry for invaluable suggestions and their friendly collaboration.

Special appreciation is due to my wife, Renate, and our daughter, Nathalie, for enduring so patiently the division of my attention during the writing of this thesis.

Table of contents

Part I – RF measurements of superconducting niobium film resonators

1. Introduction.....	1
2. Superconducting rf cavities for particle accelerators.....	4
2.1. Resonating cavities.....	4
2.2. The niobium film technology for accelerating cavities.....	5
3. Microwave properties of superconductors.....	8
3.1. Conventional cavity characteristics.....	8
3.2. The surface impedance of superconductors.....	10
4. Experimental method and procedure.....	20
4.1. Preparation and characterisation of the copper substrate.....	20
4.2. Magnetron sputter deposition of niobium thin films.....	28
4.3. Measurement technique for accelerating cavities.....	34
5. Experimental results.....	38
5.1. Bulk niobium resonators.....	39
5.1.1. The BCS resistance.....	40
5.1.2. The penetration depth.....	42
5.1.3. The residual resistance.....	44
5.2. Niobium film resonators.....	45
5.2.1. Standard films.....	45
5.2.2. Results from films sputter deposited in the two-electrode system.....	51
5.3. The residual resistance of film resonators.....	53
6. Conclusions.....	61
7. References.....	62

Part II – Characterisation of niobium film samples

1. Preparation and characterisation techniques.....	67
2. The critical temperature.....	69
3. Determination of the lattice parameter by X-ray diffraction.....	77
3.1. Experimental procedure.....	77
3.2. Mechanisms of stress generation in sputter deposited films.....	79
3.3. Results and discussion.....	81
4. Noble gas incorporation during film growth.....	85
4.1. Implantation mechanisms.....	85
4.2. Results on the gas content and the lattice parameter of neon implanted films.....	87
5. Analysis of the degree of orientation.....	92
5.1. Niobium film growth.....	92

5.2. Orientation distribution of grains.....	99
6. Hardness and elastic moduli of niobium films.....	103
6.1. Theoretical considerations and experimental procedure.....	103
6.2. Results and discussion.....	106
7. Stress analysis by diffraction.....	112
7.1. ω -Goniometer (Seemann-Bohlin method).....	112
7.2. ψ -Goniometer (Eulerian cradle).....	118
8. Effective crystallite size and microstrain.....	127
8.1. The Williamson-Hall method for microstrain analysis.....	127
8.2. Fourier analysis of diffraction peaks.....	129
8.2.1. Theoretical considerations and experimental procedure.....	129
8.2.2. Analysis of microstrain.....	133
8.3. The determination of the effective grain size.....	137
9. The low temperature resistivity of niobium films.....	141
10. Measurements of the critical fields.....	148
10.1. The upper critical field.....	148
10.2. The lower critical field.....	152
11. Summary.....	155
12. References.....	159
13. Appendix.....	165

Part I – RF measurements of superconducting niobium film resonators

1. Introduction

Most applications of rf superconductivity involve resonant cavities. Cavities are being developed for particle accelerators for elementary particle or nuclear research and for free electron lasers (FEL). Other applications of cavities take advantage of their excellent frequency stability in superconducting cavity-stabilised oscillators (SCSO). A long-term frequency stability $f/\Delta f$ of 10^{16} has been obtained, better than that of the caesium clock, the standard used for the definition of the second. Superconducting cavities are also used for measurements of the relative permittivity of dielectric samples, as microwave filters or as gravitational wave detectors for the detection of very weak mechanical displacements in the range of 10^{-10} nm.

The most important field of application of superconducting resonators is particle accelerators for high-energy particles, may they be electrons, protons or heavy ions. A modern particle accelerator is mainly composed of superconducting rf accelerating sections providing the high accelerating voltage needed both in electron storage rings to compensate for severe energy losses from synchrotron radiation, and in linear accelerators to attain high energies within reasonable accelerating lengths. The particles travel through the cavity in synchronism with an accelerating rf wave having an axial accelerating electric field, E_a . The interest in superconducting accelerating rf cavities is a consequence of the potentially very high accelerating fields they should provide at low power dissipation. The figure of merit for resonators, the quality factor, Q , is defined as the energy stored in the cavity divided by the energy lost per rf cycle. It is always less than a few times 10^4 for copper resonators at room temperatures but may attain values in the range 10^{10} - 10^{11} for superconducting cavities at high accelerating fields and operating temperatures well below the critical temperature of the material.

Among pure superconducting metals, niobium has been most intensively studied for resonator use. In fact, nearly all existing or planned particle resonators rely on the bulk niobium technology, using massive niobium resonators either made in one piece from solid reactor-grade niobium or in different pieces, which are then assembled by electron-beam welding. Bulk niobium rf cavities are now routinely produced at a number of laboratories around the world. They are expensive and somewhat difficult to make with reliable performance. The Large Electron Positron collider (LEP2) at CERN and the Large Hadron collider (LHC) presently under construction at CERN also rely on niobium as the superconducting material, but use a different technology for cavity construction. A $1.5\mu\text{m}$ thick niobium film is sputter deposited by magnetron sputtering on the inner surface of OFE copper resonators.

At the present stage of development, the niobium film technology represents a serious alternative to massive niobium, including several significant advantages,

- The lower costs due to the small quantity of niobium required for cavity fabrication,
- The decoupling of the requirements on thermal conductivity and on superconducting properties,
- The possibility to use alloyed materials with a higher transition temperature than niobium.

Despite the arguments listed above in favour of the film technology, no serious efforts are presently undertaken in other laboratories to study in detail the superconducting rf properties of

niobium films. The main reason is the belief that the structural properties of niobium films give intrinsic limitations to the use of film cavities in linear accelerators, demanding high gradients to be reached. Therefore, several years ago a research project started at CERN aiming at a complete understanding of the structural and rf properties of niobium films with regard to the optimisation of the superconducting rf performance of niobium-copper cavities. Early experience, accumulated with about 250 niobium-copper cavities developed for the LEP2 machine and operating at lower accelerating gradients at 4.2K, rose the intriguing possibility that the rf quality of the film cavities could actually surpass that of bulk cavities, provided the technological and materials issues are sufficiently well understood. This thesis has been performed in the framework of the 1.5GHz niobium-copper R&D project at CERN and in many respects stimulating results have been obtained, which are of particular practical importance for the TESLA collider, a linear e^+e^- accelerator planned in Germany.

The response of a superconductor to an incident electromagnetic wave has been calculated by *Mattis and Bardeen* (1958) and by *Abrikosov et al.* (1959) from the BCS theory (1957). Before this time the main conceptual tools used in the discussion of the rf behaviour of superconductors were the two-fluid model of *Gorter and Casimir* (1934) and the electrodynamics of the *London* theory (1935). Later contributions were made by *Pippard* (1953), who proposed an empirical, non-local current-field relation, which might replace the *London* equations. Experimental observations of the temperature dependence of the surface resistance of superconductors are in reasonable agreement within these early theories.

According to the BCS theory, the surface resistance should vanish exponentially with temperature. Experimentally the surface resistance in superconducting cavities is seldom reduced to zero at very low temperatures but shows a residual resistance, which, in the case of niobium films, may increase with accelerating field. Although several conjectures about the origin of this resistance exist, there is no experimental proof of the physical mechanisms leading to these losses in the existing literature. It is frequently believed that microscopic *Josephson* junctions at grain boundaries significantly contribute to resistive losses as the critical current is exceeded.

Residual losses form the most important limitations on the accelerating field that can be achieved in an accelerating cavity. A reduced surface resistance would mean that higher gradients could be achieved for a given amount of heat dissipated in the cavity walls, reducing the possibility of thermal breakdown as one of the practical limits on cavity performance. In the present study serious efforts were devoted to the identification and explanation of the loss mechanisms in niobium films and the reduction of these losses. The method, used to obtain the surface resistance of a superconducting niobium film, was simply to measure the quality factor, Q , of a copper cavity coated with sputter deposited niobium and to derive the surface resistance, R_s , from this measurement.

The present work is split into two main parts. The first part deals with basic principles of resonators and of rf superconductivity and summarises the present state of the art about superconducting accelerating cavities. The experimental technique of production of high performance niobium-copper resonators will be described in detail. Taking experimental results on bulk niobium cavities as an example, the main variables describing the rf characteristics of superconducting resonators are introduced. Experimental data on film cavities will then be analysed in the same way and compared with theory. The residual resistance will be treated in a separate section and the main findings will allow for a clear assessment of the applicability of film resonators in future linear accelerators.

The structural and some non-rf superconducting properties of niobium films will be discussed in the second part of this work. There, film samples that have been cut for a ‘post-mortem’ characterisation from niobium-copper resonators or samples, specially prepared for this purpose, will be analysed. The main analytical tool used for structure analysis in this study was X-ray diffraction, but complementary investigations using other methods have been performed as well. Interesting information about the texture and the stress state in niobium films sputter deposited on different substrates and using different sputter gases have been obtained. The data are presented and compared with data available in literature. The results are discussed with special attention to the relations between the structural and the electronic properties of niobium films. A summary of the main results and a comprehensive reference list will complete this work.

2. Superconducting rf cavities for particle accelerators

2.1. Resonating cavities

A microwave resonant cavity is a hollow structure fabricated from high conductivity metal with dimensions comparable to the wavelength. Under resonance, the cavity is capable of sustaining microwave oscillations at a discrete set of frequencies determined by its shape and size [1-3]. These oscillations form a particular interference pattern (mode) of superimposed microwaves reflected from the cavity walls, i.e. a standing wave constituting a solution of Maxwell's equations in the presence of the boundary conditions imposed by the cavity walls.

To generate the standing wave, microwave energy is coupled to the cavity by means of an input antenna, which in turn is connected to the microwave power supply via an external circuit. One of the simplest geometric shapes for a resonating cavity is the so-called pillbox, represented by a cylinder. When this structure is excited in the transverse magnetic mode, TM_{mnp} , with $m = p = 0$, and $n = 1$, the electric field is parallel to the axis. The magnetic field lines are circles coaxial to the cavity. The indices, m , n and p refer to the number of half cycle variations in the standing wave pattern in the angular, radial and longitudinal directions. The dependence of the resonant frequency, f , on the radius, r , and the length, d , of a pillbox cavity is given by a simple formula [1, 3], which for the TM_{010} cavity reduces to the form,

$$f = 2.405 \frac{c}{2r\pi}, \quad (1)$$

i.e. for this particular mode the resonant frequency is independent of the length of the cavity.

The copper resonators, which are used in the present study consist of an axially symmetric cell having a nearly elliptical profile optimised for rf excitation in the fundamental 1.5GHz TM_{010} mode and for prevention of resonant absorption by multiple electron impacts [4, 5]. The resonance frequency of 1.5GHz was chosen to keep the cell diameter (0.18m) small for practical handling of the resonator in the course of the many successive operations that are necessary for this study. This frequency is much lower than the critical frequency of about 740GHz above which the energy of the incident photons is sufficient to break the Cooper pairs. While it is about four times higher than the frequency of 352MHz used for the LEP2 resonators [6], it is equal to that used at CEBAF (Continuous Electron Beam Accelerator Facility, Virginia, USA) [7, 8] and close to 1.3GHz as used in the test facility for the TeV-Superconducting Linear Accelerator (TESLA) planned in Germany [9, 10]. Whereas the CEBAF accelerator consists of 338 five-cell massive niobium cavities, equivalent to 160m accelerating length, the Large Electron-Positron storage ring (LEP2) at CERN consists of 256 four-cell copper cavities sputter coated with a thin niobium layer on the inner walls of the resonators. At CEBAF, the design criterion for the accelerating gradient, E_a is 5MV/m with a quality factor, Q , of $\geq 2.4 \times 10^9$ at 2K. For LEP2, Q is $\geq 3.2 \times 10^9$ at $E_a = 6$ MV/m at 4.2K. The design parameters of a nine-cell TESLA cavity, with an accelerating length of 1m, are ≥ 15 MV/m and 3×10^9 , but the feasibility of reaching reliably 25MV/m with the same quality factor should be demonstrated before construction will be started.

The geometry of the 1.5GHz cavity and the distribution of the amplitudes of the electric and magnetic fields on the cavity surface are shown in Figure 1. The magnetic field amplitude reaches a flat maximum at the equator and remains above 80% of its maximal value over 80% of the cell area, equal to 0.067m^2 in total, decreasing to 20% of its maximal value at the iris. In the present work this variation has been neglected, as well as the variation of the film characteristics over the cell surface and the term H_s always refers to the peak rf magnetic field at the surface. The axially directed electric field is instead maximal at the iris and vanishes at the equator. As a consequence, defects and impurities located in the equatorial region influence

preferentially the surface resistance, while those located near the iris are potential sources of field emission (chapter 3).

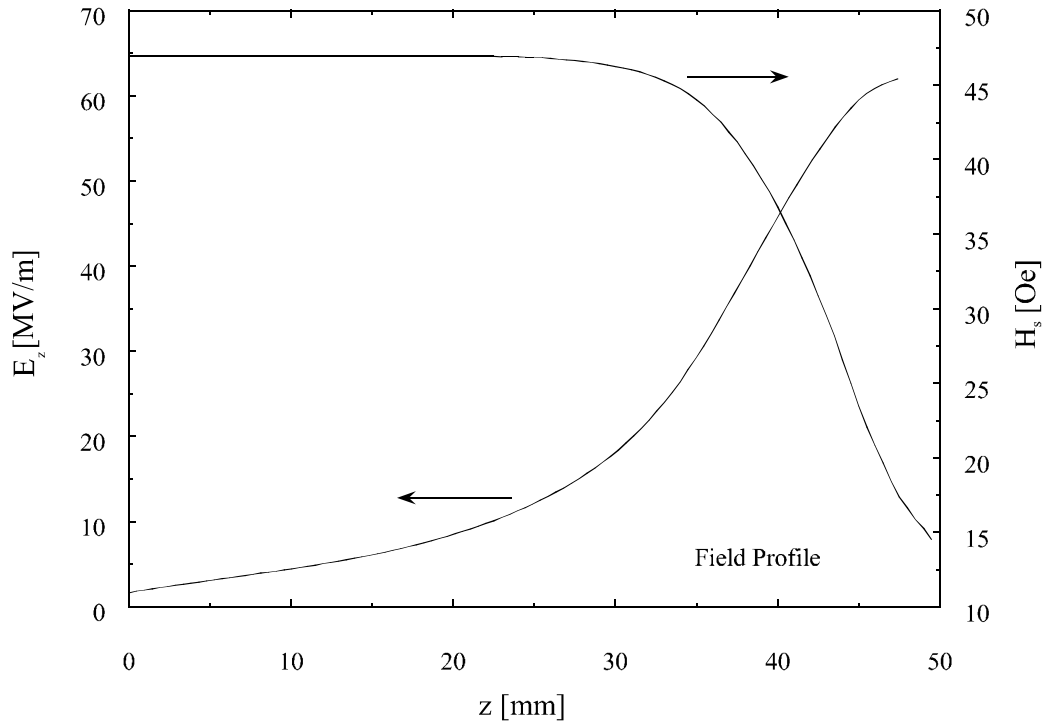


Figure 1. Distribution of the electric and magnetic field amplitudes on the cavity surface. The position $z = 0$ in the centre of a cavity, where z is the coordinate along the axis of the cylinder, corresponds to the equator and the position at $z = 50$ corresponds to the iris, i.e. the transition region between the cavity cell and the beam tube.

2.2. The niobium film technology for accelerating cavities

The majority of superconducting rf resonators presently operating in particle accelerators are made of bulk niobium [11, 12]. Among pure elements, niobium is the one with the highest critical temperature (9.3K in its bulk form) and the highest thermodynamic critical field H_{th} (1.6×10^5 A/m) [13]. Its mechanical properties are good enough to permit the manufacturing of resonating devices with the required accuracy and reliability. The production of bulk niobium cavities has been the object of an intense research and development work in several high-energy physics laboratories all over the world, and as a result of this work the performances reached by these resonators have continued to improve during the last decades. At liquid helium temperature (4.2K) the surface resistance of very pure bulk niobium is about $900\text{n}\Omega$ at 1.5GHz. For an accelerating field of 5MV/m this means that the power dissipated is only about 15W/m and increases to about 50W/m when operating at 8MV/m (chapter 3). This power has to be transferred through the niobium walls to the liquid helium bath and further transferred to the room temperature environment by a refrigerating system. According to the second principle of thermodynamics, the energy E required by an ideal refrigerator to transfer a heat quantity Q from a body at 4.2K to the environment at 300K is given by,

$$E = \frac{300 - 4.2}{4.2} Q \approx 70 Q.$$

In practice, the efficiency of the best available refrigerating equipment is about 4-5 times worse, so that the actual energetic cost for the operation of the accelerating system will be $15\text{W/m} \times 350 \approx 5.5\text{kW/m}$ at an accelerating field of 5MV/m. This value is more than a factor

100 smaller than that for an equivalent normal-conducting copper structure at the same accelerating field. The economical benefit so obtained therefore largely compensates for the cost of the superconducting cavities and of the cryogenic apparatus.

The values given above have been calculated by assuming very pure niobium without localised resistive surface defects. At higher accelerating fields, the locally enhanced power absorption by such defects may be sufficient to give rise to thermal instabilities because of the poor thermal conductivity of niobium (see chapter 3). Hence, for good thermal stability, a cavity must also be made from a material with a high thermal conductivity. Indeed, progress in the niobium bulk technology has been almost entirely governed by improving the surface treatments to minimise surface defects and by developing purification techniques to increase the thermal conductivity [14]. As this approach often requires several thermal treatments at temperatures above 1700°C, the costs involved in the bulk niobium technology are very high.

As will be discussed in the next chapter, the electromagnetic field penetrates only a thin surface layer of a superconductor. The thickness of this layer is of the order of the penetration depth, λ , which in the case of niobium is about 30nm. It follows that only a very small fraction of the total amount of material, which is required for the production of a massive niobium accelerating cavity, actually determines the superconducting properties of the device, whereas all the remaining part simply acts as a mechanical support, having poor thermal properties. Taking into account the actual costs involved, it is economically very interesting to develop a composite construction of a cavity, consisting only of a thin niobium layer and the supporting substrate. The niobium film, which determines the superconducting properties, can be sputter deposited onto the inner walls of a copper resonator. Copper was chosen as the construction material for these cavities, because of its good thermal conductivity. In addition, it is cheap, easy to machine and, because of its noble character, commercially obtainable in high purity. In principle, superconducting films other than niobium, such as Nb(Ti)N [15] or high T_c superconductors, like Y-123 cuprates [16], can also be sputter deposited. However, the present results obtained with these materials are not satisfactory, because the difficulties inherent to the reactive sputter deposition are not yet overcome.

Intense research in this direction started at CERN in 1980 in the frame of the LEP2 project, leading to the successive installation of niobium coated copper resonators in LEP1 in addition to the 128 normal-conducting copper cavities at the beginning of 1991. By the end of 1998, the upgrade of LEP2 has been completed and the beam-energy has increased from 46GeV to above 100GeV [17, 18]. All normal-conducting copper cavities have been replaced by now.

An important benefit of using sputter-deposited niobium films arises from the smaller surface resistance of film cavities compared to pure bulk niobium cavities when operating at 4.2K. As this is a result of the complicated mean free path dependence of the surface resistance, predicted by the BCS theory of superconductivity, it will be discussed later. At superfluid helium temperatures, the theoretically predictable surface resistance vanishes and one is confronted with a residual term of the resistance, which can range from a few to a few hundred nΩ, both in film and bulk niobium. The successful operation of LEP2 has demonstrated the feasibility of using the film technology on a large scale without any specific operational difficulties. In the early phase of this project, however, the research on film cavities was mainly concentrated on a fast development of the coating technology for industrial production and only little effort was undertaken to understand in detail the superconducting properties of these films. This led to the widely accepted belief that the film technology should suffer from intrinsic limitations, when operated at high accelerating gradients [19-23]. Such a conjecture has its origin in the early experimental data on LEP2 cavities, displaying a severe increase of the surface resistance with increasing rf field and in the erroneous interpretation of the results by making no explicit distinction between the residual and the theoretical components of the

surface resistance. Therefore, a more fundamental study has been started at CERN in 1994 in order to investigate in a systematic way the physical properties of niobium-copper resonators and to explore the possibility of using the film technology in future accelerators such as TESLA, demanding higher gradients than those specified for LEP2. A significant fraction of the results obtained will be presented in the next chapters.

3. Microwave properties of superconductors

3.1. Conventional cavity characteristics

The electromagnetic response of a metal, whether normal-conducting or superconducting, can be described in terms of the complex surface impedance, $Z_S = R_S + iX_S = E_S/H_S$, where both the surface resistance, R_S , and the surface reactance, X_S , are real numbers, which are frequency and temperature dependent. E_S and H_S are the tangential electric and magnetic fields at the surface of the conductor. The electromagnetic field penetrates in a thin surface layer of the metal and generates electrical currents thus giving in general rise to some absorption of power. The amount of such losses per unit surface area, P_S , is related to the surface resistance by the expression,

$$P_S = \frac{1}{2} R_S H_S^2, \quad (2)$$

where H_S is the rf magnetic field amplitude at the metal surface. The most common method for measuring the surface impedance is to take a microwave cavity of the conductor and to measure the unloaded quality factor, Q_0 , and the resonant frequency as a function of temperature for one of the cavity modes. The effect of the surface resistance is to make Q_0 finite, whereas the surface reactance, which is related to the phase shift of a wave upon reflection from the surface, shifts the resonant frequency downwards. The quality factor Q of the entire circuit is a measure of the number of oscillations a resonator will go through before dissipating a substantial fraction of its stored energy. Energy can be transferred to the particle beam travelling along the cavity axis, it can be radiated out through openings or coupling probes or it can be dissipated and converted to heat by losses in the cavity wall. Like for any resonator, the quality factor, Q , of a cavity is defined as 2π times the ratio of the energy, U , stored in the fields to the energy lost over a rf period, P . If only the losses in the cavity wall are taken into account one arrives at the quantity of interest, the unloaded Q of a cavity,

$$Q_0 = \frac{\omega U}{P_0}. \quad (3)$$

To calculate the absorbed power, P_0 , one has to know the tangential magnetic field amplitude at the conductor surface, S , according to [24]

$$P_0 = \frac{R_s}{2} \int_S |H|^2 dS. \quad (4)$$

At resonance the time-averaged stored electric and magnetic energies in a cavity volume, V , are equal and are given by

$$U_H = U_E = \frac{\mu}{2} \int_V H^2 dV = \frac{\epsilon}{2} \int_V E^2 dV, \quad (5)$$

where $H = H(\vec{r})$ and $E = E(\vec{r})$ are the amplitudes of the rf magnetic and electric fields at the point \vec{r} inside the cavity volume. When all linear dimensions of a cavity with a given geometry and the resistivity are multiplied by a constant factor N , then the resonant frequency, ω , is divided by N , and the spatial configurations of the field amplitudes remain constant. From this and from equations (3-5) it follows that U/P_0 scales like $1/\omega$ and that Q_0 is given by

$$Q_0 = \frac{G}{R_S}. \quad (6)$$

The geometry constant, G , which has the dimensions of an electrical resistance, is a function only of the relative dimensions or of the shape of a cavity and the form of the resonant mode but is independent of its frequency. For the cavities under study, the value of G is 295Ω .

The surface reactance, X_s , is related to G by the equation [25],

$$X_s = 2 \frac{\omega_0 - \omega}{\omega_0} G, \quad (7)$$

where ω_0 is the angular cavity resonant frequency at a given temperature assuming a vanishing surface reactance, that is $\lambda_L = 0$ (see chapter 3.2).

The electrical length, d , of an accelerating cavity is defined as the total length of the cavity region traversed by a particle under the action of a non-vanishing longitudinal electric field. The longitudinal electric field, $E_0(z,t)$, along the cavity axis has a harmonic time dependence, and the energy gain of a particle entering the cavity at $z = 0$ is given by

$$eV_a \equiv e \int_0^d E_0(z) \sin(\omega t(z)) dz \quad (8)$$

The average electrical field is then defined as

$$E_a = \frac{V_a}{d}. \quad (9)$$

Since the average electrical field is proportional to the field amplitude, E_0 , on the cavity axis, it is also proportional to any other magnetic or electric field amplitude anywhere else in the cavity. Combining equations 3, 5 and 6 and keeping in mind the inverse proportionality of the frequency to the linear dimensions, one finds that the power loss per unit cavity length obey a proportionality relation of the form,

$$\frac{P_0}{d} \propto \frac{R_s E_a^2}{\omega G}. \quad (10)$$

The determination of the proportionality factor requires the exact knowledge of the field distribution inside the cavity and can be calculated numerically for a given cavity shape and mode by specific computer codes [26, 27].

The complete electromagnetic field distribution inside the cavity cell was shown in figure 1 and the relation between H_s and E_a for the cavities used is

$$\frac{H_s}{E_a} = 4.55 \text{ mTm} / \text{MV}. \quad (11)$$

The electric field gradient along the cavity axis is obtained from the relation

$$\frac{E_a^2}{QP_0} = 8.27 \text{ k}\Omega\text{m}^{-2}. \quad (12)$$

It is interesting to note that for a normal-conducting copper cavity at 1.5GHz and an accelerating field of 5MV/m, which is a typical value for electron-positron storage rings, the dissipated power is about 600kW/m. This very high power dissipation in normal-conducting accelerating cavities is the main reason for the interest in rf superconductivity.

3.2. The surface impedance of superconductors

In the case of a normal-conducting cavity, the field penetrates the cavity wall over the skin depth, δ , which is given by

$$\delta = \sqrt{\frac{2}{\mu\sigma\omega}}, \quad (13)$$

where σ and μ are the electrical conductivity and the magnetic permeability of the material, respectively. The surface resistance can then be written by

$$R_s = \frac{1}{\sigma\delta} = \sqrt{\frac{\mu\omega}{2\sigma}}. \quad (14)$$

Upon cooling a normal metal, the mean free path increases, causing an increase in σ and therefore a decrease in R_s . Although the conductivity of a pure material, when cooling it down to 4.2K can be increased by more than four orders of magnitude, the corresponding surface resistance decreases only by a factor five. This is a consequence of the nonlocal relation between the current and the field, when the mean free path, l , becomes comparable to the skin depth, δ . This phenomenon is called the ‘anomalous skin effect’ and as a result, the surface impedance becomes independent of the temperature [28]. To obtain a very low surface resistance, it is therefore of no benefit to cool a normal-conducting cavity to cryogenic temperatures.

In a superconductor, on the other hand, the situation is dramatically different. At zero frequency, the resistance of a superconductor is zero. At finite frequencies, the surface resistance is not zero, but is typically about five orders of magnitude smaller than the normal state surface resistance and very much less than the surface reactance. The penetration length of the electromagnetic field is no longer given by the skin depth, δ , of equation (13), but by the penetration depth, λ , which is a characteristic parameter of the superconductor, almost independent of frequency, but dependent on temperature and on the electronic mean free path, l . It is typically two orders of magnitude smaller than δ , and is expressed in the *London* theory of superconductivity [29] as

$$\lambda_L(0) = \sqrt{\frac{m}{\mu_0 n e^2}}, \quad (15)$$

where m and e are the electron mass and charge respectively, and n is the total number of electrons. The *London* penetration depth is calculated in the clean limit and can be derived from normal-state parameters. Using the following expressions for the mean free path [30],

$$l = v_F \tau = v_F \frac{m}{n e^2 \rho}, \quad (16)$$

where v_F is the electron velocity at the Fermi level, τ the transport life time and ρ the low temperature resistivity, one can express the London penetration depth also as

$$\lambda_L(0) = \sqrt{\frac{l\rho}{\mu_0 v_F}}. \quad (17)$$

The product ρl is approximately constant for a given metal. The *London* penetration depth as defined in equation (15) should be a limiting value as $t = (T/T_c)$ approaches zero but is found to

be smaller than the experimental values, even after extrapolation of the data to zero temperature [31, 32].

The discrepancy between the experimentally observed penetration depth, λ , and the *London* penetration depth could be explained by the variation of the vector potential $\vec{A}(r)$, defined as $\text{curl } \vec{A} = \vec{B}$, on the scale of a characteristic distance, ξ_0 [31]. In the microscopic theory of superconductivity, developed by *Bardeen, Cooper and Schrieffer* in 1957 [33], and further referred to as BCS theory, ξ_0 is expressed as

$$\xi_0 = \frac{\hbar v_F}{\pi \Delta(0)} = 0.18 \frac{\hbar v_F}{k_B T_c}, \quad (18)$$

where k_B is the Boltzmann constant, v_F the Fermi velocity and $\Delta(0)$ the energy gap. At $t = 0$, Δ is given by

$$\Delta(0) = \alpha k_B T_c. \quad (19)$$

The magnitude of the energy gap, $\Delta(0)$, depends on the strength of the electron-phonon coupling. The BCS theory, valid in the weak-coupling limit and for clean superconductors, predicts a value for the coupling parameter, $\alpha = 1.76$.

Although experimental results suggest a simple analytical temperature dependence for the penetration depth, the BCS theory gives a quite complicated dependence. *Mühlischlegel* [34] calculated the penetration depth in the clean limit within the BCS theory. The best fit to the tabulated values of $\lambda(\infty)$ as a function of t is given by the expression,

$$\lambda(t, \infty) = \lambda(0, \infty) (1 - t^a)^b. \quad (20)$$

The parameters a and b are 2.33 and -0.53 , respectively [35, 36].

For $t < 0.5$, the temperature variation of the penetration depth is very small and is given by

$$\frac{\lambda(t, \infty) - \lambda(0, \infty)}{\lambda(0, \infty)} = \sqrt{\frac{\pi \Delta(t)}{2kT}} \exp\left(-\frac{\Delta(t)}{kT}\right), \quad (21)$$

which contains the characteristic signature of the energy gap, the factor $\exp(-\Delta(t)/kT)$. Taking strong coupling into account as usually accomplished using *Eliashberg's* equations [37] relatively modest deviations with respect to the *BCS* results are obtained.

In the presence of impurities, λ and ξ_0 are modified approximately as [31, 38, 39],

$$\lambda^2(T, l) \cong \lambda^2(T, \infty) \left(1 + \frac{\pi}{2} \frac{\xi_0}{l}\right), \quad (22a)$$

$$\xi_0^{-1}(l) \cong \xi_0^{-1}(\infty) + l^{-1}. \quad (23)$$

Equation (22a) is exact at $t = 0$ and reduces to

$$\lambda^2(T, l) \cong \lambda^2(T, \infty) \left(1 + \frac{3\pi}{8} \frac{\xi_0}{l}\right) \quad (22b)$$

for $T \approx T_c$. *Miller* [40] has computed the temperature dependence of the penetration depth in impure superconductors from the *BCS* theory as modified by *Mattis and Bardeen* [41] to take impurity scattering into account.

At finite temperatures, not all conduction electrons are paired into *Cooper* pairs [42], but they can change their energies by an arbitrary amount and thus behave like ordinary electrons. The ratio of densities between the paired electrons, n_s and quasi-particles, n_n , can be approximated for $k_B T \ll \Delta(0)$, or equivalently for $T < T_c/2$ by an expression of the same form as that given by a simple *Boltzmann* statistics,

$$\frac{n_n}{n_s} \approx \exp\left(-\frac{\Delta(T)}{k_B T}\right). \quad (24)$$

The temperature dependent energy gap, $\Delta(T)$, plays the same role as the energy gap introduced at zero temperature. At temperature below T_c , the presence of an energy gap leads to the number of quasi-particles, which are usually called simply ‘normal electrons’, being less than the total number of electrons.

For a cavity in the *Meissner* state, the magnetic field, H_s , at the cavity surface causes a supercurrent to flow, which excludes the magnetic field from the material. Thus the penetration of a rf magnetic field into the niobium film is nearly the same as the penetration of a dc field. The surface reactance of a superconductor is, therefore, determined by the dc penetration depth and can be measured to evaluate λ .

The *Cooper* pairs are capable of carrying a current, but they cannot scatter inelastically without an energy change of at least $2\Delta(T)$, the energy required to break a pair. In the absence of photons with $\hbar\omega \geq 2\Delta(T)$, no process will lead to pair breaking and therefore there is no power dissipation due to this current. The existence of the energy gap has therefore two implications for the behaviour of the surface resistance. First, the surface resistance will vanish as $\exp[-\Delta(T)/k_B T]$ as $T \rightarrow 0$ for any frequency $\hbar\omega < 2\Delta(T)$. This follows simply from equation (24). Second, for higher frequencies $\hbar\omega \geq 2\Delta(T)$, the microwave photons can directly break a pair and be absorbed, leading to a surface impedance, which is essentially the same as in the normal state. The normal electrons, on the other hand, are assumed to respond to an electric field in the same way as in a normal metal, that is do produce dissipation when carrying a current. The complex conductivities of the two kinds of charge carriers in a superconductor therefore sum up together to provide the total electrical conductivity of the superconductor. To evaluate the two single contributions, one can write the classical expression for the complex conductivity of a metal,

$$\sigma = \sigma_1 + i\sigma_2 = \frac{ne^2 \tau / m}{1 - i\omega\tau}, \quad (25a)$$

where n is the density of charge carriers of mass m and electrical charge e and τ the transport life time that is the mean time interval between two successive collision of one charge carrier with the atoms of the crystal lattice. The fact that *Cooper* pairs do not have any dc resistivity implies that they do not undergo any collisions with the lattice, thus their conductivity is given by the limit for $\tau \rightarrow \infty$ in equation (25a),

$$\sigma = i\sigma_2 = i \frac{n_s e^2}{m\omega}. \quad (26)$$

The substitutions, $e \rightarrow 2e$, $m \rightarrow 2m$, $n_s \rightarrow n_s/2$, which have to be made to account for the pair character of superconducting charge carriers leave equation (26) unchanged. The normal part of the conductivity can be simplified for frequencies $\omega \ll 1/\tau$, as it is commonly verified in practice, since in that case equation (25a) reduces to

$$\sigma_N = \sigma_1 = \frac{n_n e^2 \tau}{m} \quad (27)$$

The total complex conductivity of a superconductor can then be written as

$$\sigma = \sigma_1 + i\sigma_2 = \frac{n_n e^2 \tau}{m} + i \frac{n_s e^2}{m\omega} \quad (25b)$$

With the approximations that have been used, the normal electrons contribute only to the real part of the conductivity and the *Cooper* pairs only to the imaginary one. The expression obtained for σ can be used to calculate the penetration depth of the electromagnetic waves in the superconductor. At $T = 0$, $n_n = 0$ and $\sigma = i\sigma_2$. Substituting equation (26) into the classical expression for the skin depth (Eqn. 13) and taking the real part only, one gets

$$\delta = \sqrt{\frac{m}{\mu_0 n_s e^2}}, \quad (28)$$

which is identical to the London penetration depth, λ_L , given by equation (15). The derived complex conductivity given in equation (25b) can be applied for the calculation of the surface resistance. As already mentioned above, the surface resistance, R_S , is nothing else than the real part of the complex surface impedance Z_S , which for any normal or superconducting material can be defined as

$$Z_S = R_S + iX_S = \frac{E_S}{\int_0^\infty j(x) dx} = \frac{E_S}{H_S}, \quad (29)$$

where $j(x)$ is the current density at a depth x inside the conductor. Applying *Maxwell's* equations and the assumption that the displacement current is negligible leads to the classical expression,

$$Z_S = (1 + i) \sqrt{\frac{\mu\omega}{2\sigma}} = (1 + i) \frac{\mu\omega}{2} \delta \quad (30)$$

For a normal conductor, σ is real and it follows directly from the expression for the surface impedance given above

$$R_N = X_N = \sqrt{\frac{\mu\omega}{2\sigma_N}}, \quad (31)$$

where the subscript N denotes the quantities referring to a material in its normal conducting state. To express the R_S and X_S for a superconductor, one has to substitute σ in equation (30) for the total complex conductivity given by equation (25b) and calculate the real and the imaginary part of the resulting expression in the limit $\sigma_1 \ll \sigma_2$, which is certainly verified for $T < T_c/2$. This leads to the expressions,

$$\frac{R_S}{R_N} = \frac{1}{\sqrt{2}} \frac{\sigma_1}{\sigma_N} \left(\frac{\sigma_N}{\sigma_2} \right)^{3/2} = \frac{1}{\sqrt{2}} \frac{n_n}{n} \left(\frac{n}{n_s} \right)^{3/2} (\omega\tau)^{3/2} \quad (32)$$

and

$$\frac{X_S}{X_N} = \sqrt{2} \sqrt{\frac{\sigma_N}{\sigma_2}} = \sqrt{\frac{n}{n_s}} \sqrt{2\omega\tau} \quad (33)$$

where n is the total conduction electron density in the normal-conducting state. Since the energy gap varies very little with temperature for $t < 0.5$ [33], one can write (Eqns. 19 and 24),

$$n_n \approx n_s \exp\left(-\frac{\Delta(0)}{kT}\right) = n_s \exp\left(-\frac{\alpha T_c}{T}\right). \quad (34)$$

In the limit $T \ll T_c$, $n \approx n_s$, and substitution of equations (34) and (31) into equation (32) leads to the approximate expression for the surface resistance,

$$R_s = \sqrt{\frac{\mu m}{n}} \frac{l}{2ev_F} \omega^2 \exp\left(-\alpha \frac{T_c}{T}\right), \quad (35)$$

where the relation $\tau = l/v_F$ has been used. Although derived from a very elementary model, equation (35) displays some of the essential features of the surface resistance of a superconductor. It describes an exponential dependence of R_s on the ratio T_c/T at temperatures well below T_c , and the quadratic dependence on the frequency, which is to be compared with the square root dependence given by equation (31) for the normal-conducting case.

Similar it follows for the surface reactance, X_s ,

$$X_s = \omega \mu_0 \lambda_L. \quad (36)$$

According to equation (7), the quantity $\Delta\lambda = \lambda(T, l) - \lambda(0, l)$ is related to $\Delta\omega = \omega(T) - \omega(0) = 2\pi\Delta f$ by the relation,

$$f(T) - f(0) = -\frac{\lambda(0, l) \mu_0 \pi f^2}{G} (y(t) - 1), \quad (37)$$

where f_0 , the cavity resonant frequency assuming zero surface reactance for the actual mode has been replaced by $f(4.2)$, the cavity resonant frequency measured at 4.2K. The error involved in this approximation is negligible, since f_0 can deviate from $f(4.2)$ by not more than 1000Hz as follows from the measured shift in frequency from 4.2K to T_c and the observed temperature dependence of λ (chapter 5).

The surface reactance is proportional to $\lambda(T)$ and follows the same temperature law. If λ increases, then the effective length of the cavity changes by the same amount, and the resonant frequency, which is inversely proportional to the length decreases. Hence, tracking the cavity resonance frequency f when T approaches T_c provides a precise measurement of the temperature dependence of the penetration depth, $\lambda(T, l) = \lambda(0, l) y(t)$, with $\lambda(0, l) = \lambda(0, \infty) (1 + 0.5\pi\xi_0/l)^{0.5}$ and $t = T/T_c$, the reduced temperature. This measurement requires some care in ensuring that the resonance frequency is not significantly affected by external parameters, such as the helium gas pressure or mechanical vibrations in the cryostat. When there is a small pressure bump in the cryostat, the cavity resonance frequency may change in an irreversible way. Therefore it is essential to calculate the derivative df/dt , in order to obtain reliable measurements.

As a result, values of $\lambda(0, l)$ are actually values inferred from fitting data to a theory of $\lambda(T, l)$. In the pure limit, a fit to curves computed with the BCS theory as given by equation (20) should give most accurate results.

However, to the extent that $y(t)$ is a universal function, which does not depend on l close to T_c and that identical experimental conditions are realised for each resonator, these measurements provide an accurate relative value of $\lambda(0, l)$. In practice, $y(t)$ has been obtained from the best fit to all the measured rates of increase of the resonant frequencies as a function of reduced temperature. When plotting the logarithm of df/dt vs t , data from different cavities have indeed shown to display the same shape, simply shifted vertically one with respect to the other because of the different value of $\lambda(0, l)$. This gives evidence for the universality of the function $y(t)$, having the same form independent of the actual value of the mean free path. Therefore, using the data from pure bulk niobium cavities as a clean limit reference, values of

$$\frac{\lambda^2(0,l)}{\lambda^2(0,\infty)} = \left(1 + \frac{\pi}{2} \frac{\xi_0}{l}\right), \quad (38)$$

have been obtained for each cavity.

More rigorous treatments of the response of a superconductor to an incident electromagnetic wave, which are based on the same mathematical formalism as the BCS theory, can be found in the literature [41, 43]. Their predictions are more accurate than those given by the model sketched above, in particular as far as the dependence on the electronic mean free path l is concerned. Both the calculations of *Mattis* and *Bardeen* [41] and by *Abrikosov et al.* [43] use a momentum independent energy gap with the temperature dependence given by the BCS theory. In either case, the surface resistance is a multiple integral that depends on temperature and frequency as well as on several material parameters, like the mean free path, the Fermi velocity, the temperature dependent gap and the density of states at the Fermi surface. The calculations are first order in the vector potential and can therefore not predict the experimentally observed dependence on the rf magnetic field, H_S (chapter 5). It is therefore common practice [25, 44] to identify R_S with its extrapolated value at $H_S = 0$ and to assume factorisation of the H_S dependence, a procedure that is followed in the present work. The data at $H_S = 0$ will be compared with theory and their evolution with H_S are described by an ad hoc parameterisation. Computer programs for a numerical evaluation of the integrals entering the expressions of the surface resistance in [41, 43] have been written by *Turneure* and *Weissman* [45] and by *Halbritter* [46]. In the present work use has been made of the computer code written by *Halbritter*, where the temperature dependence of the energy gap is parameterised in the form,

$$\Delta(T) = \Delta(0) \cos^{0.5} \left[\frac{\pi}{2} \left(\frac{T}{T_c} \right)^2 \right]. \quad (39)$$

The formulae used in this program are exact within the framework of the BCS theory for weak coupling superconductors. The program computes the surface impedance, Z_S , for the actual temperature and resonance frequency. The input parameters are the critical temperature, T_c , the reduced energy gap $\Delta(0)/k_B T_c$, the *London* penetration depth for the pure material, $\lambda_L(0)$, the BCS coherence length, ξ_0 , and the electron mean free path, l . Alternatively, the observed temperature dependence of the measured surface impedance can be fitted to obtain information about some material parameters, like the energy gap, the mean free path or the zero temperature penetration depth. The theory of the BCS surface impedance has been extended to include the effects of anisotropy and strong coupling. The effect of anisotropy has to be taken into account at frequencies above 10GHz [47], but below this value it usually leads to small corrections to the isotropic BCS surface impedance using averaged material parameters [48]. Furthermore, according to the theory of *Anderson* [49] and to measurements of the energy gap in niobium single crystals with different residual resistivity ratios [50], anisotropy effects are expected to be smeared out by scattering when the resistivity ratio becomes low as in the case of sputter deposited films.

Strong coupling corrections to the superconducting state are usually obtained with the *Eliashberg* [37] equations. However, several authors [51-53] have discussed the weak coupling approximation made in [41, 43] and concluded that for the range of parameters relevant to the present work, strong coupling can approximately be taken into account by simply treating the energy gap as a parameter in the BCS theory.

There are two approximate formulae for the BCS resistance, which are frequently used in data analysis and valid in the regime $t < 0.5$ and $\nabla\omega \ll 2\Delta(T)$. The first expression is given by [25]

$$R_S \propto \frac{(\hbar\omega)^2}{kT} \ln\left(\frac{4kT}{\hbar\omega}\right) \exp\left(-\frac{\Delta(t)}{k_B T}\right). \quad (40)$$

This formula has been compared with the numerical computer calculations of the BCS surface resistance [54] and has been found to give the correct temperature dependence to within $\pm 5\%$. Another widely used approximation, which also has been used for data analysis in the present work, is the formula,

$$R_S = R_{BCS} = A(l, \xi_0, \lambda_L, \omega^2) \frac{l}{T} \exp\left(-\alpha \frac{T_c}{T}\right) \quad (41)$$

which is remarkably close to the result of the simple model sketched above. It also gives the correct temperature dependence of the surface resistance but yields a gap parameter, α , which is higher by approximately 10% than that obtained from equation (40) [54] and from the *Mattis* and *Bardeen* expressions. The pre-exponential factor A is temperature independent, but depends on material parameters like the coherence length, ξ_0 , the electron mean free path, l , and the London penetration depth, λ_L .

The implication of the discussion so far is that following from the temperature dependence of the quasi-particle density, one can make a superconducting resonator of arbitrarily high quality factor by operating at sufficient low temperatures. In practice, however, it is almost never observed that the surface resistance does vanish together with T but levels out at a certain value of R_S , and becomes independent of temperature. Therefore, experimental results agree with theory only after having subtracted a residual component from the measured surface resistance, which is also called residual resistance, R_{res} . The residual resistance, which is observed to vary from one cavity to the other (Figure 2) can unambiguously be separated from the theoretical surface resistance, thereafter referred to as the BCS resistance, R_{BCS} , by extending the measurements down to low temperatures where R_{BCS} has become very small. While losses described by R_{BCS} are distributed over the whole sample surface, there is clear evidence that the additional losses in niobium films are localised in the neighbourhood of surface defects and can be reduced to negligibly small values in the absence of such defects. For practical application of the niobium film technique for further large-scale projects using accelerating cavities, the lowering of these additional losses is an important task and therefore a main aspect of the present work. It is useful to expand relation (41) into

$$R_S(H_S, T) = R_{BCS}(H_S, T) + R_{res}(H_S), \quad (42)$$

to account for experimental observations.

Experimental data of the surface resistance of superconducting niobium films and massive niobium as a function of the temperature are shown in figure 2. The data have been taken at very small surface field amplitudes ranging typically from 0.5 to 4.5 mT and minor corrections have been applied in order to refer to $R_{BCS}(0, T)$. Besides the increase of the BCS surface resistance with the rf field amplitude, which does not find an explanation in the framework of the BCS theory, an enhancement of the residual resistance with the rf field amplitude is also frequently observed. This phenomenon produces a characteristic “slope” in the R_{res} vs. H_S curve and is therefore measurable in $\text{n}\Omega/\text{mT}$ or equivalently in $\text{n}\Omega/\text{MVm}^{-1}$. Whereas a small residual term of the order of, say 10 to 20 n Ω (Figure 2) would give no limitations to the use of film cavities, it was in the past frequently observed dramatic increase of this term at higher gradients, which gave rise to doubts about the applicability of the film technology in future accelerators. A detailed discussion of the residual resistance will follow in chapter 5 and the conclusion to be drawn will be that there are no fundamental limitations of the film technique preventing high accelerating fields to be reached.

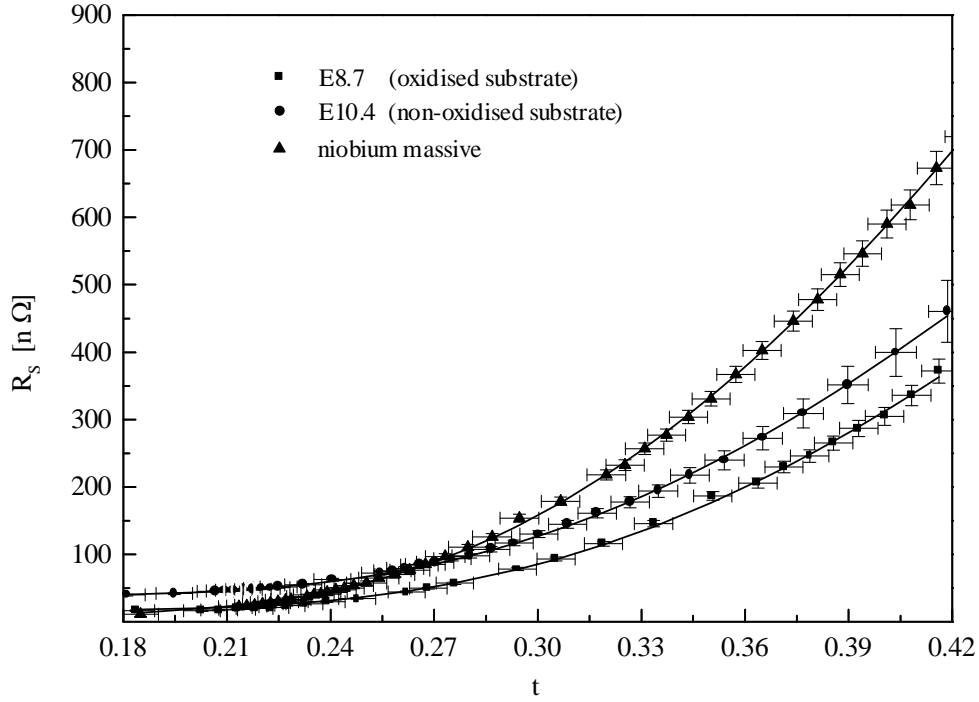


Figure 2. The temperature dependence of the apparent surface resistance of niobium films sputter deposited on oxidised copper (squares), after reverse sputtering of the substrate in the two-electrode system (circles) and of a massive niobium cavity (triangles). The full lines represent a fit to the data of the form $R_{res} + A (1/(T_c t)) \exp(-\alpha/t)$. The mean free path dependent term A , the coupling parameter α and the residual resistance R_{res} are the three free parameters in the fitting process. For the determination of the critical temperature see chapter 5 and II/2 and for a detailed description of the experimental techniques for production of niobium film cavities see chapter 4.

The only known fundamental limitation on the amplitude of the rf field inside a superconducting cavity is fixed by the value of the critical magnetic field of the material. The discussion so far was restricted to the full Meissner state [55] with values of H_s well below this critical value, where magnetic flux generated by the rf field starts to enter the material, whose normal-conducting core is an important source of rf power dissipation. In a type-II superconductor like niobium, flux penetration occurs at the lower critical field H_{c1} . However, the actual limiting value for the rf field is observed to be larger than the measured value of H_{c1} . In fact, since the nucleation time of a vortex is usually large compared to a rf period, a metastable superconducting state with no field penetration can persist up to a so-called superheating field H_{sh} , which is typically of the same order as the thermodynamical critical field H_c [56-58]. The thermodynamical critical field, $\mu_0 H_c(0)$, has been measured for niobium with varying impurity content and was found to take a value of 197 ± 5 mT, independent of the mean free path [13]. For a *Ginzburg-Landau* (GL) parameter, $\kappa \cong 1$, where κ is defined as the ratio λ/ξ_{GL} with ξ_{GL} as the distance over which the wavefunction of the centre-of-mass motion of the cooper pairs can vary without undue energy increase [59], the superheating field is approximately given by $H_{sh} \cong 1.2 H_c = 230$ mT [56]. For a niobium cavity operating at low temperatures, $T < 2$ K, this value defines the theoretical limit of the magnetic field amplitude at the surface of a niobium resonator, which corresponds to a maximum theoretical accelerating field of 50 MV/m!

In practice, parasitic losses initiating an early breakdown have always prevented this theoretical limit from being reached. These losses are present in film cavities as well as in bulk niobium cavities and at the present technological state of advancement, two sources of additional losses are encountered for at higher fields,

- a) Small normal-conducting defects like foreign material inclusions with dimensions larger than the coherence length, ξ_0 , beads from electron beam welding of the half-cells, faulty welds or chemical residues in the case of massive niobium cavities [60, 61]. Typical defects in films are identified as local lacks of adherence causing blisters in bad thermal contact with the substrate, peeled-off niobium flakes and local defects caused by defective substrate treatment (see chapters 4 and 5) or by dust particles remaining on the copper surface before sputtering. In niobium films, these defects are observed to cause already a field dependent residual term of surface losses at small microwave field amplitudes. At higher fields, dissipation of an excess amount of heat will finally bring about a drastic decrease in the Q of the resonator. If a surface region develops a higher surface resistance than the average, a significant fraction of the total power fed into the cavity will be dissipated in this region, which will increase the temperature locally. There the critical field H_{sh} is thus lowered, and when it becomes smaller than the rf field a transition to the normal state occurs, which can eventually extend to the whole resonator and produce a quench (thermomagnetic breakdown). Similarly, surface roughness or protrusions on the surface may also cause increased local power dissipation due to local field enhancement in regions, which are already in reduced thermal contact with the bulk of the film and therefore with the copper substrate.
- b) The presence of field emitted electrons induced by the electric rf field at particular sites inside the cavity, which is still the main limitation in reaching very high field amplitudes in both, film and bulk niobium resonators. Though field emission or non-resonant electron loading has been studied intensively in the past by several authors [62-67], its detailed mechanism remains still a subject for further investigations. In particular it is not well understood why certain defects behave as emitters when the electric rf field normal to the surface becomes intense enough, while others do not emit and what role the insulating layer between the particle and the substrate plays. In most cases, active emitters in bulk niobium cavities are identified as local inclusions of sulphur or tantalum, loose metallic particles or dust particles, and geometric defects, where the amplitude of the electric field is greatly enhanced. The field-emitted electrons are accelerated by the electric field in phase with the microwaves and their trajectories may end up somewhere on the cavity wall, generating heat and X-radiation by bremsstrahlung and dissipation of kinetic energy. Electron impact at the equator will therefore deteriorate the surface resistance considerably. Several diagnostic techniques, like temperature or X-ray mapping [68] allow for indirect studies of the emitting sites and for visualisation of the electron trajectories.

Though for most film cavities discussed in the present work, field emission was the dominating loss mechanism at typical values of accelerating fields between 8 and 15MV/m, it occasionally happened that a cavity could sustain also accelerating fields beyond 20MV/m. Collaborative studies together with the CEA laboratory at Saclay, France, have shown that film cavities produced at CERN and measured to have strong field emission at about 10MV/m could easily reach higher field gradients by an improved high pressure water rinsing under clean room conditions. These observations provide clear evidence that enhanced field emission is not an intrinsic feature of the film technology and that accelerating fields up to 25MV/m at 1.5GHz with quality factors of 5×10^9 as required for the TESLA project and already obtained on prototype bulk niobium resonators at CERN (chapter 5) and in other laboratories [14], can also be reached with film cavities. The data presented in this study, however, are restricted to a field range from which electron emission effects are absent. Since some electron trajectories reach through the cavity beam tube the coupling antenna, the latter is capacitively coupled to the external circuit in order to allow for the detection of the resulting current, which is typically in

the nA range and increases steeply with the rf field (chapter 5). In addition, the onset of field emission was signalled by an X-ray counter, which has been installed outside the cryostat.

Thermal breakdown at local defects has been shifted for massive niobium cavities to surface fields above 130mT by improving the surface cleaning techniques and by a heat treatment together with solid state gettering (chapter 4) at 1200-1700°C [69, 70]. The latter technique improves considerably the residual resistivity and hence the thermal conductivity at cryogenic temperatures, which increases the field threshold for thermal instabilities. The quench-field has been found to increase approximately proportional to the square root of the cavity thermal conductivity [71]. The thermal conductivity at 10K is 1420W/Km for copper ($RRR \sim 100$) and of the order of 500W/Km for niobium [72], which of course will be drastically reduced in the superconducting state. In addition, the latter value implies a residual resistivity ratio of 400, which is feasible only after application of costly purification techniques.

In most cases, however, field emission remains the ultimate limiting factor for the achievable accelerating field, but procedures have been found to displace statistically the onset of this phenomenon continuously to higher field values.

4. Experimental method and procedure

The following section describes the standard manufacturing processes of copper resonators, which have been developed by industry or other laboratories outside CERN. Also described in this section is the chemical treatment of copper substrates according to a standard recipe, developed at CERN several years ago. Electroplating of copper resonators and electrochemical polishing were studied and developed in the framework of this work. Section 4.2 will then describe the sputtering procedure, as optimised for sputter deposition of LEP cavities. Use has been made of two sputtering systems, which were slightly modified to allow for the sputter deposition of the 1.5GHz copper resonators.

4.1. Preparation and characterisation of the copper substrate

The cavity walls, serving as a substrate for the deposition of the niobium film, are made of high conductivity copper in order to minimise the temperature gradient across the walls during rf operation, while maintaining a sufficient mechanical rigidity. The importance of having a copper substrate free from macroscopic defects when starting deposition of the niobium film has been recognised soon and this information is partly based on earlier observations at CERN but mainly on results of the present study. Inspection of the cavity interior by optical microscopy, allowing for a topographical characterisation of both, the film and the underlying copper surface, has shown that the quality of the niobium coating is often limited by a defective copper substrate. These investigations were routinely carried out by inserting a mechanical device with an electronically controlled, moveable mirror through the lower flange of the cavity into the interior of the cell. The mirror image is collected by a video camera connected to an optical system. Changing stepwise the inclination of the mirror and rotating the cavity slowly around its axis enables a visual inspection of the inner surface of the cell. The obtained images have a magnification factor of 50 to 100.

Frequently observed macroscopic defects are scratches, protrusive zones or grooves on the copper substrate. Shadowing effects causing differences in the density of the sputtered atoms around geometrical substrate defects like trenches, holes or steeper steps are responsible for poor defect coverage also leading to an irregular thickness profile of the sputtered niobium film [73]. Since the residual term of the surface resistance as well as its dependence on the electromagnetic field is found to be strongly related to the macrostructural quality of the film (chapter 5), efforts were made to minimise the quantity of local and structural surface defects on the copper substrate. First of all, several processes have been used to manufacture the cavities, namely hydroforming, lathe spinning and electroplating. Hydroforming as a production method for niobium cavities was first used at HEPL (Stanford) [74]. Hydroformed copper cavities are made starting from oxygen free electronic grade (OFE) tubes inflated at high pressure (up to 2×10^7 Pa) inside a rigid die in three successive steps, each preceded by vacuum annealing at 600°C for one hour [75]. Spun cavities have been provided by the INFN laboratories in Legnaro (Italy), where lathe spinning for the production of cavities has first been introduced, and by the CERN main workshop. These cavities are made starting from 3mm thick OFE sheets, previously vacuum annealed at 250°C for two hours, and shaped over a collapsible inner mandrel [76]. For the production of electroplated cavities, the pulse plating technique from the pyrophosphate bath has been chosen. Deposition is started on a metallised (by magnetron sputtering of 3µm of copper) glass mandrel, which is subsequently dissolved in hydrofluoric acid. All three manufacturing techniques have the advantage of avoiding the need for an equatorial weld, at variance with the more common technique of deep drawing.

As will be shown in chapter 5, a good hydroformed cavity does not nearly reach as low a surface resistance as obtained with the best spun cavities. A great part of this behaviour must be

attributed to the observed large surface raggedness on the scale of the grain size (50 to 100 μm), which is also known as ‘orange peel’ effect. Already at an initial stage of this work, it has therefore been decided to stop the activities on hydroformed cavities and to concentrate on the spun technique and on electroplating.

First results obtained on niobium films deposited on electroplated copper cavities produced at CERN are included in the subsequent analysis, but they are not predicative. Pinhole formation and local structural irregularities, as identified by optical and scanning electron microscopy (SEM), mask the benefits one may gain from a smooth, uniform and fine-grained copper substrate, which in addition should be free of macrostresses. These initial difficulties in producing defect and pore free copper deposits by electroplating arise partly from the use of a pyrophosphate bath, which is known to be very sensitive to organic impurities and to require very careful control [77] but had to be chosen for its neutral and non-toxic nature. In the meantime the activities on electroplating are again restricted to laboratory tests to optimise the process.

However, another preparation technique to improve the quality of the copper surface, namely electropolishing of spun cavities, has already been implemented successfully and this technology will be described in more detail below.

Cavities made by spinning have a small average surface roughness⁽¹⁾ (0.2-0.3 μm after chemical polishing) and show no ‘orange-peel’ effect. The copper grains are elongated and typically 100 \times 10 μm^2 in size. The thermal conductivity was measured to be $540\pm 70\text{Wm}^{-1}\text{K}^{-1}$. The cavity surface still suffers from numerous local defects, which are caused by the machining tool and are typically between 10 and 200 μm in diameter (Figure 3). Fortunately, chemical etching of 150-200 μm copper is usually sufficient to flatten these defects and to restore a smooth surface. The cavity cell, close to the transition to the cut-off tube, called iris, however, often shows several radial cracks, which cannot easily be removed by chemical etching. These cracks, which are a few hundred μm deep, are caused by bending stresses reaching their maximum value at the iris.



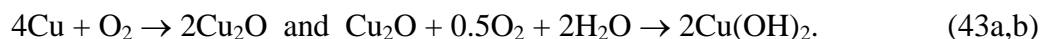
Figure 3. SEM photograph showing the surface morphology of a copper sample after chemical polishing of 80 μm .

⁽¹⁾Roughness was measured using a standard stylus instrument, having a tip diameter of ten micrometers. The average roughness R_a according to standards DIN 4768 and ISO/DIS 4287/1 is defined as the arithmetic mean of all values of the roughness profile within the evaluation length, L .

Significant improvement has been achieved with cavities spun as a sandwich made from the copper blank and a thinner iron blank [76]. With this technique, the roller is not in direct contact with the copper and the iron blank should absorb most of the stress otherwise released to the copper.

As mentioned above, the machined copper cavity is chemically etched and polished in order to obtain a clean and smooth surface before coating. The rather complex polishing agent, which has been developed at CERN [78] and called 'SUBU', is a mixture of sulfamic acid ($\text{NH}_2\text{SO}_3\text{H}$, 5g/l), hydrogen peroxide (H_2O_2 , 50ml/l), n-butanol ($\text{C}_4\text{H}_9\text{OH}$, 50ml/l) and di-ammonium hydrogencitrate ($\text{C}_6\text{H}_{14}\text{N}_2\text{O}_7$, 1g/l) in aqueous solution. Though each of these chemicals are not very corrosive to copper, the mixture in the given concentration can remove 15-20 μm of copper ($\sim 1\mu\text{m}/\text{min}$) before the effectiveness of the bath slows down considerably. Increasing the concentration of sulfamic acid to 20g/l, the polishing rate can be raised to a maximum value of $\sim 4.5\mu\text{m}/\text{min}$. However, this rate is not constant but increases continuously at the beginning and stabilises at a certain value after activation of the bath. The process of etching with 'SUBU' is based on the oxidation of copper by hydrogen peroxide and the subsequent dissolution of the copper oxide by the sulfamic acid and ammonium citrate. To control the oxidation rate of copper, hydrogen peroxide is stabilised by butanol. Oxidation of butanol, leading to the formation of n-butyric acid and viscous fatty acid ester is desirable to achieve the polishing effect by passivation of the copper surface. The primary reaction product of ammonium citrate and copper, a voluminous complex in octahedral arrangement, contributes efficiently to the formation of the passive surface layer. Operation temperature of the bath is 70°C and stability is ensured for forty minutes after addition of hydrogen peroxide. The bath is kept in a stainless steel tank under stirring and the cavity is mounted in a closed circuit with this tank. The polishing mixture is then pumped through the cavity having a turbulent bath circulation. After exhaustion of the polishing bath, the cavity is first rinsed with sulfamic acid to remove residual copper oxide and then with high purity, dust free demineralised water. To obtain high cleanliness of the inner cavity surface prior to coating, the final step of surface preparation consists of high-pressure water rinsing under filtered nitrogen atmosphere. To avoid re-contamination of the wet cavity surface, the assembly steps are carried out in front of a laminar flow. The high pressure rinsing system consists of a high-pressure pump, a filter, a spray nozzle and a mechanical system, which allows for scanning of the interior surface with the high-pressure water jet. The high-pressure pump supplies approximately 8 litres of water per minute at 10^7Pa , measured at the filter inlet. The connecting lines are made of teflon with stainless steel braids; the spray nozzle and the rigid feed pipe from the filter to the spray nozzle are made of stainless steel. The scanning system moves the feed pipe up and down in the cavity at a constant low speed. The resistivity of the output water is monitored and stabilises at its input value, in excess of 17M Ωcm , after typically 500 litres. A major disadvantage of the rinsing system described above is the need to expose the cavity again to the external atmosphere in order to remove the feed line and the spray nozzle. Thereafter the cavity is heated up to 60-70°C and dried by pumping. The drying time is approximately 2 hours and care has been taken not to freeze the water inside the cavity. After drying, the cavity has been transported to the clean room, exposed to atmospheric pressure under a class 10-100 laminar flow and assembled for mounting on the sputtering system.

Alternatively, the wet cavity has directly been dried in the clean room. Both drying procedures have proven to give the same results for cavities coated under otherwise identical conditions, in spite of the fact that the nature of the copper oxide may change considerably, according to the chemical reactions,



For subsequent coatings, after having stripped the preceding niobium film with a solution containing hydrofluoric acid and sodium benzoate, the removal of 10 to 20 micrometers of copper is usually sufficient. Typically ten successive coatings can be made on the same substrate depending on the initial thickness, after which its mechanical rigidity may become too low for further use.

A significant improvement in the superconducting rf performance of niobium coated copper resonators has been obtained by replacing chemical polishing by electropolishing. It was already known for a long time [79] that chemical polishing with the complex mixture described above could lead to etching pits. The complex nature of the polishing agent implies a precise control of all process parameters to benefit from the excellent polishing capability of this bath, which turned out to be difficult to master for polishing of closed structures. An example of a defect introduced by a locally preferred chemical attack is shown in figure 4. Such defects result from gas bubbles, which adhere to the copper and grow during their stay at the surface. The effect of the bath is to erode preferentially the region just around the bubble, leading to a molehill like defect. It also happened occasionally that the whole surface treatment had to be repeated because of serious local corrosion of copper during chemical polishing with ‘SUBU’. Experiments to study electropolishing of 352MHz copper resonators have already been performed at CERN and other laboratories several years ago [80, 81] but first results did not encourage investing further efforts. The main problem was the bad adherence of the niobium coating on an electropolished surface, leading to the formation of local blisters and to peel off. However, following the ultimate goal of the present study to maintain a negligible surface resistance at high rf field amplitudes naturally implies the use of a defect free copper resonator.

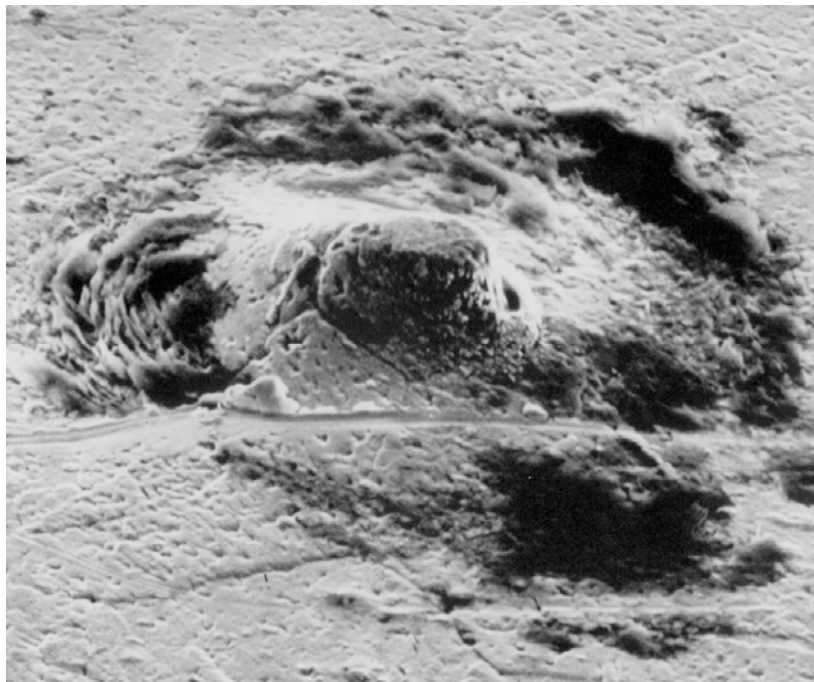


Figure 4. SEM photograph of a niobium film showing a typical defect caused by etching pits on the underlying copper substrate ($\times 2500$).

Electropolishing of metals was first studied systematically by *Jacquet* [82], who already obtained a patent in 1930 [83]. Though electropolishing of metals has now been widely used, its detailed mechanism remained unclear, and different ideas have been proposed [84]. The original ideas of *Jacquet* and *Wagner* [85] are based on the establishment of a diffusion layer at the metal/electrolyte interface composed of a metal ion acceptor diffusing through a

concentration gradient to the metal surface. The thickness of this stationary layer is between 5×10^{-3} and 5×10^{-2} cm in a motionless electrolyte. This theory implies that electropolishing is a diffusion-controlled process and that the electrochemical current density is given by Fick's law. Other authors proposed that surface brightening might exclusively be caused by the formation of a viscous film with high resistance [86]. Regarding the formation of surface films on copper in a phosphoric acid electropolishing solution, as used in the present work, the formation of a viscous dehydration film with a complex composition is experimentally well established [87-90].

The cavity is used as an anode and copper is dissolved by chemical reaction with a metal ion acceptor of the electrolyte. The zone close to the metal surface will soon be saturated with dissolution products and the thickness of this resistive layer will vary according to the roughness of the surface resulting in a higher current density around protrusions and thus giving a levelling effect.

Before electropolishing, the cavities were chemically degreased, dipped in sulphuric acid and rinsed with deionised water. The experimental set-up for electropolishing 1.5GHz resonators is shown in figure 5.

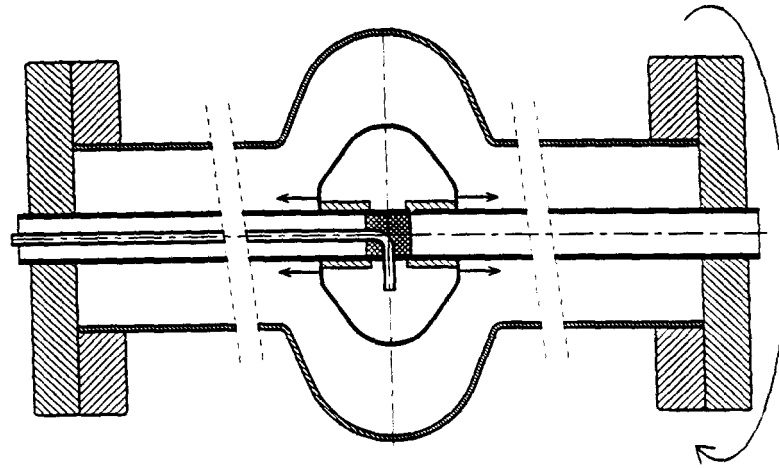


Figure 5. Schematic drawing of the cavity after assembling the main parts for electropolishing (see text).

The basic components defining the electrolysis cell are a perforated stationary cathode, which is designed like an umbrella to maximise the cathodic surface area and the cavity, which is rotating with constant speed. Polishing is made under nitrogen atmosphere with continuous bath circulation. The cathode, a copper tube with a special central part composed of bendable perforated sheet copper, is introduced with the help of a guide rail into the cavity via a central opening in the end plates. The end plates are made of teflon serving as an insulation material. A special clamping device located in protective steel housing inside the tube enables the opening of the cathodic sheets in the centre of the cell. The copper tube, which accommodates the feed pipe for nitrogen serves as a feeding for the polishing bath. After assembling, the electrolysis cell is directly connected to a motor, allowing for rotation of the cavity around its axis but keeping the cathode in a fixed position. A pump for electrolyte circulation, a 300 litres storage tank for the bath, and a cooling coil in front of the cavity are the other components forming a closed circuit. The cathodic surface area is 120cm^2 and the active surface to be polished is defined by the electrolyte level in the cavity cell, which can be reduced by increasing the partial pressure of nitrogen above liquid. Under operating conditions, a surface ratio of 1:3 between cathode and anode is maintained. The nitrogen atmosphere also prevents the part of the cavity

cell, which is just out from liquid, from uncontrolled oxidation. The distance between the electrodes varies from 15mm at the cavity iris to approximately 25mm at the equator. This variation should be small enough to avoid gradients in the electrochemical potential along the cavity cell [80]. The classical electropolishing solution, a mixture of 45vol% butyl alcohol and 55% phosphoric acid ($\rho = 1.71\text{g/dm}^3$) was already in use at CERN and has not been optimised further. However, more recently, organic additives are described in literature, which stabilise the optimum range of polishing [91]. Excessive dilution of the bath with water should be avoided, because it gives a tarnished copper surface after polishing. The electrolyte was cooled down to 17-18°C before entering the electrolysis cell and the temperature raised to ~21°C as measured at the cavity outlet. The circulating pump supplies approximately 30 litres of electrolyte per minute, but the circulation has to be reduced to smaller values for polishing. An optimised flow of 3-6 litres per minute was adjusted with the help of a mechanical valve. All parameters treated above have been optimised by optical inspection of the polished surface and by following the current-voltage characteristics of the process. Three regions can be distinguished from the final curve, which is shown in figure 6.

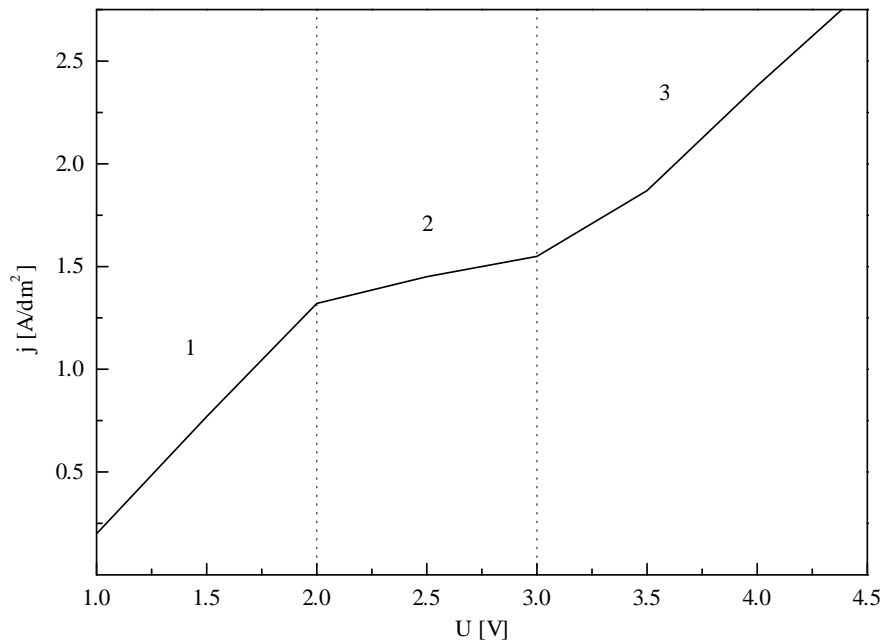
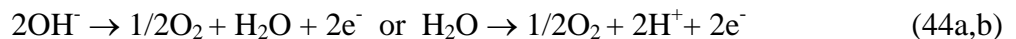


Figure 6. Current-voltage characteristic of the copper resonator in a phosphoric acid/butyl alcohol electrolyte under optimised conditions. Note that the plotted potential is not the electrochemical potential of the anode measured against a third reference electrode but simply the potential measured between the cathode and the cavity.

In region 1 (active zone), the current density increases with potential and copper is corroded by a progressive formation of a solid layer of CuO and $\text{Cu}_3(\text{PO}_4)_2$. Region 2 (passive zone) is the effective (micro)-polishing zone. The solid layer has peeled off and the viscous diffusion layer defines the conditions of molecule transport near the copper surface. The resistance increases with the average thickness of the viscous film and the measured current density should remain nearly constant. Chemical reaction of copper ions with an ion acceptor and diffusion of these complex molecules into the electrolyte are in equilibrium. Seeking for a distinct passive zone defined the optimisation procedure for electropolishing of the copper resonators.

In region 3, the viscous layer breaks down and the current yield is reduced by formation of O_2 at the anode according to the electrochemical reactions,



At higher current densities, butyl alcohol will also be oxidised and gaseous CO_2 is formed. (Macro-) polishing in zone 3 is still possible but local corrosion can occur due to gaseous bubbles adhering to the copper surface. From figure 6 it can be seen that the optimum current density for electropolishing lies between 1.4 and 1.6A/dm^2 .

The electrochemical process at the cathode consists in the formation of hydrogen and in the reduction of copper. Such a reaction has the advantage of self-regeneration of the polishing bath but makes it necessary to interrupt the process for cleaning the cathode from refined copper before the layer becomes too thick and fine powder can fall off. Removing the damaged surface layer of a new cavity prior to the first coating by micropolishing would therefore be very cumbersome, not only because of the low polishing rate. It was, therefore, decided to adopt the process of electrochemical machining for eliminating the macroscopic roughness of new spun cavities. In practice, this simply means to work at current densities above 6A/dm^2 and to increase the bath circulation to the maximum value of 30 litres per minute. Refined copper will immediately be swept out and the polishing rate increases to approximately $2\mu\text{m/min}$. The final polishing is then always done in zone 2.

As mentioned above, problems arose with film adherence on electrochemically polished surfaces. A convenient method to overcome these difficulties quickly was to apply a final chemical polishing of the resonators with the chemical bath described above, but to reduce the immersion time. Optical and chemical analysis of copper samples, treated in the same way as cavities, showed, that chemical residues remained on the electrochemically-polished surface. Though no detailed analysis has been made to identify the chemical nature of the residues, the reason for the formation of a dull film at the surface was identified soon and appropriate cures were devised. The main cause was a wrong surface cleaning, which initially consists of distilled water rinsing of the electrolysis cell immediately after having finished polishing. As a consequence, the cavity was exposed to an electrolyte, which has been diluted with water, and this mixture was found to be corrosive to copper. A modified procedure avoids this step by removing the emptied electrolysis cell from the circuit and disassembling all parts before re-dipping the cavity into the electrolyte to dissolve residuals of the polishing bath adhering to the dry surface. This process has been optimised to take as little time as possible. Thereafter the cavity is washed with distilled water, followed by methyl alcohol and dried under a laminar flow. A final chemical treatment to remove copper oxide before high-pressure water rinsing consists in rinsing the cavity with ammonium hydrogencitrate (0.05mole/l) and sulfamic acid. This treatment has been found to produce maximum brightening of copper and to give perfect film adherence. The improvements in terms of the residual surface resistance will be shown in a later chapter. Starting in 1999, chemical polishing has finally completely been replaced by electrochemical polishing as the substrate preparation technique for 1.5GHz copper resonators.



Figure 7. SEM photograph showing the surface morphology of a copper sample after electrochemical polishing of 130 μ m ($\times 2500$).

In a few cases bulk niobium cavities were used to serve as a reference when discussing the superconducting properties of niobium film cavities. These cavities are made from high purity niobium sheets with a nominal *RRR* of approximately 300, either by spinning as described above or by electron beam welding of two deep-drawn half-cells [92]. In order to remove the damaged superficial layer, the cavities were chemically treated with buffered chemical solution of equal parts of hydrofluoric (HF, 48%), nitric (HNO₃, 69%) and phosphoric (H₃PO₄, 87%) acid followed by high pressure rinsing. After measurement, the cavities have been heat treated at 1000°C or 1100°C in a UHV furnace in order to study the resulting evolution of their superconducting properties. The cavity to be treated was enclosed, together with test samples in a niobium box, itself enclosed in a titanium box used as getter material. These two boxes are in turn enclosed in an external niobium box, ensuring optimal getter efficiency for desorbed gases, while protecting the cavity from the furnace residual pressure and from contamination by titanium atoms. At the end of the firing, the UHV furnace is brought to atmospheric pressure with dry nitrogen. The furnace lid is removed, and as the substructure consisting of the cavity and protection/gettering setup as described above is lifted from the furnace it is sealed into a clean plastic foil and transported to the clean room. The design of the niobium/titanium getter-box is shown in figure 8. Secondary ion mass spectrometry (SIMS) measurements of the titanium content on test samples indicated that contamination in deeper surface layers could be kept below 100ppm.

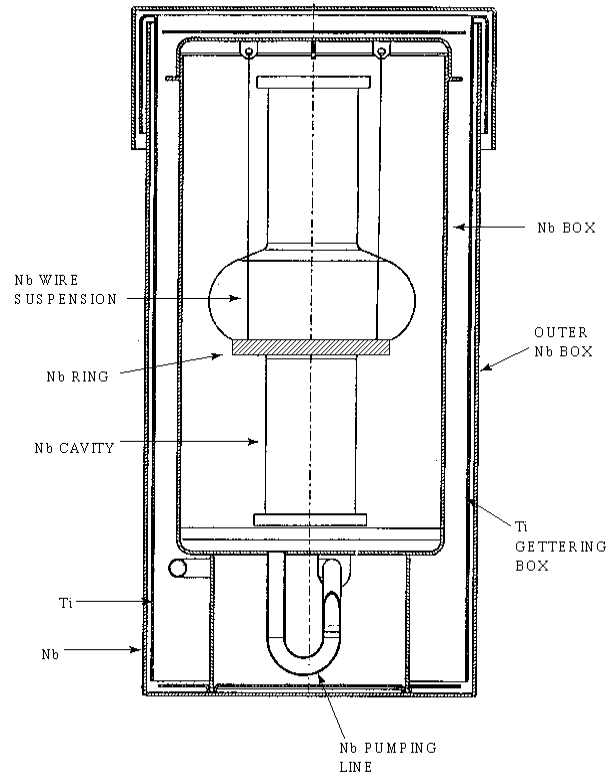


Fig. 8. Schematic view of a bulk niobium cavity enclosed in a protection/gettering set-up for heat treatment.

4.2. Magnetron sputter-deposition of niobium thin films

The layout of the standard sputtering system is shown in figure 9. It is based on the cylindrical magnetron technology [93-95], and was adopted at CERN in 1984 for the deposition of superconducting niobium films on the inner walls of copper resonators [18]. The copper cavity to be coated is assembled with the niobium cathode and a bakeable valve in a clean room of class 10 to 100. A ceramic section on top of the cavity tightly links the cathode to the stainless steel Conflat⁽¹⁾ flanges brazed to the cavity. At the same time it acts as an insulator between the cavity, which is held on ground potential, and the cathode. The latter is a hollow stainless steel barrel surrounded by a niobium liner and is mounted on the cavity axis. The liner is 48mm in diameter and made in three parts, a central zone of high purity niobium with a *RRR* of 300 used as target material for coating the cavity cell and the outer zones of reactor grade niobium used for coating the cut-off tubes of the cavity. During assembly all operations are carefully handled to prevent unnecessary contamination of the inner cavity surface. The final assembly, consisting of the copper cavity, the cathode with the ceramic insulator and a transition piece on which the valve is mounted, is connected vertically onto the sputtering system in such a way that the cavity wall stands as a part of the vacuum chamber. An external steel frame is subsequently mounted to support the cavity. The valve isolates the cavity and the cathode from the laboratory atmosphere during transfer from and to the clean room. A small permanent magnet, an alloy of samarium and cobalt, is introduced into the cathode and can be moved up and down along the cavity axis in order to sustain the discharge at the desired level. Cooling the stainless steel cylinder with compressed air prevents the magnet from reaching the Curie temperature during sputtering. The magnetic induction is about 10mT on the outer surface of the cathode. The magnetic field, which is parallel to the cathode surface, confines the discharge

⁽¹⁾Registered trademark of Varian Associates, Palo Alto, USA.

and restrains the primary electron motion in the vicinity of the cathode, thereby increasing the ionisation efficiency of the sputter gas by approximately two orders of magnitude. The advantages of using the cylindrical magnetron sputtering are a high sputtering rate, a uniform erosion profile around the cathode and the possibility to sustain a stable discharge at low pressures. The operating pressure can be low enough to make the mean free path of both the working gas and the sputtered atoms of the same order of magnitude as the target-to-substrate distance. Thus the sputtered niobium atoms pass to the substrate with little loss of kinetic energy, as do energetic argon atoms (ions that are neutralised and reflected at the target surface). Bombarding the substrate with energetic sputter atoms significantly improves film adhesion. The influence of the reflected, energetic argon neutrals on film morphology will be discussed in part II of this work when discussing the general properties of sputter deposited films.

Whereas the cut-off tubes of a cavity are sputtered in various steps by moving the magnet along the cavity axis, the cavity cell is sputtered in a single step by placing the magnet exactly in the centre of the cavity. Since variations in the erosion rate around the barrel do not occur, the cavity does not have to be rotated around the cathode. The length of the magnet, which defines the erosion zone and the diameter of the cathode, were optimised in order to achieve a uniform film thickness over the cavity cell. Ignoring gas-phase collisions, the growth rate, C , can be represented by

$$C \propto \frac{1}{x^2} \cos \theta \cos \alpha, \quad (45)$$

where x is the distance from the substrate to the cathode surface, θ is the angle between the cathode normal and the substrate and α is the incident angle of the atoms incident on the cavity wall. The coating rate falls off inversely to the square of the distance and decreases with the angles, θ and α . A proper choice of the length of the magnet and of the cathode diameter compensates the opposing effects of distance and emission angle, allowing a uniform thickness profile to be obtained in the cavity cell. From the visible erosion of the cathode surface, it is possible to infer the size of the active region, which is typically $\pm 1\text{cm}$ along the cavity axis from its centre. Such a source size implies mean incidence angles of the atoms on the cavity wall of typically $15 \pm 5^\circ$, varying from $9 \pm 4^\circ$ at the equator to $50 \pm 10^\circ$ near the irises. Sample studies indicate that the incidence angle must be kept below 50° in order to ensure a good film quality. SEM observations of the film in cross-section, surface density and X-ray fluorescence measurements made on samples cut from coated cavities show that the film thickness does not deviate by more than $\pm 10\%$ from its average value, provided that the magnet is positioned in the centre of the cavity cell.

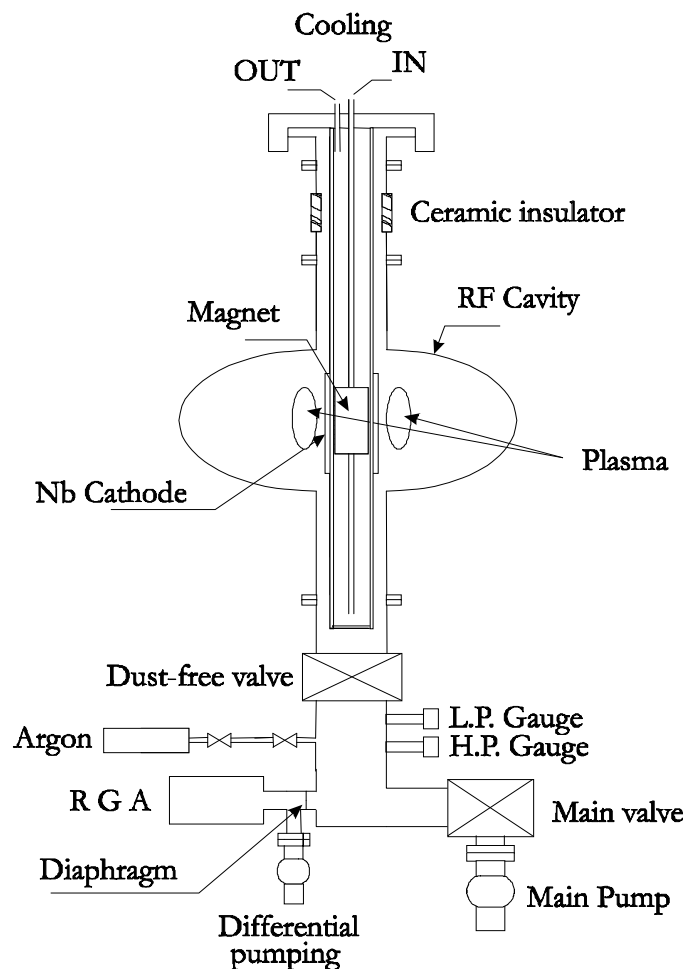


Figure 9. Schematic drawing of the 1.5GHz single-cell cavity sputtering system.

The residual pressure in the sputtering system and in the cavity is maintained by a turbomolecular pump. To obtain a residual pressure in the low 10^{-7} Pa range, the cavity part of the vacuum system is baked at a mean temperature of 150°C for 20 hours. The sputtering system and the injection lines for sputter gas and dry air are kept at 200°C during the cavity bake-out. For a semiquantitative analysis of the residual gases, a BalzersTM quadrupole mass spectrometer is linked to the sputtering system through a small conductance. Several spectra are taken in order to control the residual gas composition in the vacuum chamber at various stages of the sputtering process. Differential pumping by a second turbomolecular pump maintains a pressure in the low 10^{-4} Pa range at the analyser side even after injection of the working gas and allows for an analysis of the gas composition in the vacuum system during deposition. A high-pressure ionisation gauge is used to measure the working gas pressure in the sputtering system during film deposition. Hydrogen always dominates the residual pressure at room temperature after bake-out, regardless whether a cavity is mounted or a stainless steel tube.

Pre-sputtering was done for about nine minutes at the desired operating conditions by scanning the magnet back and forth over the whole cathode length. This procedure removes the oxide layer from the cathode surface but leads to the deposition of a contaminated pre-layer with a thickness of about 50 nm in the central cell. The cavity cell is sputtered at an argon pressure of 1.5×10^{-1} Pa and a stable current of 3 A is set between the cathode and the cavity on ground potential, corresponding to a voltage of approximately 360 V. Argon with a purity greater than 99.9999% (main impurities are other noble gases) was injected through a variable leak valve into the vacuum system and the pressure was maintained constant during deposition. The cut-off tubes are sputtered in successive steps under slightly different conditions, moving the

magnet inside the cathode stepwise from the cavity flange towards the cell. This is done prior to film deposition in the cavity cell in order to take advantage of the getter capability of a pure niobium film when sputtering the cell region. Since the beam tubes are exposed to very small rf surface magnetic fields only, a possibly enhanced contamination in these regions is less harmful. At a typical cell deposition rate of approximately $1.7\text{\AA}/\text{s}$ the substrate heat load, primarily due to the kinetic energy and the heat of condensation of coating atoms, and plasma radiation lead to a substrate temperature in excess of 200°C . Thus the cavity had to be cooled in order to obtain the desired substrate temperature of 150°C , a compromise between lower temperatures causing an increase of the film residual resistivity ratio [96] and higher temperatures causing the copper substrate to become softer. In practice, the substrate temperature is kept within $150\pm 5^\circ\text{C}$ by three fans located on the supporting steel frame around the cavity. The temperature was controlled by thermocouples, which were directly clamped onto the outer cavity wall.

After coating, the cavity compartment of the sputtering system is vented to dry air as soon as the temperature reaches room temperature. Oxidation of the surface by dry air favours the exclusive formation of a Nb_2O_5 layer [97, 98], while venting to wet air might result in an uncontrolled formation of other compounds, in particular niobium hydroxides. Typically 12 hours after air injection, the section including the cavity is dissociated from the system with the valve closed and disassembled in the clean room. The niobium cathode is stored in the clean room for further use and thus not protected from re-oxidation. After assembly of the end flanges and coupling probes, the coated cavity is rinsed with high-pressure water and dried by pumping, following the same procedure as described in section 4.1. The cavity can then be installed into the cryostat where its surface resistance and other superconducting parameters are measured.

Alternatively, it was tried to avoid final rinsing of the cavity by assembling the cleaned end flanges directly in the clean room. However, since any clean room operation creates particles or even small metal flakes, which may lead to a contamination of the inner cavity surface, this procedure turned out not to be clean enough to suppress field emission.

The hydrogen content of sputtered niobium films was analysed by Elastic Recoil Detection Analysis (ERDA) [99]. This method is very sensitive for determining the depth distribution of hydrogen in the first several hundreds of nanometres. The analysis gave a hydrogen concentration of about 4at% in the uppermost surface layer, which decreases to $\leq 1\text{at}\%$ after depth profiling of the first $17\text{nm}^{(1)}$. This value remained constant over the sampled depth of 200nm . Auger Electron Spectroscopy (AES) depth profile analysis of the niobium films resulted in detection of chemisorbed carbon on top of the surface, but gave no detectable carbon signal after having started sputtering the surface. A strong oxygen signal was detected within the first 10nm , which has been identified by X-ray Photoelectron Spectroscopy (XPS) to correspond to the compound Nb_2O_5 (chapter II/2). However, the oxygen signal in deeper layers was not distinguishable from the baseline. A more sensitive technique to obtain the concentration profile over the whole film thickness is Secondary Emission Mass Spectroscopy (SIMS). An analysis of standard films with this technique showed that the concentration of carbon and oxygen does not exceed approximately 100ppm in the bulk of the film.

The principle of the coating technique described so far was originally developed for sputtering the 352MHz superconducting accelerating cavities for LEP2 at CERN and was only slightly modified to adapt it to 1.5GHz cavities and to implement some minor improvements. This sputter-technique is therefore referred to as the method of producing ‘standard’ cavities. These cavities should correctly be seen as $\text{Cu}/\text{CuO}/\text{Nb}$ resonators since an oxide layer is present at the

⁽¹⁾The depth resolution in niobium is 17nm .

interface between the copper substrate and the niobium film, which has been found to influence the structure of the growing film.

In order to deposit niobium films on oxide-free copper and to study the resulting effect on the superconducting film properties, the technique of reverse- or backsputtering from the copper substrate has been used in the present work. The initial purpose of this study was mainly to improve the cleanliness of the sputtering operation in order to lower the impurity content in the film. In the standard system, both the copper oxide formed on the substrate and the niobium oxide on the cathode were considered as important sources for impurities, which get efficiently trapped in the first layers of the growing film due to the getter capabilities of niobium. It has later been realised that it is not a purer film in terms of contaminants, which led to a significant change in the superconducting film properties, but the different microstructure as observed by diffraction analysis. A detailed description of the structural properties of niobium films sputter deposited on both copper and copper oxide is available in the second part of this work. Important results, however, will already be mentioned in the present part when discussing the superconducting rf properties of film cavities.

Sputter cleaning of copper resonators has been made possible by a second coating system, which is sketched in figure 10. This system is equipped with two separate electrodes, one made of copper and one made of niobium, located on either side of the central part where the cavity is mounted. The electrodes are stored in vacuum chambers, consisting of bakeable stainless steel bellows, which can be isolated from the central part of the coating system by gate valves. Ion pumps maintain an ultimate pressure in the order of 10^{-8} Pa. By compressing the bellows and after having opened the gate valves, the electrodes can be introduced independently from each other into the cavity.

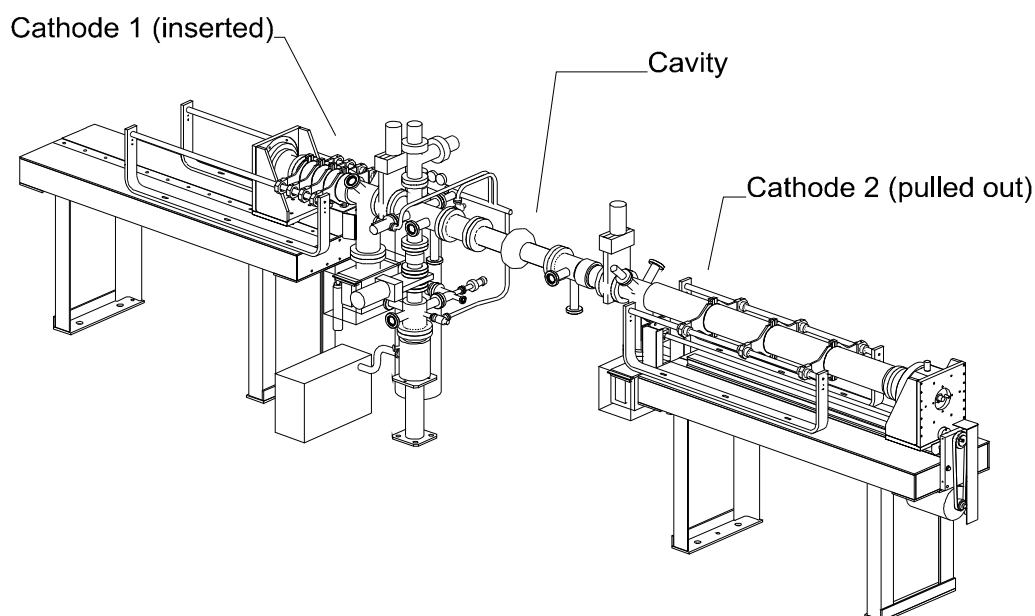


Figure 10. View of the two-electrode system.

The copper electrode is used as anode by setting a positive potential of 350V, while the cavity is kept at ground potential. The plasma discharge is sustained in argon at 10Pa and the power applied is 175W. The gas discharge and hence ion bombardment of the cavity surface is maintained in eight successive steps of one minute each. During sputtering, the central parts of the system are kept at 100°C to avoid re-adsorption of desorbed gases on cold surfaces.

Published data on sputtering yields⁽¹⁾ for polycrystalline Cu targets bombarded by argon ions are close to unity, indicating a high sputtering efficiency [100-102]. The irradiation dose of approximately 10^{18} ions/cm², averaged over the entire cavity surface, results in the removal of approximately 100nm of copper.

A residual gas analyser was connected to the central chamber of the system and the relative partial pressures were monitored during each cleaning cycle. The evolution of the partial pressure with successive sputtering steps is shown in figure 11 for several gases. In order to pump out the residual gases, the main valve of the system was opened after each cleaning cycle.

The sputter-cleaned cavity is then coated in the standard magnetron configuration as described earlier. Thus the copper anode has to be replaced by the niobium electrode at negative potential. Pre-sputtering is not necessary because the niobium electrode is always kept under UHV conditions and is therefore oxide free. The coating parameters are identical to those applied in the standard system. As a consistency check of the coherence of the results obtained with the standard and the two-electrode system and in order to verify that no damage is produced on the surface by ion bombardment, a few films have been grown in the latter on a re-oxidised copper substrate. For this purpose the cavity has been vented to dust-free air after the reverse-sputtering phase, followed by a bake out at 150°C in order to recover a residual pressure in the low 10^{-7} Pa range prior to niobium deposition. As in this case no pre-sputtering has been applied, contrary to the production of cavities in the standard system, a small difference exists between the two manufacturing methods but it does not cause any measurable difference between the properties of the two cavities.

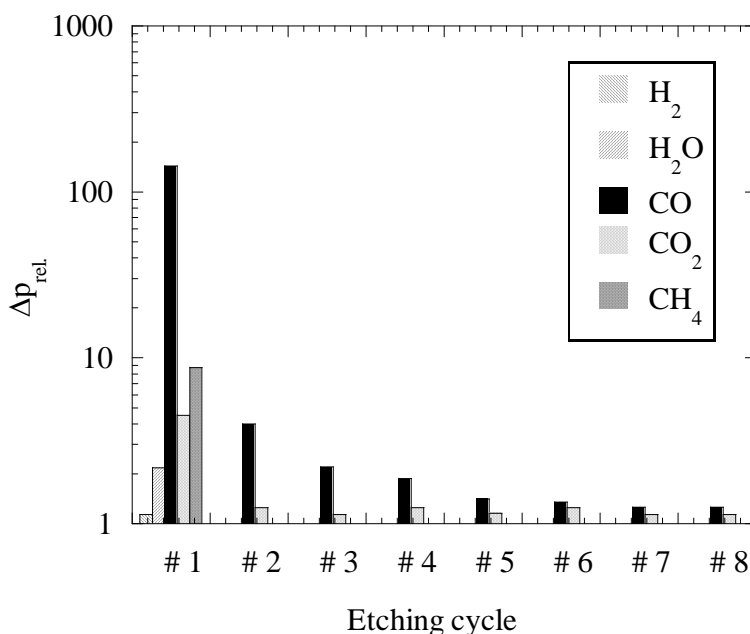


Figure 11. Relative pressure rise of the desorbed gases at each etching cycle. A large increase of the partial pressure of the desorbed gases, mainly CO and CO₂, is observed at the first etching cycle, while at the last cycles this rise is minimal.

Varying the nature of the plasma sustaining discharge gas is a convenient method of changing the electron mean free path in sputter deposited films. The transferable energy from an energetic ion to a stationary target atom in a binary elastic collision depends on the atomic mass of the sputter gas. Heavier sputter gases will transfer a main fraction of their initial energy to

⁽¹⁾The erosion in sputtering is measured by the sputtering yield, which is defined as the mean number of atoms removed from the surface of a solid per incident particle.

the target atom thus increasing the sputtering yield. As a consequence, they are reflected with too little kinetic energy for becoming efficiently trapped in the growing film. This effect has been exploited to study the mean free path dependence of superconducting film properties. Other sputter gases used for coating 1.5GHz cavities were neon, krypton and xenon. Whereas the coating time had to be adapted to account for the different sputtering yields in order to keep a film thickness of 1.5 μ m, the other sputtering parameters remained practically unchanged.

4.3. Measurement technique for accelerating cavities

Once a cavity has been coated and rinsed, it is mounted vertically into an insert for installation into the cryostat where the rf measurements are performed. The cavity is set into a lower ring and loosely fixed by an aluminium clamp on the top. Copper gaskets sealing the rf feedthrough/vacuum assembly to the cavity flange have already been mounted before rinsing the cavity. The cavity is pumped through an all-metal valve to reach an ultimate pressure of about 10⁻⁵Pa before cool down. The temperature is measured at the cavity equator with a germanium resistor and at the irises with Allen-BradleyTM carbon resistors. All thermometers are directly attached to the outer cavity wall by adhesive tapes and usually agree to within 0.01K. A solenoidal coil wound around the cryostat produces a dc magnetic field, $\mu_0 H_a$ up to 0.9mT. The coil itself is surrounded by a μ -metal sheet, shielding the cryostat from the earth field to better than 0.001mT. Hall probes located along an outer meridian of the resonator are used to measure the component of the magnetic field normal to the cavity surface. For the purpose of measuring the critical temperature, a weak magnetic field (0.2mT) is applied below the transition temperature and the response of the Hall probes is monitored while increasing the cavity temperature. Whereas the magnetic field is excluded from entering the interior of the cavity below T_c , it penetrates into the cavity when the transition into the normal conducting state is reached leading to a change in the field distribution outside the cavity, which is signalled by the Hall probes.

Two coupling probes (cylindrical antennas), made either of stainless steel or of niobium, are connected to the 50 Ω ceramic feedthroughs, one on each of the end plates, coupling the cavity to the external circuit via coaxial cables. The external circuit consists of the rf power source, providing a rf signal of power adjustable between 0 and 20mW, a travelling wave tube amplifier having a gain of 40dB and a 20dB directional coupler separating power going into the cavity from reflected power coming out. A spectrum analyser measures the incident, reflected and transmitted powers and a variable phase shifter is used to tune the incident phase in order to minimise the reflected power. The phase difference between the rf drive signal and the signal transmitted from the cavity is detected and used to stabilise the generator to the centre frequency of the cavity (frequency stabilisation system).

Power travels from the source via the amplifier into the directional coupler and down the feedline to the input probe in the cavity, exciting the field oscillations in the cavity. Some of the power is then reflected back to the directional coupler, which sends it out through a different port to the detector. The rf output probe serves to detect the amplitude and phase of the field excited in the cavity and is capacitively coupled to the external circuit to be simultaneously used as an electrode for the detection of a possible dc current caused by the field emitted electrons. As a consistency check, the incident, P_i , reflected, P_r , and transmitted, P_t , powers are also measured independently from the spectrum analyser by power meters.

In chapter 3, the unloaded quality factor of the resonator was defined as

$$Q_0 = \frac{\omega U}{P_0}, \quad (3)$$

where U is the energy stored inside the cavity, ω its resonance angular frequency and P_0 the power dissipated in its walls. The measurement directly provides the total (or loaded) quality factor Q_L of the system composed by the cavity and the two coupling circuits. If P_1 and P_2 are the powers dissipated in the input and output circuits respectively, one can define the two quality factors,

$$Q_1 = \frac{\omega U}{P_1} \text{ and } Q_2 = \frac{\omega U}{P_2} \quad (46)$$

and two coupling factors, which depend on both the losses in the cavity and in the external circuit,

$$\beta_1 = \frac{Q_0}{Q_1} = \frac{P_1}{P_0} \text{ and } \beta_2 = \frac{Q_0}{Q_2} = \frac{P_2}{P_0}. \quad (47)$$

The external quality factors, Q_1 and Q_2 , are defined by the coupling geometry and do not depend on Q_0 . From the measured values of the loaded quality factor and of the two coupling factors, the unloaded quality factor of the cavity can be calculated using the relation,

$$\frac{1}{Q_L} = \frac{P_0 + P_1 + P_2}{\omega U} = \frac{1}{Q_0} + \frac{1}{Q_1} + \frac{1}{Q_2} = \frac{1 + \beta_1 + \beta_2}{Q_0}. \quad (48)$$

In steady state conditions, as maintained during the measurement of a cavity, the incident power that is not dissipated in the cavity walls is either reflected towards the input or transmitted to the output circuit. Therefore,

$$P_i = P_0 + P_r + P_t, \quad (49)$$

and from the measurements of P_i , P_r and P_t , the dissipated power can easily be calculated.

The evaluation of Q_L is based on the transient method, i.e. the measurement of the decay time of the energy stored in the circuit, after the rf generator is turned off.

A square wave pulse of incident power, P_i , is turned on at the time $t = 0$ and off at $t = 1$ and the reflected wave from the resonator is detected at the spectrum analyser by means of the directional coupler. The oscillator is tuned to the resonant frequency of the cavity, a condition that is obtained by maximising the reflected signal, P_r . At $t = 0$, P_i is almost totally reflected from the coupling network and the measured reflected signal $P_r(0)$ is P_i . As the resonator fills, the energy of the field inside the cavity increases and stationary values of the dissipated power, $P_0(t)$ and the reflected power, $P_r(t)$, are reached, provided that the pulse is kept sufficiently long. With energy U stored in the resonator and the incident power switched off at $t = 1$, a certain power, $P_1 \propto U$ will be emitted out the transmission line and $P_i(1)$ consists only of the emitted wave, P_1 . It can be shown [103] that,

$$P_0 = \frac{4\beta_1}{(1 + \beta_1 + \beta_2)^2} P_i \quad (50a)$$

$$P_r = \left(\frac{1 + \beta_2 - \beta_1}{1 + \beta_1 + \beta_2} \right)^2 P_i \quad (50b)$$

$$P_1 = \frac{4\beta_1^2}{(1 + \beta_1 + \beta_2)^2} P_i. \quad (50c)$$

An optimal situation for the measurement is given by the condition $\beta_1 = 1 + \beta_2$, for which the reflected power is zero and best use is made of the available power (critical coupling). The load, represented by the cavity is said to be matched to the generator. In practice, this condition

cannot be maintained throughout the measurement, since the cavity quality factor varies considerably with temperature and field. Nevertheless, the length of the input antenna is adjusted to keep the input coupling for reasonably good cavities within a factor of 10 of the critical value over the measured range, while the output probe is chosen to make $\beta_2 \ll 1$. When the incident power is turned off, the energy stored in the cavity will decay according to the equation,

$$-\frac{dU}{dt} = P_0 + P_i + P_2 = \frac{\omega U}{Q_L}, \quad (51)$$

which, when solved for U , gives,

$$U(t) = Ue^{-t\omega/Q_L}. \quad (52)$$

The characteristic time constant for the exponential decay of the cavity field, τ_L , can be measured by monitoring the signal of the emitted power after having turned off the incident power, P_i , and gives a direct measurement of the loaded quality factor, Q_L ,

$$\tau_L = Q_L/\omega. \quad (53)$$

In addition, the measurements of P_i and P_r , as well as of the emitted power, P_l , allow for the calculation of the coupling factors, β_1 and β_2 and therefore of the external quality factors, Q_1 and Q_2 . A calibration of the circuit parameters as described above is performed at 4.2 and 2K, respectively, at different values of the incident power. Average values of Q_1 and Q_2 are calculated and used for subsequent calculations of the Q_0 vs E_a data.

Once the external quality factors have been determined, the transient method does not need to be repeated for each other value of the rf field, since a varying Q_0 can be monitored continuously by simply measuring the transmitted, reflected and incident powers.

The accelerating field, E_a , can directly be determined from the measured values of P_0 and Q_0 . In fact, since $U \propto E_a^2$, it follows from equation (3) that the quantity $E_a^2/(Q_0 P_0)$ is a constant depending exclusively on the shape and dimensions of the cavity, which is given by (chapter 3),

$$\frac{E_a^2}{Q_0 P_0} = 8.27 \text{ k}\Omega/\text{m}^2. \quad (12)$$

For each cavity, a series of measurements of Q and E_a is performed at different temperatures and incident input powers (Figure 12). The data are recorded for subsequent off-line analysis using optimised circuit parameters, and measurement errors are evaluated and propagated through the various steps of the calculations. The final errors in the measurements of the surface resistance and field levels are of the order of 2 to 5%, when reasonably good coupling was maintained during the measurements. The temperature is a weighted average of the thermometer measurements corrected for the temperature gradient across the cavity wall and its uncertainty includes their root mean square deviations with respect to the mean.

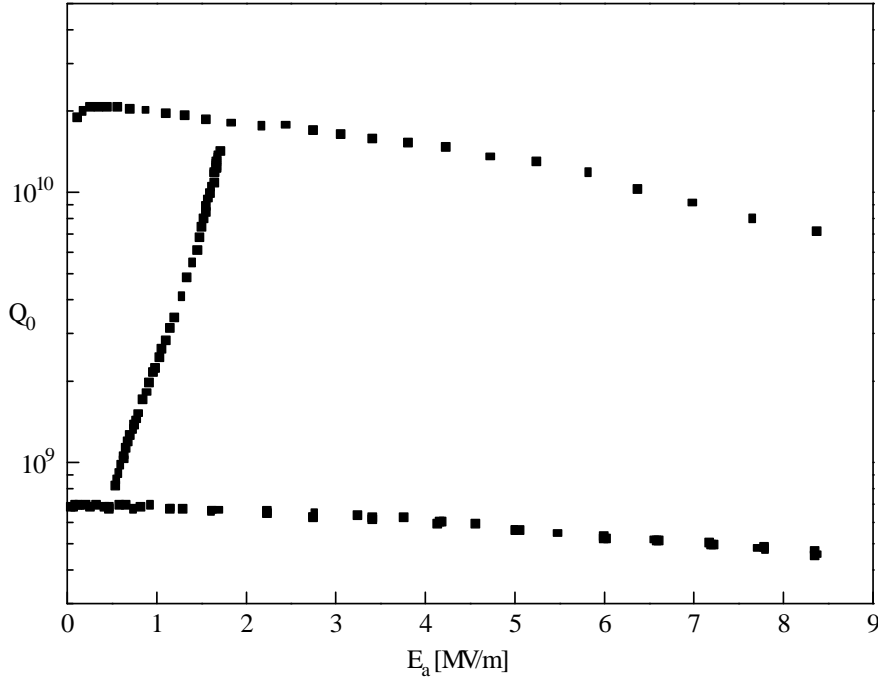


Figure 12. A typical set of Q_0 vs E_a measurements. The upper and the lower branches are isotherms taken at 1.75 ± 0.1 K when the resonator has been cooled in a pumped liquid helium bath and at 4.19 ± 0.05 K, respectively. The data between the two curves were taken at intermediate temperatures while pumping on the cryostat.

E_a and Q_0 are the two quantities that describe the performance of a cavity in the most direct way, in view of its practical use in a particle accelerator. However, two other quantities exist, which are more directly related to the physical properties of the superconducting material under consideration. These are the average rf magnetic field H_S at the cavity surface and the cavity surface resistance, R_S , quantities which have been introduced in chapter 3. The former is directly proportional to E_a according to the relation,

$$H_S \text{ (mT)} = 4.55 E_a \text{ (MV/m)}. \quad (11)$$

The surface resistance is inversely proportional to Q_0 according to,

$$R_S = \frac{295 \Omega}{Q_0}. \quad (6)$$

Measurements above the boiling temperature of liquid helium have been performed at constant incident power and in steady state conditions to measure the cavity resonant frequency as a function of temperature close to T_c . The cavity was kept in gas after total evaporation of liquid helium at the bottom of the cryostat. This method provides a direct measurement of the temperature dependence of the penetration depth as already discussed in chapter 3.

5. Experimental results

In the course of this work, a representative number of niobium coated copper cavities was produced and tested. The study focused on a few parameters, such as the nature of the copper substrate and the sputtering gas conditions. The results deduced from the rf measurements are described on the next pages.

Most copper cavities were coated according to the standard sputtering technique described in chapter 4. This implies that the film always grows on an oxidised copper substrate, whereas the discharge gas composition can be varied defining the concentration and composition of the noble gas in the film. Besides, a significant number of cavities was sputter deposited using the two-electrode system, allowing for a pre-cleaning of the copper substrate or the deposition of underlayers before coating with niobium⁽¹⁾. Films are grown in xenon, krypton, argon or argon-neon mixtures of various proportions, on underlayers of copper, titanium and aluminium, and on oxidised or oxide-free copper. In addition, a few films have been loaded with a defined amount of hydrogen immediately after deposition and before being exposed to oxygen. The present chapter describes in detail the results of the analysis of a significant number of cavities sputter deposited on oxidised and on oxide-free copper, using argon as the discharge gas. Data obtained from film cavities, which have been produced using different discharge gases, are included in the analysis and will be presented in the specific sections. The first section, however, will discuss the results obtained on bulk niobium cavities in order to provide the possibility of a direct comparison between the microwave response of superconducting film and bulk resonators.

According to relation (42) in chapter 3 the surface resistance R_S can be written in terms of two separate components,

- a) The BCS resistance, R_{BCS} , a global property of a superconductor depending on the energy gap, $\Delta(0)$, and the mean free path, l ,
- b) The zero temperature limit of the surface resistance, R_{res} , not directly related to intrinsic properties of the superconductor, but indicating the presence of defects or impurities, the effects of which are not accounted for by the mean free path.

Despite the fact that films and the bulk show different values of the above mentioned quantities, a parameterisation of the same form can be used to describe the dependence of R_{BCS} and R_{res} on different variables, such as temperature or rf magnetic field, H_S . As a result it is possible to reduce the quantitative differences observed between the different types of resonators to a small set of variables.

The BCS resistance identified by its value at 4.2K and at zero rf field is denoted by R_{BCS}^0 and the value of the mean rf field, where $R_{BCS} = 1.5 R_{BCS}^0$, is denoted by H_S' . This quantity is a simple measure of the rate of increase of R_{BCS} with H_S .

In addition to the surface resistance, other cavity parameters, which were independently measured, are the critical temperature, T_c , and the penetration depth, λ , or equivalently its normalised value,

$$\frac{\lambda(0, l)}{\lambda(0, \infty)} = \sqrt{1 + \frac{\pi \xi_0}{2 l}}. \quad (38)$$

⁽¹⁾ Replacing the copper electrode in the two-electrode system by an electrode made from another material offers the possibility to grow an underlayer on the oxidised copper substrate.

5.1. Bulk niobium resonators

Three cavities have been studied, one of which (L14) was manufactured by lathe spinning at INFN [76], the other two (C1 and C2) being CEBAF cavities, made of two deep-drawn half-cells, electron welded at the equator [92]. The data presented in this chapter are obtained after heat treatment of the resonators to 1000°C as described in chapter 4. Cavity L14 was subsequently re-treated at 1100°C (L14-3), but no significant change of the BCS resistance was observed.

Figure 13 shows the evolution of the residual and the BCS resistances of cavity L14 with successive treatments. A significant decrease of the BCS resistance following heat treatment signals a corresponding decrease of the mean free path, suggesting an accumulation of impurities (mainly titanium) in the thin superficial layer where the rf field penetrates. It is restored to a higher value after removal of a 10µm layer (L14-1) by chemical polishing consistent with the expected evolution of the RRR value with heat treatment. Further etching has practically no effect on the surface resistance (L14-2). The residual resistance is not significantly affected by etching, suggesting that it is relatively insensitive to the presence of such impurities. The effect of firing on the residual resistance seems to be important when its initial value is not too low, but no significant change has been observed on the deep-drawn cavities, which already had a very small initial residual resistance.

Table 1 summarises the results obtained on different bulk niobium resonators, which have undergone similar treatments. It can be seen that, apart from the residual resistance, the data display sufficient consistency to justify a description in terms of a single set of variables. As will be shown in the next chapters, this feature is not specific of bulk niobium resonators but applies also to the different types of film cavities. Data analysis has been restricted to a field region, where field emission effects are absent.

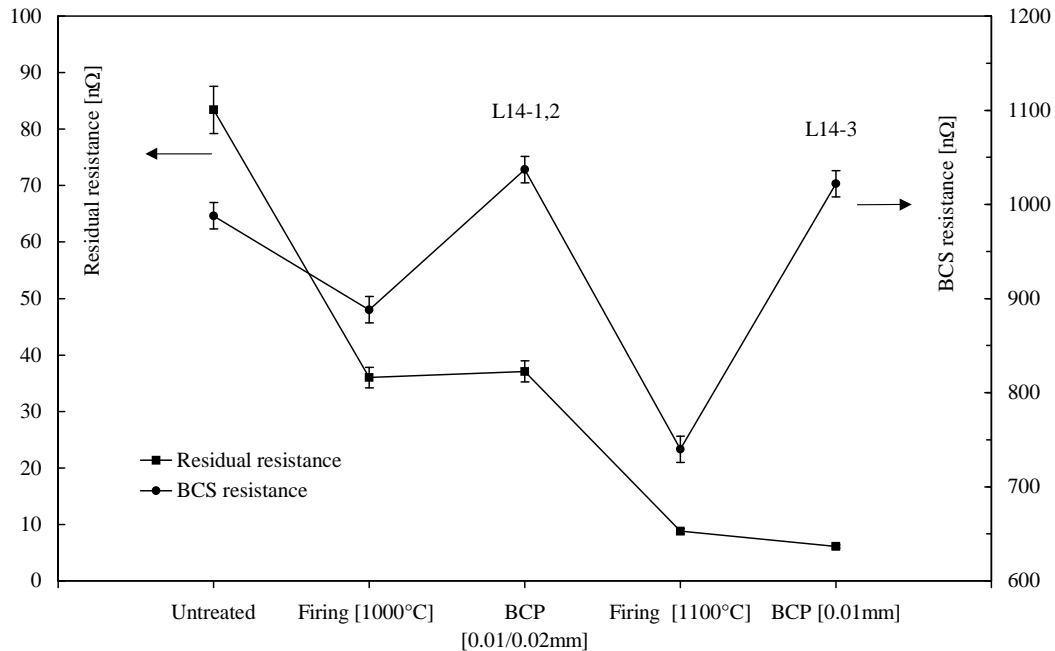


Figure 13. Effect of surface treatments of a spun cavity on R_{res} and R_{BCS}^0 . Cavity L14-1 has been re-measured after a further chemical polishing of 10µm (L14-2) and consistent results were obtained.

Cavity	T_c [K]	λ [nm]	H_S' [mT]	R_{BCS}^0 [n Ω]	R_{res} [n Ω]	$\Delta(0)/k_B$ [K]
C1		---	44 \pm 2	1064 \pm 22	8.5 \pm 0.6	19.8 \pm 0.2
C2	9.28 \pm 0.01	29 \pm 0.3	33 \pm 1	912 \pm 28	9.1 \pm 0.5	19.0 \pm 0.2
L14-1	---	---	29 \pm 1	1049 \pm 30	45 \pm 2	18.8 \pm 0.3
L14-2	---	---	31 \pm 1	1037 \pm 22	42 \pm 1	20.0 \pm 0.2
L14-3	9.29 \pm 0.03	30.4 \pm 0.2	34 \pm 1	1017 \pm 34	11 \pm 1	18.5 \pm 0.1
Mean	9.28\pm0.02	30.2\pm0.2	33\pm0.5	1022\pm12	---	19.0\pm0.1

Table 1. Summary of variables characterising the rf properties of bulk niobium resonators. The penetration depth given for cavity L14-3 represents an average value of five successive measurements.

5.1.1. The BCS resistance

Each set of measurements includes isothermal H_S scans of the surface resistance with the cavity immersed in liquid helium at $T \cong 4.2$ K under atmospheric pressure and in superfluid helium at $T \cong 1.7$ K. In between these extreme temperatures, when slowly pumping on the cryostat, measurements of the surface resistance as a function of temperature at a given low rf field were performed. In the present data sample, R_{BCS}^0 decreases from above 1 $\mu\Omega$ to about 5 n Ω , when the temperature is decreased from 4.2 to 1.7K. Therefore the values of R_S measured at 1.7K are, in general, good approximations to R_{res} , providing an unambiguous separation of the two components of the surface resistance, R_{res} and R_{BCS} , can be made.

The BCS resistance, $R_{BCS}(T, H_S)$, can therefore be determined from the measured surface resistance, $R_S(T, H_S)$ according to the relation,

$$R_{BCS}(T, H_S) = R_S(T, H_S) - R_S(1.7K, H_S), \quad (54)$$

with $R_S(1.7K, H_S) = R_{res}(H_S) + R_{BCS}(1.7K, H_S)$. As mentioned above, the BCS resistance becomes very small at 1.7K and can be determined from the temperature dependence of R_S , measured at $H_S \leq 5$ mT, as shown for different cavities in figure 2 (chapter 3).

The dependence of R_{BCS} on H_S is shown in figure 14. Small temperature corrections of less than 2% were applied to take into account the fact that the actual measuring temperature may have differed slightly from its reference value of 4.2K. The spread of the data of the different bulk niobium cavities listed above is small and has been included in the measurement errors when performing the average. The BCS resistance at 4.2K is observed to increase with H_S by 50% between 0 and $H_S' = 33 \pm 0.5$ mT. A parameterisation of the form

$$R_{BCS} = R_{BCS}^0 (1 + \alpha H_S + \beta H_S^2) \quad (55)$$

has been chosen to describe the data.

This effect is not discussed in the literature. The limitation to the lowest order in the rf field of the perturbative expansion used in the standard BCS calculations available in the literature [41, 43, 46] prevents also a comparison of the data with theory. It is therefore appropriate to present the data in the simple form described above, demonstrating the need for further theoretical work.

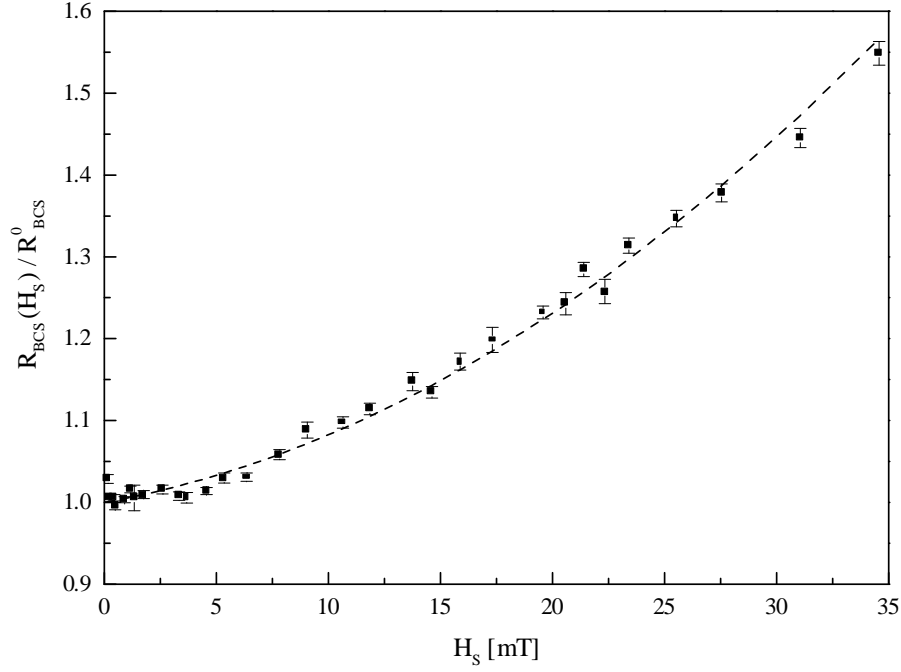


Figure 14. Dependence of the BCS resistance at 4.2K on the rf field. The error bars include the spread between five different bulk niobium resonators. The line is the result of a quadratic fit (see text).

The temperature dependence of the BCS resistance has been analysed by using the approximate expression,

$$R_{BCS}(T) = A(l, \omega) \frac{l}{T} \exp\left(-\alpha \frac{T_c}{T}\right) \quad (41)$$

Figure 15 shows the temperature dependence of the ratio $r = R_{BCS}(T)/R_{BCS}(4.2K)$, where the measured values of the numerator and denominator have been corrected to a value of $H_S = 4.55mT$ precisely, using the experimentally observed field dependence of the BCS resistance as described above. The temperature spans the range from 1.9 to 4K ($t = 0.2$ to 0.45). Data obtained from all five bulk resonators, as listed in table 1, are plotted in figure 15. A global fit of the form,

$$r = \frac{4.2}{T} \exp\left[-\frac{\Delta(0)}{k_B} \left(\frac{1}{T} - \frac{1}{4.2}\right)\right] \quad (56)$$

gives the value $\Delta(0)/k_B = 19.03 \pm 0.05K$ or $\alpha = 2.04 \pm 0.01$ for $T_c = 9.28 \pm 0.02K$.

The above evaluation is only approximate, as is relation (41) from which it has been derived. A more accurate comparison of the experimental results with theory implies the numerical calculation of the integrals entering the expression of the surface resistance given in references [41, 43]. For this purpose, use has been made of the computer code of reference [46], treating α and the mean free path l as free parameters (chapter 3). The value of $\lambda_L(0) = 26.5 \pm 1nm$ used in the calculations has been obtained from the ratio $\lambda(0, \infty)/\lambda_L(0)$ at $\xi_0/\lambda_L(0) = 1.33 \pm 0.01$ as given by the BCS theory for the boundary condition of random scattering of the electrons from the surface (considering specular reflection results in a value $\lambda_L(0) = 28.5 \pm 1nm$). The value of $\xi_0/\lambda_L(0)$ is obtained from the ratio $\kappa_0 = 0.96 \lambda_L(0)/\xi_0$ [59, 104] taking the clean limit value of the Ginzburg-Landau parameter $\kappa_0 = 0.72 \pm 0.01$. The latter value is deduced from extrapolation of the experimental data given by *Weber et al.* [13] on niobium with RRR values ranging from 2100 to 10. This value of κ_0 is consistent with but lower than earlier results reported by

Kerchner et al. [105] on a niobium monocrystal with $RRR = 450$ and by *Auer et al.* [106] on polycrystalline niobium having $RRR \sim 2000$. Other parameters which have been fixed in fitting the theory to the data are the critical temperature, $T_c = 9.28\text{K}$ and the BCS coherence length, $\xi_0 = 36 \pm 1\text{nm}$ (see above). The calculations were made assuming the BCS temperature dependence of $\Delta(T)/\Delta(0)$ (Eqn. 39) and random scattering of electrons from the surface. The resulting value of $\alpha = 1.850 \pm 0.001$ deviates from the approximate value of $\alpha = 2.04 \pm 0.01$ obtained above by 0.19 ± 0.01 , a measure of the approximate nature of relation (41). The first value is in agreement with the result $\alpha = 1.85 \pm 0.02$ of other published measurements on niobium cavities [25, 45, 107-110] using slightly different material parameters ($T_c = 9.2\text{-}9.25\text{K}$, $\xi_0 = 39\text{nm}$ and $\lambda_L(0) = 32\text{-}33\text{nm}$) and with theoretical expectation [113]. The value of the energy gap of niobium obtained from electron tunneling spectroscopy is $\alpha = 1.96 \pm 0.01$ [50, 111, 112].

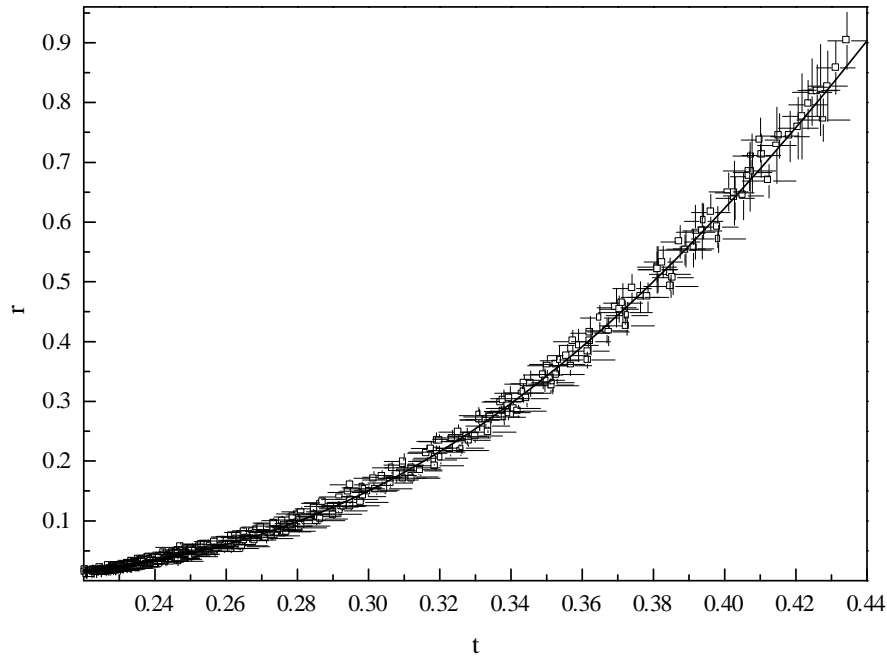


Figure 15. Temperature dependence of $r = R_{BCS}(T) / R_{BCS}(4.2\text{K})$. Data obtained from measurements of different bulk niobium resonators are included. The line is the result of a global fit according to relation (56), giving the approximate value $\alpha = 2.05$ (see text).

The BCS resistance at 4.2K and $H_S = 0$, R_{BCS}^0 , has been determined separately for each cavity from relation (56). The results are summarised in table 1 and are in excellent agreement with expectations from the theoretical mean free path dependence of the surface resistance derived in [41, 43] and computed in section 5.2.

5.1.2. The penetration depth

The experimental procedure to determine the penetration depth from measurements of the surface reactance has already been introduced in chapter 3. Several measurements of the temperature dependence of λ have been performed on cavity L14-3, the results of which are used as a clean limit reference, $\lambda(0, \infty)$, for successive measurements on niobium film resonators. Determining relative values of the penetration depth, $\lambda_{rel} = \lambda(0, l) / \lambda(0, \infty)$ instead of their absolute values is sufficient to obtain an estimate of the mean free path and considerably reduces the effects of systematic uncertainties. Plotting the experimentally

measured rates of increase of the resonant frequency, df/dt as a function of the reduced temperature t defines the shape of the universal function $y(t)$ according to,

$$(1-t) \frac{df}{dt} \propto \lambda(0, l) y(t). \quad (57)$$

This function is displayed in figure 14. Each cavity is observed to display the same frequency dependence, but is simply shifted vertically because of the different value of $\lambda(0, l)$. Therefore, fitting all data to a single universal shape as shown below and determining the scaling coefficients for each cavity with respect to bulk niobium cavities defines λ_{rel} , which by definition is equal to unity for the bulk resonators.

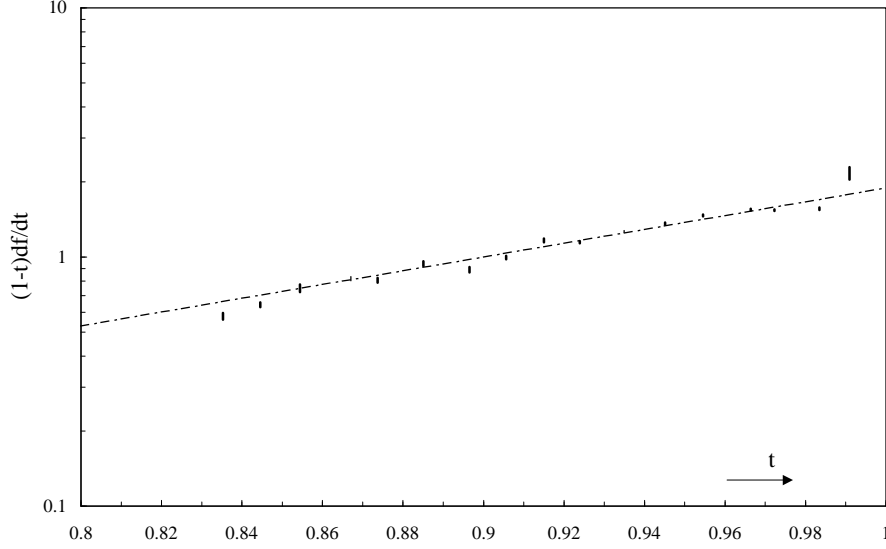


Figure 14. Temperature dependence of the resonant frequency normalised to unity at $t = 0.9$. The dotted line is the result of a linear fit to the logarithm of the quantity plotted.

In the clean limit, the temperature dependence of the penetration depth is predicted by the BCS theory and the shape of the function $y(t)$ can be determined from the best fit to the numerical values in the tabulation of the penetration depth as a function of t given by *Mühlschlegel* [34]. Fitting the same function $y(t)_{BCS}$ to the measured increase of the resonant frequency of bulk niobium cavities near T_c allows for the calculation of an absolute value of $\lambda(0, \infty)$. This is shown in figure 15, where the derivative of the frequency shift is plotted as a function of the reduced temperature. The dotted line in figure 15 represents a fit to the data of the form,

$$\frac{df}{dt} = 1.23 A (1-t^{2.33})^{-1.53} t^{1.33}, \quad (58)$$

with $A = \lambda(0, \infty) \mu_0 f^2 / G$. Values of the penetration depth for pure niobium measured this way are listed in table 1. Analysing the data with the two-fluid expression results in an average value, $\lambda = 44 \pm 2 \text{ nm}$.

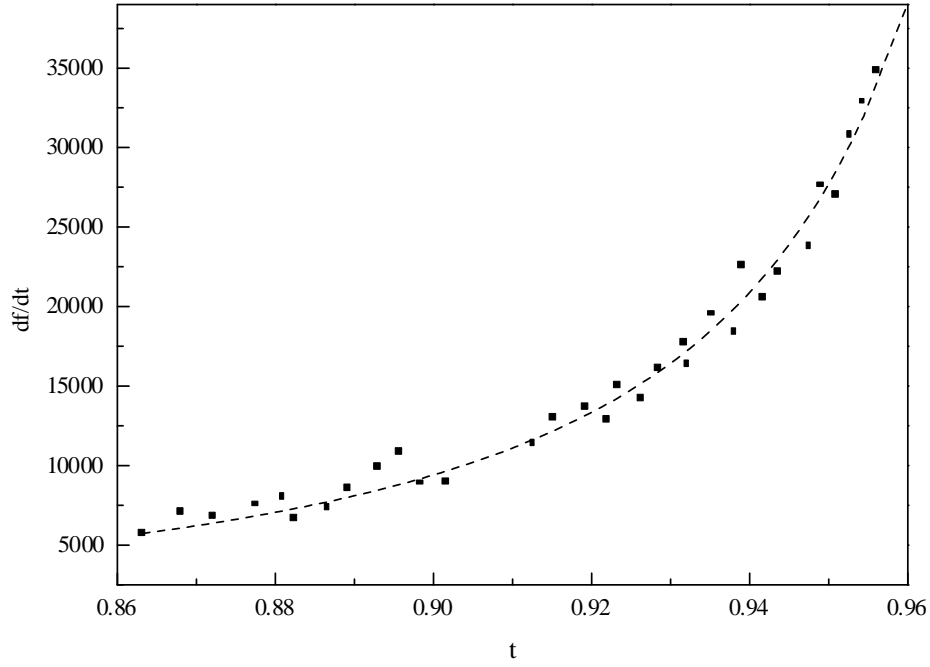


Figure 15. The resonant frequency change as a function of reduced temperature for pure niobium at 1.5GHz. A fit to the data according to relation (58) gives $\lambda = 30 \pm 0.3 \text{ nm}$. When calculating the derivative of the frequency shift, the final result is not affected by pressure variations in the cryostat, which may cause an irreversible change of the resonant frequency.

Calculating the surface reactance at zero temperature, $X_S(0)$ from the *Mattis and Bardeen* theory [41], taking the value of $\alpha = 1.85$, a mean free path, $l \geq 200 \text{ nm}$, $T_c = 9.28 \text{ K}$, $\xi_0 = 36 \text{ nm}$ and $\lambda_L = 27 \text{ nm}$ allows a direct calculation of the penetration depth, $\lambda(0, \infty) = 33 \text{ nm}$.

5.1.3. The residual resistance

Figure 16 summarises the rf properties of accelerating cavities which are of most interest to the accelerator community. The surface resistance measured at 1.7K and corrected for the contribution of $R_{BCS}(1.7\text{K}, H_S)$ is plotted as a function of the rf surface magnetic field.

It is of no interest to repeat here the possible causes leading to a non-zero value of R_{res} in bulk resonators (see for example cavity L14-1 in figure 16) since there exists already an abundant amount of literature on this topic [114-121] and possible cures are well known [14, 21, 114, 122]. Mechanisms, leading also to the generation of a non-zero residual resistance in film resonators, will be discussed later.

Apart from the low field region $0 \leq H_S \leq 5 \text{ mT}$, the residual resistance is independent of the magnetic component H_S of the microwave amplitude as long as it does not exceed some field emission threshold, H_{fe} , beyond which R_{res} increases exponentially. The maximum attainable electrical accelerating field strength in superconducting niobium cavities is therefore limited by enhanced electron field emission or by thermal instabilities (quenches), causes of which have been discussed in chapter 3. The data analysed and presented in the previous sections have been taken from a field range, where such effects are absent, that is over the range, where the residual resistance is observed to be field independent. Cavity C1 is an exceptionally good cavity, which would meet the specifications foreseen for the TESLA machine [61]. This result was obtained after having repeated the high-pressure water rinsing several times.

The initial decrease of the surface resistance, which is not understood yet, is significant enough not to be ignored when describing the essential features of the field dependence of R_{res} and has been considered when calculating R_{BCS} . This effect is not new and has already been reported in literature [21].

The values of R_{res} given in table 1 are obtained from a linear extrapolation of the low field data, $H_S \leq 6\text{mT}$, to zero field.

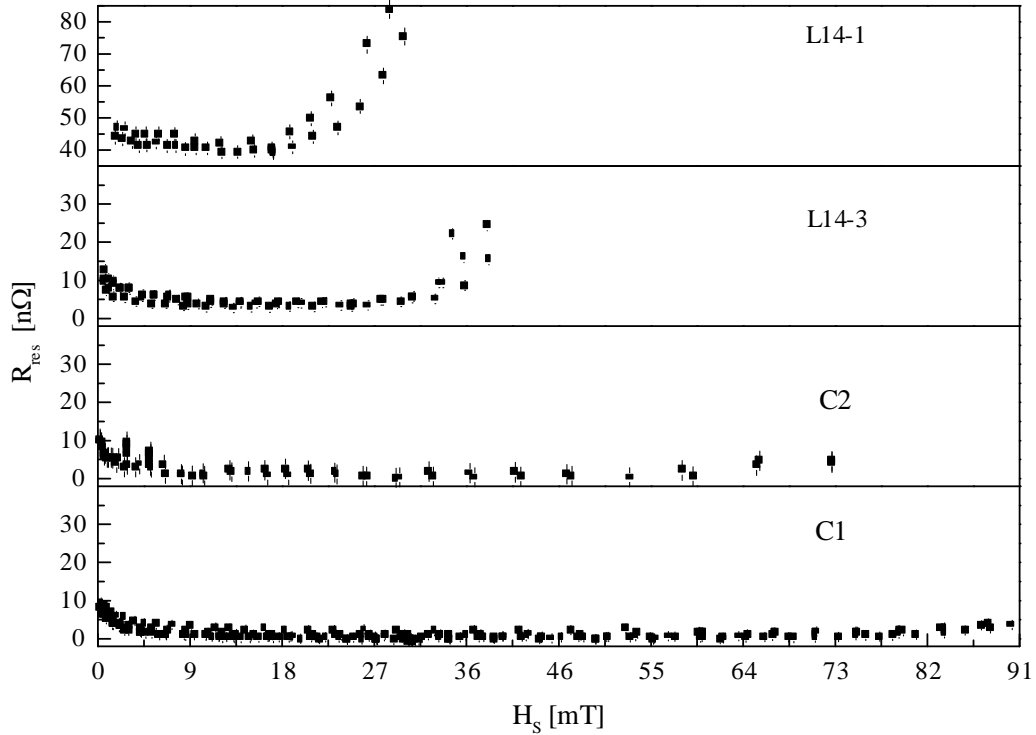


Figure 16. The H_S dependence of R_{res} for heat treated bulk niobium cavities. Cavities L14-1 and C2 were field limited by electron emission with a measured current of 1nA at 35mT and 0.3nA at 72mT, respectively. The highest obtainable field for cavity C1 was 123mT limited by thermal breakdown at a surface resistance of about 30nΩ. Thermal breakdown at a much lower field was also observed for cavity L14-3. Each measurement was repeated and the data were merged yielding a single curve for each cavity below the field emission threshold.

5.2. Niobium film resonators

5.2.1. Standard films

The present section discusses results obtained on films, which have been sputter deposited in the standard system on the oxidised inner surface of copper bulk resonators. Parameterisations having the same form as for bulk niobium resonators will be used. The preparation of the specific type of film considered in the present section follows the standard procedure described in chapter 4. Only cavities yielding $R_{res} < 100 \text{ n}\Omega$ are considered in the present analysis. In cases where there was indication of the presence of field emission, H_S was kept below the threshold. A total of 28 different films prepared according to the same standard method are included in the data sample. The discussion of the residual resistance will follow in a separate section when having presented the results obtained on other films as well.

In the present data sample, R_{BCS}^0 decreases from 400nΩ to less than 1.7nΩ when T decreases from 4.2K to 1.7K. The dependence of $R_{BCS}(4.2\text{K})$ on H_S is shown in figure 17. The spread of

the data is small and has been included in the errors when performing the average. As the residual resistances of different films display instead a large spread, this result supports the assumption of temperature independence of the residual resistance. The BCS resistance at 4.2K is observed to increase with H_S by 50% between 0 and $H_S' \cong 35\text{mT}$. As already demonstrated in section 5.1.1, this feature is not specific to films and a similar increase is observed in bulk niobium, implying a larger effect in absolute terms for massive niobium than for films. The parameterisation $R_{BCS} = R_{BCS}^0 (1 + \alpha H_S + \beta H_S^2)$ gives a good description of the data, better than for the bulk case. In particular, the quadratic term β is observed to be of higher significance for film than for bulk cavities and $\alpha_{film} < \alpha_{bulk}$. The value of H_S' is in both cases about one sixth of the thermodynamic critical field.

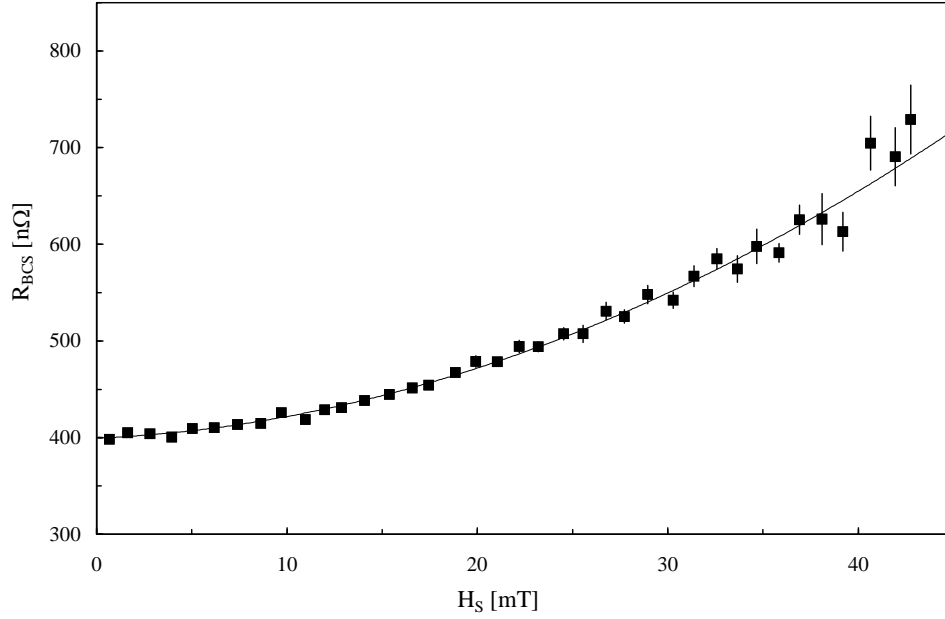


Figure 17. Dependence of R_{BCS} (4.2K) on H_S . Error bars include the effect of the spread between different films of the same kind. The line is the result of a quadratic fit (see text).

In order to check the hypothesis that the H_S and T dependencies of R_{BCS} factorise, a few isothermal scans were performed at intermediate temperatures. Such a data set is shown in figure 18 where the validity of the factorisation is illustrated by the fact that different isothermal scans display a same relative H_S dependence.

The temperature dependence of the ratio $r = R_{BCS}(T)/R_{BCS}(4.2\text{K})$ is shown in figure 19. The data are taken at equal values of H_S . A fit to the data according to relation (56) allows the approximate evaluation of the energy gap for standard film cavities. The value obtained is $\Delta(0)/k_B = 19.7 \pm 0.1\text{K}$ or $\alpha = 2.07 \pm 0.02$ for $T_c = 9.54 \pm 0.02$, measured for standard films as characterised in chapter 4. While the value of α is consistent with that of bulk niobium, the transition temperature is $0.26 \pm 0.03\text{K}$ higher. This deviation is understood in terms of an intrinsic compressive stress state present in those films and will be discussed in detail in part II of this work.

The value of the BCS resistance, $R_{BCS}^0 = 401 \pm 3\text{n}\Omega$ is significantly smaller than the value $1022 \pm 12\text{n}\Omega$ obtained for pure bulk niobium. This result will be compared with theory below.

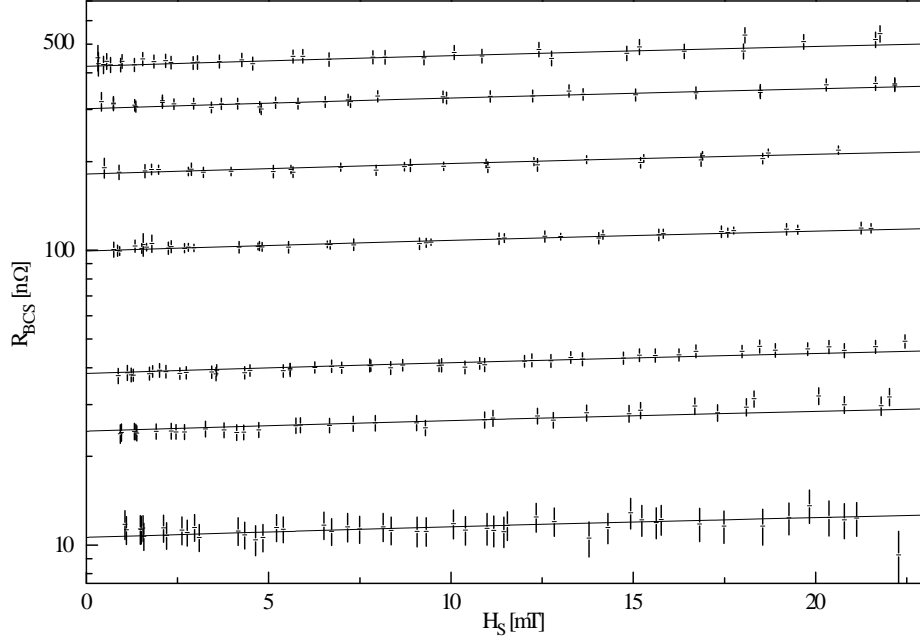


Figure 18. Isothermal H_{rf} scans measured on a particular film. $R_{BCS}(T)$ is plotted as a function of H_{rf} for $T = 4.23$ K, 3.90K, 3.47K, 3.07K, 2.59K, 2.41K and 2.15K (from top to bottom). The lines represent a same H_S dependence for all values of T .

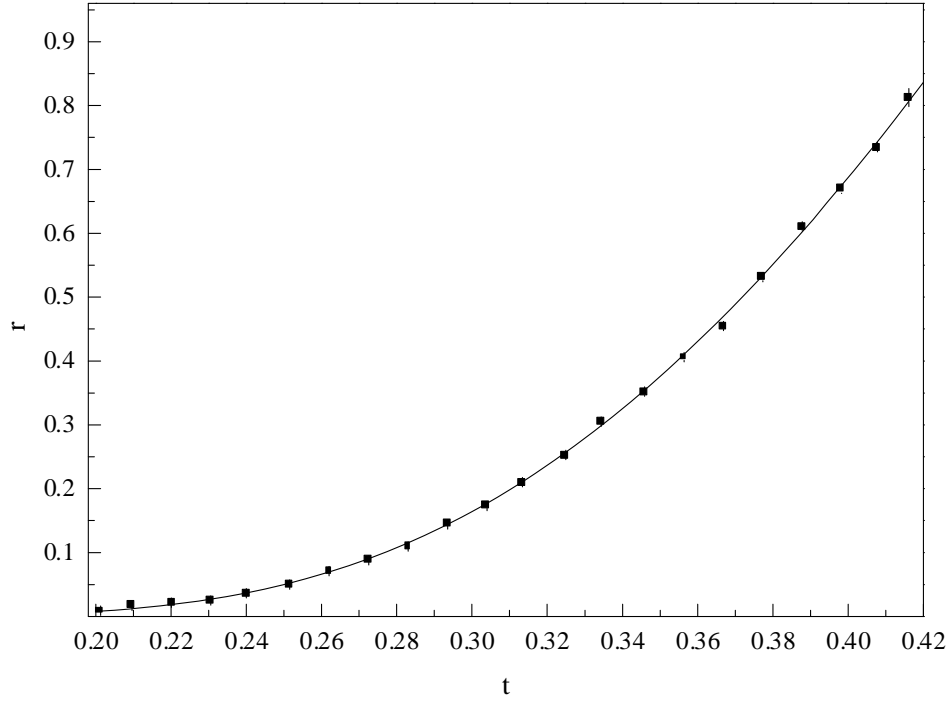


Figure 19. Temperature dependence of $r = R_{BCS}(T) / R_{BCS}(4.2\text{K})$. Error bars include the spread between 28 different films of the same kind. The line is the result of a global fit according to relation (56), giving the approximate value $\alpha = 2.07$ (see text).

A comparison of the measured temperature dependence of the BCS resistance with theory results in a value of the reduced energy gap, $\alpha = 1.87 \pm 0.01$. This value has been obtained by fixing the parameters $T_c = 9.54\text{K}$, $\lambda_L = 27\text{nm}$, $\xi_0 = 36\text{nm}$ and the mean free path $l = 27\text{nm}$. The latter value has been derived from a measurement of the normal state resistance just above T_c .

(see chapter II/9). In order to test the significance of these results, the calculations were repeated with the values $\xi_0 = 39\text{nm}$ and $\lambda_L = 29\pm 0.2\text{nm}$ as obtained from independent measurements given in reference [13] but leaving the other parameters unchanged. The resulting value of $\alpha = 1.89\pm 0.01$ is close to the value calculated above showing that the *London* penetration depth and the BCS coherence length do not strongly influence the temperature dependence for $T/T_c \leq 0.5$ but they are important in the determination of the absolute value of the surface impedance.

The results obtained on standard films are summarised in table 2. Included in this table are the measured relative values of the penetration depth normalised to their values in the bulk heat treated case taken as a clean limit reference. Results obtained on films produced in the standard system with sputter gases other than argon are also listed. Neon discharges result in a very high contamination of the film, to such an extent that its superconducting properties severely deteriorate. In order to keep the explored range of gas concentration in the film within reasonable limits, neon-argon mixtures have been used in various proportions. A mixture of 50% argon and 50% neon has already been found to result in a gas concentration in the film approximately 10 times as large as for standard argon films ($435\pm 70\text{ppm}$) increasing the penetration depth of the magnetic field into the film by $\sim 40\%$. Figure 20 relates the neon partial pressure in the discharge to the neon concentration in the film. A detailed discussion of the experimental technique to measure the noble gas content in films will follow in chapter II/4.

Sputter gas	T_c [K]	$\lambda_{\text{rel.}}$	R_{BCS}^0 [$n\Omega$]	$\Delta(0)/k_B$ [K]
Xenon	9.48 ± 0.03	1.62 ± 0.12	438 ± 12	18.7 ± 0.5
Krypton	9.49 ± 0.03	1.49 ± 0.11	400 ± 7	19.0 ± 0.4
Argon	9.54 ± 0.02	1.56 ± 0.05	401 ± 3	19.7 ± 0.1
Ar:Ne 4:1	9.51 ± 0.03	1.85 ± 0.13	384 ± 6	18.3 ± 0.6
Ar:Ne 1:1	9.53 ± 0.03	2.13 ± 0.23	406 ± 12	18.6 ± 0.6
Ar:Ne 3:7	9.50 ± 0.03	2.37 ± 0.19	444 ± 8	19.1 ± 0.6
Ar:Ne 1:9	9.13 ± 0.03	3.16 ± 0.31	655 ± 15	18.5 ± 0.5

Table 2. Summary of variables. Error bars include the effect of spread between at least two films grown under standard conditions with sputter gases as defined in the first column. The reduced energy gap given in this table (and in table 3 below) is the result of the best fit of equation (56) to the data.

The critical temperature and the energy gap are observed to be relatively insensitive to the presence of noble gas impurities up to concentrations of the order of 2at%, higher than measured for other gases such as oxygen [120, 123] and nitrogen [13, 124].

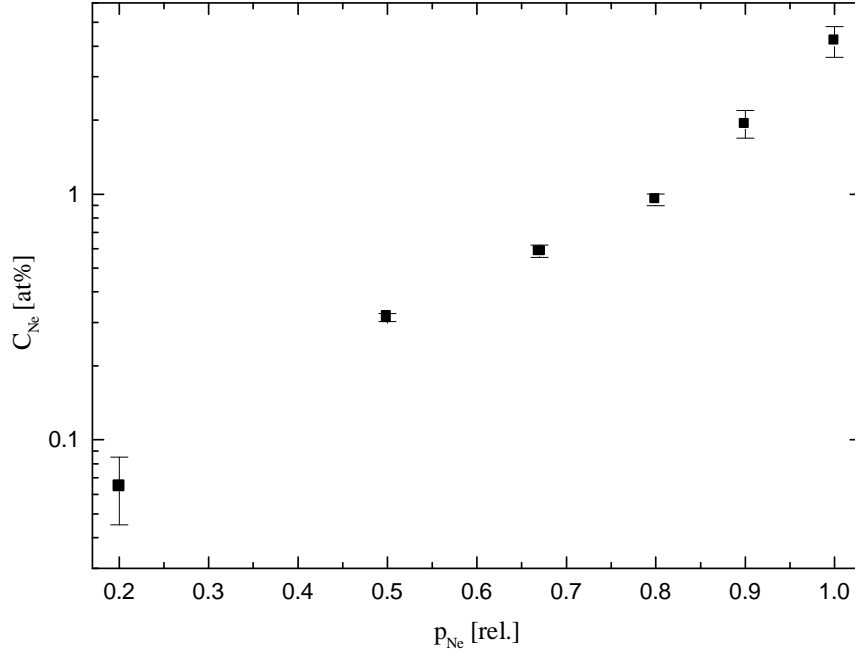


Figure 20. Relative partial pressure of neon in the argon-neon discharge and the corresponding concentration of implanted neon in the film.

The penetration depth data can again be used for a crude evaluation of the London penetration depth. Using the relation between $\lambda(0, l)/\lambda_L(0)$ and $2l/\pi\xi_0$, the inverse of the quantity actually measured, at $\xi_0/\lambda_L = 1.33$, as tabulated in the paper of *Miller* [40] and calculated in the framework of the *Mattis-Bardeen* theory for impure superconductors, gives a mean value of $\lambda_L(0) = 30.5 \pm 1 \text{ nm}$.

The penetration depth in standard films is found to be $\cong 1.56$ times larger than the clean limit value. This is in agreement with expectations from the mean free path dependence of $\lambda(0, l)$. Figure 21 compares the values of ξ_0/λ calculated from the penetration depth measurements according to formula (22a), with independent evaluations deduced from measurements of the residual resistivity ratio of films prepared under similar conditions (chapter II/9). The data are from films grown in argon-neon mixtures of different proportions. The good agreement between both data sets gives confidence in the overall procedure.

The absolute value, $\lambda(0, l) = 46 \text{ nm}$ for standard films is obtained from the calculation of the surface impedance, $X_S(0)$, taking proper film parameters. This value agrees well with the relative measurement of $\lambda(0, l)$, when taking the clean limit value, $\lambda(0, \infty) = 30.2 \text{ nm}$, as obtained in section 5.1.2.

Figure 22 compares the observed BCS resistance, R_{BCS}^0 with theoretical values of the surface resistance, calculated from the *Mattis* and *Bardeen* expression [46]. It can be seen that the complete calculation of the mean free path dependence on the surface resistance adequately represents the experimental values. These data, which cover a broad range of the mean free path l , in particular the minimum of R_{BCS} just below $l = \xi_0$, are the first for a pure metal being compared in detail with theoretical expectations. The calculations were performed for $T_c = 9.54 \text{ K}$ and $\alpha = 1.87$, using a London penetration depth, $\lambda_L = 27 \text{ nm}$ and a BCS coherence length, $\xi_0 = 36 \text{ nm}$. The abscissa is $l + (\pi/2)(\xi_0/l)$, which is measured from the temperature dependence of the resonance frequency near T_c . Together with data of this section (table 2), figure 22 includes data measured on other types of niobium films (see the following section) and on bulk niobium cavities prior to firing. The data are scaled to $T_c = 9.54 \text{ K}$ by a normalisation factor $\exp(-\alpha [9.54 - T_c]/4.2)$ in order to ease the comparison.

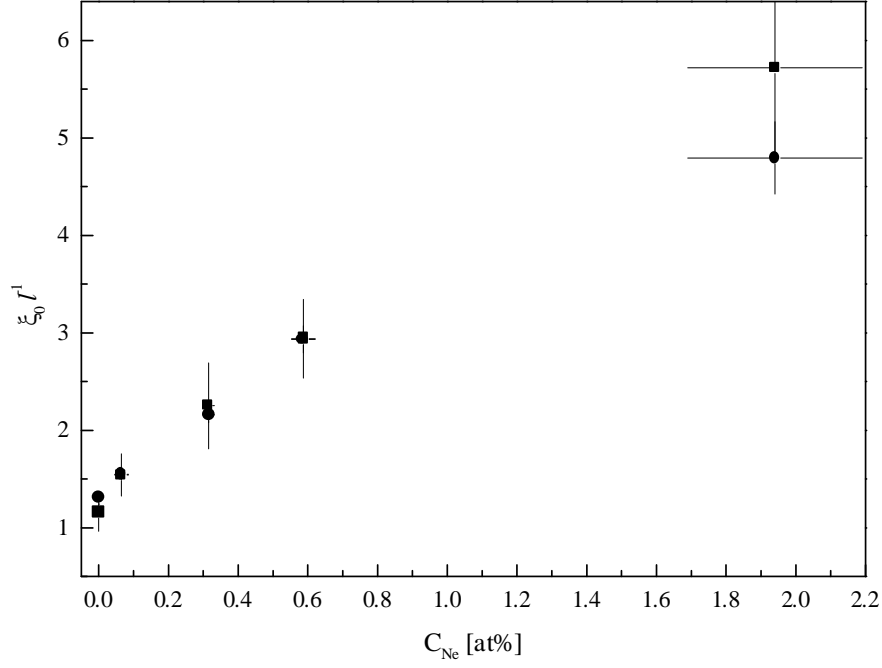


Figure 21. The values of l/ξ_0 measured on resonators from $\lambda_{rel}^2 = 1 + (\pi/2)(\xi_0/l)$ (squares) and on samples from RRR data (circles). The latter values are calculated using $\xi_0 = 36 \pm 1 \text{ nm}$. The films were grown in an argon-neon mixture. The neon content, measured in the films according to the procedure described in part II/chapter 4, is plotted on the abscissa. Data given for the pure argon discharge are calculated from measurements of the RRR and λ_{rel} on the same film, other data are deduced from measurements of RRR and λ_{rel} on different films prepared under similar conditions.

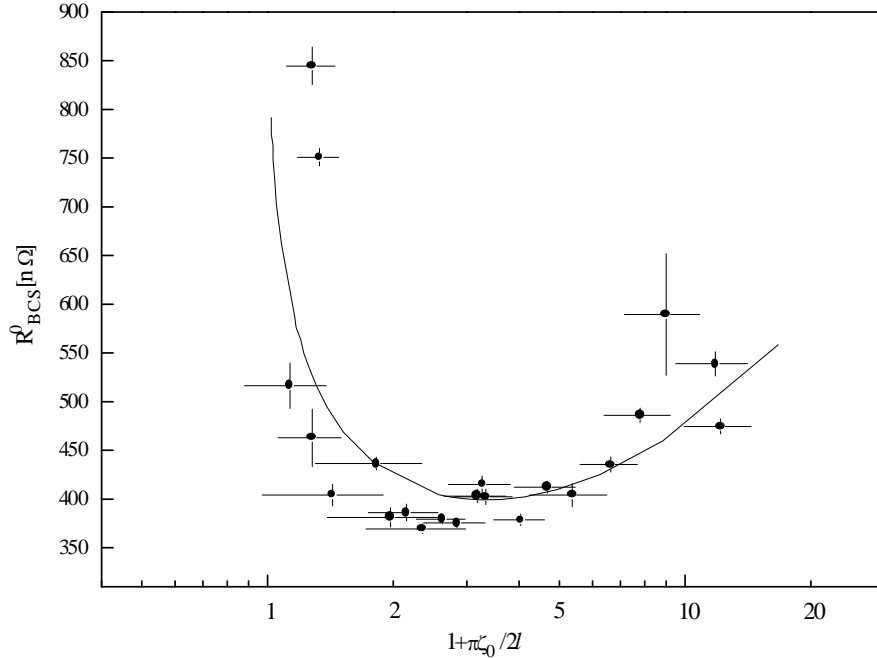


Figure 22. The dependence of R_{BCS}^0 on the mean free path, l , for different cavities (see table 2 and 3). The line is the result of the Mattis-Bardeen calculation using $\lambda_L = 27 \text{ nm}$, $\xi_0 = 36 \text{ nm}$ and $\alpha = 1.87$. The experimental data are scaled to $T_c = 9.54 \text{ K}$ (see text).

The values of $\lambda_L(0)$ and ξ_0 used in the calculations have been tuned to best fit the experimental data. They were evaluated by fixing the ratio $\lambda_L(0)/\xi_0$ to 0.75 (see section 5.1.1). The result,

$\lambda_L(0) = 27 \pm 2 \text{ nm}$, is consistent with the values obtained from the penetration depth data. However, the data scatter significantly around the calculated curve, limiting somewhat the quality of the fit.

The mean free path dependence of the surface resistance is rather complex. In theory, the existence of a minimum is the result of the resonant behaviour of photon absorption by thermally excited quasiparticles [107]. The depth of the minimum is greater for superconductors with larger values of $\lambda_L(0)/\xi_0$ [25, 107, 125]. The present data confirm well theoretical expectations even if the agreement is of limited quality. The significant spread of the data points around the predicted curve is not the result of a lack of reproducibility in the production of several cavities of the same kind, but simply the effect of relatively small differences in λ and R_{BCS}^0 associated with the detailed conditions under which the film was grown. A single parameter l is therefore sufficient to describe the gross features of the data, but does not account for the finer details.

5.2.2. Results on films sputter deposited in the two-electrode system

The present section reviews measurements made on films prepared in the second sputtering system, as discussed in chapter 4. Whereas the sputtering parameters used for growing the niobium films were kept the same, this system allows an in situ pre-treatment of the copper surface changing the nature of the interface between the film and the substrate. The data analysis was performed using the same parameterisation as for standard films or massive niobium resonators and will not be repeated here. A summary of these measurements in terms of the parameters discussed in the previous sections is presented in table 3.

Sputter gas	T_c [K]	$\lambda_{\text{rel.}}$	R_{BCS}^0 [n Ω]	$\Delta(0)/k_B$ [K]
Xenon	9.35 \pm 0.03	1.24 \pm 0.10	530 \pm 10	18.2 \pm 0.6
Krypton	9.31 \pm 0.03	1.02 \pm 0.07	554 \pm 20	17.3 \pm 0.5
Argon	9.44 \pm 0.02	1.14 \pm 0.08	464 \pm 11	18.7 \pm 0.2
Ar:Ne 4:1	9.53 \pm 0.03	1.29 \pm 0.19	383 \pm 10	19.4 \pm 0.9
Ar:Ne 7:3	9.56 \pm 0.03	1.41 \pm 0.19	365 \pm 5	18.9 \pm 0.6
Ar:Ne 1:1	9.50 \pm 0.03	1.99 \pm 0.17	420 \pm 6	19.5 \pm 0.5
Ar:Ne 1:4	9.41 \pm 0.03	2.81 \pm 0.22	511 \pm 8	18.6 \pm 0.5
Argon on Ti	9.52 \pm 0.02	1.60 \pm 0.13	395 \pm 15	18.8 \pm 0.1
Krypton on Cu	9.32 \pm 0.02	1.04 \pm 0.07	563 \pm 20	18.2 \pm 0.4
Argon (340°C)	9.44 \pm 0.03	1.32 \pm 0.18	451 \pm 11	18.9 \pm 0.1

Table 3. Summary of variables. The data were obtained from measurements on films grown on oxide-free copper, on titanium and on a copper pre-layer. All cavities have been sputter deposited in the two-electrode system except those, which have been baked at high temperature before sputter deposition (last row). The given errors include the effect of spread between at least two films grown under standard conditions with sputter gases as defined in the first column.

The results differ from the data obtained on standard films in many respects. In particular, for the sputter gases, argon, xenon and krypton, reverse sputtering results in films with a larger mean free path and hence a shorter penetration depth. For the same composition of the discharge gas the absence of an oxide layer at the interface results in a decrease of ξ_0/l by nearly one order of magnitude. This result has been confirmed by measurements of the normal

state resistivity (chapter II/9). The data obtained on oxide-free cavities lie in a range on the left of the minimum of R_{BCS}^0 in figure 22 towards the ‘clean’ limit reference of bulk niobium data. The minimum itself is given by the standard data and the neon-argon film cavities are in a region towards the ‘dirty’ limit, $\xi_0/l > 1$, on the right hand side of the minimum in figure 22. For the neon-argon mixtures in excess of 50% neon, no clear mean free path difference between both types of films can be observed.

An increase of the BCS resistance, with the amplitude of the rf field, by 50% between 0 and 32 ± 5 mT has also been observed on the films treated in the current section, showing this value to be independent of the mean free path. For films grown on oxide-free copper using argon as a discharge gas, ($T_c = 9.44$ K and $l = 74$ nm), a coupling parameter, $\alpha = 1.86 \pm 0.01$ has been derived from the fit of the temperature dependence of the measured surface resistance to the theory of *Mattis* and *Bardeen*. This value is consistent with those obtained for bulk niobium and standard niobium films.

Table 3 includes measurements made on films grown with argon on a $1 \mu\text{m}$ thick titanium underlayer and on films grown with krypton on a 1.5 mm thick underlayer of copper, sputter deposited on the oxidised copper substrate but itself prevented from getting oxidised. For each set of data, the coupling parameters take mutually consistent values, whereas the critical temperature displays significant differences. Titanium has been chosen as an underlayer because its high getter efficiency prevents a possible diffusion of reactive impurities from the copper substrate or the interface into the niobium film. If the mean free path difference observed between films grown on sputter cleaned and oxidised copper is the result of a higher impurity concentration in the latter, a Cu/CuO/Ti/Nb cavity should behave exactly as a Cu/Nb cavity. In fact, it is observed that films grown in the two-electrode system on titanium have the same critical temperature as standard films and the same values of all other variables (table 3). On the other hand, films grown on a pre-deposited copper layer behave as expected, i.e. all variables are observed to take values identical with those obtained from sputter cleaned cavities.

It might be argued that the difference in critical temperature could be restricted to a region near the interface between the film and the substrate (T_c is measured by the penetration of the magnetic field in the film from the side of the interface, see chapter 4). A separate method, which provides an alternative measurement of the transition temperature of the film, is to observe the decrease of the transmitted power, when the cavity becomes normal conducting. Accordingly, the superficial and interfacial values of T_c could be checked to within ~ 0.05 K.

Finally, it is interesting to note, that films sputter deposited in an argon-neon discharge gas composition do not show the difference in T_c observed for films grown under heavier discharge gases like argon, krypton or xenon. This could be attributed to the higher growth stresses induced in those films and the change of the effective atomic volume due to the dissolution of neon in the niobium lattice, leading also to an increase of T_c at small noble gas concentrations (see also chapter II/2).

A few measurements have also been made on films grown in the standard system after having baked out the copper substrate at 340°C in UHV for at least 20 h. The results are practically identical with those obtained for sputter cleaned cavities and this is in agreement with the fact that annealing of copper above 300°C has the same effect as sputter etching, i.e. to remove the surface oxide.

5.3. The residual resistance of film resonators

The residual term of the surface resistance subsists even at zero temperature. It is the quantity that has to be minimised for achieving high accelerating fields in a superconducting cavity, operated at temperatures below 2K, such as those at CEBAF and TESLA. The residual resistance is often observed to increase with H_S , first to a good approximation linearly and then exponentially beyond some field emission threshold, H_{fe} , [126],

$$\begin{aligned} R_{res} &= R_{res}(0) + R_{res}^I H_S \\ H_S &< H_{fe} \end{aligned} \quad (59)$$

The exponential increase of R_{res} at $H_S \geq H_{fe}$ is observed for both film and bulk resonators as demonstrated in section 5.1 (figure 16) and will not be analysed further since field emission has already been abundantly studied in the literature.

As the term at zero rf field, R_{res}^0 , is usually observed to be in the range from 0 to 60nΩ in film and bulk cavities, it is the non zero value of R_{res}^I , which is exclusively observed in film cavities. In the past, this led to the conjecture that sputter deposited niobium films should suffer from fundamental limitations preventing high accelerating gradients at low values of the residual resistance. The weak link model [19, 127-130], postulating the existence of weak links at grain boundaries, acting as *Josephson* junctions and thus inducing losses related to the value of their critical current has been adopted [19-22] to explain the occurrence of enhanced residual losses with resistive grain boundaries.

A typical set of data describing the form of the H_S dependence of the surface resistance at 1.7K is shown in figure 23. As already stated above, in most cases, the residual resistance can be described by a linear fit when data points at very low field and beyond H_{fe} are neglected. The latter is correlated with field emission, often signalled by the presence of X-rays and a small electron current at the output probe (chapter 3) and, for high values of R_{res} , with excessive heat dissipation leading to cavity quenching.

The largest interval, over which R_{res} depends linearly on field was obtained by excluding all studentised residuals greater than 3 in absolute value⁽¹⁾ from a linear fit.

Data points taken at very low fields are some times observed to deviate from the linear model (Figure 23). They have therefore been treated separately in order to extrapolate the residual resistance at zero field, R_{res}^0 . Normal probability plotting of these data often shows a significant curvature, indicating skewness, which is caused by an initial increase of Q at very low fields, similar to the observation made for bulk niobium cavities (Figure 16). In most cases, however, the initial decrease is small enough to be ignored and a simple average over the low field data defines R_{res}^0 . Niobium films having a residual resistance $>30\text{n}\Omega$ often show no deviation from relation (59) in the interval $0 \leq H_S \leq H_{fe}$ and $R_{res}(0) = R_{res}^0$.

Figure 24 shows the R_{res}^I vs R_{res}^0 plot for numerous niobium films studied in this work. The data include films sputter deposited under different conditions on hydroformed and spun copper substrates subjected to different chemical treatments (chapter 4).

⁽¹⁾Studentised residuals measure how many standard deviations each observed value of $R_{res}(H_S)$ deviates from a model fitted using all of the data except that observation

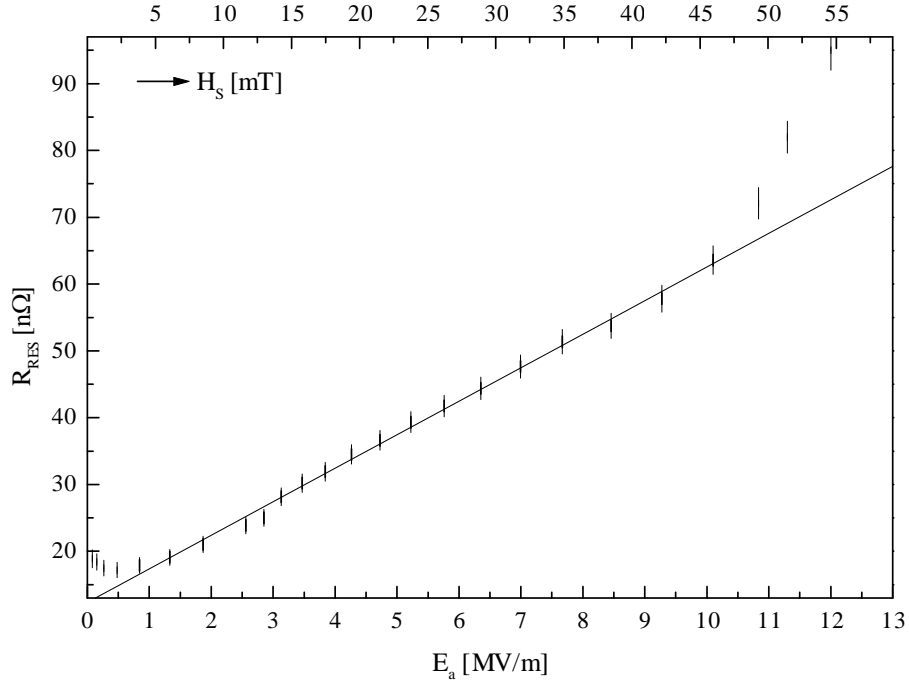


Figure 23. The typical dependence of the residual resistance on the accelerating field for niobium coated copper resonators subjected to chemical polishing before sputtering. The line is the result of a linear fit in the range $[0.7-10\text{MV/m}]$ with $R_{res}^l = 5.0 \pm 0.1 \text{ n}\Omega/\text{MVm}^{-1}$.

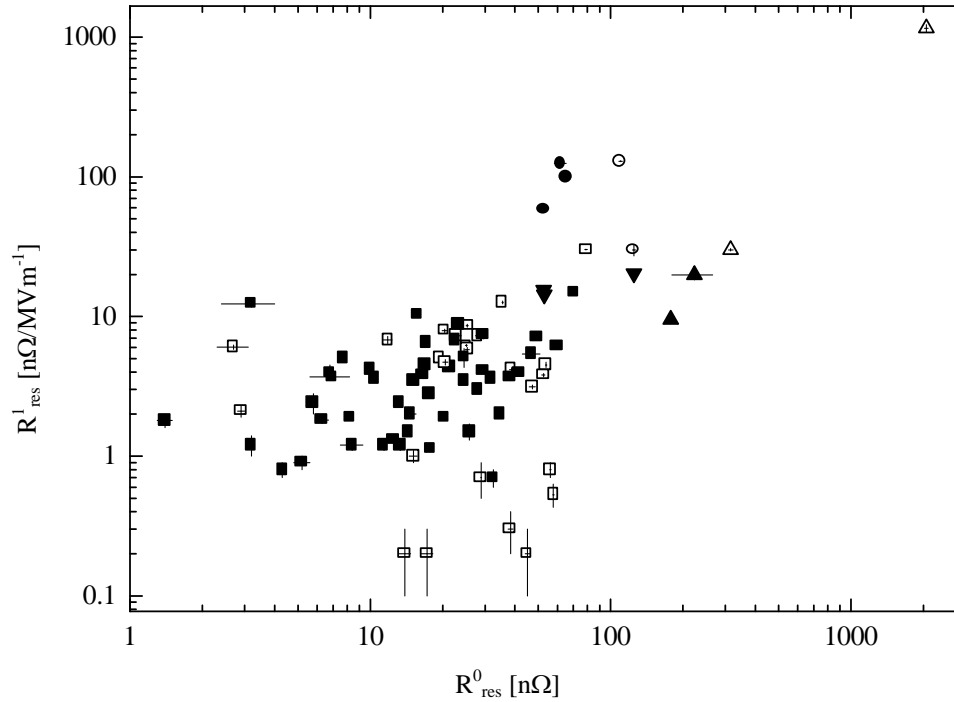


Figure 24. The residual resistance and its dependence on the accelerating field for various kinds of films studied in this work. Films grown in the standard system are labelled with full symbols and films grown in the two-electrode system are labelled with open symbols. The data also include films loaded with hydrogen (up triangles), films coated at substrate temperatures above 250°C (down triangles) and films coated in a pure neon discharge (squares). These films are observed to give a particularly high residual resistance (see text).

An important result is the lack of any significant correlation between the residual resistance (as long as it does not exceed a few 100n Ω , where an unambiguous separation of R_{res} from R_{BCS} becomes difficult) and the other measured variables described in the previous sections. Films prepared under exactly the same conditions yield mutually consistent values of the critical temperature, the energy gap, the penetration depth and the BCS surface resistance, but often inconsistent values of the residual resistance as readily derived from figure 24.

An important deterioration, both of the residual resistance at $H_S = 0$ and of the rate of increase with H_S is observed for films sputter deposited at substrate temperatures above 250°C, for films containing more than 3at-% neon and for films which have been loaded with hydrogen immediately after deposition. Hydrogen is always present in standard films, owing to the presence of hydrogen in the system during sputtering and re-absorption from the atmosphere or from adsorbed water vapour even after formation of the oxide barrier. Its content has been measured for a few cavities by recording the thermal desorption spectra up to 350°C in UHV under dynamic conditions with a calibrated mass analyser. The integrated intensity of the very strong desorption peak at 295°C has been taken as the measure of the hydrogen concentration in films taking into proper account background effects resulting from a continuous degassing of hydrogen from the cavity flanges and the copper substrate itself. The estimated value, $C_0(\text{H}) = 0.2 \pm 0.05 \text{at-\%}$ is consistent with the value $< 0.6 \text{at-\%}$ obtained from independent measurements using elastic recoil detection analysis. Accordingly, hydrogen as a main impurity in niobium films has to be taken into consideration when discussing the mechanisms, which are potentially contributing to the generation of a non-zero residual resistance. Indeed, hydrogen is known to be an important cause of residual resistance for bulk niobium cavities [121, 131, 132].

The presence of impurities having dimensions smaller than the coherence length of a superconductor will generate no residual term, which would add to the surface resistance of a superconductor, but modifies only slightly its BCS resistance [25, 41, 43]. The situation changes when the dimensions of such impurities exceed the coherence length, disturbing the overall coherence of the superconducting state across their boundaries. On condition that such impurities are clustered in the surface region of a superconductor, which is seen by the incident microwave, they may generate additional losses even at zero temperature.

Hydrogen was deliberately introduced into the film as part of a study aimed at investigating the contribution of hydrogen to the residual resistance in niobium films. Hydrogen loading was done at room temperature in the sputtering system by exposure of the as-deposited niobium film to an H_2 atmosphere. Due to the excellent getter capability of niobium, the time required for loading the cavity film with 1.4at-% hydrogen was only about 10min. Following the loading and prior to the exposure to dry air, the films were aged for several hours under UHV conditions at room temperature to homogenise the hydrogen concentration throughout the film. Since the diffusion coefficient of hydrogen in niobium is very high ($D = 6 \times 10^{-6} \text{cm}^2/\text{s}$ at 20°C) [133], a good uniformity of the hydrogen concentration in the niobium film is expected by room-temperature aging.

According to the phase diagram of the niobium-hydrogen system [134], hydrogen enters into niobium bcc cells at room temperature up to a composition $\text{NbH}_{0.05}$ as an interstitial solute (α -phase). However, the solubility limit is drastically reduced when the temperature is lowered and precipitation of the ζ - and ε -hydride phases occurs. Finally, at 77K hydrogen exists in niobium only in the ε -hydride phase. Typical sizes of the non-superconducting hydride precipitates range from several nm to about 0.25 μm [135].

Since a phase diagram only describes equilibrium conditions between components of a system, it is possible to preserve the α -phase by a fast cool down of the cavity to 4.2K, where H_2 diffusion becomes very slow. Another method to suppress the formation of the ε -hydride phase is to shift the occurrence of precipitation to higher hydrogen concentrations. This can be

achieved by trapping hydrogen at lattice defects and impurities, since traps are energetically favourable compared with ordinary interstitial sites [136, 137]. Sputter deposited niobium films are known to have a relatively high density of lattice defects (chapter II/8) and are therefore relatively insensitive to small concentrations of hydrogen in the film, as demonstrated by the small residual resistance, which can be achieved with films (figure 24). The need for a high thermal conductivity to avoid thermal instabilities does, of course, not allow the presence of trapping centres in bulk niobium cavities. In the case of the film technology, excellent thermal conductivity is automatically fulfilled by the copper substrate.

As a first step to investigate the effect of enhanced hydrogen contamination on the residual resistance, both a standard film cavity and a cavity prepared in the two-electrode system under argon were charged with 1.4at-% hydrogen. Residual resistances as large as a few $\mu\Omega$ in the latter case and a correlation between R_{res}^0 and R_{res}^I were obtained this way, with virtually no implication on the other superconducting variables. An important result of this study is the different sensitivity to hydrogen observed between both kind of films. Films grown on oxidised copper are less sensitive to the presence of hydrogen, yielding an increase of R_{res}^0 by one order of magnitude compared to the average taken over all measured values of the residual resistance for standard films. Films grown on oxide-free copper are observed to deteriorate approximately by a factor 200 when charging with the same amount of hydrogen. This comparison may show evidence for strong hydrogen trapping at lattice defects. Films grown on oxidised copper are found to have a higher density of microstructural defects than films grown on oxide-free copper (chapter II/8). However, further studies of the thermodynamics of gaseous hydrogen in equilibrium with the α -phase in niobium films are necessary to quantify the amount of dissolved hydrogen that can be trapped at such defects.

Table 4 summarises the effect of charging film cavities with different amounts of hydrogen on the residual resistance. For the sake of comparison, average values of R_{res}^0 and R_{res}^I observed on films, which have not been loaded with hydrogen but prepared under otherwise identical conditions, are also listed.

H ₂ injected [at%]	R_{res}^0 [n Ω]	R_{res}^I [n Ω /MVm ⁻¹]
Films grown on oxide-free copper		
1.36	$\sim 10^4$	4750
1.36	2058 \pm 38	1160 \pm 69
0.043	316 \pm 7	30 \pm 1
0	36 (20)	11 (9)
Films grown on oxidised copper		
1.36	178 \pm 0.5	9.5 \pm 0.3
0	21 (12)	4.5 (4.8)

Table 4. The residual resistance of niobium films charged with hydrogen. The numbers in parenthesis represent the root mean square deviation from the mean value taken over a total of 29 films prepared in the standard system and 7 films prepared in the two-cathode system on oxide-free copper in an argon discharge on chemically polished substrates.

The influence of the noble gas concentration on the residual resistance is difficult to evaluate because of the large spreads observed between films grown following the same procedure. It is known that at least part of the heavier noble gases, argon, xenon and krypton will precipitate in clusters (chapter II/4) with typical dimensions ranging between 1 and 10nm, depending on the temperature and the defect density created in the growing film. The density of such gas

precipitates will of course depend on the number of gas atoms implanted into the film, which varies with the atomic mass of the gas. The small dimensions of gas agglomerates and the fact that they are not expected to contain free electrons makes it difficult to think about implanted noble gas as a possible source of residual resistance. In fact, as shown in figure 25, the residual resistances of xenon, krypton and argon films, which are expected to contain different concentrations of gas agglomerates, do not significantly differ. However, the large spread of the data of a same type around their mean, typically between ± 50 and $\pm 100\%$ in both R_{res}^0 and R_{res}^I , makes it difficult to exclude small effects with certainty.

Important deterioration, both of R_{res}^0 and R_{res}^I is observed for neon concentrations larger than about 3at-%. This cannot be attributed to a larger number of noble gas precipitates present in those films, because there is strong evidence in the literature and also some confirmation from the present data (chapter II/4), that pure neon clusters do not exist in bulk niobium as long as no high temperature treatment is performed. Diffraction measurements indicate instead that films grown in a neon discharge suffer not only from a severe deterioration of the electronic properties, but show structural defects, which are very different from those observed in other films (chapter II/9). It may therefore not be too surprising to notice also an effect on the residual resistance. However, only direct observations by transmission electron microscopy could tell more about the morphology of those films and possible consequences on the residual resistance.

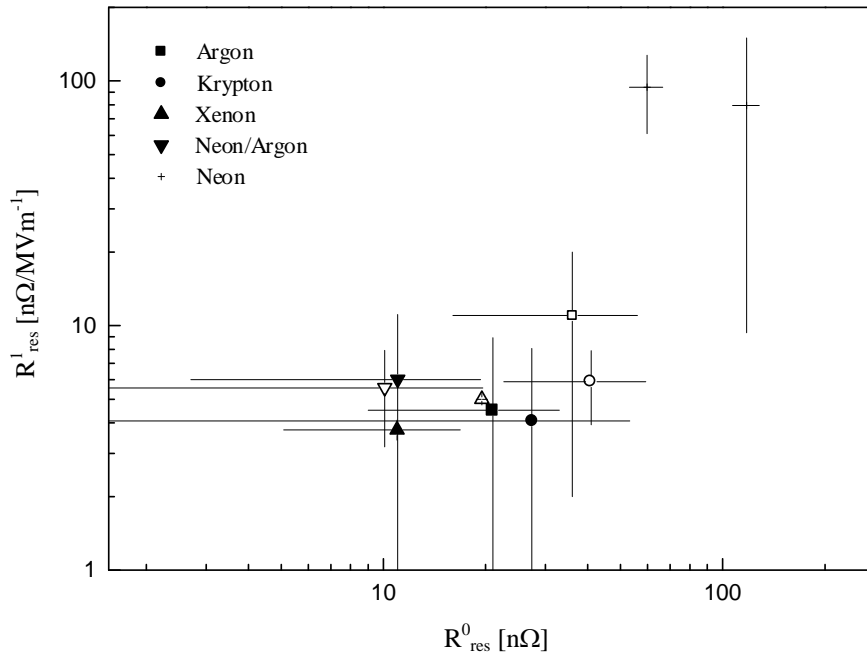


Figure 25. The influence of the discharge gas composition on the residual resistance. Full symbols identify films grown on oxidised copper sputter deposited in the single cathode system and open symbols refer to films grown in the two-electrode system on oxide-free copper or on sputter deposited copper. The bars give the standard deviation from the mean taken over at least three cavities of the same type. The data point for a film grown in the two-electrode system in xenon as discharge gas represents a single measurement only.

Figure 26 presents data that have been obtained over more than two years of intensive research on the niobium/copper technique for the production of 1.5GHz resonators. As can be seen from this figure, very low residual losses, in the nΩ range, have been occasionally observed and could even be maintained over a broad range of accelerating gradients. Such data provided early but strong evidence against the existence of any fundamental intrinsic limitations, preventing the use of the film technology in future accelerators and stimulated further research aiming exclusively at the improvement of the film performance. Significant steps, which have

been taken towards a reliable production of high performance film cavities are the implementation of electropolishing as a surface treatment technique for copper resonators to improve the quality of the substrate (see chapter 4) and a modification of the rinsing station to operate in cleaner conditions.

The improvement achieved by electrochemically polished copper substrates is demonstrated in figure 26. The value of R_{res}^0 but in particular its H_s dependence, R_{res}^I has become comparable to those obtained with bulk niobium, in sharp disagreement with ‘weak link’ model predictions blaming the small grain size of niobium films to be the cause of an unavoidable field dependent term in R_{res} .

For film deposition on electrochemically polished copper, krypton has been used as discharge gas. The production conditions are otherwise the same as described in chapter 4. The values of R_{res}^0 and R_{res}^I are $6.8 \pm 1.9 \text{ n}\Omega$ and $1.4 \pm 0.5 \text{ n}\Omega/\text{MVm}^{-1}$, respectively, for films grown in the standard system; the errors represent again the standard deviation from the mean taken over four cavities. For the same number of cavities produced in the two-electrode system but used as a single cathode system, that is no reverse sputtering or deposition of a copper pre-layer, these values are $38 \pm 18 \text{ n}\Omega$ and $0.3 \pm 0.3 \text{ n}\Omega/\text{MVm}^{-1}$, respectively. For films grown in the two-cathode system on a pre-deposited copper layer, similar results have been obtained. At variance with earlier data presented in figure 25, the present data demonstrate the clear improvement of both, R_{res}^0 and R_{res}^I in terms of their absolute values and their reproducibility as well. A small fraction of data obtained with some upgrades of the rinsing station mentioned in chapter 4, provide further experimental evidence that the current limitation of the accelerating field at typically 10 MV/m as a result of field emission can be shifted to above 20 MV/m . However, further improvements in terms of cleanliness in the production process are necessary to reliably reach such high accelerating fields. Since this is a common feature of the film and bulk technology, enough experience should be available to overcome this very last problem [14].

The present data suggest macroscopic defects on the substrate as the main cause of the residual resistance in film cavities. As discussed in chapter 4 these defects mostly arise from defective chemical polishing and are reproduced by the sputtered layer. Deposition problems in and around geometrical substrate defects, such as poor coverage including areas of no film growth or the build-up of cavities within grooves and holes, porous film growth and irregularities at the film surface on a step in the substrate [73, 138, 139, 140] can account for a non-zero residual resistance. In worst cases these defects may lead to a local peel-off of the film. These topographical limitations to the sputtering of substrate defects are the result of geometrical shadowing; surface points in the depression of the structure are in direct line of sight only with some part of the target erosion zone, whereas the entire target is seen from points on the top surface. Particularly effective to the formation of cavities and cracks in grooves and holes are rough irregularities like surface protrusions on the side-walls of the defects [138]. Shadowing effects are enhanced by an off-normal angle of incidence of sputtered atoms arriving on the substrate. In the present sputtering configuration, the mean angle of incidence is off normal by 15° ; this value increases to 50° near the iris. A displacement of the magnet or an asymmetry of the magnetic field profile around the cathode in the cavity cell will significantly change the angular distribution of the impinging atom flux, further enhancing geometrical shadowing, which will generally lead to less dense columnar grains. This may explain the larger values of the residual resistance in average observed with the two-electrode system (see table 4 and figure 25), since the permanent magnet used to support the plasma discharge in this system was found to produce an inhomogeneous magnetic field. When this magnet was replaced, similar values of the residual resistance could be obtained in both systems.

Surface roughness of the substrate also interacts with the angular distribution of the arriving atoms resulting in shadowing phenomena. It can therefore be expected that a film, sputter

deposited on a rough surface, will give a higher residual resistance, if geometric shadowing is indeed an important parameter to be considered when optimising the rf performance of a superconducting film. As can be seen from figure 26, films grown on hydroformed copper with an average roughness of approximately $1\mu\text{m}$ show an average increase of the residual resistance by $R_{res}^0 \sim 16\text{n}\Omega$, but no deterioration of the field dependent term, R_{res}^1 . The same observation is made when sputtering onto electrochemically polished substrates, which are assumed to be defect-free, by decreasing the average angle of incidence, as accidentally realised by the faulty magnet in the two-cathode system (figure 26).

A simple model of typical film defects caused by a defective substrate, such as local areas of enhanced power dissipation, normal conducting spots or blisters associated with a higher thermal impedance at the film-substrate interface can indeed simulate the measured values of R_{res}^0 and their dependence on H_S [141]. Such blisters also cause hysteresis, i.e. the measured values of R_{res} are higher when scanning the H_S range downward rather than upward, an effect, which has been observed when using chemically polished copper substrates.

The recent data suggest such macroscopic film defects to be the only serious cause of the field dependent term in R_{res} , observed in the past for standard niobium-copper resonators. Other parameters, which in addition could contribute to both, R_{res}^0 and R_{res}^1 , like contamination of the film with hydrogen or a serious structural damage induced by enhanced bombardment of the growing film with noble gas atoms, can easily be kept below a dangerous level.

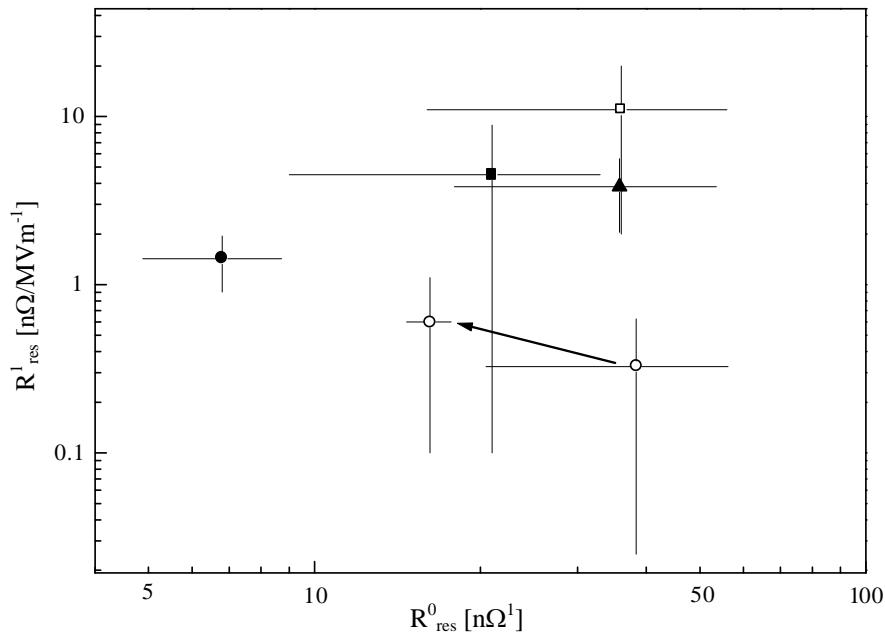


Figure 26. The dependence of the residual resistance on the substrate. The data include standard films (full symbols) and films grown on non-oxidised copper (open symbols), on chemically polished substrates (squares) and electrochemically polished substrates (circles). An average value obtained from standard films grown on hydroformed copper substrates, subjected to chemical polishing is also shown (up triangle). The arrow indicates the improvement of R_{res}^0 after having exchanged the faulty magnet in the two-electrode system.

Figure 27 summarises the good rf performance for a representative number of film cavities, which can now be achieved with extreme reliability. This plot has to be compared with figure 16 in section 5.1, summarising the results obtained on bulk niobium resonators.

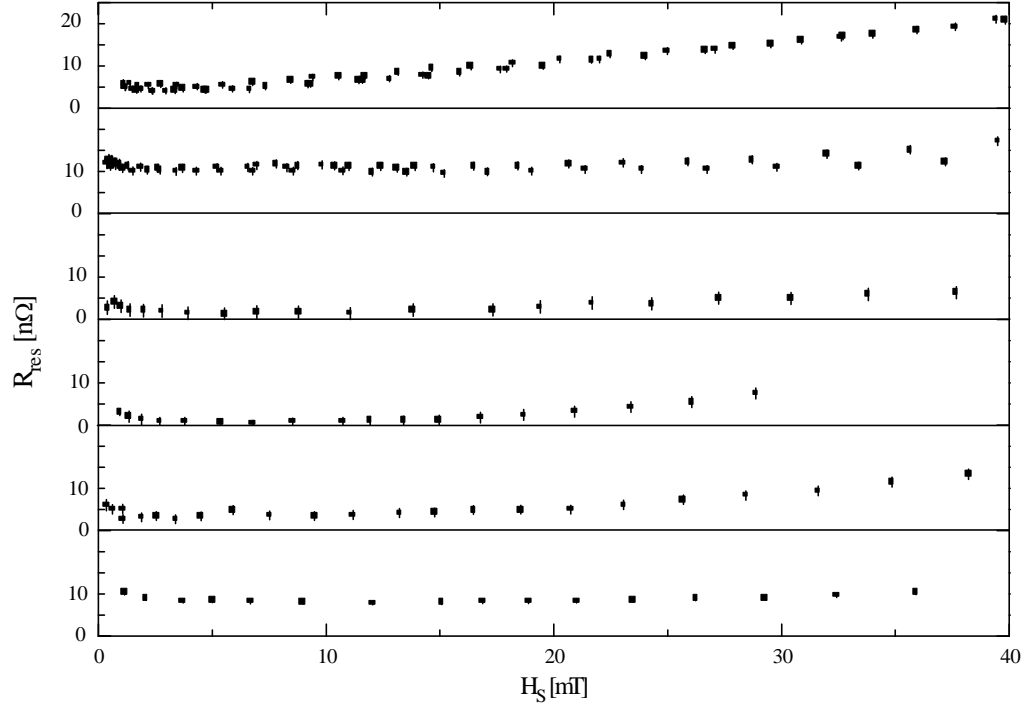


Figure 27. The H_S dependence of R_{res} for niobium film cavities having a good rf performance ($H_S/4.55 = 1\text{MV/m}$). Data are limited to the H_S range below field emission. All cavities have been deposited in the standard system using krypton or argon as discharge gas.

6. Conclusions

The *Mattis* and *Bardeen* theoretical result, which describes the microwave surface resistance of a superconductor, was compared in detail to data obtained from TM_{010} mode niobium film cavity measurements and was shown to fit very well. Important superconducting quantities, such as the critical temperature, the energy gap, the penetration depth and the BCS surface resistance, were found to be consistent within errors, when measured on different resonators prepared under identical conditions. The energy gap, derived from the observed temperature dependence of the surface resistance, was shown to be insensitive to the presence of noble gas impurities up to $\sim 2\text{at\%}$ in the film and is in agreement with other types of measurement on bulk niobium.

Changing the nature of the discharge gas allowed for the production of niobium films with different mean free paths, without introducing reactive impurities or severe changes of the film structure. Theoretical values of the BCS surface impedance have been compared with measurements taken over a wide range of mean free paths with values of l ranging from $\sim 10\text{nm}$ for neon implanted films to $\sim 70\text{nm}$ for films grown in an argon discharge on oxide-free copper. The experimental data suggest a significant sensitivity of the critical temperature and the mean free path to the nature of the interface between the film and the substrate. This result requires additional information about the film structure. This information will be provided in the next part of this work, together with a thorough discussion of possible mechanisms, which can account for the differences between films grown on oxidised copper or on a titanium underlayer and films grown on oxide free copper.

The reasons for the residual resistance, which was initially found to vary in an apparently uncontrolled manner among cavities produced under identical conditions, were identified. The main contribution to the residual resistance of film cavities comes from islands of macroscopic film defects, resulting from surface irregularities of the copper substrate, rather than from weak links at grain boundaries. Other mechanisms, which potentially contribute to the generation of a non-zero residual resistance in film cavities, have also been reviewed and studied. Thereupon, appropriate measures have been taken to reproduce routinely films with a residual surface resistance, which does not increase with rf field by more than $1\text{n}\Omega/\text{MVm}^{-1}$.

As this is an important breakthrough in the development of the niobium film technology for rf superconducting cavities, it can be expected that this technology will seriously be considered as an alternative solution to bulk niobium-copper cavities in future large-scale projects. An achievement of the full potential of the niobium-copper technology, however, still requires further advances in the engineering aspects of copper resonators and higher cleanliness conditions to be maintained during all steps of the fabrication process.

7. References

- [1] J.D. Jackson, '*Classical Electrodynamics*', John Wiley & Sons, New York (1962)
- [2] H. Piel, Proc. of the CERN Accelerator School (CAS), CERN 89-04, S. Turner ed., Hamburg, Germany, page149, (1988)
- [3] P.C. Poole, '*Electron Spin Resonance*', John Wiley & Sons, New York (1967)
- [4] V. Lagomarsino, G. Manuzio, R. Parodi and R. Vaccarone, IEEE Trans. Mag. 15, 1, 25, (1979)
- [5] P. Kneisel, R. Vincon and J. Halbritter, Nucl. Inst. Meth. 188, 669, (1981)
- [6] J.P.H. Slaten, Proc. of the 8th Workshop on rf Superconductivity, V. Palmieri and A. Lombardi, eds., Abano Terme, Padova, Italy, 1, page 117, (1997)
- [7] H.A. Grunder, Proc. of the 16th Particle Accelerator Conference - PAC 95, Dallas, USA, 1, page 1 (1995)
- [8] J. Mammosser, Proc. of the 6th Workshop on rf Superconductivity, R. Sundelin ed., CEBAF, Newport News, USA, 1, page 33, (1993)
- [9] D. Proch, Proc. of the 6th Workshop on rf Superconductivity, R. Sundelin ed., CEBAF, Newport News, USA, 1, page 382, (1993)
- [10] R. Brinkmann, Proc of the 4th European Particle Accelerator Conference - EPAC 94, London, page 383 (1994)
- [11] Ph. Bernard, G. Cavallari, E. Chiaveri, E. Haebel, H. Heinrichs, H. Lengeler, E. Picasso, V. Picciarelli and J. Tückmantel, J. Nucl. Instr. and Meth. 190, 257, (1981)
- [12] H. Padamsee, Proc. of the 1989/90 US Particle Accelerator School, Brookhaven National Lab (1989)
- [13] H.W. Weber, E. Seidl, C. Laa, E. Schachinger and M. Prohammer, Phys. Rev. B44, 14, 7585, (1991)
- [14] For a general overview about the status of research on bulk niobium resonators see for example: Proc. of the 8th Workshop on rf Superconductivity, V. Palmieri and A. Lombardi, eds., Abano Terme, Padova, Italy, vol. 1-4, (1997)
- [15] M. Marino, Proc. of the 8th Workshop on rf Superconductivity, V. Palmieri and A. Lombardi, eds., Abano Terme, Padova, Italy, 4, page 1074, (1997)
- [16] C. Liang, Proc. of the 6th Workshop on rf Superconductivity, R. Sundelin ed., CEBAF, Newport News, USA, 1, page 307, (1993)
- [17] D. Boussard, Proc. of the 5th European Part. Conf.-EPAC 96, S. Myers ed., Spain, page 187, (1996)
- [18] C. Benvenuti, Part. Accel. 40, 43, (1992) and references therein
- [19] B. Bonin and H. Safa, Supercond. Sci. Technol. 4, 257, (1991)
- [20] W. Weingarten, Part. Acc. 53, 199, (1996)
- [21] H. Padamsee, J. Knobloch and T. Hays, '*RF Superconductivity for Accelerators*', John Wiley & Sons, New York, (1998) and references therein
- [22] B. Bonin, Proc. of the CERN Accelerator School (CAS), CERN 96-03, S. Turner ed., Hamburg, Germany, page191, (1995)
- [23] J. Halbritter, J. Supercond. 10, 91, (1997)
- [24] D.M. Pozar, '*Microwave Engineering*', Addison-Wesley, (1990)
- [25] J.P. Turneure, J. Halbritter and H.A. Schwettman, J. Supercond. 4, 5, (1991)
- [26] K. Halbach and R.F. Holsinger, Part. Accel. 7, 213, (1976)
- [27] T. Weiland, DESY 82-015, DESY M-82-24, (unpublished) and IEEE Trans. Nucl. Sci. NS-32, 2738, (1985)
- [28] G.E.H. Reuter and E.H. Sondheimer, Proc. Roy. Soc. A195, 336, (1948)
- [29] F. London and H. London, Proc. Roy. Soc. A149, 71, (1935)
- [30] L.F. Mattheiss and L.R. Testardi, Phys. Rev. B20, 2196, (1979)
- [31] A.B. Pippard, Proc. Roy. Soc. (London) A216, 547, (1953)

- [32] T.F. Faber and A.B. Pippard, Proc. Roy. Soc. (London) A231, 336, (1955)
- [33] J. Bardeen, L.N. Cooper and J.R. Schrieffer, Phys. Rev. 108, 1175, (1957)
- [34] B. Mühlischlegel, Z. Physik 155, 313, (1959)
- [35] G. Brandstätter, Ph.D. thesis, Vienna Technical University, Austria, (1994), unpublished
- [36] S. Foner and E.J. Niff, Phys. Lett. 58A, 318, (1976)
- [37] G.M. Eliashberg, Sov. Phys.-JETP 11, 696, (1960)
- [38] M. Tinkham, '*Introduction to Superconductivity*', McGraw-Hill, (1975)
- [39] J. Halbritter, Z. Physik 238, 466, (1970) and Z. Physik 243, 201, (1971)
- [40] P.B. Miller, Phys. Rev. 113, 5, 1209, (1958)
- [41] D.C. Mattis and J. Bardeen, Phys. Rev. 111, 412, (1958)
- [42] L.N. Cooper, Phys. Rev. 104, 1189, (1956)
- [43] A.A. Abrikosov, L.P. Gor'kov and L.M. Khalatnikov, Sov. Phys.-JETP 35, 182, (1959)
- [44] H. Diepers and H. Martens, Phys. Lett. 38A, 337, (1972)
- [45] J. P. Turneure and I. Weissman, J. Appl. Phys. 39, 4417, (1968)
- [46] J. Halbritter, Z. Phys. 238, 466 (1970) and Ext. Bericht 3/70-6, Kernforschungszentrum Karlsruhe, Germany, (1970)
- [47] R. Blaschke, '*Recent Developments in Condensed Matter Physics*', J.T. Devresse ed., Plenum Press, New York, USA, vol. 4, 425, (1981)
- [48] R. Blaschke and R. Blocksdorf, Z. Physik B49, 99, (1982)
- [49] P.W. Anderson, J. Phys. Chem. Solids 11, 26, (1959)
- [50] M.L.A. MacVicar and R.M. Rose, J. Appl. Phys. 39, 3, 1721, (1968)
- [51] R. Blaschke, J. Askenazi, O. Pictet, D.D. Koelling, A.T. von Kessel and F.M. Müller, J. Phys. F14, 175, (1984) and references therein
- [52] P.B. Miller, Phys. Rev. 118, 4, 928, (1960)
- [53] S.B. Nam, Phys. Rev. 156, 470, (1966) and Phys. Rev. 156, 487, (1966)
- [54] P. Wilson, SLAC-TN-70-35, internal report, Stanford, USA, (1970), unpublished
- [55] W. Meissner and R. Ochsenfeld, Naturwiss. 21, 787, (1933)
- [56] J. Matricon and D. S. James, Phys. Lett. 24A, 241, (1967)
- [57] T. Yogi, G.J. Dick and J.E. Mercerau, Phys. Rev. Lett. 39, 826, (1977)
- [58] L. Kramer, Phys. Rev. 170, 475, (1968)
- [59] V.L. Ginzburg and L.D. Landau, Zh. Eksperim. i Teor. Fiz. 20, 1064, (1950)
- [60] H. Padamsee, J. Tückmantel and W. Weingarten, IEEE Trans. Mag. 19, 1308, (1983)
- [61] B. H. Wiik, Proc. of the 8th Workshop on rf Superconductivity, V. Palmieri and A. Lombardi, eds., Abano Terme, Padova, Italy, 1, page 54, (1997)
- [62] R.J. Noer, Appl. Phys. A28, 1, (1982)
- [63] Ph. Niedermann, N. Sankarraman, R.J. Noer and O. Fischer, J. Appl. Phys. 59, 3851, (1986)
- [64] J. Tan, Proc. of the 7th Workshop on RF Superconductivity, B. Bonin ed., Gif sur Yvette, France, 1, page 105, (1995)
- [65] K.H. Bayliss and R.V. Latham, Proc. Roy. Soc. (London) A403, 285, (1986)
- [66] B. Bonin, Proc. of the 6th Workshop on RF Superconductivity, R. Sundelin ed., CEBAF, Newport News, USA, 1, page 794, (1993)
- [67] R.V. Latham, '*High Voltage Vacuum Insulation-The Physical Basics*', Academic Press, London, (1981)
- [68] Ph. Bernard, Nucl. Instrum. Meth. 190, 257, (1981)
- [69] D. Reschke, Ph.D. thesis, WUB-DIS 95-5, Bergische Universität Wuppertal, Germany, (1995), unpublished
- [70] H. Padamsee, K.W. Shepard and R. Sundelin, Annu. Rev. Nucl. Part. Sci. 43, 635, (1993)
- [71] H. Padamsee, IEEE Trans. Mag. 19, 1322, (1983)

- [72] C. Benvenuti, V. Palmieri and R. Vaglio, 'Superconductivity and Superconducting Materials Technologies, P. Vincenzini, ed., Techna, page 637, (1995)
- [73] D.L. Smith, '*Thin-Film Deposition*', McGraw-Hill, New York, (1995)
- [74] J. Turneaure, H.A. Schwettman, H.D. Schwarz and M.S. McAshan, Appl. Phys. Lett. 25, 247, (1974)
- [75] C. Hauviller, Proc. of the 14th IEEE Particle Accelerator Conference - PAC 89, F. Bennett and J. Kopta eds., Chigago, USA, 1, page 485, (1989)
- [76] V. Palmieri, Part. Accel. 53, 217, (1996)
- [77] M. Viswanathan, Proc. of the International Conference on Electrodeposition and Electroforming, E.S. Dwarakadasa, R.P. Dampal and J. Balachandra eds., Indian Institute of Science, Bangalore, India, page 177, (1986)
- [78] J-P. Birabeau and J.M.A. Guerin, Patent N° 88 09820, Institut National de la Propriété Industrielle, (1993)
- [79] C. Benvenuti, R. Cosso, M. Hauer, N. Hellgren and D. Lacarrère, Proc. of the 7th Workshop on RF Superconductivity, B. Bonin ed., Gif sur Yvette, France, 2, page 491, (1995)
- [80] L. Ponto, unpublished results, CERN (1986)
- [81] V. Palmieri, V.L. Ruzinov, S.Y. Stark and F. Stivanello, Proc. of the 7th Workshop on RF Superconductivity, B. Bonin ed., Gif sur Yvette, France, 2, page 605, (1995)
- [82] P.A. Jacquet, Trans. Electrochem. Soc. 69, 629, (1936), Bull. Soc. Chim. France 3, 705, (1936) and Compt. Rend. 202, 402, (1936)
- [83] H. Figour and P.A. Jacquet, French Patent N° 707526, (1930)
- [84] D. Landolt, Electrochim. Acta, 32, 1, (1987)
- [85] C. Wagner, J. Electrochem. Soc. 101, 225, (1954).
- [86] M. Novak, A.K.N. Reddy and H.W. Wroblowa, J. Electrochem. Soc. 117, 733, (1970)
- [87] S.H. Glarum and J.H. Marshall, J. Electrochem. Soc. 132, 2872, (1985)
- [88] T.P. Hoar, D.C. Mears and G.P. Rothwell, Corr. Sci. 5, 279, (1965)
- [89] H.F. Walton, J. Electrochem. Soc. 97, 219, (1950)
- [90] D. Laforge-Kantzner, C.R Acad. Sci. 233, 547, (1951)
- [91] M.E. Baumgärtner and C.J. Raub, Galvanotechnik 86, 2, 376, (1995)
- [92] P. Kneisel, J. Mammosser, G. Rao, K. Saito and R. Sunderlin, Conf. Record of the 15th IEEE Particle Accelerator Conference – PAC 91, San Francisco, USA, 4, page 2384, (1991).
- [93] F.M. Penning, Physica 3, 873, (1936)
- [94] A.S. Penfold and J.A. Thornton, U.S. Patent 3, 884, 793, (1974), U.S. Patent 4, 030, 996, (1977) and U.S. Patent 4, 031, 424, (1977)
- [95] J.A. Thornton, J. Vac. Sci. Technol. 15, 171, (1978)
- [96] R. Russo and S. Sgobba, Part. Accel. 60, 135, (1998)
- [97] J. Halbritter, Appl. Phys. A43, 1, (1987) and references therein
- [98] K.E. Gray, Appl. Phys. Lett. 27, 462, (1975)
- [99] B. Roux, A. Chevarier, N. Chevarier, B. Wybourn, C. Antoine, B. Bonin, P. Bosland and S. Cantacuzene, Vacuum 49, 7, 629, (1995)
- [100] N. Laegreid and G.K. Wehner, J. Appl. Phys. 32, 365, (1961)
- [101] C.H. Weijsenfeld, A. Hoogendorn and M. Koedam, Physica 27, 763, (1961)
- [102] H.M. Windawi, J.R. Katzer and C.B. Cooper, Phys. Lett. 59A, 62, (1976)
- [103] H. Lengeler, '*RF Measurements with SC Cavities*', Technical note, CERN/EF/3741H/HL/ed, (1987), unpublished
- [104] L.P. Gor'kov, Sov. Phys.-JETP 36, 1364, (1959)
- [105] H.R. Kerchner, D.K. Christen and S.T. Sekula, Phys. Rev. B21, 1, 86, (1980) and references therein
- [106] J. Auer and H. Ullmaier, Phys. Rev. B7, 1, 136, (1973)

- [107] J. Halbritter, Z. Physik 266, 209, (1974)
- [108] A. Philipp and J. Halbritter, IEEE Trans. Mag., MAG-17, 951 (1981) and 19, 999, (1983)
- [109] W. Bauer, S. Giordano and H. Hahn, J. Appl. Phys. 45, 11, 5023, (1974)
- [110] M.A. Allen, Z.D. Farkas, H.A. Hogg, E.W. Hoyt and P.B. Wilson, IEEE Trans. Nucl. Sci. NS-18, 168, (1971)
- [111] E.L. Wolf, J. Zasadzinski, J.W. Osmun and G.B. Arnold, J. Low. Temp. Phys. 40, 19, (1980)
- [112] J. Bostock, K. Agyeman, M.H. Frommer and M.L.A. MacVicar, J. Appl. Phys. 44, 12, 5567, (1973)
- [113] J.B. Carbotte, Rev. Mod. Phys. 62, 1027, (1990) and references therein
- [114] F.L. Palmer, Ph.D. thesis, Cornell University, New York, USA (1988), unpublished and references therein
- [115] H.A. Schwettman, J.P. Turneaure, W.M. Fairbank, T.I. Smith, M.S. McAshan, P.B. Wilson and E.E. Chambers, IEEE Trans. Nucl. Sci., NS-14, 336 (1967)
- [116] C. Passow, Phys. Rev. Lett. 28, 7, 427, (1972)
- [117] J. Halbritter, J. Appl. Phys. 42, 1, 82, (1972)
- [118] P.B. Wilson, Z.D. Farkas, H.A. Hogg, and E.W. Hoyt, IEEE Trans. Nucl. Sci., NS-20, 3, 104, (1973)
- [119] B. Pioscyk, P. Kneisel, O. Stoltz and J. Halbritter, IEEE Trans. Nucl. Sci., NS-20, 3, 108, (1973)
- [120] S. Giordano, H. Hahn, H.J. Halama, C. Varmazis and L. Rinderer, J. Appl. Phys. 44, 9, 4185, (1973)
- [121] S. Isagawa, J. Appl. Phys. 51, 8, 4460, (1980)
- [122] J.P. Turneaure and N.T. Viet, Appl. Phys. Lett. 16, 9, 333, (1970)
- [123] W. De Sorbo, Phys. Rev. 132, 107, (1963) and Phys. Rev. 134, A1119, (1964)
- [124] E. Seidl, H.W. Weber and H. Teichler, J. Low Temp. Phys. 30, 3/4, 273, (1978)
- [125] P. Flécher, Ph.D. thesis, University of Karlsruhe, Germany, (1977), unpublished
- [126] D. Moffat, P. Barnes, T. Flynn, J. Graber, L. Hand, W. Hartung, T. Hays, J. Kirchgessner, J. Knobloch, R. Noer, H. Padamsee, D. Rubin and J. Sears, Part. Acc. 40, 85, (1992) and references therein
- [127] C. Attanasio, L. Maritato and R. Vaglio, Phys. Rev. B43, 6128, (1991) and IEEE Trans. Mag. 27, 1920, (1991)
- [128] T.L. Hylton, A. Kapitulnik, M.R. Beasley, J.P. Carini, L. Drabek and G. Gruener, Appl. Phys. Lett. 53, 1343, (1988)
- [129] A.M. Portis, D.W. Cooke, E.R. Gray, P.N. Arendt, C.L. Bohn, J.R. Delayen, C.T. Roche, M. Hein, N. Klein, G. Müller, S. Orbach and H. Piel, Appl. Phys. Lett. 58, 307, (1991)
- [130] P. Nguyen, D.E. Oates, G. Dresselhaus and M.S. Dresselhaus, Phys. Rev. B48, 6400, (1993)
- [131] B. Bonin and R.W. Röth, Part. Accel. 40, 59, (1992)
- [132] T. Schober, Scripta Metallurgica, 7, 1119, (1973)
- [133] G. Schaumann, J. Völkl and G. Alefeld, Phys. Status Solidi 42, 401, (1970)
- [134] H. Wenzel and J.M. Welter, 'Current Topics in Material Science', E. Kaldis, ed., vol. 1, page 670, North-Holland, Amsterdam, (1977)
- [135] T. Schober, 'Hydrogen in Metals I', G. Alefeld and J. Völkl, eds., page 11, Springer Verlag, Berlin, (1978)
- [136] G. Pfeiffer and H. Wipf, J. Phys. F: Metal Phys. 6, 2, 167, (1976)
- [137] B. Roux, H. Jaffrezic, A. Chevarier, N. Chevarier and M.T. Magda, Phys. Rev. B52, 6, 4162, (1995)

- [138] T.C. Tisone and J.B. Bindell, J. Vac. Sci. Technol. 11, 2, 519, (1974)
- [139] H.P. Bader and A.M. Lardon, J. Vac. Sci. Technol. B4, 5, 1192, (1986)
- [140] I.A. Blech and H.A. Vander-Plas, J. Appl. Phys. 54, 3489, (1983)
- [141] J. Tückmantel, '*Thermal Effects in Superconducting RF-Cavities*', Technical note, CERN/EF/RF 84-6, (1984), unpublished

Part II – Characterisation of niobium film samples

1. Preparation and characterisation techniques

The following chapters provide additional information about the electrical and superconducting properties of magnetron sputtered niobium films as well as results obtained by X-ray diffraction (XRD). A detailed description of the microstructure of niobium films grown on oxidised and on sputter cleaned copper substrates will be given in order to get a better understanding of the observed differences in the superconducting properties of those films. Complementary information has been obtained by the technique of nanoindentation to measure *Young's* modulus of the material, Transmission Electron Microscopy (TEM) to observe the apparent grain size and thermal desorption up to the melting point to measure the noble gas concentration. In addition, surface analysis by depth-sensitive analytical methods, like X-ray Photoelectron Spectroscopy (XPS), Auger Electron Spectroscopy (AES) and Secondary Emission Mass Spectrometry (SIMS) has been carried out.

Results of inductive measurements of the transition temperature, of the upper and lower critical fields in a SQUID magnetometer and of the residual resistivity will also be presented in the following chapters. Each method will be introduced briefly and the main results will be documented in detail.

In the present work emphasis was laid on a rather complete description of niobium films by XRD as the primary analytical technique, since it allows a comprehensive analysis of important parameters such as the lattice constant, the residual macrostrain and the related stress as well as the film texture. In addition, a line profile analysis of the diffraction pattern provides information about the microstrain, which can be further related to the density of defects, the stacking fault probability and the coherently diffracting domain or crystallite size. An analysis was made on samples cut from cavities and on samples sputtered under similar conditions to those maintained during coating a 1.5GHz copper cavity. For that purpose, flat copper substrates with an approximate size of $10 \times 35 \text{ mm}^2$ were cut from OFE copper sheets and mounted on three sample holders placed along the equator of a 500MHz stainless steel cavity. A single sample holder can host up to six substrates, which can be sputter deposited either simultaneously or alternately by using a protective screen. The target-to-substrate distance in this 'sample system' is about 25cm. Thermocouples fixed on each sample holder allowed to monitor the temperature during deposition. Pre-sputtering at the desired operating conditions was done with the substrates shielded. The system has already been described in detail elsewhere [1].

Samples coated under different discharge conditions were produced in this way and the transition temperature (T_c), the lattice parameter, the microstrain, and the residual resistance ratio (RRR) were measured. All parameters except the resistivity were measured before and after removal of the copper substrate. The film thickness was determined by weighting the films after dissolution of the copper substrate or on niobium deposited quartz samples, which were mounted on the system together with the copper substrates. The method applied for a direct estimation of the film thickness was tip-profilometry, which measures the height of a step between the film and an adjacent portion of uncovered substrate, by moving a conical stylus tip across the edge of the film (Talystep™, Rank Precision Industries LTD). This measurement allows to calculate the growth rate of the film deposition in the 'sample' system, which is found to be $0.52 \pm 0.03 \text{ nm/s}$ under pure argon discharge gas.

The main emphasis, however, was placed on the characterisation of samples cut from the equatorial region of 1.5GHz cavities, since they provide information on films, whose superconducting rf properties are well known. The sample size was less than 1.5cm^2 , small enough to minimise disturbing effects in diffraction measurements due to the curvature of the sample. The cavities, which were cut for these experiments, are:

- E8.7, a spun cavity coated under ‘standard’ conditions,
- E10.4, a spun cavity that was reverse sputtered prior to niobium deposition, and
- E9.6, a spun cavity that was produced in the same way as E10.4, but loaded with 1.4% hydrogen after niobium deposition, measured and again degassed at $300\pm 10^\circ\text{C}$ for approximately 14 hours (see also chapter I/5).

The notations E8.7, E10.4 and E9.6 were kept and refer in the following to samples cut from a particular cavity. The subscripts *i* and *e* have been introduced to refer to samples cut from the cavity cell close to the iris and from the equator, respectively.

2. The critical temperature

The experimental procedure consists of placing the sample between two small solenoids enclosed in a copper cell and of transferring this assembly into a liquid helium cryostat. There the sample temperature can be varied from 4.19K to well above the transition point by allowing helium vapour to enter the cell through a heated copper tube. A calibrated carbon-glass resistor in good thermal contact with the sample was used as a temperature sensor. The error in T_c determined by the calibration error of the thermometer is about $\pm 4\text{mK}$. The principle of the measurement is to apply a low frequency alternating current to the primary (excitation) coil and to record the voltage in the secondary (pick-up) coil as a function of temperature. When the sample is in the normal conducting state, the currents induced in the sample reduce the mutual inductance only slightly, and a current is induced in the secondary coil. When the transition occurs, the shielding currents induced in the sample surface prevent the ac magnetic field from penetrating through the sample and a significant decrease of the current induced in the secondary coil is recorded. With a phase sensitive lock-in amplifier, the in- and out-of-phase component (V' and V'' , resp.) of the induced voltage are measured. The critical temperature T_c and the transition width ΔT were determined from a fit of the in-phase data to the function

$$\frac{V_n - V_s}{1 + \exp\left\{\frac{T - T_c}{\Delta T}\right\}} + V_s + aT, \quad (1)$$

where the term aT is introduced to allow for a possible slope in both the normal conducting, V_n , and the superconducting in-phase component of the signal, V_s .

In addition, for sample E8.7e and E10.4e, ac susceptibility measurements at zero dc field were performed with a SQUID magnetometer (see also chapter 10). The temperature dependence of the in-phase and the out-of-phase parts of the complex susceptibility, χ' , and χ'' are shown in figure 1. The applied ac field, H_{ac} , was 10^{-4}T and the frequency, f , was 31Hz. A steplike change in $\chi'(T)$ and an absorption peak in $\chi''(T)$, proportional to the energy dissipation, W , per unit volume per cycle, due to the motion of fluxoids, is usually observed when the transition into the superconducting state occurs [2]. At the temperature, where the skin depth, δ , is of the order of the film thickness, the imaginary part of the ac susceptibility has a maximum [2, 3]. Below this temperature χ'' decreases because the ac field no longer penetrates the whole film and the volume in which losses occur shrinks.

The temperature dependence of the imaginary part of the susceptibility reflects the screening capabilities, i.e. the critical current densities and the corresponding loss behaviour of the intragrain and intergrain material [3, 4, 5]. Measurements on low quality specimens would reveal a relative broad transition or a shoulder in $\chi'(T)$ and an asymmetric or double peak in $\chi''(T)$. This is the consequence of weak links existing between grains, which carry supercurrents only below the so-called phase locking temperature, which can be considerably lower than the intragrain T_c .

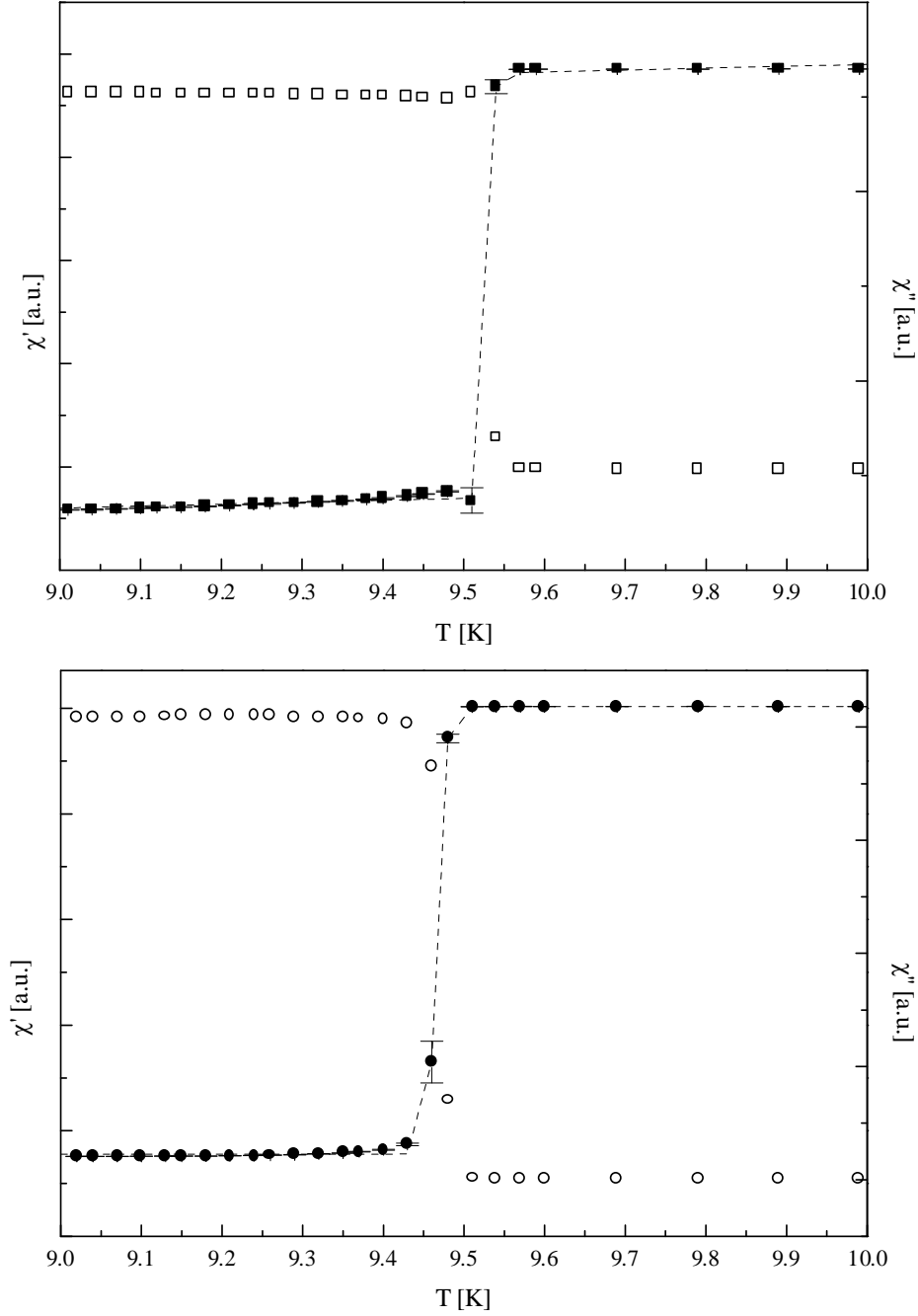


Figure 1. Temperature dependence of the real (χ' , full symbols) and imaginary (χ'' , open symbols) parts of the ac susceptibility for sample E8.7e (top figure, squares) and E10.4e (bottom figure, circles), measured at $h_{dc} = 0$, $h_{ac} = 10^{-4}T$ and $f = 31\text{Hz}$.

The small transition widths of niobium films, comparable to those observed for bulk niobium samples, do not indicate the presence of any intergrain loss behaviour. The steplike change in $\chi''(T)$ is the result of the ac losses in the copper substrate, which are present even when the niobium film is perfectly superconducting. The values of T_c and ΔT , measured on samples cut from cavities by fitting equation (1) to the in-phase signals, are listed in table 1. The onsets of the transition (T_{on}) are also given in table 1, since these values are observed to be almost ac frequency independent. Fit errors were evaluated by calculating the rms of several measurements, including the spread in the data obtained from different samples cut from the same area of the cavity cell. Results obtained with the SQUID magnetometer represent data from a single measurement only. The values of the critical temperature however, are in

excellent agreement with those measured with the simple two-coil arrangement described above.

Sample	T_c [K]	T_{on} [K]	ΔT [mK]
E8.7i (1)	9.544 ± 0.008	9.59 ± 0.02	19 ± 5
E8.7i (2)	9.547 ± 0.012	9.59 ± 0.02	16 ± 3
E8.7e	9.534 ± 0.011	9.56 ± 0.01	13 ± 1
E10.4i (1)*	9.526 ± 0.005	9.57 ± 0.01	23 ± 3
E10.4i (2)	9.481 ± 0.008	9.53 ± 0.02	33 ± 4
E10.4e	9.456 ± 0.004	9.50 ± 0.01	19 ± 2
E9.6i (1)*	9.369 ± 0.006	9.42 ± 0.01	30 ± 1
E9.6i (2)	9.243 ± 0.012	9.30 ± 0.01	28 ± 2
E9.6e	9.186 ± 0.007	9.23 ± 0.01	19 ± 2
Heat treatment in UHV to 350°C:			
E8.7e	9.172 ± 0.026	9.33 ± 0.02	45 ± 10
E10.4e	9.164 ± 0.012	9.27 ± 0.02	37 ± 5
AC susceptibility measurement in the SQUID magnetometer before			
E8.7e	9.529 ± 0.003	9.542 ± 0.005	4 ± 1
E10.4e	9.467 ± 0.001	9.482 ± 0.004	5 ± 1
and after substrate removal			
E8.7e	9.315 ± 0.002	9.36 ± 0.02	15 ± 2
E10.4e	9.313 ± 0.002	9.36 ± 0.02	15 ± 1

Table 1. Critical temperature of niobium films sputter-deposited on oxidised copper cavities (E8.7), oxide-free copper cavities (E10.4) and after annealing in UHV conditions at 300°C (E9.6) and 350°C. The films of sample E10.4i (1) and E9.6 (1) were measured to have a thickness of $2.4 \pm 0.1 \mu\text{m}$, i.e. $0.9 \pm 0.1 \mu\text{m}$ above the nominal value of $1.5 \mu\text{m}$.

The data display again a significant difference in T_c , as has already been noticed from the measurements made on cavities with Hall probes as described in part I of this work. Films grown on oxide-free copper have a lower critical temperature than films grown on oxidised copper. In the special case of cavity E10.4 and E8.7, the difference is $0.078 \pm 0.003 \text{K}$ on the cavity equator. Sample E10.4i (1) has an apparently higher transition temperature, which approaches the value observed for niobium films grown on oxidised copper. It seems reasonable to ascribe the higher T_c values obtained for thicker films as well as the observed differences between both types of films to the observed differences in strain, as will be discussed in detail in the next chapters.

Measurements of the pressure dependence of the critical temperature of niobium were shown to give quite different results for the coefficient dT_c/dp , depending on how the pressure is applied to the sample [6-10]. The latest measurements reported by *Struzhkin et al.* [6], applying a quasi-hydrostatic stress by a NaCl pressure medium up to 70 GPa yield, after an initial decrease of approximately 0.2 K at pressures up to 3 GPa, a 0.7 K increase of T_c close to 5 GPa. These changes were reported to be reversible and partly related to changes in the topology of the Fermi surface, induced by volumetric compression. The results obtained by *Smith* [7], which reveal also a decrease of T_c (-0.018K/GPa) upon applying a hydrostatic stress by an organic

fluid transmitting medium up to 4GPa, were re-plotted in Ref. [11], together with data in the lattice dilation regime on sputtered niobium films. This plot, which correlates the increase in T_c in superconducting films with the stress via the measured lattice constant, is shown in figure 2 together with the experimental results of the present work. The data represent films grown on sapphire [11] and copper substrates with noble gas concentrations of the order of a few 100ppm, probably agglomerated in rare gas clusters (chapter 4). A lattice dilation of $\sim 30\text{m}\text{\AA}$, measured perpendicular to the surface plane, was reported to give a maximum raise of T_c by $0.4\pm 0.1\text{K}$ [11]. It must be noted that in the case of films, the forces acting on any face of a unit cell of niobium consist only of the in-plane components and the film is free to expand in the perpendicular direction according to *Poisson's* ratio. This effect causes the observed increase of the out of-plane lattice parameter, Δa_{\perp} , compared to the reference value for unstressed niobium (3.307\AA , as given in Ref. [11]). According to *Poisson's* ratio, ν , which has been estimated experimentally to be close to 0.5 (chapter 7), a volume conservation of the unit cell is expected for the films. On the contrary, the hydrostatic pressure experiments on bulk niobium always lead to significant volume compression, which does not follow elastic theory, but is given by the compressibility of the metal. This difference may explain the discrepancy, which appears in the literature when discussing the influence of stress on the critical temperature. Starting from the well-known expression for T_c given by the *BCS* theory [12], the derivative of T_c with respect to the pressure under hydrostatic conditions has been expressed in terms of the lattice compressibility and the *Grüneisen* constants of the electrons and of the lattice [13]. The calculated results are in good agreement with the experimentally observed negative values of dT_c/dp given in [6, 7] at pressures up to 5GPa.

Considering now measurements, which were obtained upon applying a force in the direction perpendicular to the surface, a situation similar to the distribution of forces acting on the sputtered-deposited films adhering to a rigid substrate, dT_c/dp was always found to be positive [9, 10]. The results obtained by these authors are comparable and yield a dT_c/dp of $+1.1\pm 0.03\times 10^{-1}\text{K/GPa}$ up to 3GPa.

When the copper substrate is removed by dissolution in ammoniumpersulfate or in nitric acid, the critical temperature of the niobium films decreases significantly and approaches the nominal value for bulk niobium⁽¹⁾. This effect is accompanied by a total stress release in films that have been sputter-deposited in an argon, krypton or xenon discharge, which confirms the expected reversible effect of the applied strain, ε , on T_c . A similar strain effect on the superconducting properties was observed in Nb_3Ge films, where a maximum, reversible increase of T_c by 0.4-0.6K due to an applied strain was measured [14].

Vacuum annealing of niobium films, previously exposed to air, results in a significant decrease of the critical temperature. This behaviour cannot be explained by structural transformations, stress release or by a significant change in the microstructure, since, these parameters are not dramatically affected by annealing the films to 350° , as will be shown in the following chapters.

It is known that oxygen will be dissolved in the lattice by vacuum annealing of niobium films after their exposure to air [15, 16]. Oxygen mainly comes from the chemical reaction,

⁽¹⁾Table 1 includes only the results on free-standing films cut from cavities and measured with the SQUID magnetometer. These values are approximately 0.015K higher than those reported for very pure niobium single crystals in the most recent literature on niobium [30]. They are also higher with respect to the mean value of $9.27\pm 0.02\text{K}$ measured on niobium films coated under standard conditions in the sample system, which have subsequently been freed from the substrate.

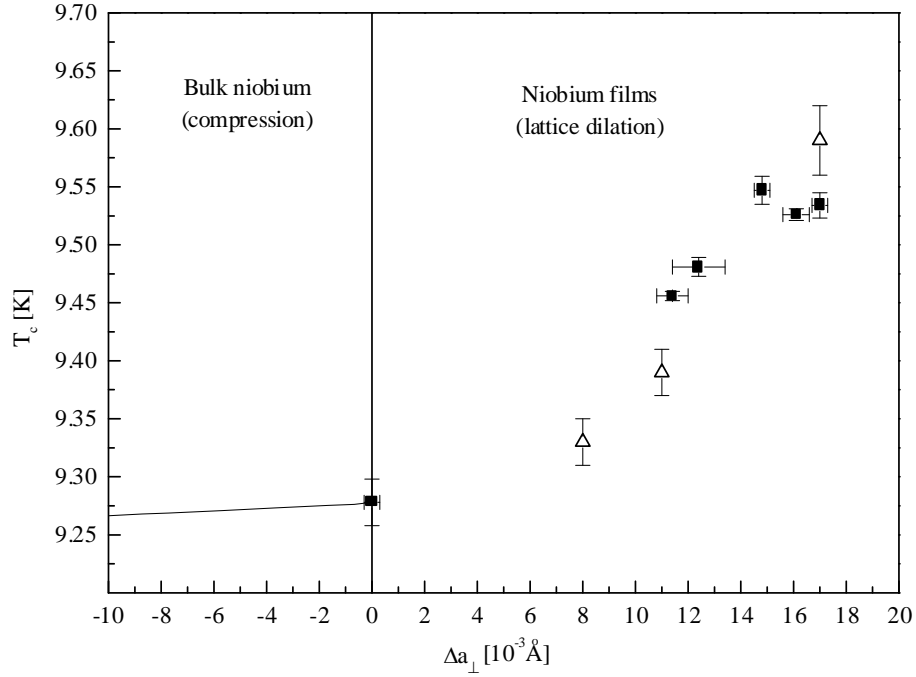
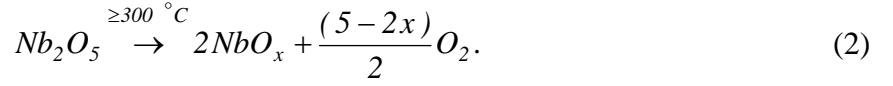


Figure 2. The transition temperature of bulk niobium under hydrostatic pressure after *Smith* (solid line) and of niobium films with a dilated lattice normal to the surface plane. Full squares represent data from cavity E8.7 and E10.4 and open triangles represent data given in Ref. [11] on films sputtered in a krypton discharge on sapphire substrates. Smith's data have been converted into Δa_{\perp} by taking the compressibility of niobium ($0.567 \times 10^{-6} \text{bar}^{-1}$) and assuming homogeneous volumetric compression.

As the most stable niobium oxide, the dielectric Nb_2O_5 forms the outermost layer of the oxides on niobium at room temperature. XPS depth profile analysis of the niobium films yields a saturation thickness of $8 \pm 1 \text{ nm}$ of Nb_2O_5 (10σ criterion), independent of the exposure time to ambient air. The XPS depth profile of a niobium film grown on oxidised copper, vented to dry air for 10 hours and stored under ambient air for several weeks is shown in figure 3. Three windows were set to record the electron binding energies of the elements C, O and Nb as a function of successive sputtering cycles. Spectra showing the carbon peak at 284.5 eV are recorded before sputtering and indicate chemisorbed surface contamination. Other spectra are taken after successive sputtering cycles by bombardment with energetic xenon atoms and show peaks at 530.8 eV (O-1s), 207.3 eV and 210.0 eV (Nb-3d_{3/2} / 3d_{5/2} of Nb_2O_5), 204.1 and 206.8 eV (Nb-3d_{3/2} / 3d_{5/2} of NbO). After approximately 10 cycles, corresponding to a depth of 8 nm, the oxygen peak at 530.8 eV disappears and the position of the niobium lines shifts to 202.2 and 204.9 eV, corresponding to the energy expected for pure niobium. The NbO_2 peak at 205.8 and 208.5 eV cannot be resolved, but is likely to be also present.

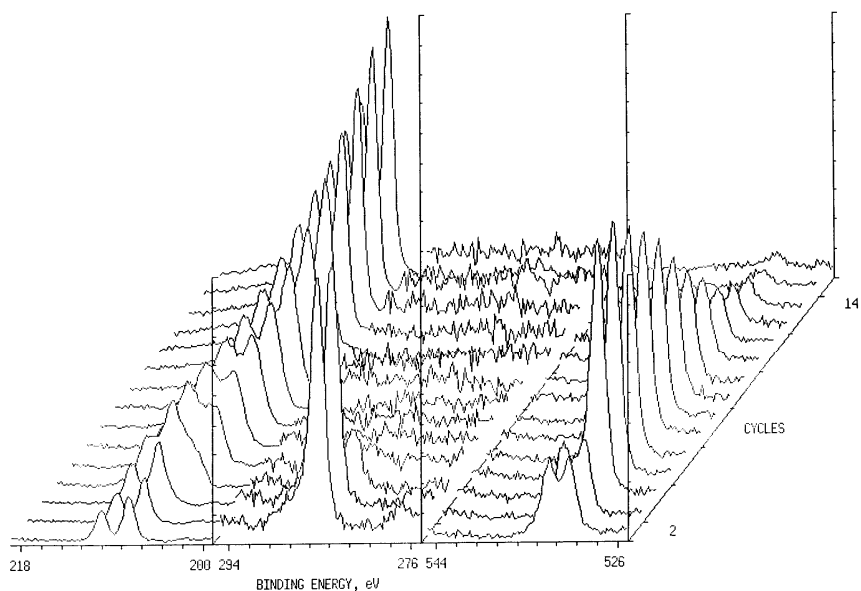


Figure 3. XPS depth profile analysis of standard niobium films after exposure to air.

Figure 4 shows the spectra of niobium films at a depth of about 3nm before (top figure) and after UHV heat treatment to 320° (bottom figure) in an energy range between 200 and 218eV. The integrated intensity of the NbO signal (204.1eV), normalised by the Nb₂O₅ signal (207.3eV) increases from 1.2 to 2.2 by annealing, indicating the transformation of Nb₂O₅ into NbO accompanied by a release of oxygen into the film.

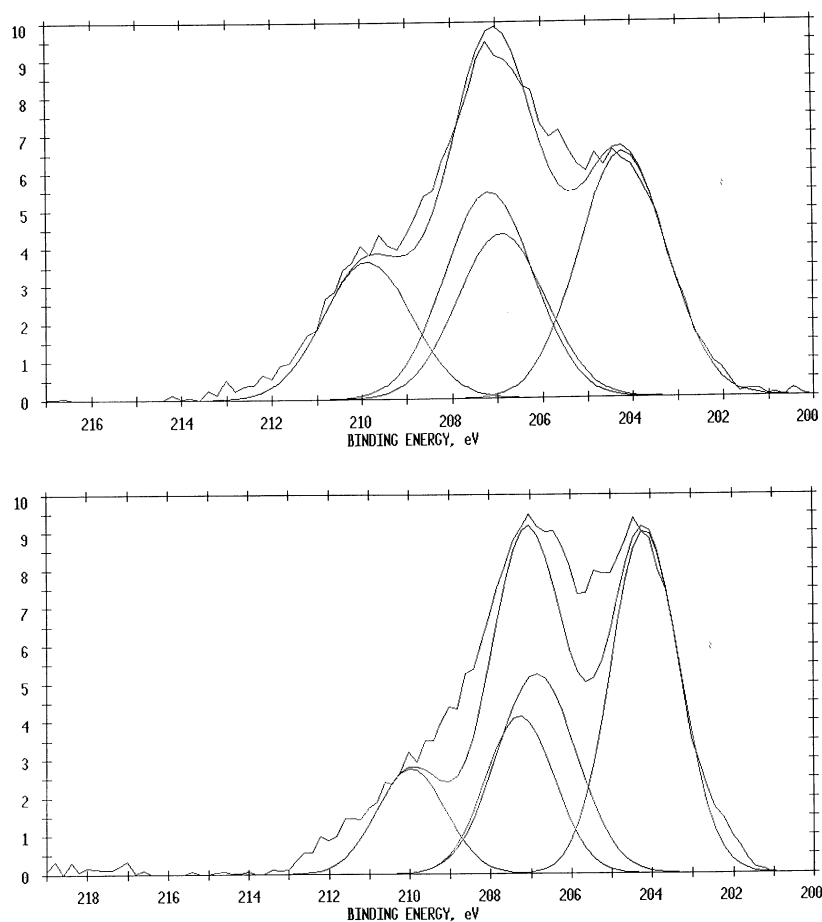


Figure 4. XPS spectra of standard niobium films showing the evolution of the NbO peak with UHV heat treatment. The resolved profiles of the Nb₂O₅ and NbO doublet are obtained from a fit to the measured profile.

At low oxygen concentrations ($C_O \leq 3\text{at-}\%$), the change of T_c follows the empirical relation [17, 18]

$$\Delta T_c = (-0.90 \pm 0.05) C_O \text{ [at-}\%] \quad (3)$$

where the factor 0.9 gives the depression of T_c for one atomic percent of oxygen dissolved in pure niobium. The observed decrease of the resistivity ratio without changing the structural properties of the film indicates a shorter electron mean free path, l , due to impurities, which can partly account for the decrease of T_c by reducing the anisotropy of the energy gap [19, 20, 21]. Koch *et al.* [17] and Crozat [22] found in argon implanted niobium films a decrease of the electron-phonon coupling constant, λ_e , and of the density of states at the Fermi level, $N(E_F)$, with increasing impurity content, which is known to depress T_c in strong-coupled transition metal superconductors [23].

As already shown in chapter I/5, the superconducting transition temperature can be depressed by large concentrations of neon in the film. However, the implantation of small amounts of an inert gas into a growing film is one of the most effective methods of changing the mean free path, l , while having little effect on the other characteristics of the metal. The main purpose of having made film cavities with different noble gas concentrations was to study the effect of the reduced mean free path on the surface resistance of the superconducting films, but other characteristics of neon implanted films have been worked out as well. Table 2 summarises the measurements of T_c on these films, which were grown on oxidised copper and subsequently removed from the substrate to relax the elastic film stresses (see also chapters 3 and 4). Different concentrations of implanted neon were obtained by varying the neon partial pressure in an argon-neon discharge (see chapter 3).

At neon concentrations, $C_{Ne} \geq 0.6\text{at-}\%$, one can describe the change of T_c by the relation

$$\Delta T_c = (-0.23 \pm 0.04) C_{Ne} \text{ [at-}\%] \quad (4)$$

This value is of a reasonable order of magnitude, if compared with the influence of argon in niobium single crystal films, $(dT_c/dC)_{Ar} = -0.30 \pm 0.15\text{K/at-}\%$ [15] and of krypton in polycrystalline niobium films, where a value of $(dT_c/dC)_{Kr} = -0.19\text{K/at-}\%$ for krypton concentrations between 0.5at-% and 2at-% has been quoted [11]. Varying the argon concentration in sputter deposited niobium films from 0.05 to 0.3at-% by reducing the discharge gas pressure, has no effect on T_c [24].

Neon [ppm]	d [nm]	T_c [K]	T_{on} [K]	ΔT [mK]
0	1500	9.28 ± 0.03	9.34 ± 0.05	46 ± 5
650 ± 200	1500	9.30 ± 0.02	9.38 ± 0.01	46 ± 4
3150 ± 120	2400	9.33 ± 0.01	9.42 ± 0.01	37 ± 2
5870 ± 340	2800	9.34 ± 0.02	9.38 ± 0.02	22 ± 1
9500 ± 520	3000	9.25 ± 0.01	9.30 ± 0.01	15 ± 1
19400 ± 2500	2900	9.20 ± 0.01	9.29 ± 0.01	41 ± 7
42000 ± 6000	2900	8.50 ± 0.06	8.62 ± 0.07	62 ± 7

Table 2. Transition temperature of niobium films with implanted neon atoms. The argon concentration in those films is 450 ± 100 ppm and does not depend on the discharge gas composition. The measured film thickness, d , is given in the second column. The observed differences are caused by an initial underestimation of the growth rate in a neon rich discharge gas mixture. The errors include the spread in the data obtained from measurements on two different samples coated simultaneously in the ‘sample’ system, whereas for 0at-% neon (pure argon discharge), the error includes the spread in the measured data from films cut from standard cavities and from films grown in the sample system.

The present data also indicate a slight increase of the transition temperature with increasing neon content at concentrations up to $C_{Ne} = 0.6\text{at-\%}$ (Figure 5). This effect has already been observed for helium bombarded indium films and was attributed mainly to a change of the effective atomic volume due to the dissolution of a small amount of helium in the indium lattice [25, 26]. As will be discussed in detail later, a deformation along the (211) planes due to neon dissolution into the lattice has been measured. Deformation of metals, like tin, thallium and indium by implanted noble gas atoms [27] was shown to increase the transition temperature and to eliminate the impurity effect at small concentrations. The effect of a lattice distortion on T_c has been discussed theoretically by *Lazarev et al.* [28]. Tunnel studies on extremely distorted films with an increased T_c with respect to the bulk values, revealed a strongly distorted phonon spectrum [29].

The data on neon implanted niobium films suggest a crossover for the impurity effect at $\sim 0.6\text{at-\%}$. However, a part of the implanted neon is possibly concentrated in gas bubbles (chapter 4) and will therefore not contribute to any mechanism, which may lead to a change in T_c .

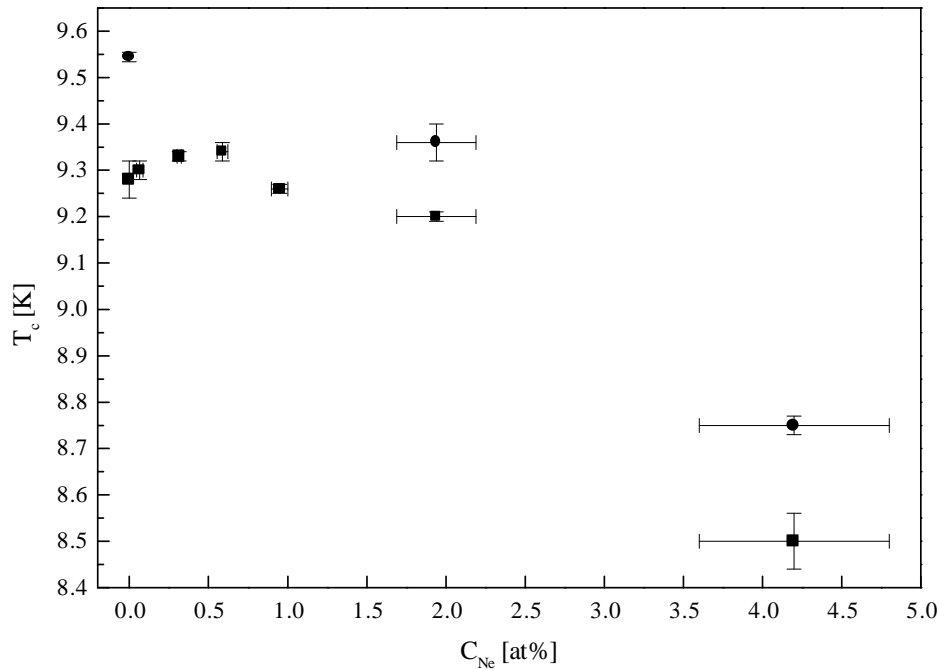


Figure 5. Dependence of the critical temperature T_c on the total neon concentration in niobium films having been dissolved from the copper substrate to release the elastic film stresses. The circles represent a few data on the same films before substrate removal.

3. Determination of the lattice parameter by X-ray diffraction

3.1. Experimental procedure

According to *Bragg's law*,

$$\sin \theta = \frac{n\lambda}{2d}, \quad (5)$$

where the integer n denotes the 'order of the reflection', and θ the angle between the atomic plane and both the incident and reflecting beams, the interplanar spacing between successive atomic planes in the crystal, d , can experimentally be determined by X-ray diffraction. For crystals of the cubic system, the value of the lattice constant a (the length of the edge of the elementary cubic cell) can be calculated for every reflection hkl by employing the equation

$$a = \frac{\lambda}{2} \frac{\sqrt{h^2 + k^2 + l^2}}{\sin \theta}, \quad (6)$$

where λ is the wavelength of the X-rays, and the integers h , k and l are the *Miller* indices of a plane.

A Siemens D5000 Cristalloflex™ diffractometer with a symmetrical reflection of X-rays with respect to the film normal was used. In this so-called *Bragg-Brentano* geometry, all diffracting planes are parallel to the film surface, and a lattice parameter a_{\perp} , perpendicular to the surface plane is measured. The following measurements use the position of the peak maximum as the quantity defining the lattice parameter of individual reflections, a_{hkl} . The measured raw profile contains contributions from angle-dependent intensity factors, such as the *Lorentz-Polarisation* (LP) [31, 32] and absorption factors, and the intensity variation caused by such factors has been removed from the profile before the peak maximum was determined. The contribution of the absorption will be discussed in detail in a later chapter, since it affects considerably the measurement of the absolute peak intensity.

After the appropriate angular corrections to the raw intensities, the absolute value of the peak position was determined by a functional representation of the whole peak profile. Most data were analysed using the modified Lorentzian, which is one of the more popular functional forms used in profile fitting [34]. It is of the form

$$I(2\theta) = A \left\{ \cos \pi \frac{(2\theta - 2\theta_p - \beta)}{B} \right\}^n \frac{k^2}{k^2 + (2\theta - 2\theta_p)^2} + S2\theta + C. \quad (7)$$

Here, A is the maximum intensity, B is the defined fitting period, β accounts for a small asymmetry in the line profile, k is a constant Lorentzian term and $2\theta_p$ is the needed two-theta value at the peak. The cosine term raised to the appropriate power, n , forces the curve to drop more rapidly in the tail regions of the line profile. The terms S and C were added to the function to fit the tails of the peak profile to the background. If the background intensity is the same on both sides of the peak, than S becomes zero.

Profile fitting as described above can give accurate results only, if there is no separation of the $K\alpha_1$ - $K\alpha_2$ doublet (Cu $K\alpha$ and $K\beta$ radiation produced at 40 kV, 30 mA was employed for all measurements). Because of the small coherently diffracting domains and the microstrain present in the niobium films (chapter 8), no resolution of the $K\alpha_1$ - $K\alpha_2$ doublet is observed and the niobium peaks can be fitted without any further modification of the fit function. In that case, the wavelength, $\lambda = 1.54178\text{\AA}$, employed to determine the lattice spacing corresponding to the peak position from *Bragg's law*, is the weighted average of $K\alpha_1$ - $K\alpha_2$. In averaging, $K\alpha_1$

is given twice the weight of $K\alpha_2$. Diffraction lines resulting from the $K\beta$ radiation were also analysed to increase the number of data points for the subsequent determination of the lattice constant. The parameters set for the measurements are listed in table 3.

Mode of operation :	θ -2 θ
Stepsize/time :	0.01°/3s
Wavelength :	1.540560/1.544390/1.392220 Å (Cu)
Variable divergence diaphragm :	0.5° (1mm) fixed
Scattered-radiation diaphragm next to sample	Pinhole, 5 mm
$K\beta$ filter (Ni) :	out
Primary/secondary soller slits :	in/in
Variable scattered radiation diaphragm :	0.3°(0.6mm) fixed
Fixed detector diaphragm :	0.2 mm
Detector slit :	out

Table 3. Parameters set for diffraction measurement of the lattice parameter and the texture.

It was found that the error on the peak location caused by non-consideration of the LP effect is quite small; it may introduce at most 0.05% difference between the ‘true’ a_{hkl} and the uncorrected value. Especially for low-angle reflections this is negligible compared to the errors introduced by the specimen curvature and specimen displacement. These latter errors are briefly discussed here, since they contribute significantly to the uncertainty in the obtained a_{hkl} values.

If the effective diffracting volume is not located at the centre of the diffractometer (Fig. 6), there is an angle-dependent peak shift, which is given by

$$\Delta\theta = \frac{180\Delta x \cos\theta}{\pi R_{GC}}. \quad (8)$$

Here Δx is the sample displacement, $\Delta\theta$ is the shift in degrees and R_{GC} is the goniometer radius (410mm). Differentiating Bragg’s law and substituting $\Delta\theta$ from equation (8), one obtains,

$$\frac{\Delta d}{d} = \frac{a_{hkl} - a_{\perp}}{a_{\perp}} = -\frac{\Delta x}{R_{GC}} \cot\theta \cos\theta. \quad (9)$$

Here, a_{hkl} is again the lattice parameter calculated from the peak maximum of a single reflection and a_{\perp} is that value of a_{hkl} extrapolated to $\cot\theta \cos\theta = 0$. When the lattice parameter, a_{hkl} , is determined for various reflections and plotted vs. $\cos^2\theta/\sin\theta$, the sample displacement can approximately be determined from the slope of this line (Eqn. 9). A positive slope indicates a negative displacement, i.e. the sample is displaced to a position behind the centre of the diffractometer. In the case of the θ -2 θ measurements, the experimentally observed displacement due to the curvature of the specimens was between 0.5 and 0.9mm. The extrapolated value, a_{\perp} , was found to be independent of the sample displacement. It should, however, be noted that the existence of stress gradients in a film would also lead to a slope in the plots presented in figures 7 and 8 (section 3.3), which results from the angle dependence of the X-ray penetration depth (see chapter 7).

Another source of error arises from the divergence of the beam in the incident plane. In practice, the specimen surface never conforms to the focusing circle. A displacement of sections of the specimen from the focusing circle broadens and displaces the X-ray peak. The error in the peak location can be shown to be related to the beam divergence by

$$\Delta 2\theta \approx \frac{\sin 2\theta}{12 \sin^2 \theta} \alpha^2, \quad (10)$$

where α is the horizontal divergence allowed in the beam by the particular slit arrangement. It is clear that errors due to these two causes vanish at $\theta = 90^\circ$. The procedure usually adopted, is therefore, to derive the cell dimensions of the material from a number of lines, preferentially at $\theta \geq 30^\circ$, to plot these values against some function of the *Bragg* angle and to extrapolate to a value corresponding to $\theta = 90^\circ$, as shown in figures 7 and 8.

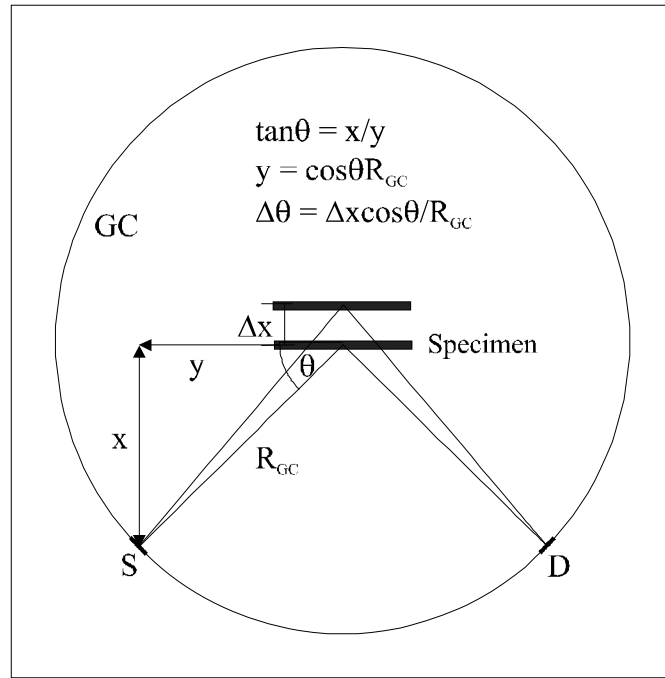


Figure 6. Effect of sample displacement on the position of 2θ .

A plot of a_{hkl} against $0.5\{[(\cos^2 \theta)/(\sin \theta)] + [(\cos^2 \theta)/\theta]\}$ was empirically shown to give a linearity down to very low angles, when absorption, displacement and divergence are the main sources of error [33]. This function is generally accepted to give best results and will be used in the present work to evaluate the value of a_\perp from the lattice constants, a_{hkl} , derived from several reflections.

3.2. Mechanisms of stress generation in sputter deposited films

The stresses induced in the growing film cause expansion or contraction of the lattice with respect to the equilibrium lattice spacing of an unstressed specimen. These stresses can be calculated from directional variations of lattice strains, which are determined from relative shifts of XRD lines, measured with a different goniometer configuration (chapter 7). Since these strains correspond to an overall change of the lattice parameter, they are characterised as macrostrains.

As the lattice parameter measured in the direction of growth, perpendicular to the surface of the substrate shows a close relation to the film stress [24], a_\perp is therefore a first indication of the

presence of stress. After having corrected for instrumental effects, the lattice parameter measured along any direction can be described by the expression [36],

$$a_{hkl} = a_0 (I + S_{I(hkl)} \sigma + D_{(hkl)}), \quad (11)$$

where S_I is the elastic constant, σ the stress and $D_{(hkl)}$ represents the influence of growth faults and lattice disorder. The exact meaning of these parameters will be explained in the following chapters.

Macrostress of the order of several hundred MPa are created in films due to different thermal contraction of the film and the substrate, due to grain competition during their growth, due to the coupling of differently oriented grains in anisotropic materials and due to the mismatch between the lattices of the film and the substrate. Moreover, it is generally accepted that bombardment of the growing coatings by energetic neutrals of the plasma-supporting noble gas causes compressive in-plane stress [37, 38, 39]. In the unbiased magnetron system used in the present work, these energetic particles result from noble gas ions, which are accelerated to the niobium cathode, neutralised by the *Auger* process [40] and scattered towards the substrate. Charged particles will not have an important effect in the deposition process, since the substrate is on ground potential. At low pressure, as employed in the present work, the mean free path is large compared to the flight path; therefore the argon ions do not suffer from collisions on their way to the target and strike the target surface at normal incidence. The kinetic energy of the incident ions is then almost equal to the cathode potential. If the cathode atoms are much heavier than the gas ion, they will be reflected with an important fraction of the initial energy and incorporated into the growing film. From the principle of conservation of energy and momentum applied to colliding particles [41, 55], it follows that for an ion of mass m_g accelerated through voltage V and colliding elastically with a stationary target atom of mass m_s , the final energy E^* of the scattered particle with mass m_g is given by

$$E^* = \frac{E_I}{(1+r)^2} \left(\cos \theta + \sqrt{r^2 - \sin^2 \theta} \right)^2, \quad (12)$$

where $r = m_s/m_g$ and θ is the angle of deflection of the primary particle m_g from its initial direction of motion in the laboratory system of coordinates. For a scattering angle, $\theta = 180^\circ$, it follows for argon on niobium a ratio E^*/E_I of 0.16, whereas for neon on niobium, E^*/E_I is 0.42. For a deposition target voltage, V_t , of 360V and low gas pressures, the energies of the reflected argon particles bombarding the substrate will therefore be less than about 60eV, whereas in the case of neon the maximum reflected energy can be as high as 150eV. However, multiple glancing angle collisions with target atoms can produce a flux of high energy reflected neutrals, which leads to finite gas absorption rates also in situations such as niobium/krypton or niobium/xenon. The kinetic energy spectrum of niobium neutrals sputtered by 360eV Ar^+ has a strong peak at energies between 4 and 8eV and a long tail up to approximately 25-30eV [42]. The average energy of the niobium neutrals sputtered by krypton is about 40% higher [43], which also manifests itself by enhanced heating of the cavity during the sputtering process at approximately the same deposition rate.

The mean free path of a sputtered atom with mass m_s , travelling through a gas of mass m_g and pressure p_g (in Pa) can be calculated according to the equation,

$$l^{-1} = 8.34 \times 10^{14} p_g \frac{(d_s + d_g)^2}{4} 1.4 \sqrt{(1 + m_s/m_g)}, \quad (13)$$

where d_s and d_g are the atom diameters (in cm) of the sputter particles and the gas atom, respectively. Equation (13) follows from kinetic gas theory, for $N_g \gg N_s$ (N is the number of

atoms per unit volume) and atoms diffusing through the sputtering gas [44]. The factor 1.4 gives a correction for the high velocity of the atoms ejected from the target. The calculated mean free path, l , for niobium in an argon discharge gas pressure of 0.15Pa is $\sim 7.5\text{cm}$, which is approximately equal to the distance between cathode and cavity cell. Therefore, the loss of energy due to gas phase collisions will be very small and thermalisation of the sputter particles before arriving at the substrate will not take place [42].

It has been reported that the stress state in niobium films prepared without bias on amorphous structures at different argon pressures can be varied from compressive stress at low operating pressures ($\leq 2\text{Pa}$) to tensile stress at higher pressures [24, 37, 45, 46]. As the sputter gas pressure is increased, appreciable gas phase scattering occurs, increasing the oblique component of the flux and decreasing the energy of the incident atom [47]. SEM micrographs show open columnar structures in films, sputter deposited at higher pressures, associated with an increase of the resistivity and lower overall levels of film stress. This is mostly related to the fact that an open microstructure cannot support much stresses in the deposit, neither growth nor thermal mismatch stresses, as these are easily accommodated at the free surfaces which exist perpendicular to the coating-substrate interface. The low discharge gas pressure of $1.48 \times 10^{-1}\text{Pa}$ used for sputter deposition of the cavities has been chosen to obtain the highest RRR with a closely packed columnar structure without introducing discharge instabilities during the sputter process. According to the structure-zone diagram of *Thornton* [46], which defines the microstructure of films deposited by magnetron sputtering as a function of growth temperature and argon pressure, the films are expected to have the observed compact columnar microstructure (zone T-structure). Surface diffusion at a deposition temperature, $T_s/T_m = 0.06$, as applied in the present work, is very limited [48] and atomic shadowing effects play the dominant role in defining the zone T morphology [49].

3.3. Results and discussion

Table 4 summarises the results of a_{\perp} obtained on samples cut from different cavities and the observed increase of a_{\perp} , Δa_{\perp} , taking the unstressed value of annealed niobium, $3.303 \pm 0.003\text{\AA}$, as a reference. The lattice parameter a_{hkl} , obtained from $K\alpha$ and $K\beta$ reflections of the (110), (220), (211) and (321) planes were plotted against the *Taylor-Sinclair-Nelson-Riley* function to obtain a_{\perp} (Figure 7 and 8). Reflections from (200) planes were not considered because of the different elastic properties along this direction (chapter 6). After substrate removal, however, the lattice parameter calculated from the (200) peak fits well with the other data. If the film is in a stress-free state then a_{\perp} will take a value of $3.303 \pm 0.003\text{\AA}$, the lattice parameter of unstressed niobium (the uncertainty arises from the spread in the data reported in literature) [50-53]. On the other hand, $a_{\perp} > a_0$ indicates a compressive stress in the plane of the material, as observed for the niobium films under investigation.

Sample	$a_{\perp} [\text{\AA}]$	$\Delta a_{\perp} [\%]$
E8.7i (1)	3.3219 ± 0.0003	0.572 ± 0.091

E8.7i (2)	3.3218±0.0003	0.569±0.091
E8.7e	3.3240±0.0010	0.636±0.096
E10.4i (1)*	3.3231±0.0005	0.609±0.092
E10.4i (2)	3.3179±0.0005	0.451±0.092
E10.4e	3.3184±0.0006	0.466±0.093
E9.6i (1)*	3.3257±0.0008	0.687±0.094
E9.6i (2)	3.3166±0.0012	0.412±0.098
E9.6e	3.3196±0.0007	0.503±0.093
E10.4e (350°C)	3.3164±0.0009	0.406±0.095
E8.7e (no Cu)	3.3038±0.0005	0.024±0.092
E10.4i (1) (no Cu)	3.2995±0.0013	-0.106±0.099
E10.4e (no Cu)	3.2973±0.0012	-0.173±0.098

Table 4. The extrapolated lattice parameter as calculated from the lattice spacing for the individual lines for 1.5µm thick niobium films sputter deposited on the inner wall of copper cavities. The values given for E10.4e, E9.6e and E8.7e are average values and their errors include the effect of the spread between different measurements along the cavity equator. *The film of sample E10.4i (1) and E9.6 (1) was measured to have a thickness of $2.4\pm0.1\mu\text{m}$ (see also chapter II/2).

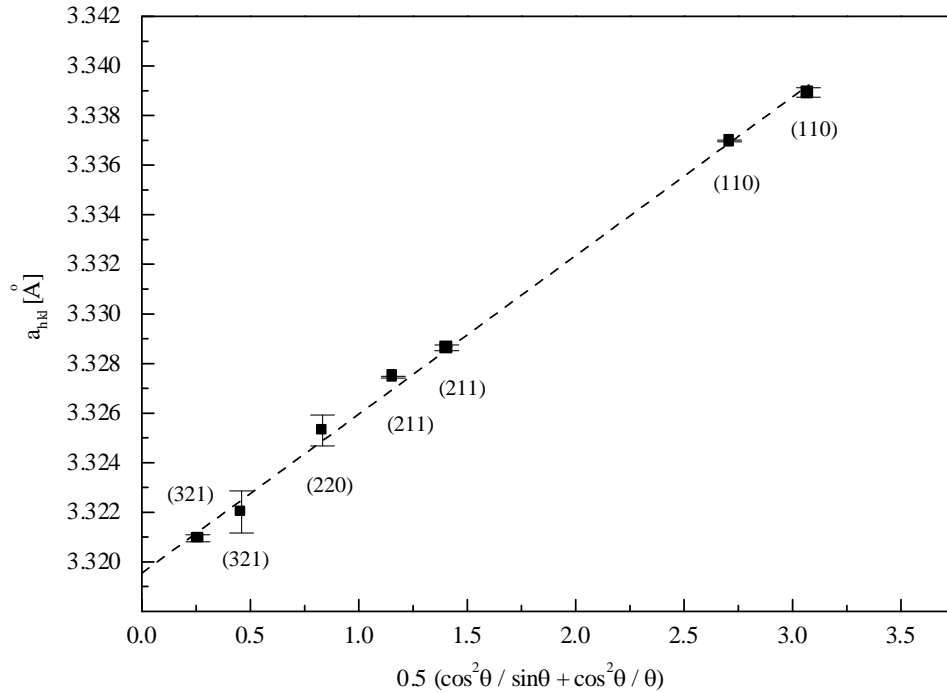


Figure 7. Precision lattice parameter measurement of sample E9.6e. The intercept value at $0.5\{\cos^2\theta/\sin\theta + \cos^2\theta/\theta\} = 0$ defines a_{\perp} . Error bars include the uncertainty in the estimation of the peak maximum.

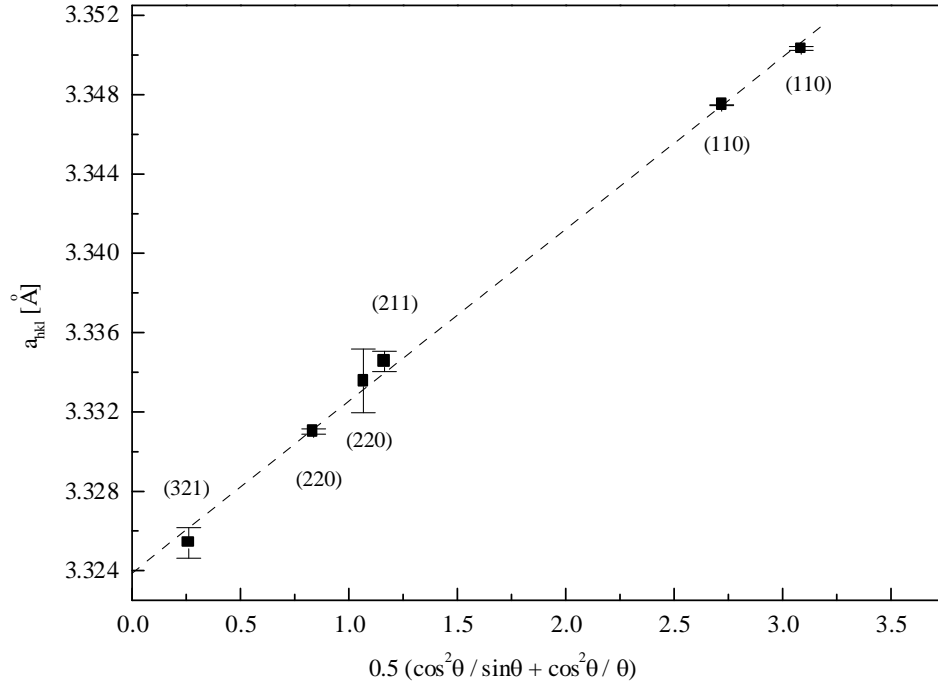


Figure 8. Precision lattice parameter measurement of sample E8.7e.

The data in table 4 indicate a slightly lower lattice constant for films grown on a sputter cleaned copper substrate, which can be explained by structural differences between both types of film (chapter 5 and 7). Heat treatments at 300°C (E9.6) and 350°C do not cause significant shifts of the peak position and consequently do not release macrostresses. The already discussed possibility of oxygen diffusion into niobium during annealing would change the lattice parameter significantly only at values higher than 1at-% [17, 54]. From the observed increase in T_c , however, and according to rough calculations taking the results of the XPS study as presented in chapter II/2, the oxygen content can be at most 0.2-0.3at-%.

The results presented in table 4 further show that the lattice parameter is higher for samples with a higher thickness. The reason for the higher film thickness at the upper iris of reverse sputtered cavities was an asymmetry of the magnetic field profile around the cathode due to a faulty magnet. The magnet was replaced at a later stage of this work and it was found that this problem did not considerably influence the main parameters characterising the superconducting rf properties (but see also chapter I/5).

Since the lattice parameter in growth direction is a good measure of the stress in the films, it can be assumed that a lattice parameter increase is also accompanied by an increase of the principal stress components. It is not clear, which mechanism could lead to an increase of internal stress with increasing thickness. Sputtered tungsten films on silicon wafer substrates have been reported to give the opposite effect, i.e. a decrease of the internal stress with film thickness, probably due to stress relief by yielding [56]. An important observation, often made when increasing the film thickness, is an increase in the average diameter of the columnar units and a decrease in the film density (porosity effect) [59]. This will result in a decrease in the yield strength and the average elastic stress, which can be supported by the film, is reduced. Thinner coatings are expected to have greater yield strengths and to support higher stresses, because the average diameter of the columnar units, which represent the microstructure of these films, is small closer to the substrate.

From the discussion above it is rather unlikely to expect higher stresses as the result of an increased film thickness. A possible explanation for the higher lattice parameter, observed at

one iris of cavities, sputter deposited in the two-electrode system, could be an enhanced bombardment of the growing film with gas atoms caused by the asymmetry of the discharge.

The stored elastic strain energy built up in the film by the continuous bombardment with atoms during growth is proportional to the film thickness, and this will cause peel off when it exceeds the interfacial fracture energy [57, 58]. This limiting energy will depend on the nature of the substrate and is sufficiently high for the niobium coatings, since 10 μ m thick films were still found to give good adherence to copper [60].

For several samples of each family, the lattice parameter was also measured after dissolution of the substrate and found to be $3.305 \pm 0.002 \text{ \AA}$ for films grown on oxidised copper and $3.298 \pm 0.001 \text{ \AA}$ for films grown on non-oxidised copper, respectively. The first value agrees, within experimental error, with the normal bulk value and with the value of 3.306 \AA , measured under the same experimental conditions on unstressed niobium powder (chapter 5), thus indicating a complete relaxation of the macrostrain. The value calculated for films grown on non-oxidised copper is slightly below the nominal value for unstressed niobium. It is interesting to note that the observed difference in the lattice parameter between films of equal thickness of family E8.7 and E10.4 is conserved even after substrate removal. Therefore, a small intrinsic, tensile stress component is likely to remain in films grown on non-oxidised copper after the substrate was dissolved. This effect is probably related to a small irreversible distortion (shape change) of the unit cell caused by the structural mismatch between the film and the substrate and manifesting itself in the occurrence of in-plane shear stresses, as discussed in chapter 7. The presence of growth defects, such as stacking faults or dislocations, which are often accompanied by an elastic distortion of the matrix, can also lead to a change in the lattice parameter (Eqn. 11). The microstrain measurements, however, which will be presented in chapter 8 are difficult to reconcile with this source of residual stress, since it is unlikely that the defect concentrations in both kinds of film vary so markedly from each other as to account for the absence of residual strain in film E8.7.

An interstitial incorporation of foreign atoms such as argon would shift the lattice parameter to higher values and would remain, when the film is removed from the substrate. It cannot account for the present observations. The result that no strain is introduced by approximately 500 atomic ppm argon incorporated into the film may indicate substitutional trapping of argon and/or the presence of void regions to accommodate incorporated argon. Anyhow, this concentration is too small to give a significant strain effect. This observation is in agreement with studies on argon implanted TiN films [61], where the lattice parameter remained practically unaffected at argon concentrations up to 1at%. Therefore, the expansion of planes and the calculated lattice parameter, a_L , on adherent films is attributed only to the Poisson ratio effect and the third term on the right hand side of equation (11) can be neglected, when considering macrostresses. The observation, that not only thermal stresses, but also large fractions of the growth stresses relax when the coating is detached from the substrate, is in agreement with published data [62, 63].

4. Noble gas incorporation during film growth

4.1. Implantation mechanisms

A series of samples were prepared to study the effect of enhanced ‘ion-peening’ by the higher energetic neon neutrals on the lattice parameter of magnetron sputtered niobium films. To extract information about lattice deformations induced by trapped neon gas, the film was removed from the substrate, and the lattice parameter was measured again.

The impact of reflected, energetic noble gas neutrals on the growing film is regarded as the main mechanism contributing to gas trapping [64, 65, 66]. The probability of incorporation of a neutral atom increases with the energy of the atom, and hence, the incorporation rate depends on the cathode operating voltage, V_t [66, 68]. This is demonstrated in figure 9, where the argon content in niobium films is shown as function of the operating voltage. At a cathode potential of $\geq 700\text{V}$, the production of irradiation-induced residual damage in the growing films may prevent a further increase of the implantation rate and will probably result in a decrease of C_{Ar} with further increases in V_t .

Reducing the energies of the neutrals and hence the incorporation probability by gas scattering through operating at higher pressures is possible, but enhanced scattering also leads to a wide range of incident angles of the sputtered atoms on the substrate. This tends to deteriorate the film microstructure significantly; especially it increases the porosity of the film because of atomic shadowing [69].

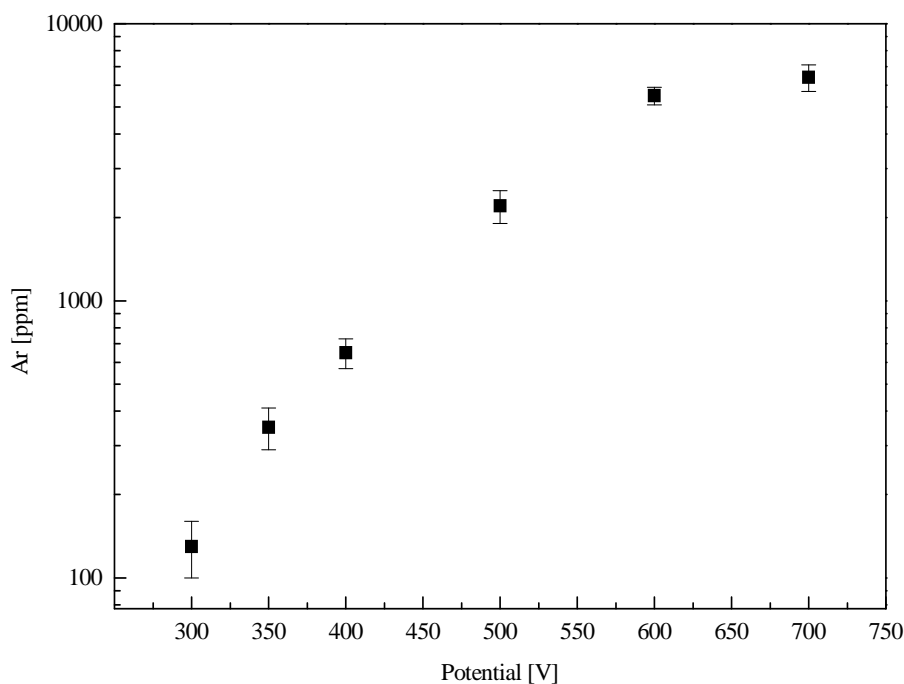


Figure 9. The argon content in magnetron-sputtered niobium films as a function of the discharge potential. The substrate temperature was held at $200 \pm 20^\circ\text{C}$.

The probability of gas incorporation into a growing film was found to be independent of the deposition rate and the film thickness [64]. *Biersack et al.* [70] performed simulations of incorporation rates based on calculations of the probability of ions being reflected from the target. These model calculations always yield very high incorporation rates, which cannot explain the relatively low amount of incorporated gas, as is observed in unbiased magnetron

sputtered films. The reason for this disagreement is an enhanced diffusion due to the high concentrations of vacancies produced by the bombarding atoms in between the implanted atom and the surface. This is consistent with the observed decrease in the noble gas content of niobium films sputter deposited at higher substrate temperatures. At increased temperatures, the implanted gas atom will have a higher probability to escape due to a thermally activated de-trapping process, including direct desorption from weak-binding sites and surface segregation followed by desorption [71].

The entrapment mechanisms and characteristics are of interest, since the trapped gas has a considerable influence on both the mechanical and the superconducting properties of niobium films [15, 65]. The noble gas atoms are only weakly physisorbed on a solid surface [72] and incorporations of significant concentrations can only occur by trapping of the incident energetic species. Since the solubility in noble gas/solid systems is essentially zero [73], supersaturations can be obtained, when atomic diffusion is not sufficient to let the implanted noble gas atom escape. The gas atoms can be retained on interstitial lattice sites, substitutional, along grain boundaries or as bubbles⁽¹⁾ nucleated by clustering around substitutional trapped gas atoms [74-77]. Considering the solution of a single inert gas atom in a metallic crystal, calculations of the energy of solution based on the interaction potentials for the inert gases and copper have been performed [78]. The result of these calculations indicates that argon, krypton and xenon dissolve substitutionally in copper, even to the extent of forcing copper atoms off the lattice sites, if no vacant sites are available. Neon should dissolve substitutionally, when vacancies are present and may go into interstitial solution, when vacancies are absent. Furthermore, the strains around krypton and xenon atoms are so large that these atoms may capture extra vacancies to reduce the strain energy. In niobium however, the relatively large interatomic spacing (2.86Å, compared with 2.56Å for Cu) is expected to make argon and krypton in this metal behave rather like neon and argon, respectively, in copper. This results in a reduced ability for krypton and xenon to capture vacancies in pure niobium.

The situation in polycrystalline films, however, is quite different from a pure metallic crystal. As will be shown in chapter 8, the dislocation density and the number of vacancies available are high and the strain energy of the lattice atoms next to the gas atom can easily be minimised by association of these vacancies with gas atoms. This effect also causes the atoms to diffuse faster in the lattice. In polycrystalline films the activation energy for diffusion of a noble gas is low due to the presence of grain boundaries, dislocation loops and void regions induced by growth defects, where many vacancies already exist. Therefore, a few gas atoms may easily meet and cluster, which would assist the process of nucleation and precipitation of gas bubbles. Preferred development of bubbles associated with dislocations is reported in literature [79]. That there may indeed be a sharp drop in the energy of solution, when the gas atoms are arranged in particular cluster configurations, and that the presence of vacancies stabilises these gas clusters, has been shown theoretically by *Rimmer et al.* [78] and by *Hosson* [80].

Often gas-phase bubbles develop, but the formation of solid phase precipitation of the noble gas confined in small cavities under high pressure has also been reported in the more recent literature [81-86].

Bubble formation by implantation of helium in niobium occurs even at very low noble gas concentrations with sizes from 100 to 300Å. At higher concentrations of approximately 1at-%, the bubble size decreases to 50 to 150Å with a density ranging from 0.7 to $6.5 \times 10^3 \mu\text{m}^{-3}$, respectively [79]. However, heat treatment to 1300°C has been applied to obtain bubbles with a regular distribution and with the sizes and densities given above. For the lighter gases, such as neon and helium, the occurrence of liquid precipitates under high pressures at room temperature was reported [84, 97]. It is probable that not all of the trapped gas resides in such

⁽¹⁾The word bubble is used to refer to the aggregate of atoms without implying a specific shape or state.

clusters and that a fraction of the implanted noble gas will be dissolved as single atoms, trapped substitutionally.

Taking oxide dissolution, dislocation migration, exaggerated grain growth and recrystallisation into account, it is not surprising that the desorption spectra of neon and argon from a niobium film will be very complex and do not allow the identification of the activation energy involved in a single operative release mechanism. *Kelly et al.* have suggested, based on their experience with radiation damage in nuclear materials, to characterise the gas release by three stages, if oxide dissolution or phase changes are unimportant [87, 88]. The essential findings of their work are that gas release due to diffusional migration of single atoms through the material will require a lower temperature than gas release due to bubble migration, where the diffusion coefficient is very low and depends on the bubble diameter. On heating the material, thermal vacancies are produced, which migrate and agglomerate at gas clusters or even at trapped gas atoms, so that the size of the bubbles and the rate of bubble precipitation also increase. The same conclusions were reached by *Tucker et al.* [89] by studying the motion of rare gas atoms in thin films. An illustrative article on the migration and coalescence of inert gas bubbles in metals is available in [90]. The size and concentration dependence of the bubbles on the annealing temperature has been studied in [79].

4.2. Results on the gas content and the lattice parameter of neon implanted films

To measure the noble gas content in the niobium films, temperature programmed desorption (TPD) in combination with a calibrated mass analyser was used. After having been dissolved from the copper substrate, the films were heated up continuously in an UHV furnace to 1300°C⁽¹⁾ with a temperature ramp of 5°C/min. The quantity of gas being released was recorded by setting the mass spectrometer on the noble gas peaks to be studied (dynamic conditions).

The migration of bubbles, which may result in a release of bursts of gas at the film surface, is certainly associated with a higher activation energy and will not occur below 1300°C, especially when coalescence of bubbles occurs. Therefore, a trick has to be used to measure the total amount of gas imbedded in the film. The film was heated in contact with a nickel foil of high purity to the eutectic point at 1175°C in the nickel-niobium phase diagram. Melting results in the complete liberation of all the trapped gas and the quantity of gas released is collected in a system of known volume (static conditions). If only one sort of noble gas is present in the film, the pressure, measured by a calibrated pressure gauge, is directly related to the number of noble gas atoms. A getter pump pumps the other gases released from the sample and the system itself. The relative accuracy in the measured noble gas content is ~20% and the limit of detection is ~5ppm. The results obtained compare well with values estimated from the observed rate of pressure decrease in the vacuum system, when the discharge was switched off after film deposition.

In the present study, the amount of neon incorporated into the film was controlled by using a mixed argon-neon discharge and by varying the partial pressure of neon rather than changing the target voltage. The substrate temperature during coating was kept at 150±10°C. To keep the same target voltage as used for sputtering of a 1.5GHz cavity (~360V, with respect to ground), the current was set to 7.5A at a total discharge gas pressure of 8-9×10⁻²Pa⁽¹⁾. Prior to film deposition, the target was pre-sputtered for 5min.

⁽¹⁾The limiting furnace temperature.

⁽²⁾This results in a the mean free path of the order of the target-to-substrate distance as is the case for cavity coatings.

Table 5 summarises the results in the form of average values from repeated measurements on different samples by the methods described above. The error is calculated from the root mean square deviation of the data. The extrapolated lattice constant, a_{\perp} , was calculated from the positions of the (110) and (220) diffraction lines in the XRD pattern and is listed in table 5. Data obtained from reference samples, which had been coated in pure argon, are included.

Sample	Growth rate [nm/s]	p_{Ar} [10^{-2} Pa]	p_{Ne} [10^{-2} Pa]	Ne content [at-ppm]	$a_{\perp(110)}$ [Å]	$a_{\perp(211)}$ [Å]
A0 (1.5)	0.52	8.0	0.0	---	3.323±0.001	3.323±0.001
A1 (1.5)	0.49	6.7	1.7	650±200	3.328±0.002	3.328±0.002
A2 (2.4)	0.44	4.3	4.3	3150±120	3.330±0.001	3.333±0.001
A3 (2.8)	0.42	3.1	6.3	5870±340	3.333±0.001	3.337±0.001
A4 (3.0)	0.41	1.8	7.3	9500±520	3.336±0.001	3.341±0.001
A5 (2.9)	0.36	1.0	8.7	19400±2500	3.340±0.001	3.346±0.001
A6 (2.9)	0.34	0.0	9.0	42000±6000	3.353±0.002	3.353±0.002

Table 5. Variation of the lattice parameter and the implanted noble gas content of niobium films sputtered at different partial pressures of neon in the discharge gas. The lattice parameter $a_{\perp(211)}$ was corrected for instrumental effects, using the slope of the linear fit through the individual lattice constants calculated from the $K\alpha$ and $K\beta$ reflections of the (110) and (220) planes. The numbers in parenthesis in the first column refer to the measured film thickness, d (in μm). The concentration of implanted argon does not depend on the neon fraction in the discharge gas and was found to be $450\pm100\text{ppm}$ in all samples, except those coated in a pure neon discharge. The table also defines unique sample numbers, which identify the samples with their neon content.

All films are found to have a strong (110) fibre texture perpendicular to the substrate plane, which is the dominant orientation in sputter deposited films on an amorphous substrate (chapter 5).

For the samples coated with a neon-argon mixture as discharge gas, $a_{(211)} > a_{(110)}$ is found. This anisotropy is illustrated in Figure 10 for a niobium film coated in an argon-neon discharge gas with a partial pressure ratio of 1:2. For films coated with pure argon or pure neon, this anisotropy has never been observed.

It can be seen from figure 11 that the dilation of the lattice parameter perpendicular to the plane of the film increases with increasing neon discharge gas pressure, due to the increasing biaxial in-plane compressive stresses. These high stresses are attributed to ‘ion-peening’ by the energetic neon neutrals, which get partly implanted into the growing film. In fact, the energetic bombardment can lead to a state of plastic flow in the niobium film, when the yield point of the metal is exceeded, as reported for tungsten and other metal films, sputter deposited in an argon discharge at moderate substrate bias⁽¹⁾ [91, 92].

When the film is separated from the copper substrate by chemical etching, strain relaxation of the free-standing film occurs. Since extrinsic stress in a thin film comes mainly from adhesion to its substrate⁽²⁾, the constraints imposed by the substrate release and the lattice parameter, a_{\perp} , decreases considerably. The film is left with its intrinsic stress, which comes from defects, such as dislocations and foreign atoms implanted into the film (solid solution effects) [62]. This feature is shown in figure 11, where the lattice parameter of the niobium films before (top curve) and after substrate removal (bottom curve) is plotted as a function of the relative partial pressure of neon in the discharge gas.

⁽¹⁾The ratio E^*/E_1 for argon rebounding from tungsten is 0.42, which is the same as in the system neon/niobium.

⁽²⁾Typical sources of extrinsic stress in a film are thermally induced lattice mismatch and/or lattice misfit with the substrate.

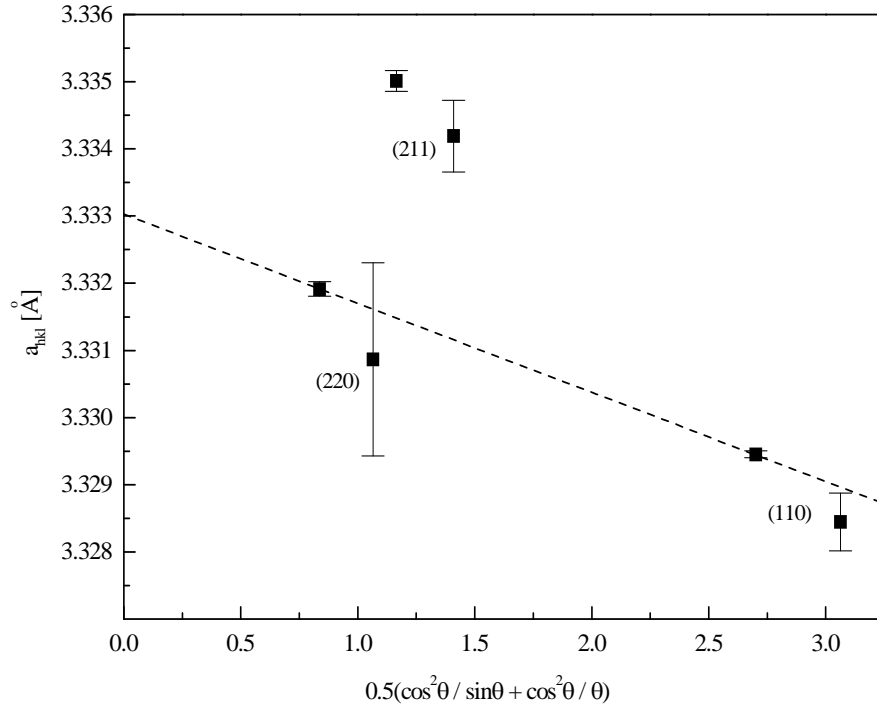


Figure 10. Effect of anisotropy on the extrapolation of the lattice parameter $a_{(110)}$ and $a_{(211)}$ to $\theta = 90^\circ$. This effect was observed for all samples coated in a neon-argon mixture as discharge gas. The example is given for sample A3, which represents a niobium film deposited on oxidised copper with $p_{Ar}/p_{Ne} = 1:2$. Diffraction peaks from both $K\alpha$ and $K\beta$ radiation were analysed.

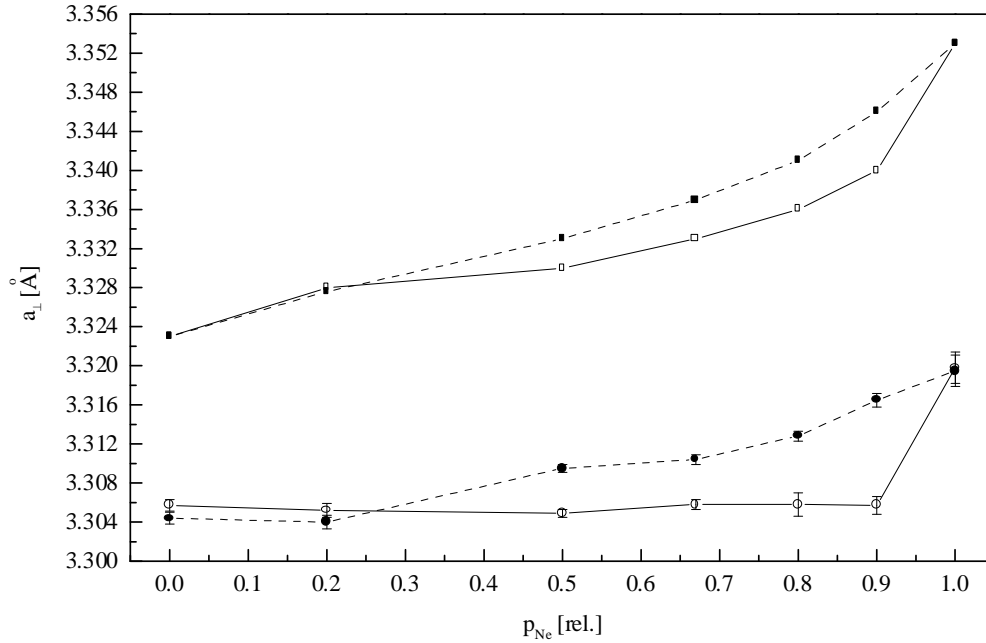


Figure 11. Evaluation of the lattice constant with increasing neon discharge gas pressure. The full symbols represent the lattice constants calculated from (211) planes and the open symbols those calculated from {110}. The lines are drawn to guide the eye.

Argon loaded into the metal lattice up to 0.05at-% does not cause any lattice distortion and therefore does not affect the lattice parameter (chapter II/3). This result may suggest that the argon atoms, coming to rest in the growing film, capture vacancies. Due to thermally activated migration of the gas atoms, there may be a considerable agglomeration of the gas even at room

temperature. When pure neon is instead used as the discharge gas, the growing film becomes considerably distorted and reveals an isotropic lattice expansion, $d(\Delta a_{\perp})/a_0/dC_{Ne}$ of $0.0035 \pm 0.0005 \text{ at.}\%^{-1}$ probably due to substitutional solution of neon. In addition, those films showed a greater tendency to bulge and crack when the substrate was removed. A different situation prevails, when argon and neon are present in the discharge during sputter deposition. Neon causes lattice expansion only along (211) planes, while giving no effect along the most widely spaced (110) plane. The reason might be that argon, which is captured in vacancies, caused by growth faults or dislocation loops on {110}, clusters with neon, assisting the process of nucleation and precipitation of mixed gas bubbles. This suggestion is supported by results showing clusters of argon and xenon being stabilised in the presence of vacancies on {111} planes of fcc metals, which are the close-packed planes in those metals [80, 83]. The preferential clustering on close-packed planes can qualitatively be explained by the greater reduction in the strain energy by an interaction with more gas atoms. Bubble ordering on (110) planes of polycrystalline bcc metals, ion implanted with 30keV He^+ and heat treated to high temperatures, was indeed found to be a pronounced feature, as shown by HRTEM [93].

There are also striking features in the evolution rate of the noble gas, when the sample was heated to 1300°C, confirming the different trapping states of neon and argon in niobium films. The results for argon desorption in films, coated in a pure argon discharge and in an argon-neon discharge gas mixture, are identical and show a slowly increasing release rate below 1300°C and a burst of argon release just after melting. The continuous release below 1300°C is a diffusion-controlled process and suggests normal mobility of a small fraction of argon implanted into the film. The single peak at the melting point of the material may suggest the presence of bubbles with low mobility, which are released only at higher temperature or when niobium melts. In principle, the same kind of spectrum is obtained with neon, except that there is now an enormous difference in the relative quantities of gas released by segregation to the surface and desorption below 1300°C and by melting of the film, depending on whether or not argon is present. The essential findings of the TPD studies are summarised in table 6.

Sample	Gas release at $T < 1300^\circ\text{C}$	Total gas release
E8.7e	$108 \pm 16 \text{ ppm argon}$	$435 \pm 70 \text{ ppm argon}$
E10.4e	$59 \pm 9 \text{ ppm argon}$	$286 \pm 43 \text{ ppm argon}$
A6	$39200 \pm 6000 \text{ ppm neon}$	$42000 \pm 6000 \text{ ppm neon}$
A5	$1950 \pm 290 \text{ ppm neon}$ $77 \pm 23 \text{ ppm argon}$	$19400 \pm 2500 \text{ ppm neon}$ $353 \pm 100 \text{ ppm argon}$

Table 6. Quantity of gas released by diffusion below 1300°C and total amount of gas implanted into different films. The errors reflect uncertainties arising from the gauge calibration.

The argon concentration in films grown on oxide-free copper is less than in films sputter deposited on oxidised copper ($C_{Ar}(\text{E10.4})/C_{Ar}(\text{E8.7}) = 0.66 \pm 0.18$). This difference is probably due to the different texture, which has been observed between these types of films (see chapter 5). The results indicate an increased trapping efficiency for films grown with orientations corresponding to close-packed planes, which are wider spaced, in good agreement with experimental observations reported in [75]. There, the argon concentration in heteroepitaxial TiN films deposited by magnetron sputtering with an applied negative substrate bias in mixed Ar/N_2 discharges was found to be highest for (110) oriented films and at least a factor of three less for (100) and (111) oriented films. For a negative bias voltage greater than 200V, the argon was reported to be trapped in polyhedral gas bubbles containing both Ar and N_2 with sizes $\leq 7 \text{ nm}$.

The ratio of argon released below 1300°C to the total amount of implanted argon is 0.23 ± 0.02 and does not depend on the type of film or on the presence of neon. This result suggests that 80% of the implanted argon contribute to substitutional argon-vacancy defects and the isolated argon fraction contains only about 20% of the implanted atoms. However, a significant amount of single argon atoms may become trapped in existing cavities during heating and the ratio given above can only be considered as a lower limit.

For neon this ratio varies enormously with the presence of argon in the lattice. Whereas about 90% of neon is released below 1300°C for films sputtered in a pure neon discharge, only 10% is released at the same temperature when ~400ppm of argon is simultaneously incorporated into the film. Thermal desorption spectra of helium implanted niobium (110) films [94] show the same intensive peak at 1250°C, which has been related to the migration of helium bubbles or atoms to the surface. The formation of helium bubbles in niobium films was reported to occur at $T \geq 750^\circ\text{C}$, whereas at lower temperatures helium does not form gas-vacancy complexes. These results are in good agreement with the observations made in the present work and suggest also for neon no clustering at temperatures below 150°C, except in the presence of heavier noble gases, for which gas clustering even at low temperatures is energetically favourable. Neon will consequently be bound to argon and argon-vacancy complexes and must therefore have the capability of becoming a mixed bubble nucleus. The latter result is confirmed by model calculations on the krypton-helium system in tungsten, available in the literature [95].

An attempt was made to obtain information on precipitated gas bubbles in niobium films from grazing incidence X-ray diffractometry. If these inert gas clusters are in the solid phase, they should diffract at a certain angle as observed for xenon, argon, and krypton implanted in metal layers [96, 98]. Argon is found to crystallise at room temperature at 1100MPa in the face-centred cubic structure with a lattice constant of 5.09Å [97, 99]. Unfortunately, the sensitivity limit of X-ray diffractometry is about 1at-%, much too high to give diffraction maxima of argon for the films under study. Investigations of niobium film samples in cross-section using transmission electron microscopy are presently under way to study the inert gas inclusions in films in a more direct way.

5. Analysis of the degree of orientation

5.1. Niobium film growth

The knowledge of the preferred orientation of the films is of fundamental importance for an understanding of the different stresses and noble gas contents observed in different films. If the grains of the polycrystalline film cluster around certain orientations, i.e. the film has a texture, more grains will be in a position to reflect at certain angles of the diffraction pattern than at others, and the diffractogram will have maxima and minima or even missing reflections. Slight or medium texture can be approximately characterised by comparing the intensities of the reflections of the measured diffractogram with a powder diffractogram of random orientation, recorded in the *Bragg-Brentano* configuration. In this configuration, sets of planes oriented parallel to the face of the specimen, are measured. *Harris* [100] applied this normalisation procedure first to describe the preferred orientation in rolled uranium bars by means of a complete pole figure⁽¹⁾. He expressed the fraction p of the total volume, which consists of crystals with the same orientations, by a texture index T_{hkl} .

In the present work, the texture index T_{hkl} will be used in a slightly modified form to measure the degree of preferred orientation in niobium films and in the underlying copper substrate [101]. T_{hkl} for any reflection, is defined by the ratio,

$$T_{hkl} = \frac{I_{hkl} / I'_{hkl}}{\frac{1}{n} \sum I_{hkl} / I'_{hkl}} \quad (14)$$

where I' are the integrated intensities above background from randomly oriented specimens and I are the intensities from preferentially oriented specimens. The summation runs over n measured reflections (higher order reflections should not be considered, if first order reflections are counted). The value of T_{hkl} as given in Eqn. (14) is a measure of the pole density in direction of the sample normal, but cannot account for possible quantity variations in the orientation distribution function of the grains. In the case of random orientation, $T = 1$ for all $\{hkl\}$; values greater than 1 show that the corresponding crystallographic direction is preferentially oriented; value less than 1 show that such orientations are preferentially avoided.

Values of I'_{hkl} were obtained by measuring a niobium powder of 99.9% purity under the same experimental conditions as the sample under investigation (Figure 12). All diffraction patterns were recorded at 22°C. The parameters set for the measurements are identical to those listed in table 3, except for the scattered-radiation diaphragm, which was now installed close to the sample surface (texture version). The relative intensities and the positions of the peak maxima of the measured powder spectrum on the 2θ scale have been compared with literature data [102] (Table 7). Before taking the observed intensities and peak positions of the partly resolved $K\alpha$ lines, the contribution of $K\alpha_2$ was eliminated. A simple correction of the observed line profile was proposed by *Rachinger* [103]. It is assumed that the $K\alpha_1$ and $K\alpha_2$ line profiles are identical in shape and not necessarily symmetrical, and that the α_2 profile is of one-half the intensity of the α_1 profile and shifted from it toward larger angles by

$$\Delta 2\theta = 2 \tan \theta \left(\frac{\Delta \lambda}{\lambda} \right), \quad (15)$$

⁽¹⁾Normalisation of intensities from the textured specimen to the intensities at the same angles by a randomly oriented specimen of the same material and same thickness circumvents the absorption problem and allows for a direct plot of pole figures of relative pole densities from these normalised intensities.

$\Delta\lambda$ being 0.00383\AA . The *Rachinger* correction as described in [103] was applied to the data and the corrected profile for the (110) reflection of the powder is shown in figure 13. The corrected peaks were analysed using the modified Lorentzian function and the value of the lattice parameter was calculated with the wavelength of the $K\alpha_1$ line (1.54056\AA). The relative intensities of the measured spectrum compare well with literature data. Although the observed positions of the peak maxima differ from the values given in [102], the resulting lattice parameter, $3.3055\pm 0.0002\text{\AA}$, calculated by extrapolation to $\theta = 90^\circ$, is within the spread of the experimental data available in literature. This discrepancy in the position of single lines, when compared to measurements performed by other authors is mainly due to displacement errors of the sample surface from the centre of the diffractometer (chapter II/3). Unlike the case of a sputter deposited film, all reflections can be taken for the correction by extrapolation because neither stress nor strain, which could lead to an anisotropy of the lattice parameter, are expected in the powder.

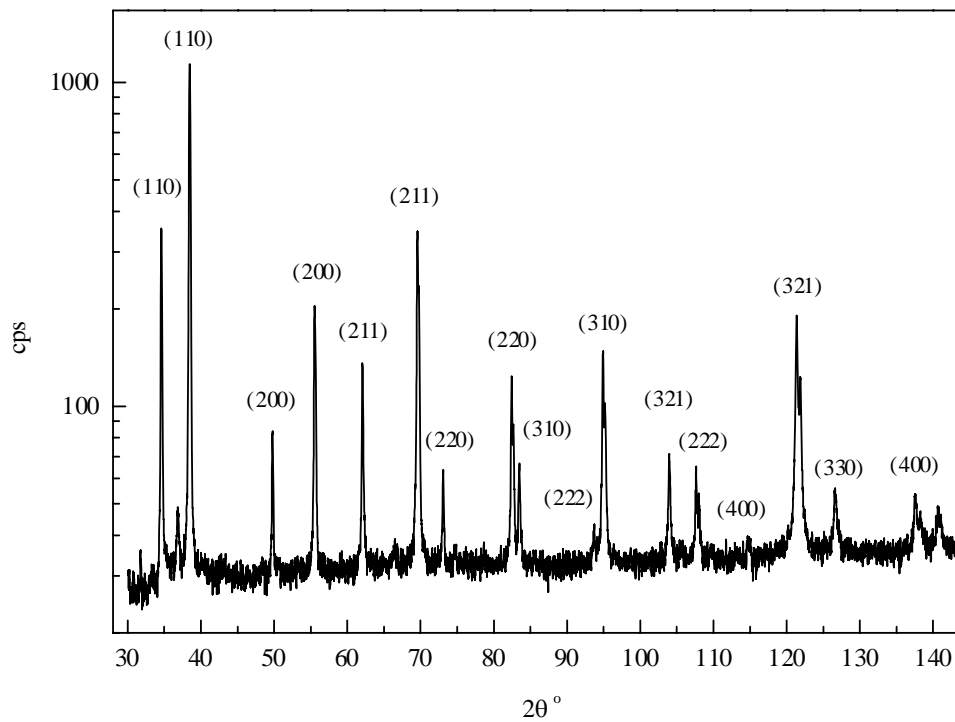


Figure 12. Measured powder diffractogram of niobium ($K\alpha_{1+2}$ and $K\beta$ lines are shown).

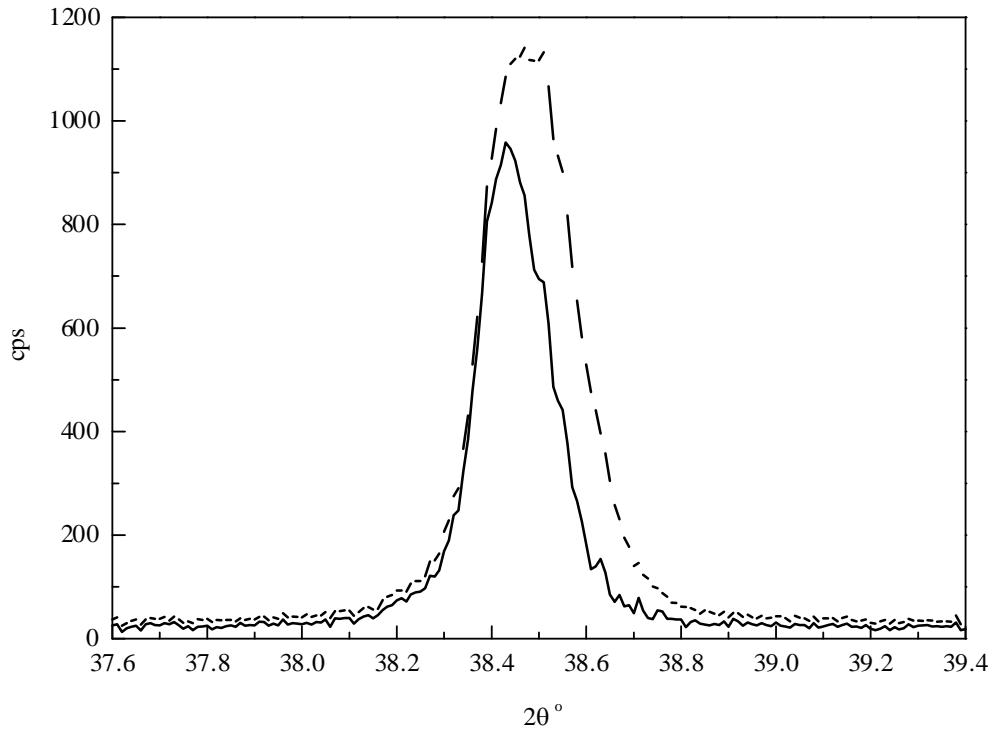


Figure 13. Profiles illustrating the Rachinger correction performed on the (110) reflection of the niobium powder. The α_I contribution (full line) and the measured combined line profile (dashed line) are shown.

Data from [102]			This work	
Reflection	2θ	$I_{\text{rel}} [\%]$	2θ	$I_{\text{rel}} [\%]$
110	38.5074	100	38.4504	100
200	55.5902	18	55.5253	17.0 ± 0.4
211	69.6775	28	69.5833	32.4 ± 1.5
220	82.5411	8	82.4445	8.90 ± 0.4
310	95.0226	11	94.9222	11.4 ± 0.3
222	107.7757	3	107.6400	2.90 ± 0.5
321	121.4695	13	121.3690	15.3 ± 0.7
400	137.7484	2	137.5735	1.90 ± 0.5

Table 7. Data for unstressed niobium are compared with values given in literature. Errors on the 2θ values obtained from the fit are quite small and are not given here.

The *Bragg-Brentano* patterns of samples E10.4e and E8.7e are shown in figure 14. Since both films are $\sim 1.5 \mu\text{m}$ thick and the penetration depth for *Cu-K α* radiation in niobium is considerably larger (Fig. 15), reflections from the copper substrate are visible. Advantage has been taken from this fact to calculate the texture index of the copper substrate from the same diffractogram. The XRD patterns reveal major differences in texture between niobium films grown on oxidised copper (E8.7) and on non-oxidised copper (E10.4). In the case of the oxidised copper substrate, other reflections from the niobium film besides (110) and multiples are practically absent. The film appears to be polycrystalline with a pronounced {110} out-of-plane orientation having the close-packed planes parallel to the surface of the substrate. In the oxide-free case, on the contrary, other planes are more probable. By measuring the intensity of the (110) and (200) *Bragg* diffraction peak of sample E8.7 over almost a full hemisphere⁽¹⁾

⁽¹⁾Realised with the Eulerian cradle (ψ -goniometer) in reflection technique, as described in chapter 7.

(from the substrate normal $\alpha = 0$ to an angle α of 75° from normal) and over the full range of azimuthal angle β (from 0° to 360°), the distribution of poles is obtained and displayed on a stereographic projection after correction for absorption effects⁽¹⁾. Figure 16, obtained in this way, is called a ‘pole figure’ and represents the spatial distribution of the orientation in all the directions relative to the polar one. The intense central spot and a weak concentric ring around 60° in the (110) pole figure correspond to the diffraction of grains oriented with their (110) planes parallel to the substrate surface. A 60° separation between the ring and the central spot represents the normal angle between the (110) and (101) planes in cubic crystals. The (200) pole figure shows a uniform azimuthal intensity around 45° due to the normal angle of 45° between (110) and (200) planes. The (200) pole figure is used instead of the (100) pole figure, because the structure factor of the {100} diffraction for a bcc crystal is zero. Both patterns indicate a strong (110) fibre texture with the axis of symmetry perpendicular to the surface plane and a random azimuthal orientation (absence of in-plane texture). This type of texture is typical for bcc metal films grown on amorphous substrates by normal-incidence sputter deposition [104, 105]. The commonly accepted mechanism for the formation of fibre texture is described in the selection model [106] and is based on differences in growth rates between different crystal faces of the grains and thence related thermodynamic considerations. An alternative approach to explain fibre texture is preferential sputtering of atoms off the surface leading to height advantages for grains with low energy surfaces [107].

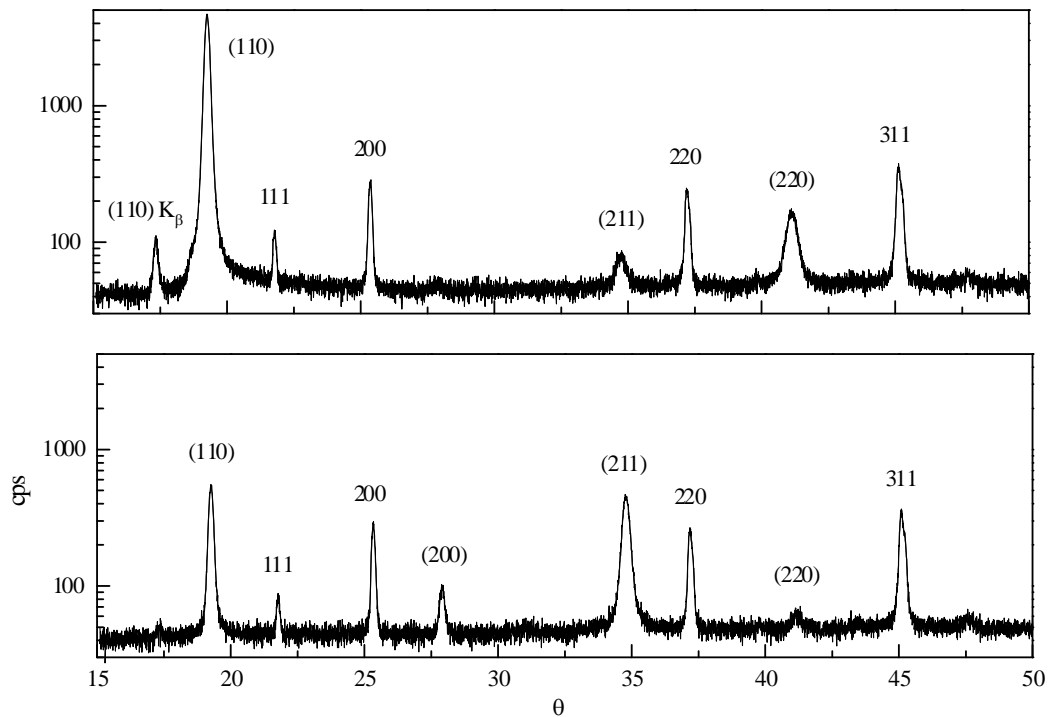


Figure 14. A comparison of the same segment of the diffraction record on a θ -scale of niobium films grown on oxidised copper (top) and oxide-free copper (bottom). Niobium planes are indexed as (hkl) and copper planes as hkl. Although a nickel filter was installed in front of the detector, a small residual K_β unfiltered component is still visible.

⁽¹⁾A general description of the absorption effect on the ψ -goniometer is available in [121, 122]. For the absorption correction on the ω -goniometer see appendix (chapter 13).

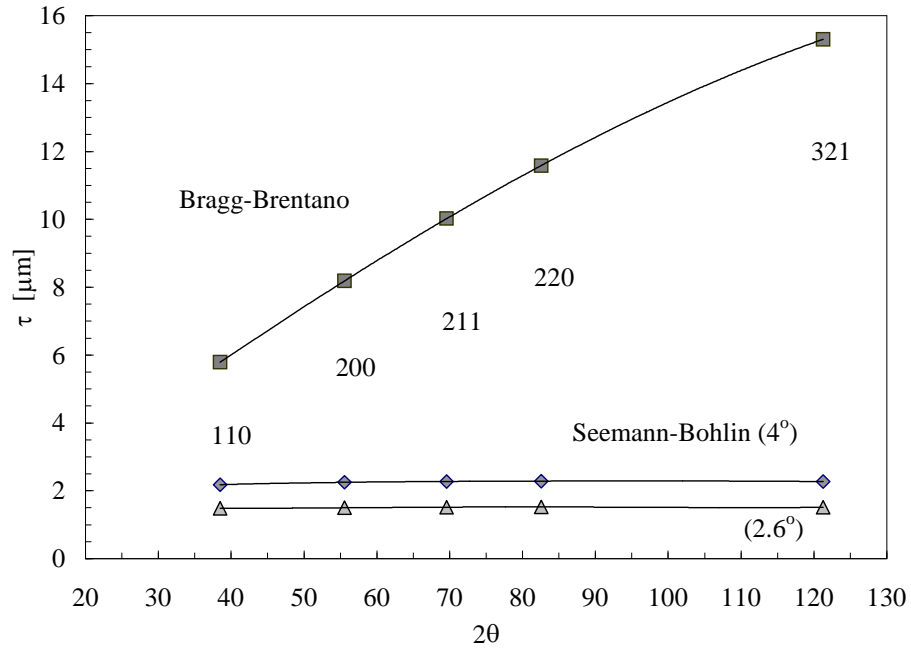


Figure 15. Calculated penetration depth, τ , for Cu $K\alpha$ radiation in Nb as a function of diffraction angle. τ is defined as the thickness that contributes 99% of the diffracted intensity. In the asymmetric Seemann-Bohlin configuration at a fixed, low angle of incidence (4° and 2.6°), the beam penetration depth of the incident X-rays below surface is small and nearly independent of θ .

Figure 16. Normalised pole figure of a standard niobium film, showing (110) fibre texture with no azimuthal orientation (see text).

To evaluate the observed texture of niobium films grown on non-oxidised copper and to check any possible correlation with the orientation of the substrate, a more detailed description by means of the texture index is necessary. Significant reflections from (110), (200), (211), (321)

and (310) planes are available and can therefore be used for the calculation of T_{hkl} . To estimate T_{hkl} of the copper substrate, reflections from (111), (200), (220), (311) and (331) planes have been analysed.

First, the diffractogram has to be corrected to the case of infinite sample thickness. In order to convert the observed intensity I_x to the intensity corresponding to a specimen of effectively infinite thickness, the following factor was applied (see appendix, section 13.1),

$$\frac{I_{\infty}}{I_x}(BB) = \left[1 - \exp\left(\frac{-2\mu x}{\sin\theta}\right) \right]^{-1}. \quad (16)$$

The correction for the $K\alpha_2$ component was simply carried out by integration of the unresolved peak and dividing by a factor 1.5.

T_{hkl} values for niobium and copper calculated after corrections of the experimental intensity lines are listed in tables 8 and 9. For the sake of completeness and to compare the texture indices among each other, the T_{hkl} values of the strong (110) oriented samples of cavity E8.7 are also listed. The texture in copper evolves from cold work during fabrication of a cavity and varies from point to point in accordance with the varying nature of the deformation, but does not differ drastically among different cavities.

Sample	T_{110}	T_{200}	T_{211}	T_{310}	T_{321}
E10.4e	0.35±0.05	0.36±0.04	2.82±0.32	0.20±0.02	1.29±0.17
E10.4i (1)	1.14±0.12	0.16±0.04	2.23±0.23	0.12±0.12	1.35±0.28
E10.4i (2)	0.54±0.08	0.31±0.05	3.39±0.38	0.08±0.08	0.66±0.10
E8.7e	4.35±0.62	0.04±0.04	0.27±0.05	0.13±0.13	0.21±0.21
E8.7i (1)	3.55±0.44	0.08±0.02	0.60±0.08	0.09±0.09	0.68±0.11
E8.7i (2)	3.17±0.57	0.16±0.03	0.70±0.13	0.31±0.31	0.67±0.12

Table 8. Harris texture indices to define the degree of orientation of grains in niobium films. Given uncertainties are based on the error in the estimation of the integrated intensity, which has been propagated through the various steps of the calculation.

Sample	T_{111}	T_{200}	T_{220}	T_{311}	T_{331}
E10.4e	0.06±0.01	0.75±0.06	1.42±0.10	2.61±0.19	0.16±0.02
E10.4i (1)	0.47±0.01	1.34±0.02	0.59±0.01	2.37±0.04	0.23±0.01
E10.4i (2)	0.03±0.00	0.83±0.13	1.22±0.19	2.90±0.25	0.03±0.01
E8.7e	0.21±0.01	0.66±0.02	1.47±0.04	2.40±0.06	0.26±0.01
E8.7i (1)	0.61±0.01	1.10±0.02	0.69±0.02	2.10±0.03	0.50±0.02
E8.7i (2)	2.73±0.02	1.30±0.01	0.12±0.01	0.72±0.02	0.13±0.00

Table 9. Harris texture indices to define the degree of orientation of grains in the copper substrate.

The calculated texture indices show a predominant orientation in (211) parallel to the copper surface for sample E10.4 and the expected (110) texture for sample E8.7, which is stronger at the equator, $T_{110} = 4.35$ than on the iris, $T_{110} = 3.55$ and 3.17 respectively. The latter result suggests a certain dependence of the film orientation on the incident angle of arriving atoms during deposition. This is in agreement with results published in [105], i.e. low energy ion-bombardment at off-normal incidence during niobium film growth on quartz causes a substantially reduced fibre texture. Calculations of the sputtering angle for the given substrate geometry have shown that the mean angle of incidence of the arriving atoms at the iris of a cavity is about 40-50°.

High energy electron diffraction (RHEED) studies of the heteroepitaxial growth of niobium on copper single crystals have shown that the epitaxial orientation of the niobium film on a copper (110) substrate is (100), whereas on a copper (111) and (100) single crystal, the positioning of niobium grains is in (110) [108]. Epitaxy at (111) fcc/(110) bcc interfaces has been treated theoretically [109-111] and crystalline superlattice growth of the system copper/niobium has been described in [112, 113]. Although epitaxial multilayer formation exists for many metal/metal combinations, the growth of a crystalline superlattice, which requires complete mutual epitaxy of the two metals, is rarely observed. It is not a small geometrical lattice mismatch or misfit in the system copper/niobium, that can lead to perfect epitaxy, but rather the uniqueness of the epitaxial orientation relationship and the energetic compatibility existing between these metals [110].

In another study carried out at CERN in 1993 [114], copper samples annealed to 800°C in UHV conditions and subsequently sputter deposited with niobium at 350°C under similar experimental conditions as used in the present work, were investigated. Coating at temperatures above 300°C should at least partly remove the oxide layer on the surface of the copper substrate and favour oriented film growth due to a higher surface mobility of the arriving sputter atoms. TEM investigations led to the conclusion that heteroepitaxial growth determines the observed crystallographic orientations present in those films. It was therefore tried to examine the presence of heteroepitaxial growth also in niobium films, deposited on a polycrystalline, sputter cleaned copper substrate.

The simplest procedure to verify a possible orientation relationship of the film with the substrate by XRD is to compare the T_{hkl} values of planes with a known heteroepitaxial relation. This is done in figure 17, where the $(T_{111} + T_{200})$ and T_{220} values of copper are plotted versus the T_{110} and T_{200} of niobium, respectively. To increase the significance of the results, data in addition to those listed in tables 8 and 9 are included in the plots. The additional samples were made available by cutting the cavity E10.4 at several positions along one meridian. The plots show indeed a positive correlation between the orientation of grains in the copper substrate and the niobium film. In addition to the known and observed heteroepitaxial relationship between the (111), (100) and (110) planes of copper and the (110) and (100) planes of niobium, a positive correlation between $T_{(211)}$ of niobium and $T_{(311)}$ of copper is also observed (Fig. 17c), which has not been reported in literature. These results indicate a textured structure in polycrystalline niobium films deposited on sputter-cleaned copper cavities induced by the orientation relationships: Nb(110)7Cu(111)(100); Nb(100)7Cu(110) and Nb(211)7Cu(311). No correlation was observed for other possible combinations of reflection pairs.

For sample E8.7, no correlation between T_{hkl} values of the film and the substrate is observed. This result is expected, since the presence of the amorphous copper-oxide interface does not allow heteroepitaxial growth. Further it should be mentioned that the heat treated samples could not be used in this comparison, since an annealing texture develops in copper at temperatures as low as 300°C [115]. The recrystallisation texture is {100} as observed by an increase of T_{200} after annealing. The T_{hkl} values of the niobium film remained instead unaffected by heat treatment to 350°.

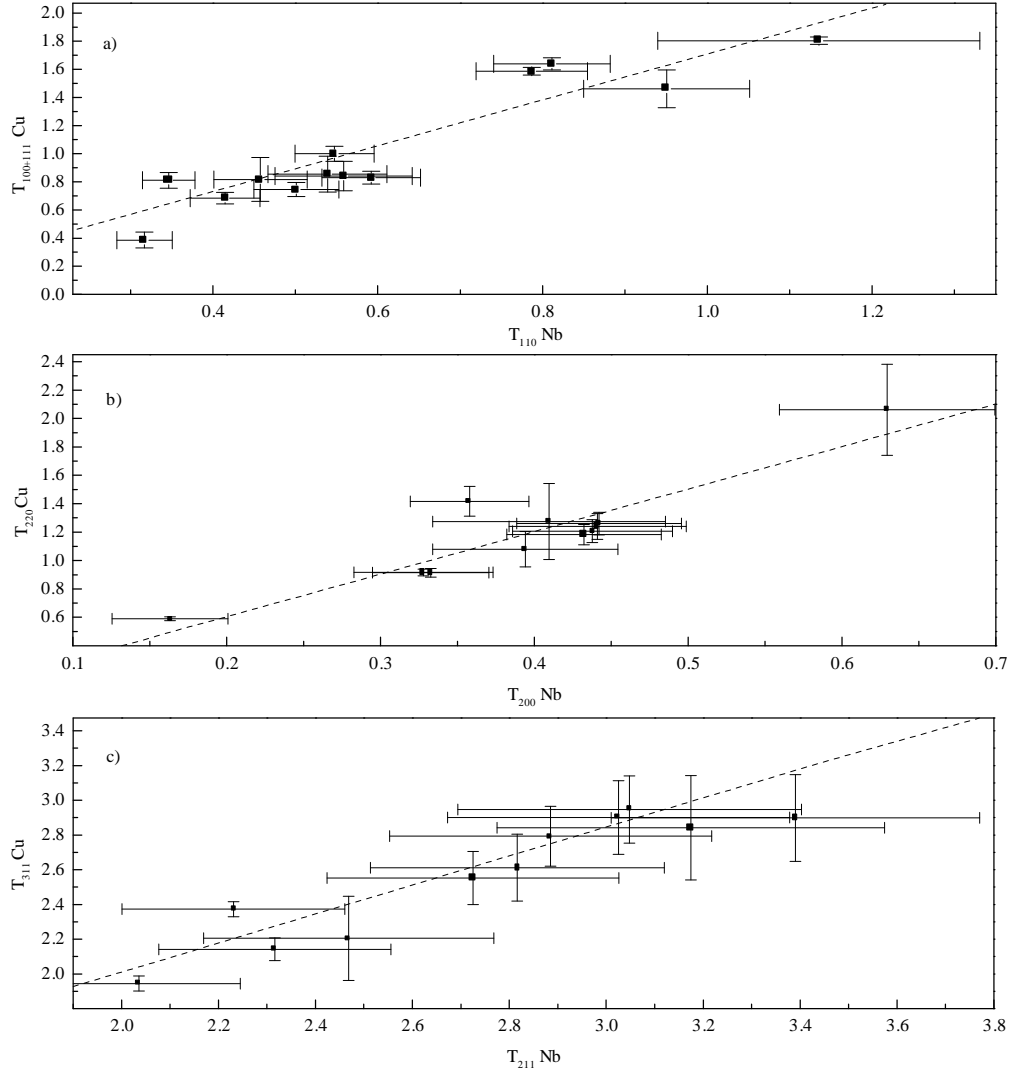


Figure 17. Quantitative comparison of the out of-plane texture between film and substrate by means of the Harris texture indices for different reflections (see text). The dotted lines represent weighted linear fits to the data.

5.2. Orientation distribution of grains

By performing an ω -scan (rocking curve) of the predominant (211) and (110) reflections, the profile of the orientation distribution function of grains can be approximately determined. In this measurement the sample and detector axes are decoupled and the sample rotates around the main axis of the *Bragg-Brentano* goniometer. The detector is fixed at the 2θ angle for the selected plane. In this configuration, the maximal possible inclination ψ_{max} of the sample is given by θ_{hkl} . The inclination ψ is given by

$$\psi = \theta_{hkl} - \omega, \quad (17)$$

where ω denotes the incident angle of the beam with respect to the sample. Defocusing effects of the diffracted beam were minimised by using a narrow divergence slit and a broad receiving slit (Table 10). A wide slit in front of the detector allows also to detect diffraction from planes with a slightly different lattice spacing due to stress. A strong texture can be quantitatively described by the width of the orientation distribution function. The narrower the distribution function, the stronger is the texture.

Mode of operation :	ω - 2θ (unlocked coupled)
---------------------	---

Step size/time :	0.005°/10s
Wavelength :	1.540560/1.544390Å (Cu)
Variable divergence diaphragm :	V3
Scattered-radiation diaphragm next to sample	Slit diaphragm
K _β filter (Ni) :	in
Primary/secondary Soller slits :	in/in
Variable scattered radiation diaphragm :	V20
Fixed detector diaphragm :	1.0 mm
Detector slit :	out

Table 10. Parameters set for measuring “rocking curves”. With a variable divergence diaphragm, the irradiated area is given by the number behind the “V” multiplied by the length of the filament (12mm). Since the scattered-radiation diaphragm next to the sample has been used to focus the beam perfectly in the centre of the sample, the variable diaphragm V3 is meaningless and could be replaced by a fixed one.

A pole figure can also be obtained in this configuration, when the specimen is rotated by one revolution about its own axis (known as angle β or φ) at a given angle of swivel ψ (in literature often called α). When passing from one angle ψ to another, a change of intensity occurs even if there is no preferred orientation. This change is caused mainly (besides the change of area irradiated by the incident X-ray) by a variation of the relative distances travelled by the incident and the diffracted rays through the specimen. It is therefore necessary to correct for the change in intensity caused by swivelling the sample to various ψ 's (absorption effect caused by tilting the sample around the goniometer axis), in order to make the intensity measurements, made at different values of ω , comparable. The measured intensities must, of course, also be corrected for the absorption effect caused by an infinite sample thickness. Both the absorption correction for the asymmetric case and for the finite thickness are derived in the appendix (chapter 13).

Since the magnitude of ψ can never be greater than θ for (hkl) planes having θ values considerably less than 90°, the pole figures that would be obtained by the present method are incomplete, lacking some of the outer latitude circles. When the sample is swivelled to an angle $+\psi = \theta$, the specimen face cuts off the incident beam; when the specimen is swivelled to an angle $-\psi = \theta$, the specimen face cuts off the reflected beam. Furthermore, since the specimens under investigation are not perfectly flat, the limit ψ_{max} cannot be reached and the beam is observed to be cut off at approximately $\theta - 5^\circ$. The second undesirable effect of the curvature of the sample is a broadening effect of the rocking curve due to the contribution of slightly differently inclined planes at a given ψ . On the other hand, a small vertical displacement of the sample does not disturb the texture measurements, because it is not essential to define an accurate determination of the peak positions. Therefore, to avoid undesired broadening of the rocking curve, the samples were flattened mechanically. The effect on the rocking curve can be seen in figure 18.

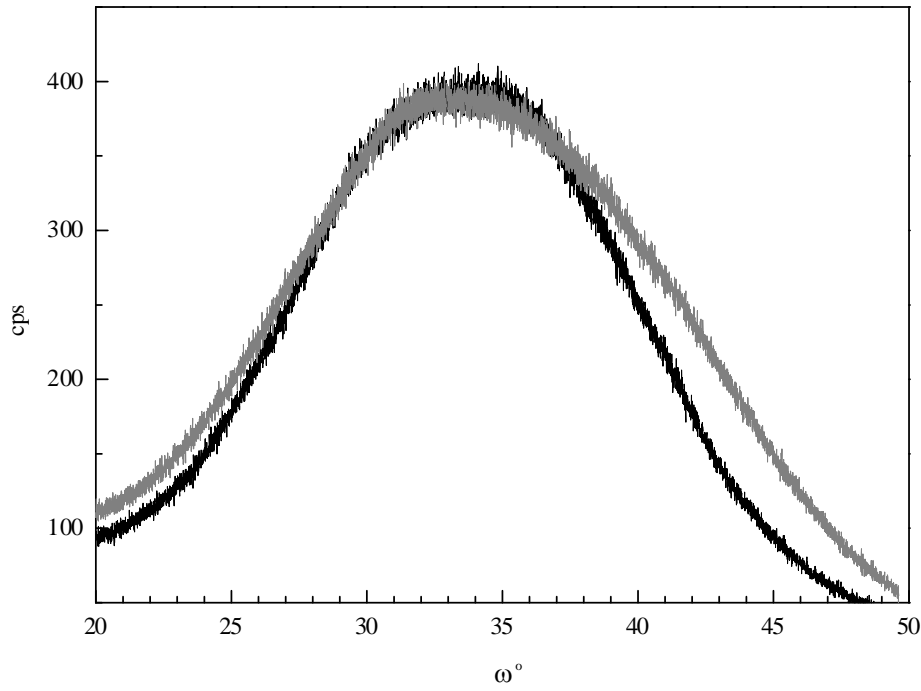


Figure 18. Raw profiles of ω -scans of reflection (211) and sample E10.4e for the curved specimen (broad peak; $2\theta = 69.241$) and the same film after flattening ($2\theta = 70.054$, black curve).

After correction for the thickness and for absorption and considering the *LP* effect [32], one obtains the correct profile of the ω - 2θ scan as shown in figures 19 and 20. Deviations from a symmetrical distribution around the surface normal are insignificant, since the peak maximum obtained from fitting the data obtained from sample E10.4e to a *Gaussian* curve, is shifted by only 0.32° . The orientational or mosaic spread of the (211) planes around the surface normal is $12.07 \pm 0.05^\circ$, a value, which is in good agreement with reported data on magnetron sputter-deposited and fibre textured thin films, but at least ten times too high compared to values of epitaxial films grown on single crystals [116-120]. The low surface mobility of ad-atoms at the surface of low temperature coatings is one reason for the observed disordering of grains. Other causes for the large orientational spread are the roughness of the copper surface and the orientational spread of the copper planes themselves. The rocking curve of the suppressed (110) reflection in sample E10.4e, however, revealed a higher preferential arrangement in the direction perpendicular to the surface with a FWHM of 8.27° . This value can be compared with the FWHM of the orientation distribution of the strong fibre textured film E8.7e. The rocking curve of the (220) reflection is shown in figure 20 and yields a FWHM of $11.55 \pm 0.05^\circ$. The maximum intensity is slightly off normal by -0.5° . Parameters influencing the distribution of grains around the fibre axis are again the surface mobility of the atoms, the morphology of the copper oxide and the angle of incidence of the arriving niobium atoms on the surface.

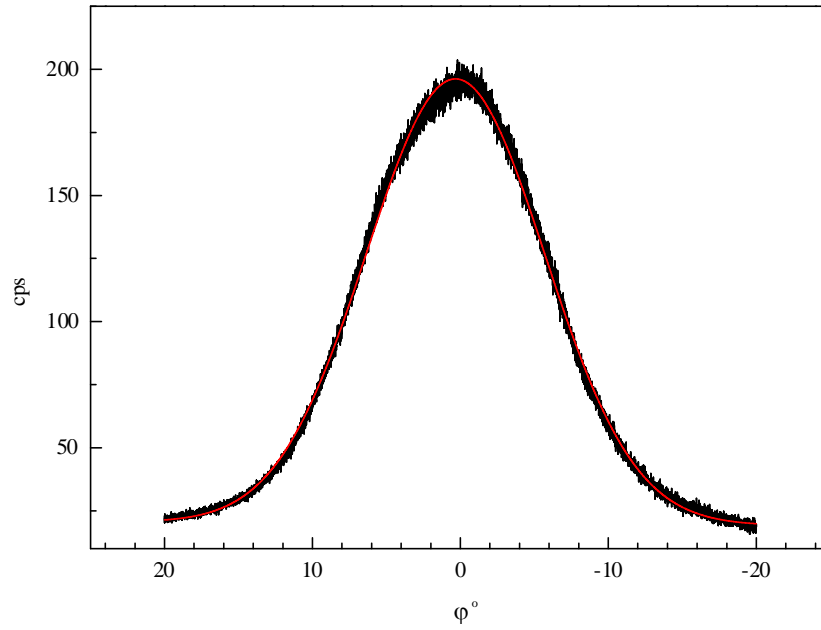


Figure 19. Rocking curve of reflection (211) of sample E10.4e after corrections according to formula (30), (37) and (9). 2θ is fixed at 70.054° . The full width at half maximum (FWHM) of this peak is 12.07° .

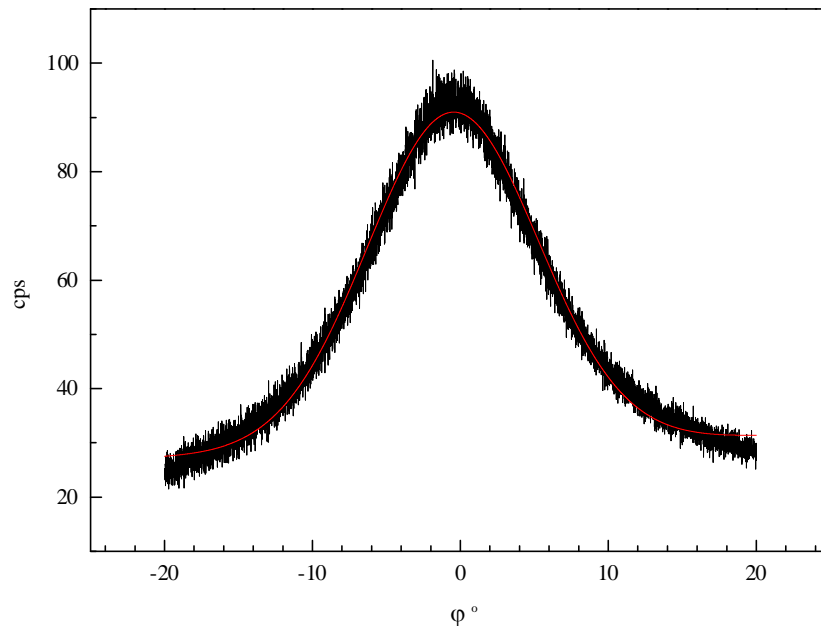


Figure 20. Rocking curve of reflection (220) of sample E8.7e (flattened). 2θ is fixed at 83.130° .

6. Hardness and elastic moduli of niobium films

6.1. Theoretical considerations and experimental procedure

The *Young's* moduli of samples E8.7e and E10.4e were determined experimentally by nanoindentation measurements performed at the EPFL⁽¹⁾. A knowledge of these values is important for the subsequent determination of the average stress in niobium films.

Nanoindentation is known to be a method to determine the mechanical properties of materials at a very low scale. In such an experiment, an indenter is pressed into the test material with a known load P . The indenter is a diamond tip with a pyramidal geometry.

The hardness H is defined as the ratio of the maximum applied load to some measure of the size of the residual indentation. The contact area, A , is often used, so that $H \equiv P_{max}/A$ (P_{max} is generally fixed by the desired penetration depth into the material, but can also be defined independently). The penetration depth of the tip into the material, h_{max} , and the load P can be measured with high precision. The contact area, A , on the contrary, cannot be measured directly and needs therefore to be derived from the measured penetration depth⁽²⁾. Figure 21 shows the surface deformation during indentation defining the various penetrations, h_s , h_f , h_c and h_{max} as explained later in the text, and figure 22 shows depth-sensing indentation data. As the load P is increased, the displacement of the indenter occurs due to both elastic and plastic deformation of the sample material (loading branch in figure 22). Finally, elastic displacements are recovered as the load is removed (unloading cycle).

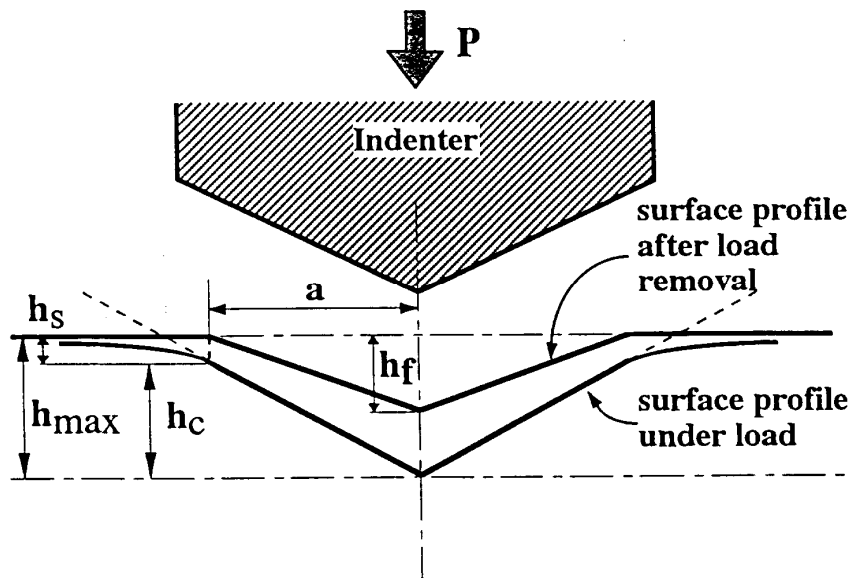


Figure 21. Surface displacement during indentation.

⁽¹⁾École Polytechnique Fédérale de Lausanne, Institut de Génie Atomique.

⁽²⁾Unlike the estimation of the well-known Vicker's hardness, where the contact area is bigger and therefore directly accessible to optical imaging.

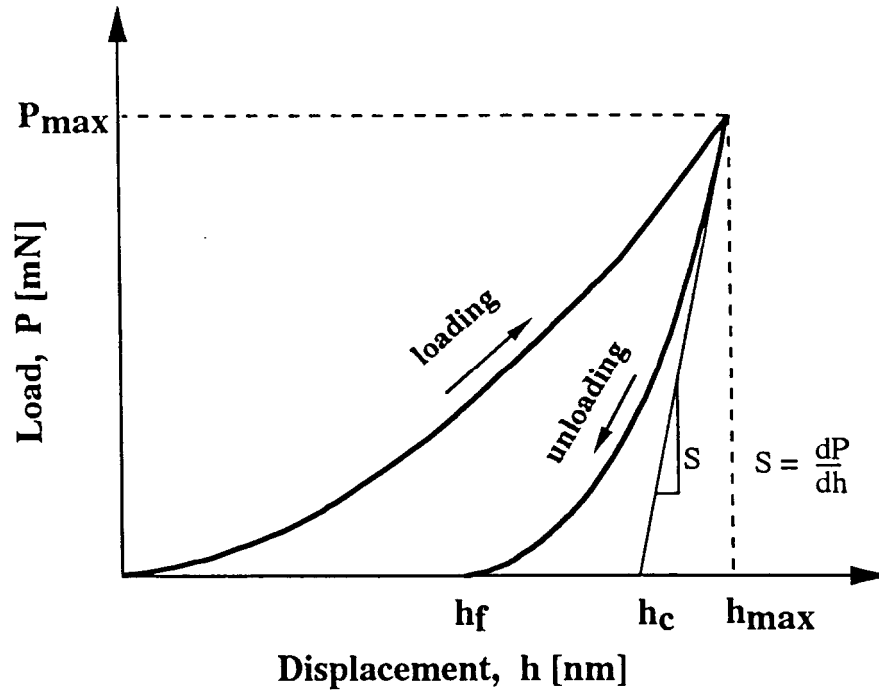


Figure 22. Indentation load-displacement curve.

The basic work of modern interpretation of depth-sensing indentation data has been performed in the seventies at the *Baikov Institute of Metallurgy in Moscow* [126]. Elastic theory provides the following relationship:

$$S = \left. \frac{dP}{dh} \right|_{\text{elastic}} = \frac{2}{\sqrt{\pi}} E_r \sqrt{A}, \quad (18)$$

where S is the contact stiffness, A is the contact area and E_r , the “reduced modulus” of the contact, which is defined by the formula,

$$\frac{1}{E_r} = \left(\frac{1 - \nu_i^2}{E_i} \right) + \left(\frac{1 - \nu_m^2}{E_m} \right). \quad (19)$$

The subscripts i and m refer to the indenter and the sample material, respectively and ν is *Poisson's* ratio. As can be seen from figure 22, S is just the derivative of the unloading curve. Since indentation stressing acts in all directions, the estimated *Young's* modulus can be very different from that measured by the commonly used bulge test, where the applied stress is only parallel to the surface [162]. For isotropic materials, however, comparable values should be measured.

The estimation of E_m from the load-displacement data requires a precise knowledge of the contact area and of *Poisson's* ratio, ν_m . It is common practice to ignore the anisotropy of *Poisson's* ratio and to take the value for the polycrystalline, untextured material. In the present estimation of E_m , *Poisson's* ratio as obtained from XRD analysis and described in chapter 7 has been used.

The occurrence of piling up or sinking down of the material around the contact surface and the deformation of the indenter are the main sources of error when estimating the contact area. The importance of the former effects can experimentally be assessed by optical inspection and taken into account when calculating the contact area [123-125]. In order to minimise the error due to indenter deformation, a re-calibration of the area function by indentation into fused silica (an

isotropic material for which E is well known) has been performed after the measurements of the niobium samples.

By indenting an isotropic material with a known elastic modulus, such as SiO_2 , to different depths, the values of A derived from Eqn. (18) can be fitted as a function of the contact depth, h_c , according to the formula,

$$A = 24.5h_c^2 + \sum_{n=0}^{n=7} C_n h_c^{1/2n}, \quad (20)$$

where the first term describes the geometric shape of a perfect *Berkovitch* indenter, while the other terms represent deviations due to blunting at the tip. The contact depth, h_c , is a measure of the distance along the indenter axis, over which the indenter is in contact with the sample. Formula (20) can then be applied as a general relation between the contact area and the contact depth, valid for any successive measurement.

Doerner and Nix [124] obtain h_c by fitting a straight line to the initial unloading data and extrapolating this line to the depth axis (*D&N* method). As a crude assumption, they take the indenter is a rigid flat punch, i.e. the contact area remains constant during the initial phase of unloading, which implies a linear unloading behaviour. The depth intercept of the linear fit is also called h_i , the intercept depth, and is equal to h_c in the *D&N* method (Figure 22).

Oliver and Pharr [125], applying general results previously derived by *Sneddon* [127] on elastic deformation, take instead a variation of the contact area during the unloading process into consideration, which implies a load-displacement relationship of the form,

$$P = a(h - h_f)^m. \quad (21)$$

In this formula, which is well confirmed by experimental data, h_f , the final depth, is the depth, at which the indenter is in contact with the material for the last time, and is equal to zero in the elastic regime, while m is a parameter dependent on the tip geometry and a is a material constant. In practice, due to deviations from the model, a dependence of m on the sample material is often observed.

In the *Oliver and Pharr* model, the contact depth, h_c , is related to the stiffness S , given by the derivative at P_{max} of the unloading curve, by the relation

$$h_c = h_{max} - \varepsilon \frac{P_{max}}{S} = h_{max} - \varepsilon(h_{max} - h_i) \quad (22)$$

where ε is related to the tip geometry and can be calculated analytically for the simplest cases (for a flat punch, $\varepsilon = 1$ and the *D&N* result with $h_c = h_i$ is obtained). The *Oliver and Pharr* method can be implemented by fitting a power law according to equation (21) to the experimentally determined unloading data. Using the derivative of the fit at P_{max} also determines the intercept depth, h_i , as shown in figure 26 (section 6.2). In this work, the model of *Oliver and Pharr* is used for calculations of the hardness and the *Young's* modulus of the samples.

Accordingly, the three key parameters needed to determine hardness and modulus are the peak load, P_{max} , the depth at peak load, h_{max} , and the initial unloading stiffness, S . These parameters as well as the power law exponent m are subsequently used to calculate the corrected depth of contact, h_c . Because of displacement of the surface at the contact perimeter, $h_c = h_{max} - h_s$. The deflection of the surface, h_s , depends on the indenter geometry and is given by

$$h_s = \varepsilon \left(\frac{P_{max}}{S} \right) = \varepsilon (h_{max} - h_i). \quad (23)$$

In this work, ε has been taken from table 12, which relates experimentally accessible m exponents with the geometrical constant, ε . The contact depth h_c should then be used in conjunction with the experimentally determined indenter shape function (Eqn. 20) to establish the contact area at peak load, A .

ε	m
1 (flat punch)	1
0.75 (paraboloid)	1.5
0.72 (conical)	2
0.829	1.1
0.793	1.2
0.772	1.3
0.759	1.4
0.743	1.6
0.738	1.7
0.733	1.8
0.73	1.9

Table 12. Punch parameters used in the data analysis (reprinted from [131]). Analytical solutions for the elastic contact problem with the *Berkovich* shape are not available.

An example of the data analysis obtained during unloading is given in figure 26. The actual relationship used to describe the unloading data is given by Eqn. (21). The initial unloading slope, S , is found by differentiation of this expression and evaluating the derivative at the peak load and peak displacement.

Experiments were performed using a Nanoindenter XP™, with a load and displacement resolution of 1.0mN and 0.02mm, respectively. This instrument provides also a mode of operation for continuous measurements of the contact stiffness during indentation. An oscillatory movement superimposed on the force signal during indentation and monitoring of the corresponding displacement oscillation gives a dynamic measurement of the hardness H and the *Young's* modulus E as a function of the penetration depth (Figure 27). A *Berkovich* indenter, a three-sided pyramid with an area-to-depth function (cross sectional area of the indenter as a function of the distance from its tip) of $24.5h_c^2$ was used. The loading rate was 500μN/s. Following the loading period, a 15s hold period at peak load allowed the time-dependent plastic effects to diminish. The specimen was then unloaded to 20% of the peak load with another hold period of 120s (used to establish thermal drift). The peak load was fixed by the condition of having 500nm maximum displacement (h_{max}) in the loading cycle.

6.2. Results and discussion

Twelve separate indentations at the equator were investigated for each sample. The hardness data are actually of minor interest for niobium coatings, but obtained as a by-product resulting from the dynamic measurements of the *Young's* moduli. They are plotted in figure 23. The initial increase in the measured data is a surface effect resulting from roughness and surface corrosion. The slope in the data observed at increasing load is often explained by plastic deformation in the substrate, since the radius of the activated area is larger than that of the contact area [127]. This explanation may hold for hard coatings, like TiN, where a high peak

load is applied and E for film and substrate is often very different. For the system niobium-copper, this effect seems to be rather an intrinsic property of the film and associated with the formation of dislocation loops when an external load is applied [128].

The difference in hardness between the samples (4.3 ± 0.1 GPa maximum hardness for film E8.7e and 3.0 ± 0.1 GPa for E10.4e, respectively) is apparent from the different applied maximum load, P_{max} , necessary to get 500nm indentation. The lower hardness of sample E10.4e indicates a reduced load bearing capacity, which could mean a less dense microstructure in those films with respect to films grown on oxidised copper. Preliminary analysis with TEM, however, does not confirm such a microstructural difference. Another, more likely explanation may be a positive correlation between compressive stress and hardness as reported in the literature for PVD coatings [130].

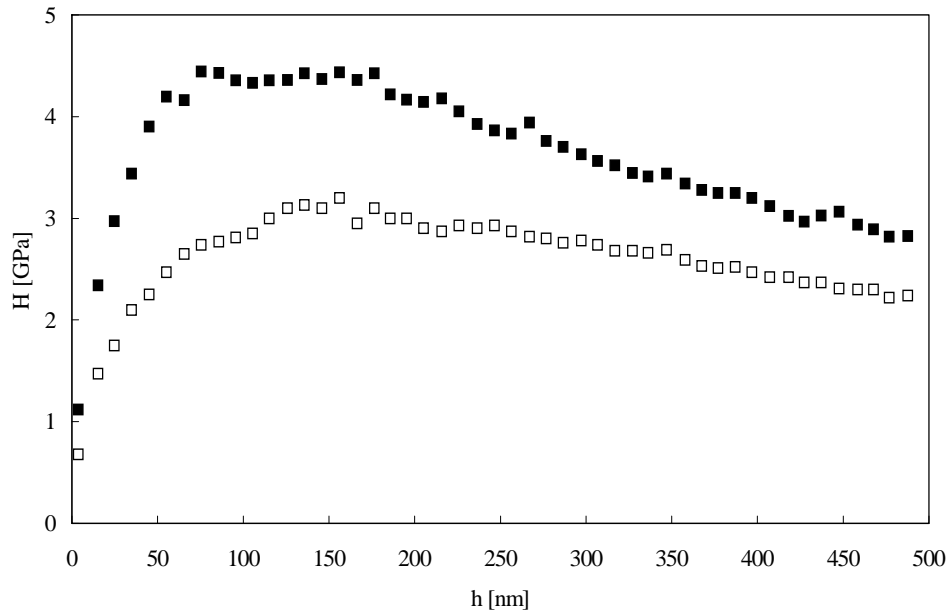


Figure 23. Microhardness of niobium films measured by nanoindentation. The full squares represent data measured on sample E8.7e and the open squares data on sample E10.4e.

As observed in most metals, the hardness is relatively small compared to the modulus and most of the indenter displacement is accommodated plastically, allowing only very little recovery on unloading. The classical load-displacement curves for both samples are shown in figures 24 and 25.

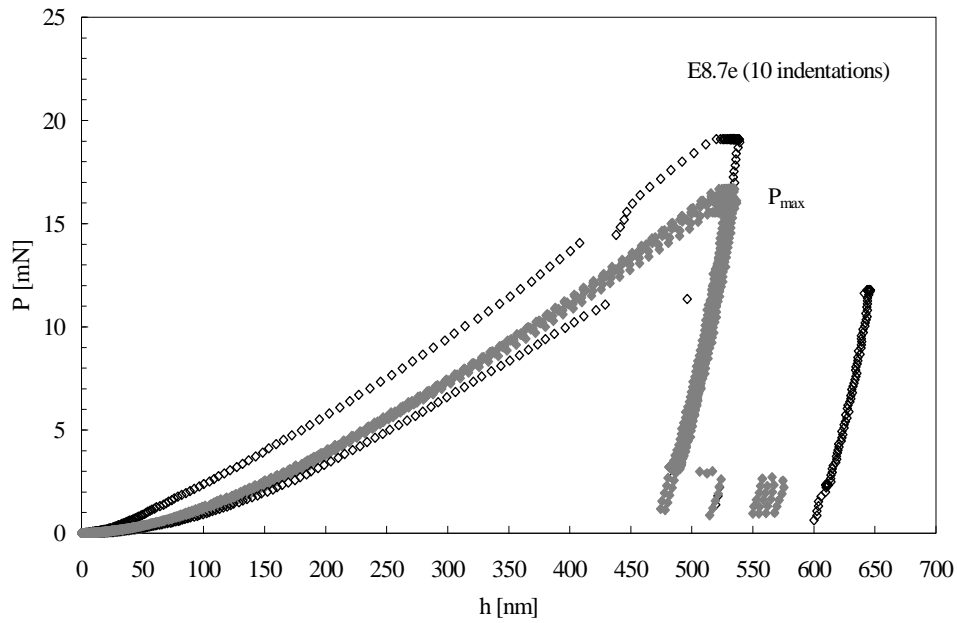


Figure 24. Load versus indenter displacement data of sample E8.7e. Data points labelled with open symbols are not considered for analysis. Two cycles have been made for initial calibration and are not shown here.

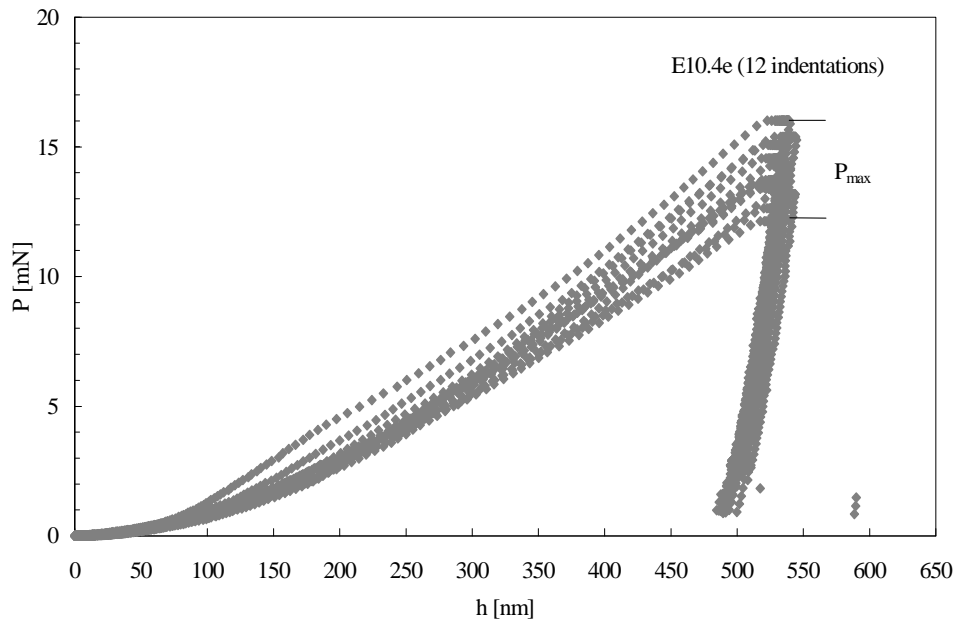


Figure 25. Load versus indenter displacement data of sample E10.4e. All measured indentation data have been analysed.

The peak load displacement shifts to higher values during the 15s hold period (Δh at peak load $\sim 20\text{nm}$). This creep occurs because of time-dependent plastic deformation in niobium and is present also in other materials, such as aluminium or tungsten. The shift after 80% of unloading, often observed on sample E8.7e, does not occur during the hold period, but takes place abruptly when the load is further decreased. An understanding of this effect certainly needs more data and is beyond the scope of this work.

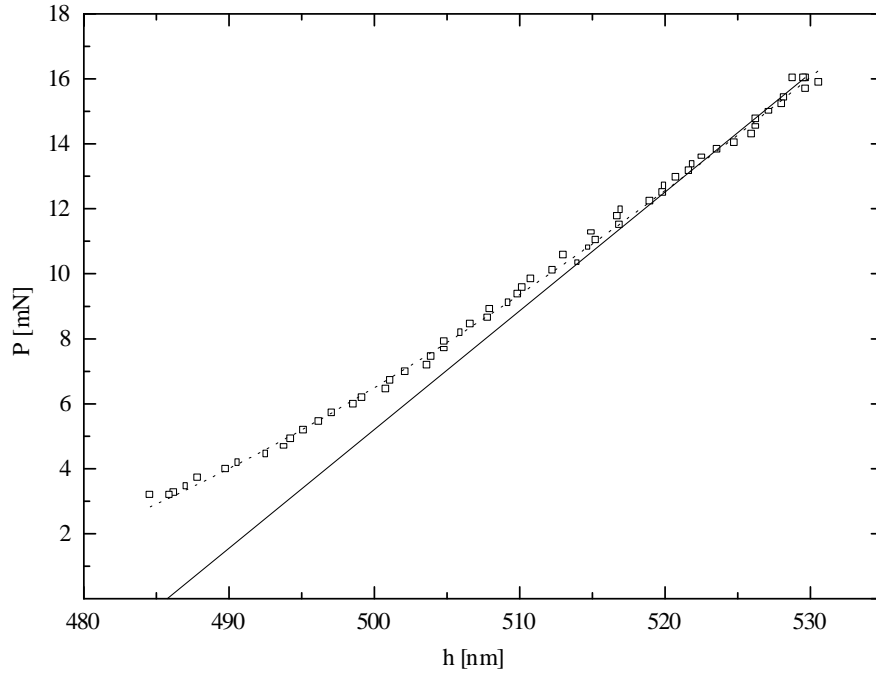


Figure 26. Example of an unloading curve analysis for sample E8.7e. The equation for the tangent in (P_{max}, h_{max}) (full line) is $15.92+0.36(h-529.6)$, from which the stiffness S and h_i are directly obtained. Fitting equation (21) to the data (dotted line) gives $m = 1.50 \pm 0.07$ and $h_f = 464 \pm 2 \text{ nm}$.

The values of experimentally observed power law exponents defined in Eqn. (21) range from about 1.5 to 1.9. The averaged values of the relevant indent parameters obtained by an analysis of all data, given in figures 24 and 25, are summarised in table 13.

Sample	m	h_f [nm]	P_{max} [mN]	h_{max} [nm]	S [N/ μm]	h_i [nm]
E10.4e	1.72 ± 0.16	479 ± 6	13.9 ± 1.2	535 ± 5	0.42 ± 0.04	502 ± 5
E8.7e	1.70 ± 0.14	461 ± 7	16.5 ± 1.0	534 ± 5	0.39 ± 0.02	491 ± 4

Table 13. Data obtained from analysing the unloading curves. Errors mainly represent the spread in the data. Fit errors are small and considered when performing the average.

For $m = 1.71$, the ε coefficient is approximately 0.737 (Table 12). Using equation (22) one can calculate h_c . The values obtained in this way are $511 \pm 7 \text{ nm}$ for sample E10.4 and $503 \pm 5 \text{ nm}$ for sample E8.7, respectively.

The final computation of the contact area and the elastic modulus E requires the knowledge of the area function and of *Poisson's* ratio for both, the diamond and the sample under investigation.

The contact area for a perfect *Berkovich* indenter is given by $A(h_c) = 24.5h_c^2$. Since deviations from the *Berkovich* geometry due to blunting of the tip have to be considered, a calibration procedure with standard materials was applied. Aluminium and fused silica were chosen for this purpose, because both materials are elastically isotropic and their elastic moduli are well known and independent of the indentation depth. The new area function is established by calculating the contact area as a function of h_c for those materials and fitting the data to the extended formula (Eqn. 20) to estimate the coefficients C_0 - C_7 . The non-perfect indenter geometry was found to increase the contact area by approximately 10%. The values of the elastic constants for diamond, which have to be known to calculate the sample moduli from the reduced moduli obtained by equation (19), are $E_i = 1141 \text{ GPa}$ and $\nu_i = 0.07$. Taking *Poisson's*

ratio as obtained from the stress measurement itself (chapter 7), the *Young's* modulus is $126 \pm 15 \text{ GPa}$ for E10.4e and $116 \pm 8 \text{ GPa}$ for E8.7e, measured at 500nm indentation.

The data obtained from the continuous measurement of the contact stiffness are plotted in Figure 27. They were computed with the *Poisson's* ratio, $\nu = 0.38$, given in the literature [132] for bulk niobium, and are in agreement with the values quoted above, when recalculated for the experimentally obtained *Poisson's* ratio.

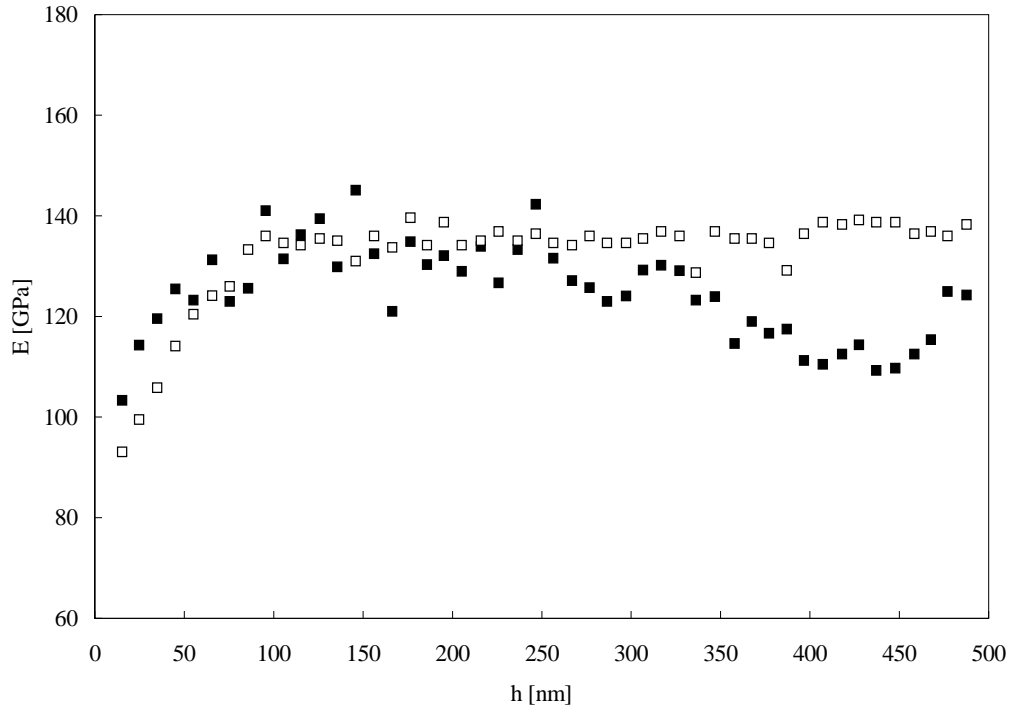


Figure 27. Young modulus of sample E8.7 (full symbols) and E10.4 (open symbols) as a function of indentation depth obtained from continuous measurements of the contact stiffness and calculated for $\nu = 0.38$.

The isotropic modulus for random oriented niobium given in literature is 103GPa. This quantity defines the magnitude of the resulting strain for a stressed, isotropic material, as described by *Hooke's* law and discussed in chapter 7. Now, as has already been shown in chapter 5, the niobium films are neither isotropic⁽¹⁾ nor single crystalline, but show preferred orientation, which is more or less pronounced depending on the film under consideration. *Hooke's* law for anisotropic materials introduces the compliance, S , and stiffness moduli, C , to express strains in terms of stresses and vice versa.

The compliance and stiffness values, given in table 14 below, are taken from reference [133] and are defined in the unit cube axis, [100], which is also termed the crystal axis, C' . The values in any other coordinate system can be calculated with the help of the direction cosines between the new system and the crystal axis by the transformation law for fourth rank tensors [134, 135]. Summation over all relevant components of the compliance tensor for a cubic crystal leads to the anisotropic *Young's* modulus as a function of the direction cosines and relates them to the elastic compliance terms defined in the crystal axis by

$$\left(\frac{1}{E} \right)_{hkl} = S_{11} - 2 \left[(S_{11} - S_{22}) - \frac{1}{2} S_{44} \right] (a_{11}^2 a_{12}^2 + a_{12}^2 a_{13}^2 + a_{11}^2 a_{13}^2). \quad (24)$$

⁽¹⁾Un textured polycrystalline materials are often treated as isotropic solids.

The elastic compliance terms entering into equation (24) and listed in table 14 are expressed in the contracted or matrix notation, which is obtained by contracting the first and last pair of suffixes in the tensor notation into a single number, according to the set of rules given in [134].

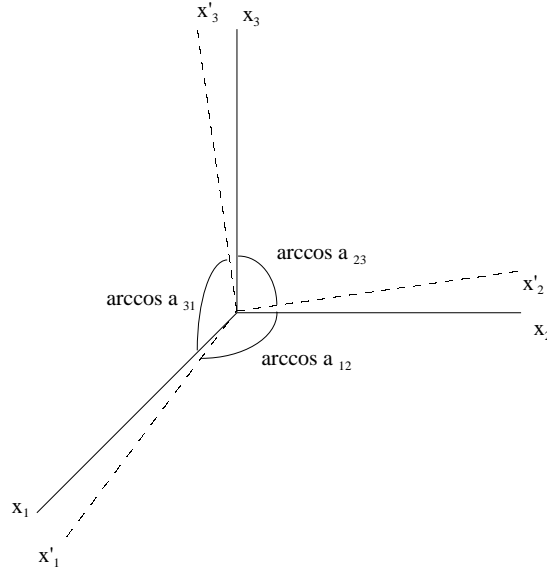


Figure 28. The ‘new’ and ‘old’ coordinate systems (x'_i) and (x_i) and the definition of the direction cosine between them.

The direction cosine term on the right hand side of equation (24) varies between 0 for the {100} family of directions and 1/3 for the {111} family. In table 14, the value of $2(S_{11}-S_{12})/S_{44}$, which is often termed anisotropy factor, and the calculated E in [GPa] for various directions are given. $(S_{11}-S_{12}) = 0.5S_{44}$ and thus $(S_{11}-S_{12})/S_{44}$ is 1 for isotropic materials.

S_{11} [GPa ⁻¹]	S_{12} [GPa ⁻¹]	S_{44} [GPa ⁻¹]	$2(S_{11}-$	$E_{\{100\}}$	$E_{\{111\}}$	$E_{\{110,211,311\}}$
0.006597	-0.002331	0.034843	0.5125	151.6	81.6	92.2

Table 14. Elastic compliance values and relative anisotropy of niobium.

A small difference in the measured *Young's* moduli of film E10.4e and E8.7e is expected due to the different texture in those films. The strong (110) orientation in film E8.7 lowers the elastic modulus with respect to the moderate texture in film E10.4, where the (200) oriented grains contribute approximately with the same fraction to the total amount of crystallographic oriented grains as in randomly oriented samples. The errors associated with experimentally determined values of the *Young's* modulus are dominated by the uncertainty involved in the determination of *Poisson's* ratio, as discussed in the next chapter.

7. Stress analysis by diffraction

7.1. ω -Goniometer (Seemann-Bohlin method)

Reflections from different crystallographic planes, which are inclined by different angles with respect to the surface of the substrate, were used to measure an average biaxial stress existing in the irradiated layer, applying the $\sin^2\psi$ technique. For this purpose the incident beam made a fixed angle ω with the sample surface (10, 4 and 1°, respectively) and the detector moved around the goniometer circle (detector scan in the asymmetric configuration). The relevant inclination ψ is given by

$$\psi = \theta - \omega. \quad (25)$$

The presence of high angle reflections and similar strains along different crystallographic directions are, therefore, basic requirements to get reliable results with this method. Contributions from angle-dependent intensity factors were removed from the raw profile and the absolute value, $2\theta_p$, of the peak position has thereafter been obtained by fitting the modified Lorentzian function to the corrected profile. The measurements were performed using the grazing incidence attachment of the diffractometer, mainly consisting of a collimator block, containing the Soller slits, and a plane crystal monochromator in front of the detector. No scattered radiation diaphragm or detector diaphragm were installed.

In the $\sin^2\psi$ technique, the residual stress σ_ϕ is determined from the slope of a plot of the interplanar spacing d_ψ (or equivalent the lattice parameter a_ψ) vs. $\sin^2\psi$. Such plots were constructed for both types of niobium films, represented by sample E8.7e and E10.4e, respectively. The interplanar spacing, d_ψ is calculated from $2\theta_p$ and the errors associated with them are obtained from

- a) the uncertainty of the peak location considering a maximum sample displacement of 0.5mm⁽¹⁾
- b) a focusing error due to the deviation of the specimen surface from the focusing circle, calculated for a flat specimen⁽²⁾ (Eqn. 10) and
- c) the statistical error obtained from the fit.

In the most general case, where a cubic material contains a general triaxial stress, the stress tensor is of the form

$$\sigma_{ij} = \begin{vmatrix} \sigma_{11} & \sigma_{12} & \sigma_{13} \\ \sigma_{21} & \sigma_{22} & \sigma_{23} \\ \sigma_{31} & \sigma_{32} & \sigma_{33} \end{vmatrix}. \quad (26)$$

The second index defines the normal of the face of a homogeneously loaded unit cube, in which the stress acts, and the first index refers to its direction. Normal stresses act along the direction of the axis and are indicated by the repeated index, and shear stresses are indicated by the mixed index. Since the body is in equilibrium and the stress distribution is homogeneous, $\sigma_{ij} = \sigma_{ji}$.

⁽¹⁾The assumption of 0.5mm is based on calculations of the height displacement by the method described in chapter 3 after having slightly modified the sample holder to allow a better positioning of curved samples. The error resulting from the relative peak shift between $\psi=0$ and $\psi=\psi$, caused by sample displacement, is small and has not considered.

⁽²⁾In the case, where the samples were cut from the equatorial region of a cavity, the calculated error may be slightly overestimated due to the specimen concavity.

The linear relationship between stress and strain along [hkl], as given by *Hooke's* law, makes it possible to determine the residual stress field in a specimen by X-ray diffraction. The interplanar spacing acts as an internal strain gauge and is affected by both micro- and macrostresses. If the surface of the material is in compression, the planes parallel to the sample surface, as detected in the Bragg Brentano configuration, are further apart than in the stress free state because of the *Poisson's* ratio. After the specimen is tilted, diffraction occurs from other grains, but from the same planes, and these are more nearly perpendicular to the stress direction. Consequently, the interplanar spacing will change according to the elastic properties of the material. The general definition of strain is the deformation per unit length. The lattice spacing $d_{\phi\psi}$ for a given reflection is therefore related to the strain ε'_{33} by the relationship,

$$(\varepsilon'_{33})_{\phi\psi} = \frac{d_{\phi\psi} - d_0}{d_0}, \quad (27)$$

where $(\varepsilon'_{33})_{\phi\psi}$ is the normal strain in the direction defined by the angles ψ and ϕ (Figure 29). The primed tensor quantity refers to the laboratory system L_i , which is defined such that L_3 is in the direction of the normal of the family of planes, whose spacing is actually measured by X-rays. L_2 is in the surface plane defined by the axis S_1 and S_2 of the sample coordinate system and makes an angle ϕ with S_2 . In practice, the angles ψ and ϕ are realised by using a four circle goniometer (Eulerian cradle), the standard equipment in conventional X-ray residual stress and texture analysis (see section 7.2).

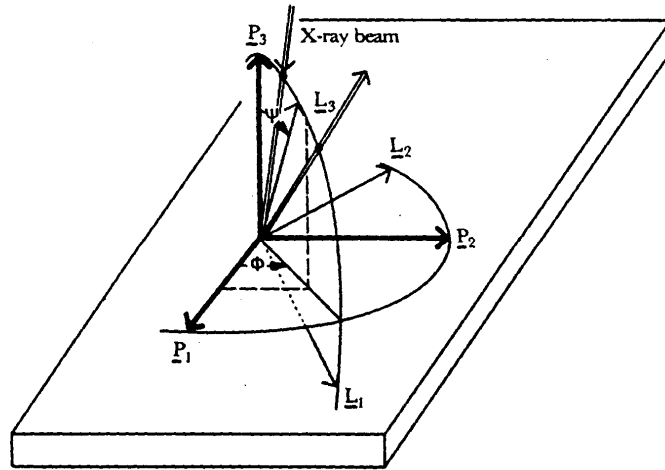


Figure 29. Illustration of the laboratory coordinate system, L_i , the sample coordinate system S_i and the angles ϕ and ψ as used in texture and stress analysis [136, 137]. The interplanar spacing of planes normal to L_3 are measured in stress determination.

In order to transform the strain from the laboratory system into a strain ε_{ij} defined in the specimen coordinate system, one has to consider the angular relationships between S and L , which are given by the direction cosines between all the axis S_i and L_i . With the transformation rule for strain, a second rank tensor, one obtains the fundamental equation for strain determination from X-ray diffraction data,

$$\begin{aligned} (\varepsilon'_{33})_{\phi\psi} = \frac{d_{\phi\psi} - d_0}{d_0} = & \varepsilon_{11} \cos^2 \phi \sin^2 \psi + \varepsilon_{12} \sin^2 \psi \sin 2\phi + \varepsilon_{22} \sin^2 \psi \sin^2 \phi + \\ & + \varepsilon_{13} \cos \phi \sin 2\psi + \varepsilon_{23} \sin \phi \sin 2\psi + \varepsilon_{33} \cos^2 \psi. \end{aligned} \quad (28)$$

The strains given in equation (28) are the average strains in the diffracting crystals and are correlated to the principal stresses by elastic stress-strain relations, as given for an isotropic

solid, or in the most general case for an anisotropic crystal. In the following, the isotropic case is assumed to express the strains in the sample coordinate system in terms of stresses. The anisotropic case will be considered later by substituting the isotropic *Young's* modulus and *Poisson's* ratio by elastic compliance terms.

For a unit cube, subjected to three normal stresses, σ_{11} , σ_{22} , σ_{33} , the strain along any direction is the sum of the strain caused by the stress in that direction and the strains caused by the stresses acting in the transverse directions. Normal stresses cause only lattice dilatation, but distortion or shape change occurs, when a shear stress, σ_{ij} ($i \neq j$), is applied to the material. The resulting shear strain is defined by the shear modulus, μ , by $2\varepsilon_{ij} = (1/\mu) \sigma_{ij}$ and μ is related to E and ν by $2\mu = E/(1+\nu)$. All this is described by *Hooke's* law for isotropic materials expressed in the suffix notation,

$$\varepsilon_{ij} = \frac{1+\nu}{E} \sigma_{ij} - \delta_{ij} \frac{\nu}{E} \sigma_{kk}, \quad (29)$$

where k is the dummy suffix and δ_{ij} is *Kronecker's* delta. Equation (29) can be written in terms of the stress components related to the specimen coordinate system as follows,

$$\begin{aligned} \frac{d_{\varphi\psi} - d_0}{d_0} &= \frac{1+\nu}{E} (\sigma_{11} \cos^2 \varphi + \sigma_{12} \sin 2\varphi + \sigma_{22} \sin^2 \varphi - \sigma_{33}) \sin^2 \psi + \\ &+ \frac{1+\nu}{E} \sigma_{33} - \frac{\nu}{E} (\sigma_{11} + \sigma_{22} + \sigma_{33}) + \\ &+ \frac{1+\nu}{E} (\sigma_{13} \cos \varphi + \sigma_{23} \sin \varphi) \sin 2\psi. \end{aligned} \quad (30)$$

The simplest case of stress evaluation, as considered in the *Seemann-Bohlin* method, assumes a biaxial stress with the components σ_{i3} to be zero (as it is the boundary condition at the free surface of the material) and does not allow an estimation of the in-plane shear stress σ_{12} . Furthermore it is assumed that the normal stress components or principal stresses, σ_{11} and σ_{22} , acting along the two principal axis in the plane of the film are equal and that the stress is almost constant within the X-ray penetration depth. Under these assumptions equation (30) can be transformed into,

$$\begin{aligned} \frac{d_{\varphi\psi} - d_0}{d_0} &= \frac{1+\nu}{E} (\sigma_{11} \cos^2 \varphi + \sigma_{12} \sin 2\varphi + \sigma_{22} \sin^2 \varphi) \sin^2 \psi \\ &- \frac{\nu}{E} (\sigma_{11} + \sigma_{22}). \end{aligned} \quad (31)$$

For $\varphi = 0$, the normal in-plane stress components may directly be calculated from the slope of the $\sin^2 \psi$ plot (Fig. 30ab) with the help of the bulk elastic constants for an elastically isotropic material. If the material is elastically anisotropic, a situation, which is more or less true for all crystalline materials⁽¹⁾, the *Young's* modulus along $[hkl]$ must be used instead.

⁽¹⁾Since the interatomic spacing is different along various directions in the point lattices, the variation of the potential energy with distance and, hence, the elastic modulus will change with direction, causing anisotropy.

Furthermore, since a volume average of strains is measured by X-ray diffraction, the elastic constants, which relate the measured strains to the stresses should also be averaged values⁽¹⁾. Therefore, effective diffraction elastic constants of single-phase polycrystals (X_1 , X_2) have been defined for each [hkl] [138, 139]. They are expressed in terms of

$$\left(\frac{1+\nu}{E} \right) = X_1, \quad \left(\frac{-\nu}{E} \right) = X_2, \quad (32)$$

since they appear in the fundamental X-ray stress equation (Equation 30). If high accuracy is needed, experimental values should be used, which may be obtained directly from the sample under investigation⁽²⁾. Since in the present work the X-ray elastic constants were experimentally not accessible, they were calculated along the measured crystallographic direction from single crystal compliance data of niobium (section 7.2). On the other hand, the mechanically measured *Young's* modulus obtained by indentation measurements is an average value over all crystallographic directions as the strains are, which have been derived from the Seemann-Bohlin method. Together with the measured *Poisson's* ratio (see below), these values can be used to determine the stresses. Rewriting equation (31) for $\varphi = 0$, $\sigma_{22} = \sigma_{11}$ and using the lattice parameter a instead of the interplanar spacing d ,

$$a_\psi = \frac{1}{E} a_0 \sigma_{11} ((1+\nu) \sin^2 \psi - 2\nu) + a_0, \quad (33)$$

one can verify immediately that the value of the unstressed lattice parameter a_0 is the value of a_ψ at $\sin^2 \psi = 2\nu/(1+\nu)$. On the other hand, if the unstressed lattice parameter is well known, as from the measurements on films without the substrate (chapter II/3), the value of *Poisson's* ratio can be calculated instead. It should be noted, that this method to determine an exact value of a_0 (or ν) from the data obtained during stress measurements, needs a biaxial stress state within the irradiated volume, which has been verified to be indeed the case (see section 7.2). It does not necessarily require that $\sigma_{22} = \sigma_{11}$.

The value of the slope derived from a fit through all data points, except those resulting from the [h00] family of planes, defines the principal stress (Figure 30). The latter planes cannot be considered because of the different elastic properties (Table 14). The lattice parameters a_\perp and a_\parallel , perpendicular and parallel to the surface plane, are given by the ordinate intercepts at $\sin^2 \psi$ equal to zero and unity, respectively.

⁽¹⁾In a polycrystalline sample adjacent grains of different crystallographic directions (and hence elastic constants S_{ij}) are subjected to a homogeneous stress at the surface. The grains are in rigid contact and displacements across the grain boundary must be constant, in order to avoid having voids at the boundary. Therefore, a microstress field is built up, which modifies the applied stress and constrains the displacements in the material surrounding the grain boundaries. Since information is obtained over a large number of grains, a volume average of the elastic constants is required, in order to obtain the principal stress σ_{ij} . The averaging is not over all of the grains in the material volume, but over grains in a particular orientation.

⁽²⁾The X-ray elastic constants can be determined from the change of the slope and the intercept of the $\sin^2 \psi$ diagram when stressing the specimen on the diffractometer by the application of several known loads.

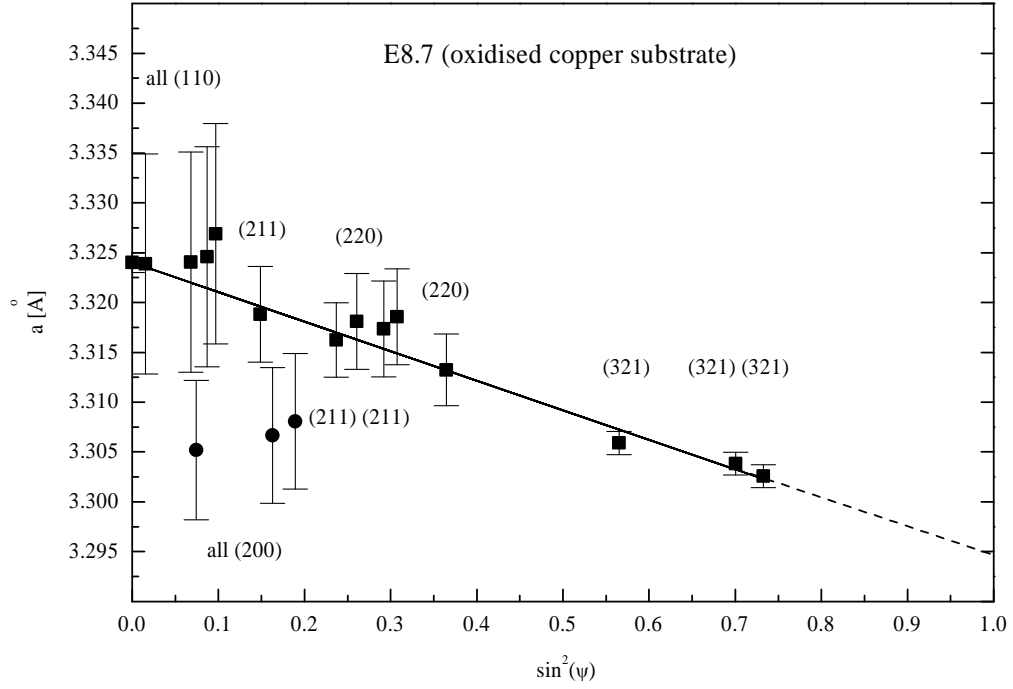


Figure 30a. Determination of the Poisson's ratio and the average normal stress component $\sigma_{11} = \sigma_{22}$ of sample E8.7 in the Seemann-Bohlin geometry. The line is the result of a weighted linear fit to all data except the reflections from (200) planes (circles) and corresponds to the relation $a_\psi = -0.0297 \pm 0.0009 \sin^2 \psi + 3.3240 \pm 0.0005$. The data were measured with an angle of incidence ω of 1, 4 and 10°, respectively.

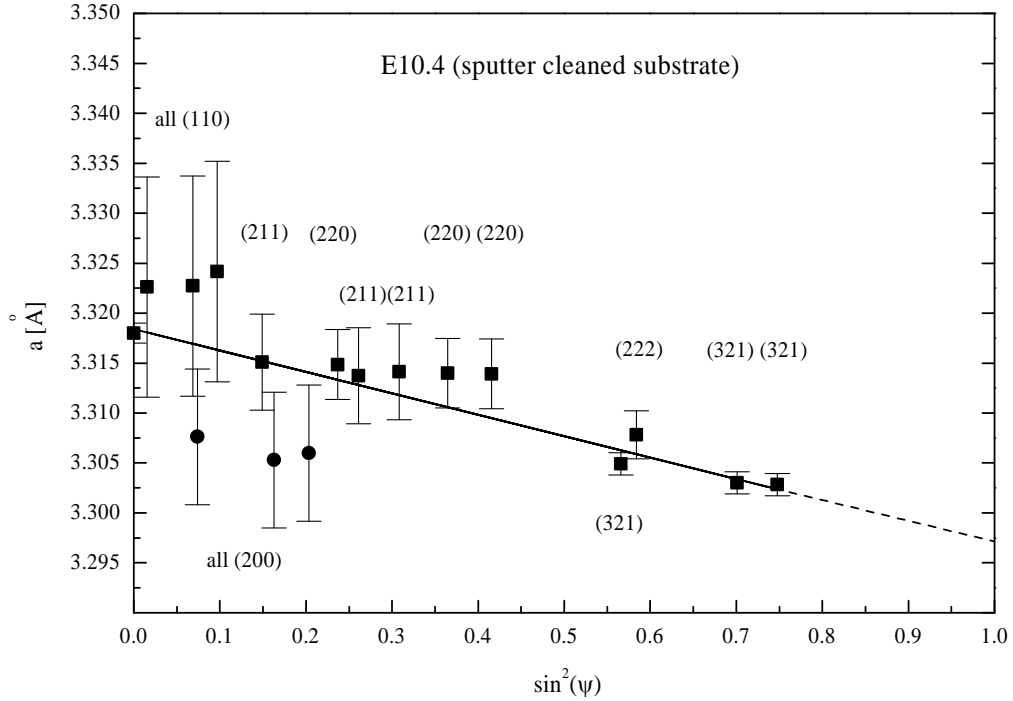


Figure 30b. Results obtained for sample E10.4 (see caption of figure 31a). The solid line corresponds to the relation $a_\psi = -0.0215 \pm 0.0012 \sin^2 \psi + 3.3184 \pm 0.0007$.

The stress can also directly be determined from a_\perp , according to

$$a_\perp = a_0 + 2X_2\sigma_\phi a_0, \quad (34)$$

which predicts a linear relationship between the increase in lattice parameter and the internal stress as a result of the *Poisson's* ratio effect. Thus having verified the existence of a biaxial stress state and determined *Poisson's* ratio from the procedure described above, a single measurement of the lattice parameter perpendicular to the surface plane provides a good approximation of the principal stress. Table 15 summarises all results obtained on sample E8.7e and E10.4e, respectively.

Sample	ν_{SB}	E [GPa]	σ_{11} [MPa]	a^\perp [Å]	a^\parallel [Å]
E10.4e	0.45±0.05	126±15	-565±78	3.3184±0.0007	3.2969±0.0014
E8.7e	0.47±0.03	116±8	-706±56	3.3240±0.0005	3.2943±0.0010

Table 15. Results from stress measurements in the Seemann-Bohlin configuration. The *Young's* modulus was obtained from nanoindentation using *Poisson's* ratio calculated from equation (33) (see text).

The errors involved in stress calculations are dominated by the uncertainty on the experimentally obtained elastic constants. Taking for example *Poisson's* ratio for isotropic niobium, 0.38, the principal stress components will be higher by almost 25% compared to the values listed in table 15.

It should be pointed out that the experimentally determined value of *Poisson's* ratio is very sensitive to a proper choice of the stress free lattice parameter. In the present calculations, $a_0 = 3.305 \pm 0.002 \text{ Å}$, as obtained from measurements on standard films freed from the substrate and from measurements on niobium powder (chapters II/3 and II/5). Taking instead the average value of literature data [50-53], $a_0 = 3.303 \text{ Å}$, a *Poisson's* ratio of greater than 0.5 is calculated, which is physically not possible, showing the limitations when seeking for high accuracy with the present method. Despite these uncertainties, the results clearly indicate that a film grown on oxidised copper suffers from a higher residual normal stress than a niobium film grown on oxide-free copper. The thermal mismatch stress, which is related to the difference in the thermal expansion coefficients between the substrate and the film is approximately the same in both cases and can be subtracted from the measured total stress value. The thermal expansion of the thin oxide layer at the interface, present in standard films, has not been considered. The thermally induced in-plane stress is given by [141],

$$\sigma_{therm} = \frac{E}{1-\nu} (f_{Nb} - f_{Cu}) (T_D - T_M), \quad (35)$$

where f_{Nb} and f_{Cu} are the coefficients of thermal expansion of the film ($7.18 \times 10^{-6} \text{ K}^{-1}$) and the substrate ($1.72 \times 10^{-5} \text{ K}^{-1}$) [132], E and ν are the elastic moduli of the film and T_D and T_M are the temperatures during film deposition ($423 \pm 5 \text{ K}$) and diffraction measurements (299 K), respectively. Since $f_{Nb} < f_{Cu}$, on cooling from the deposition temperature, the thermal stress brings the columnar units closer together and a compressive stress is set up. The calculated value of σ_{therm} is $-307 \pm 22 \text{ MPa}$.

Sputter deposition of a niobium film on a niobium substrate allows a direct estimation of the thermally induced stress component [140]. Using equation (34) for the calculation of the stress from the lattice constant of films grown on annealed bulk niobium samples, $a_\perp = 3.3190 \pm 0.001 \text{ Å}$, yields a compressive in-plane stress of $-520 \pm 56 \text{ MPa}$. This value is about 35% lower than the value of -795 ± 62 , the stress calculated from the measured lattice constant of niobium films grown in the sample system under the same conditions on an oxidised copper substrate⁽¹⁾. Accordingly, the thermal stress contributes a significant fraction to the residual

⁽¹⁾The lattice constant of standard niobium films grown in the sample system, as described in chapter II/1, was found to be somewhat higher than that measured on samples cut from cavity E8.7.

extrinsic stress at room temperature. The experimentally determined value of $\sigma_{therm} = -275 \pm 83 \text{ MPa}$ is consistent with the calculated one. On a planar substrate, the stress due to differential thermal expansion experienced by the thin film is always biaxial and a calculation from the lattice constant in the normal direction is fully valid.

These numbers emphasise the predominance of growth-induced stresses as a component of total stress. Possible causes of growth-induced stresses in magnetron sputtered films have already been mentioned in chapter II/3. A discussion of the observed difference in the stress state of films grown under the same conditions on oxidised and non-oxidised copper will be presented in the next chapter together with data from the more detailed conventional stress analysis. The expected consistency in the level of residual stress measured on different lattice planes with similar elastic properties, as indicated by the linearity in the *Taylor-Sinclair-Nelson-Riley* plots (Figs. 7 and 8 in chapter II/3), is confirmed by the small differences between the measured points and the interpolated values in figure 30ab.

7.2. ψ -Goniometer (Eulerian cradle)

The tilts required for residual strain/stress measurements can also be achieved by the geometry shown in figure 31. This particular geometry is referred to as the ψ -goniometer and the whole equipment is called *Eulerian* cradle. The lattice plane distances are measured for one family of lattice planes, coming from a set of grains having different orientation in the sample, by systematically changing the angle ψ . The advantages of this system are the direct achievement of an inclination ψ , independent of the *Bragg* angle θ and an additional degree of freedom allowing a rotation around the sample axis φ . Since the specimen is in the correct focusing condition at all tilts, obeying the 1:2 relationship between θ and 2θ , the incident and the diffracted beams have equal path lengths, independently of ψ . Thus, in this case, there is no absorption correction, if the samples have a thickness greater than the X-ray penetration depth.

In the present case, the data generated from step counting over the diffraction peaks chosen for the analysis, have to be corrected for the finite thickness:

$$\frac{I_{\infty}}{I_x}(\psi) = \left[1 - \exp\left(\frac{-2\mu x}{\sin \theta \cos \psi}\right) \right]^{-1}, \quad (36)$$

following similar geometrical considerations as described in the appendix for the ω -goniometer. The corrected data were fitted with the modified Lorentzian function to estimate θ_p as a function of φ and ψ . The parameters set for these measurements are listed in table 16.

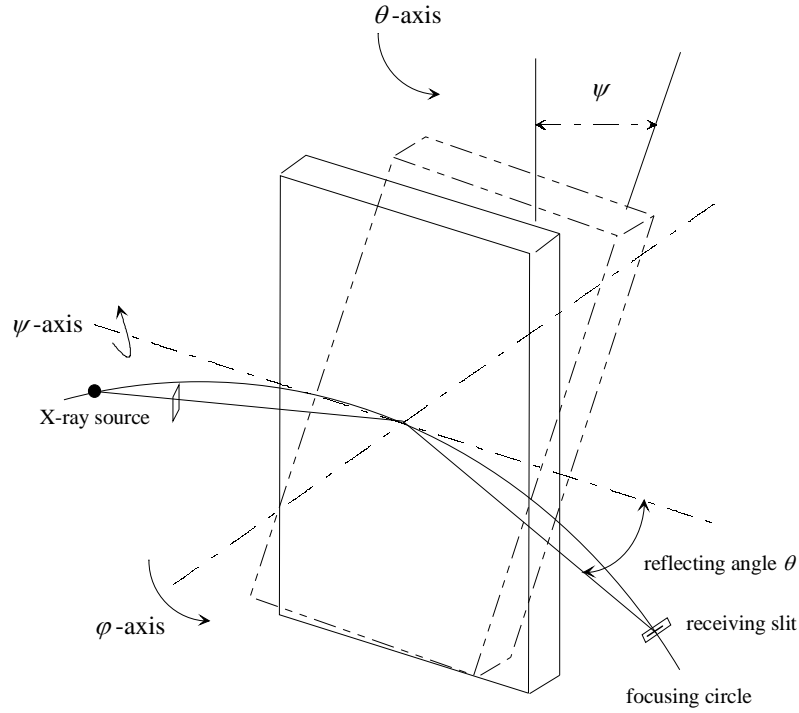


Figure 31. ψ -goniometer geometry for stress and texture measurements.

Mode of operation :	θ - 2θ (locked coupled)
Step size/time :	$0.008^\circ/7s$
Wavelength :	$1.540560/1.544390\text{\AA}$ (Cu)
Variable divergence diaphragm :	0.5° (1mm) fixed
Sattered-radiation diaphragm next to sample :	Slit diaphragm
K_β filter (Ni) :	in
Primary/secondary soller slits :	in/in
Variable scattered radiation diaphragm :	0.3° (0.6mm) fixed
Fixed detector slit diaphragm :	0.6 mm
Detector slit :	out

Table 16. Parameters set for measurements of lattice strains with the Eulerian cradle.

Allowing now non-zero stress components in the direction of the surface normal, S_3 , the six unknowns, σ_{11} , σ_{12} , σ_{22} , σ_{13} , σ_{23} , σ_{33} , given in equation (26), can be calculated by measuring $d_{\phi\psi}$ along at least 6 independent directions in the laboratory coordinate system, L . Due to the presence of the components σ_{13} and σ_{23} and the function $\sin 2\psi$ associated with these terms, a $\sin^2 \psi$ plot, as shown in figure 30, will not be linear any longer, but exhibit both a curvature and ψ -splitting, as d is measured at positive and negative ψ tilts [137]. The present data were analysed seeking for the complete triaxial stress tensor [142], but ignoring curvature and oscillations in the data, that is to simplify the data towards a linear distribution and as a result loosing all its “fine structure”, which may appear because of stress gradients and texture present in the sample.

As, for all rotations, the X-ray penetration depth is greater than the film thickness, the total gradient is sampled at all times and stress gradients will give only a small contribution to curvature in the data. As a result, Cu $K\alpha$ radiation, which has a high penetration depth into

niobium, is not the best choice, when seeking for confirmation of an inhomogeneous average strain state in thin films, and Cr K α ($\lambda = 0.2229\text{nm}$) radiation should be used in addition [63, 143]. However, since attenuation of the incident beam is proportional to the thickness of the material, the contribution to the diffracted beam from layers close to the interface within the irradiated volume is less. Furthermore, the diffracted beam has to traverse still more material before it can exit from the surface, suffering even more attenuation. Thus, the $d_{\varphi\psi}$ values from planes in the shallower depths will contribute more to the measured stress than $d_{\varphi\psi}$ from layers deeper down in the film and averaging will occur closer to the surface as the tilt angle increases.

Texture fluctuations on the contrary continuously change the microstress fields, arising from an elastic incompatibility between mutually coupled grains of different crystallographic directions, which can lead to residual strain distributions and these may cause $\sin^2\psi$ oscillations too. These oscillations follow closely the variation in peak intensity due to texture [144] and are well reproduced by weighting the *XEC*'s, calculated in the *Reuss* and *Voigt* limits (see below) on the real fraction of (110) orientated grains at each ψ -tilt [145-148]. Averaging their values over the orientation distribution function of the sample, instead of taking a simple average over all reflections assuming random orientation, will lead to modified values of X_1 and X_2 , which can subsequently be used to calculate the average stress by the method outlined below. Time consuming measurements and calculations, however, and a relatively small change in the magnitude of the final stress ($\sim 15\%$ for a strong fibre texture [146]) do not motivate to analyse the data in this way. In the literature, it is rather common practice to take the isotropic values of the elastic constants to calculate macrostresses, if experimental data are not available.

Defining the parameters a_1 and a_2 ,

$$\begin{aligned} a_1 &= \frac{I}{2} \left(\varepsilon_{\varphi\psi^+} + \varepsilon_{\varphi\psi^-} \right) = \left(\frac{d_{\varphi\psi^+} + d_{\varphi\psi^-}}{2d_0} - 1 \right) = \\ &= X_1 \left(\sigma_{11} \cos^2 \varphi + \sigma_{12} \sin 2\varphi + \sigma_{22} \sin^2 \varphi - \sigma_{33} \right) \sin^2 \psi + \\ &+ X_2 \left(\sigma_{11} + \sigma_{22} + \sigma_{33} \right) + X_1 \sigma_{33} \end{aligned} \quad (37)$$

$$a_2 = \frac{I}{2} \left(\varepsilon_{\varphi\psi^+} - \varepsilon_{\varphi\psi^-} \right) = \left(\frac{d_{\varphi\psi^+} - d_{\varphi\psi^-}}{2d_0} \right) = X_1 \left(\sigma_{13} \cos \varphi + \sigma_{23} \sin \varphi \right) \sin 2\psi, \quad (38)$$

the stress tensor may be obtained from the slope and the intercept of a_1 vs. $\sin^2\psi$ and from the slope of a_2 vs. $\sin 2\psi$ for $\varphi = 0^\circ, 45^\circ, 90^\circ$ and $\varphi = 0^\circ$ and 90° , respectively (Fig. 32). In practice, measurements were performed at $\varphi = 0^\circ, 45^\circ, 60^\circ$ and 90° to obtain an over-determined system of linear equations, $Ax = b$, which was solved by means of the least-squares method, minimising the sum,

$$S(x) = \sum_{n=1}^N \left(\sum_{m=1}^M A_{n,m} x_m - b_n \right)^2. \quad (39)$$

Here, A is a matrix of $n \times m$ dimensions, x is a vector of m elements, b is a vector of n elements and $n > m$. The influence of error of the matrix elements A_{mn} (elastic constants) and the vector elements b_n (slope and intercept, respectively) on the precision of the solution vector elements x_m has been considered.

When seeking the exact solution for the unknowns $s_{11}, s_{22}, s_{33}, s_{12}$ in equation (37) by writing the system matrix A with $m = n = 4$, no definite result has been obtained. The determinant of this matrix was actually found to be zero, which means that there exists no definite solution for this system of equations. A physically sensible approach to continue the calculations of the

stress tensor is to choose the solution $\sigma_{33} = 0$, i.e. to reduce the number m of unknowns to 3 in equation (37). The justification for this procedure can be found in the equations for equilibrium in the direction normal to the surface [149, 150],

$$\frac{\partial \sigma_{31}}{\partial x_1} + \frac{\partial \sigma_{32}}{\partial x_2} + \frac{\partial \sigma_{33}}{\partial x_3} = 0. \quad (40a)$$

The actual results indicate that σ_{31} and σ_{32} are very small, if not zero (see below). Consequently, their gradients will be negligible and $\partial \sigma_{33} / \partial x_3$ should be negligible too. With the boundary condition at the free surface,

$$\sigma_{33}(x_3 = 0) = 0, \quad (40b)$$

σ_{33} must be zero anywhere else in the sample and the atomic distances along this direction expand freely [143, 150, 154].

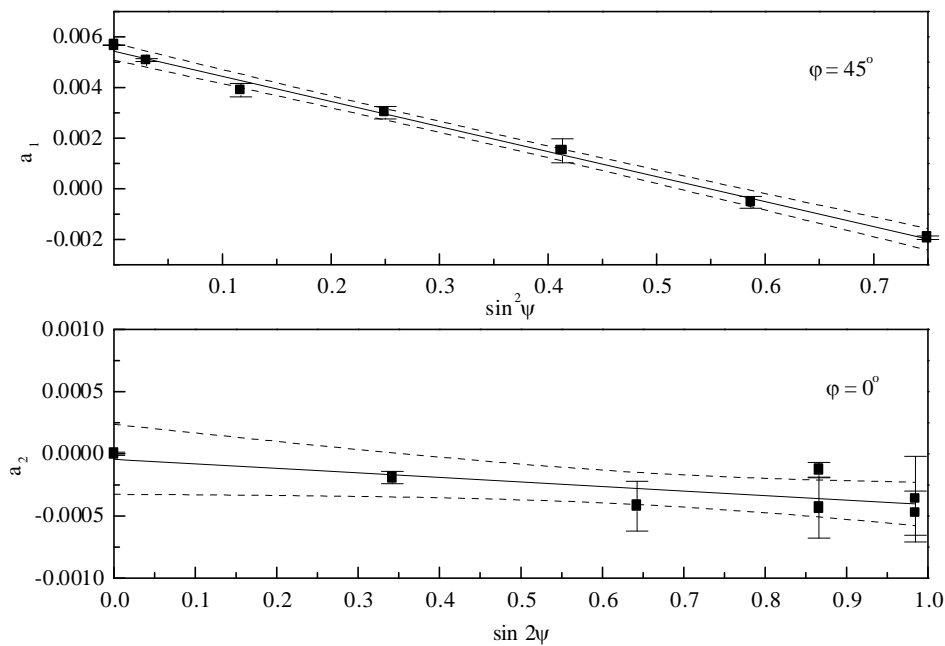


Figure 32. Variation in a_1 of Eqn. (37) with $\sin^2 \psi$ calculated from the data given in figure 33 (top) and variation in a_2 of Eqn. (38) with $\sin 2\psi$ from which values of the shear stresses σ_{13} and σ_{23} can be obtained (bottom). The lines represent a linear least-squares fit through the data. In these plots, the curvature or deviation from linearity is due to texture and/or stress gradients (see text).

Measurements were carried out on the (220) plane for film E8.7e and on the (321) plane for sample E10.4e, and typical sets of data are shown in figures 33 and 35. As can be seen from these plots, ψ -splitting, i.e. the plot separating into two branches for positive and negative ψ inclinations, is not an important feature of the data and the assumption of a biaxial stress state, as described in section 7.1, is subsequently justified. The fact, that there is nevertheless a small ψ_+ or ψ_- dependence, may indirectly be related to the preferential orientation, leading to a different position of θ_p for the ψ_+ or ψ_- case. This occurs, because grains with planes slightly tilted from the orientation dictated by Bragg's law can contribute for a given θ to the diffracted beam due to the finite X-ray beam dimensions and the sample curvature. Having a strong texture, the number of crystallites, which reflect as a consequence of the above mentioned effects, can be larger than the number of those in the nominal diffraction condition. As this has opposite effects on the position of the Bragg peak measured at opposite tilts, different values of $d_{hkl}(\psi_+)$ and $d_{hkl}(\psi_-)$ are obtained [120].

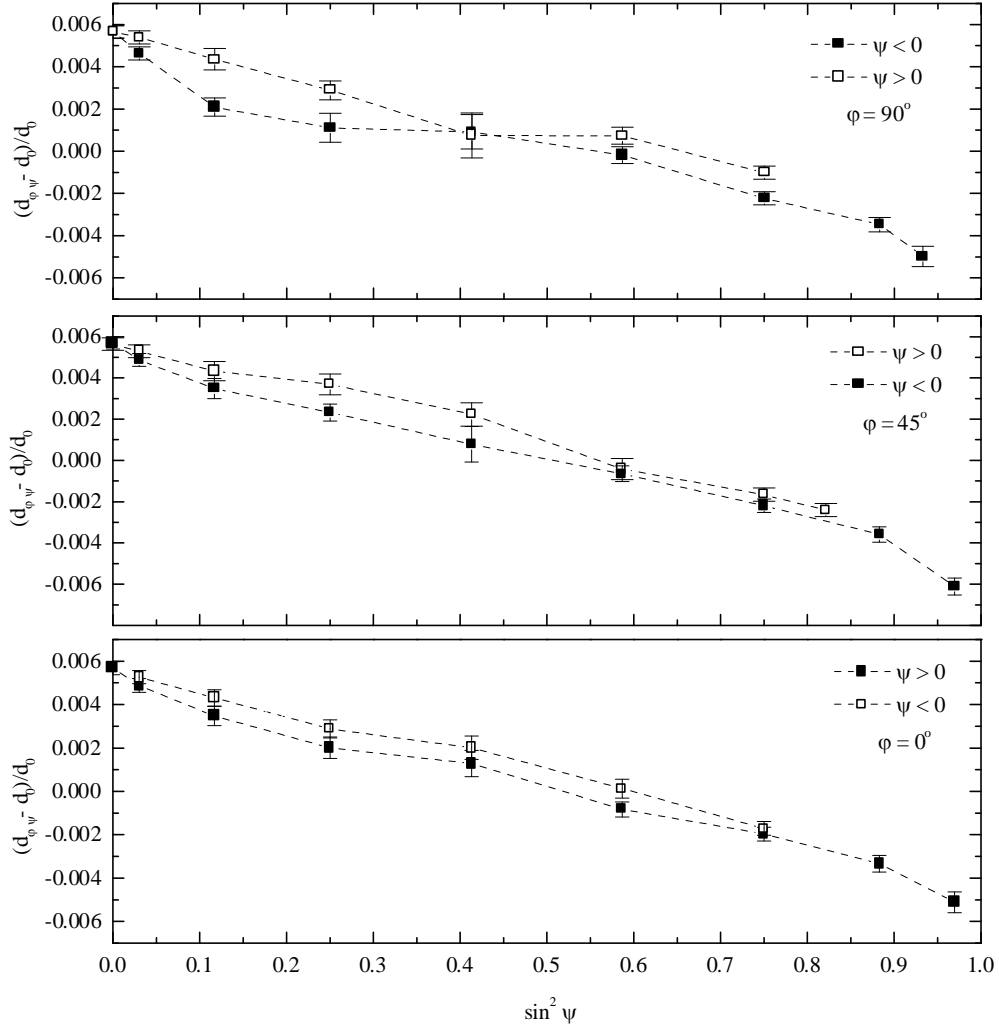


Figure 33. ε_{33} vs. $\sin^2 \psi$ profiles of a magnetron-sputtered niobium film grown on oxidised copper. The (220) reflection was measured with nickel filtered Cu radiation.

The accuracy of the analysis was indeed reduced by the strong texture (in the case of sample E8.7e), which also caused the Bragg reflections from the (110) planes to be significantly depressed at several ψ -tilt values (Fig. 34). The resulting oscillatory form of the plots causes significant errors in b_m , obtained from least-squares linear fits to the data. This is shown in figure 32 (bottom figure), where the slope, here defining the component σ_{I3} , is small and curvature effects are dominant, thus not allowing a sensitive determination of possible small finite terms. In the case of sample E10.4e, these terms could be determined with higher precision, but were found to be negligible anyway.

The complete stress tensor obtained for a niobium film sputter-deposited on oxidised copper is finally given by

$$\sigma_{ij} = \begin{vmatrix} -721 \pm 54 & -49 \pm 51 & -20 \pm 25 \\ -49 \pm 51 & -760 \pm 51 & -38 \pm 16 \\ -20 \pm 25 & -38 \pm 16 & 0 \end{vmatrix}.$$

These data, obtained from the strongly textured film E8.7e were interpreted using the average elastic constants of $116 \pm 8 \text{ GPa}$ and 0.47 ± 0.03 , obtained for the *Young's* modulus and *Poisson's* ratio, as described in chapter 6 and section 7.1. The diffraction elastic constants X_I (E8.7) and

X_2 (E8.7) are therefore 0.0127 ± 0.0009 and $-0.0041 \pm 0.0004 \text{ GPa}^{-1}$, respectively. The equilibrium lattice spacing, $d_0 = 1.1681 \pm 0.0004$, used for the stress evaluation in both types of film, was taken from the precise measurement of the equilibrium lattice constant, a_0 , of the free-standing film E8.7e.

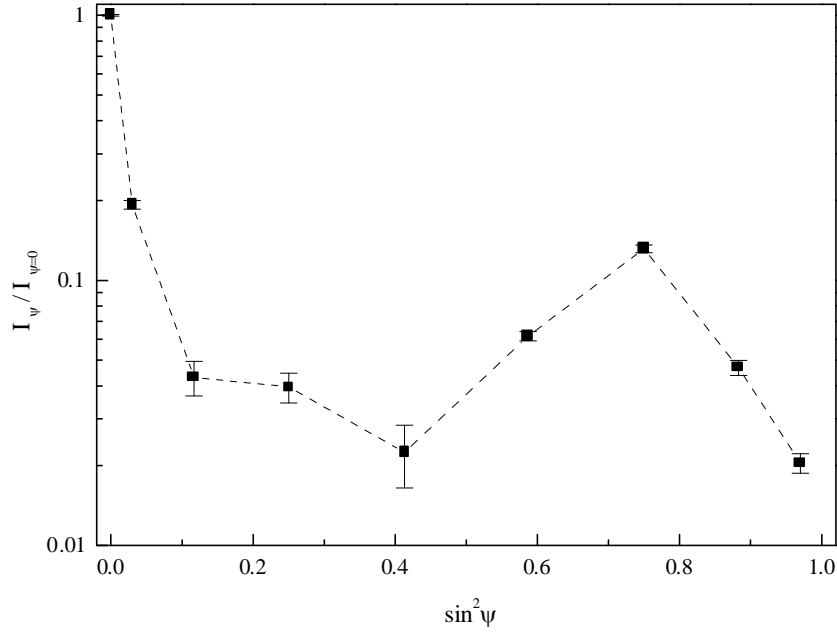


Figure 34. Normalised integral intensity of the (110) diffraction peak of a niobium film grown on oxidised copper as a function of the ψ -angle at $\varphi=45^\circ$. A random orientation would give a straight line.

The data suggest a simple biaxial compressive stress situation to be present in films sputter deposited on an amorphous substrate under the specified conditions, since the shear stresses σ_{13} and σ_{23} are practically within the error estimate. No stress is introduced by a lattice mismatch between the film and the substrate as this would introduce both lattice distortion [151] and shear stresses thereto. The in-plane rotationally symmetrical stresses, as defined by $\sigma_{11} \cong \sigma_{22}$, are known to be a common feature of PVD coatings [63]. The compressive stress state is a consequence of thermal contraction differences between copper and niobium and of growth stresses resulting from impinging film-forming atoms and energetic neutrals of the plasma-supporting noble gas. The latter mechanism is supported by the observed increase of the compressive stress state when a negative substrate bias voltage is applied [152, 153], associated with enhanced incorporation of noble gas and an increasing dispersion of the lattice parameter a_{hkl} [63, 155] as observed for the neon-incorporated films (chapter II/4).

The oscillatory form of the data can be attributed to stress gradients in the film and differences in the X-ray crystallographic constants.

The complete stress tensor in the specimen coordinate system obtained for a niobium film sputter-deposited on non-oxidised copper is

$$\sigma_{ij} = \begin{vmatrix} -644 \pm 70 & -133 \pm 68 & -15 \pm 6 \\ -133 \pm 68 & -499 \pm 50 & 19 \pm 9 \\ -15 \pm 6 & 19 \pm 9 & 0 \end{vmatrix}.$$

For this film, it is assumed that the diffracting population consists of a sufficient number of randomly orientated grains at all ψ -tilts, and a volume average of the diffraction elastic constants was calculated for a comparison with experimental values.

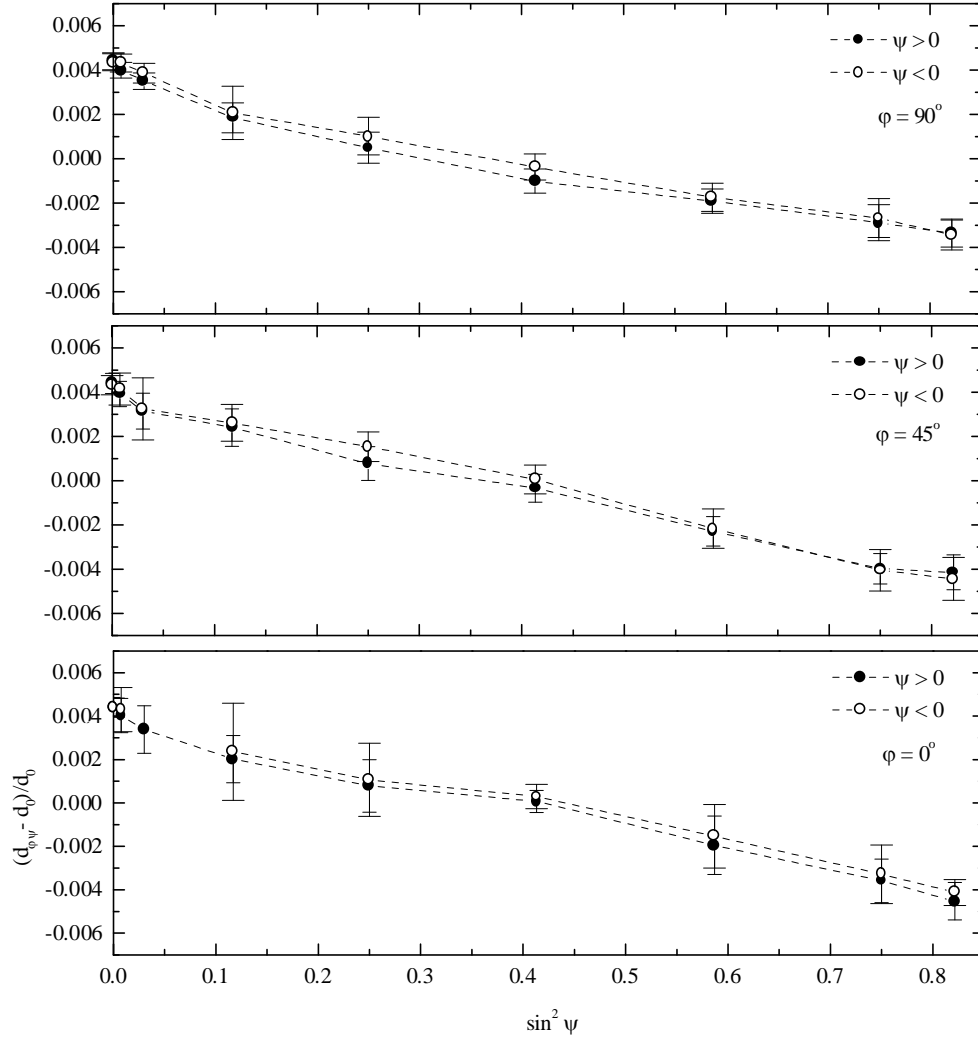


Figure 35. ε_{33} vs. $\sin^2 \psi$ profiles of a magnetron-sputtered niobium film grown on oxide-free copper. The (321) reflection was measured with nickel filtered Cu radiation.

A number of methods were employed to calculate macroscopic averages of elastic constants for polycrystalline materials from the single crystal data [156-158], which were applied to calculate the XEC's by averaging over a particular set of grains [138, 139]. Both constant strain and stress conditions were analysed by *Voigt* [156] and *Reuss* [157], respectively. In the *Voigt* limit it is assumed that a stress at the boundary of a polycrystalline material causes all composite grains to suffer the same uniform strain, regardless of orientation. Expressed in terms of X_1 and X_2 , and using elastic compliance values in matrix notation, the *Voigt* values in cubic systems are [139],

$$X_{1(V)} = \frac{5(S_{11} - 2S_{12})S_{44}}{6S_0 + 5S_{44}}, \quad (41)$$

and

$$X_{2(V)} = \frac{2S_0(S_{11} + 2S_{12}) + 5S_{12}S_{44}}{6S_0 + 5S_{44}}. \quad (42)$$

In the *Reuss* approximation, on the other hand, it is assumed that the stress in all grains of a polycrystalline material is equal to the average stress applied to the material. But this means that grains with different crystallographic directions along the stress axis suffer different strains

due to elastic anisotropy and the values of $X_{I(R)}$ and $X_{2(R)}$ will depend on the crystallographic direction considered.

This dependence is expressed by the orientation term, Γ , which is also called crystallographic parameter. Γ is a function of hkl only and is given by,

$$\Gamma = \frac{h^2 k^2 + k^2 l^2 + h^2 l^2}{(h^2 + k^2 + l^2)^2}. \quad (43)$$

The Reuss averages for the elastic constants can be shown to be

$$X_{I(R)} = S_{11} - S_{12} - 3\Gamma S_0, \quad X_{2(R)} = S_{12} + \Gamma S_0 \quad (44)$$

with

$$S_0 = S_{11} - S_{12} - \frac{1}{2} S_{44}. \quad (45)$$

The calculations of the orientation dependent, polycrystalline diffraction elasticity constants in the *Voigt* and *Reuss* limit have been performed, taking the elastic compliance values from table 14 and using the expressions given above. The latter were taken from [139], since the original papers [156, 157] were not available. Although equations (41), (42) and (44) were not verified in detail because of the time consuming calculations, they were checked by calculating X_I and X_2 for different materials and comparing them to experimentally determined data [159]. In agreement with the *Neerfeld-Hill* limit [160], it was found that the average of the *Voigt* and *Reuss* values were close to the experimental values. The *XEC*'s calculated in this way for the (211), (110) and (321) planes of polycrystalline niobium are 0.0139 and -0.0040 GPa^{-1} for X_I and X_2 , respectively. These values may be compared with $(1+\nu)/E = 0.0115 \pm 0.0014$ and $-\nu/E = 0.0036 \pm 0.0006 \text{ GPa}^{-1}$ calculated using the elastic constants of $126 \pm 15 \text{ GPa}$ and 0.45 ± 0.05 , as determined experimentally. The reasonable agreement between theoretical and experimental data gives confidence in the method of indirect estimation of the *XEC*'s by separate measurements of E and ν . It should, however, be noted, that also the film E10.4 exhibits a weak texture, which will introduce errors when calculating the *XEC*'s by taking a random distribution of grains in the polycrystalline film, as commonly assumed in all those calculations. The stress tensor presented above for sample E10.4e was obtained by taking the calculated *XEC*'s. Using the experimental values increases the stress components by approximately 10-15%.

It can be seen that the principal compressive stress components are significantly smaller for a niobium film grown on non-oxidised copper than those obtained on a film grown under identical conditions on an oxidised copper substrate. This has already been observed in section 7.1 from the stress measurements on both types of film in the *Seemann-Bohlin* configuration. The reason is the interplay of three stress generating mechanisms. Two mechanisms, the difference in the thermal expansion coefficient between niobium and copper causing thermal stress, and the continuous bombardment of the growing film by niobium and argon atoms giving a large contribution to growth stresses, have already been discussed. There is no reason to believe that these stresses should be different for a film grown on non-oxidised copper, if the sputtering parameters do not change. However, it was shown that the crystal planes in a film grown on non-oxidised copper try to align with the crystal planes in the substrate and this will introduce stresses in the niobium film due to lattice misfit [163]. For a cubic structure of film and substrate, having lattice parameters a_f and a_s respectively, this elastic misfit strain, ε_f , required to make the film epitaxial with the substrate, upon which it is deposited, is defined as

$$\varepsilon_f = \frac{a_s - a_f}{a_s}, \quad (46)$$

with $\varepsilon_f = 0.0174$ for the heteroepitaxial system niobium on copper, which represents a considerable mismatch in heteroepitaxial structures. The lattice mismatch is accommodated by a uniform strain in the plane of the film, also called coherency strain, and this typically leads to biaxial stresses in the film. Essentially all of the elastic accommodation must take place in the film, because the substrate, being three orders of magnitude thicker than the film, is essentially rigid.

Strained layer epitaxy results in lattice distortion, i.e. a conversion to a non-cubic structure with a tetragonal cell [151] as further indicated by the non-zero shear stress component σ_{12} . If the lattice constant of the layer material is smaller than that of the substrate, the cell must be stretched in the in-plane direction and a tensile coherency strain builds up. This tensile film strain component is observed to remain after substrate removal (chapter II/3) and can be calculated according to equation (34), taking the measured lattice constant, $3.2995 \pm 0.0013 \text{ \AA}$ of film E10.4e and the unstressed lattice parameter, $3.305 \pm 0.001 \text{ \AA}$. The result, $\sigma_{11} = \sigma_{22} = +220 \pm 60 \text{ MPa}$ gives the magnitude of the difference of the normal in-plane stress components between both types of film. According to equation (46) one may expect larger stresses to build up, but most of them are relaxed by plastic flow in the film through dislocation nucleation and motion associated with a recovery of strain energy.

8. Effective crystallite size and microstrain

8.1 The Williamson-Hall method for microstrain analysis

From the broadening of diffraction lines, information was obtained on the imperfect crystalline structure in terms of the amplitude of the fluctuations of residual strain $\delta d/d$, also called microstrain, ε , and the effective crystallite (domain) size, D_{eff} . The microstrain is caused by the presence of dislocations, imbedded atoms or composition fluctuations. A Fourier analysis of the {110} line profiles, based on the theory of *Warren and Averbach* [164] was performed, since this method is considered to give the most accurate results. An alternative method to estimate the root mean square strain $\langle \varepsilon^2 \rangle^{0.5}$ and D_{eff} from XRD line broadening, is the so-called *Williamson-Hall* plot [165] of integral breadth β_w against $\sin \theta$,

$$\beta_w = K / < D_{eff} > + 5L \langle \varepsilon^2 \rangle^{0.5} \sin \theta / \lambda)^q. \quad (47)$$

In the absence of microstrain, this formula reduces to the *Scherrer* relation between peak broadening and crystallite size. In the limit $D_{eff} \rightarrow \infty$, i.e. neglecting the first term on the right hand side, Eqn. (47) can be obtained by differentiating the Bragg relation $\lambda = 2d \sin \theta$. The constants K , L and q depend on the approximations made on the peak shape and are unity, if both strain and size broadening correspond to Cauchy distributions, as is frequently assumed in the literature (original *Williamson-Hall* plot) [63, 166-168]. This method, like all other approaches to calculate the microstrain contribution to peak broadening, depends on the fact that strain is a function of the order of reflection, while crystallite size is not. It is standard practice, to use two orders of the same family of planes to separate D_{eff} from the mean square strain, although in polycrystalline materials, all reflections with a similar orientation term Γ may be used. Unfortunately, if growth faults occur on the (110) planes, the two orders of reflection that are used in making such a plot can be affected differently by faulting, and the slopes of the lines will be proportional to $\langle \varepsilon^2 \rangle^{0.5}$ only after the subtraction of a small correction term [169].

The situation illustrated in figure 36, like others referring to different samples and different inclinations, ψ , is in agreement with equation (47), and the slope of the linear fit directly provides an approximate value of $\langle \varepsilon^2 \rangle^{0.5}$. Despite principal limitations of the above method, the basic microstructural differences between the films are well visualised. The results of this analysis let suppose that peak broadening in magnetron-sputtered niobium films is dominated by microstrain (see also references 63 and 140). However, it was also found that a reasonable estimation of the effective crystallite size is not possible from the data, since the intercept value is too close to the origin in the *Williamson-Hall* plot, resulting in large errors on D_{eff} and in sizes between 70 and 400nm. This magnitude is in sharp contradiction with the values obtained from the Fourier analysis and would assume that films can be deposited without any growth faults and dislocations. This difficulty has also been realised by several authors [31, 170], who stressed the need for a Fourier analysis to obtain reliable values of D_{eff} .

The data presented in figure 36 indicate a higher dislocation density and/or a higher concentration of embedded atoms, present in standard films. An important, but expected result, which is also shown in this figure, is, that no relaxation of the microstrain broadening occurs upon dissolution of the substrate.

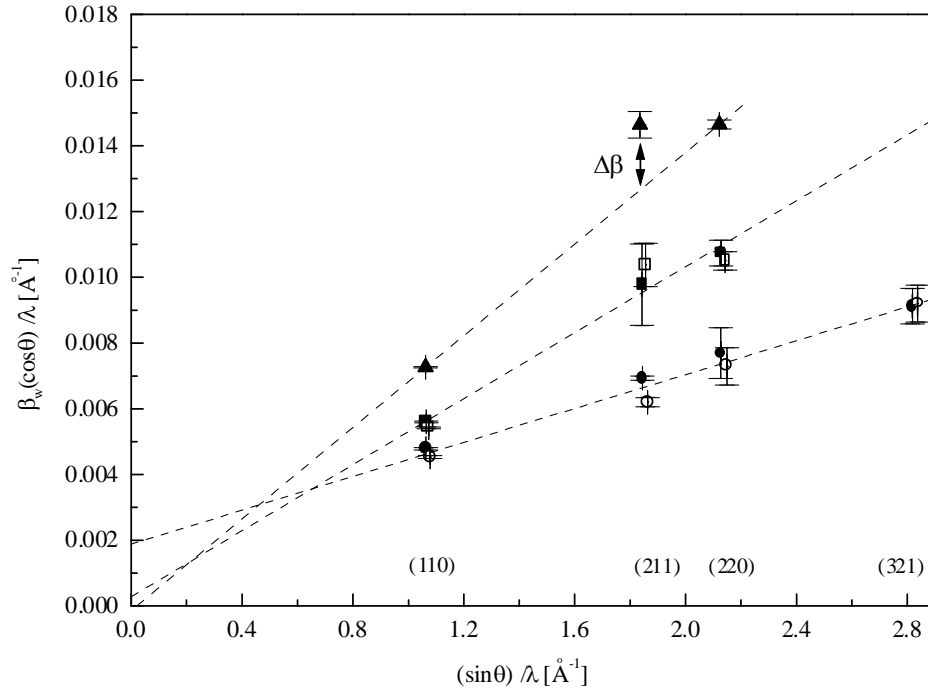


Figure 36. The Williamson-Hall plot constructed from the *BB* diffraction data of sample E10.4e (circles), E8.7e (squares) and A3 (67% neon in the discharge; triangles). The open symbols refer to the same film after substrate dissolution. The root mean square microstrain, as given from the slope of a linear fit through the points, is 0.0026 ± 0.0002 and 0.0049 ± 0.0004 for sample E10.4e and E8.7e, respectively. The effect of instrumental broadening on the peak profile was not considered and causes an additional, but small error ($\sim 2\%$) on the values given above.

Since the values of $\langle \varepsilon^2 \rangle^{0.5}$, obtained by Fourier analysis, show qualitative agreement with those obtained from the *Williamson-Hall* plot (see next section), the latter method was used to explore the evolution of microstructural defects with increasing neon content in magnetron-sputtered niobium films. The results are summarised in figure 37.

The root mean square microstrain in neon implanted films was evaluated from the (110)-(220) reflection pair only, since a systematic XRD line broadening anisotropy was observed (Figure 36). Straight lines were drawn through the (110)-(220) points in the *Williamson-Hall* plots for each sample. The differences, $\Delta\beta$, between the calculated ordinate values for (211) and the interpolated values, were found to remain consistently positive and to increase with increasing neon concentration. The absolute values of $\Delta\beta$ are too large to be explained by an increased stacking fault population along (211)⁽¹⁾. In chapter II/4, this anisotropy has already been reported for the lattice parameter, a_{\perp} , when calculated from different reflections with identical elastic constants. There, it has been suggested that different types of lattice defects, caused by mutual interactions of implanted neon and argon and an inhomogeneous distribution of the noble gas, are responsible for this anisotropy. The same effect, namely a higher concentration of substitutionally dissolved neon, which is not clustered along (211), may cause a higher defect density and consequently more microstrain on this crystallographic plane. Unfortunately, no data are available for the film, sputter deposited in pure neon as discharge gas, since the absolute intensities of the reflections were drastically reduced and too small for a reliable estimation of the integral breadth.

⁽¹⁾Although stacking faults in bcc metals may broaden the individual reflections to different extents, they do not lead to significant shifts of the peaks [169, 171].

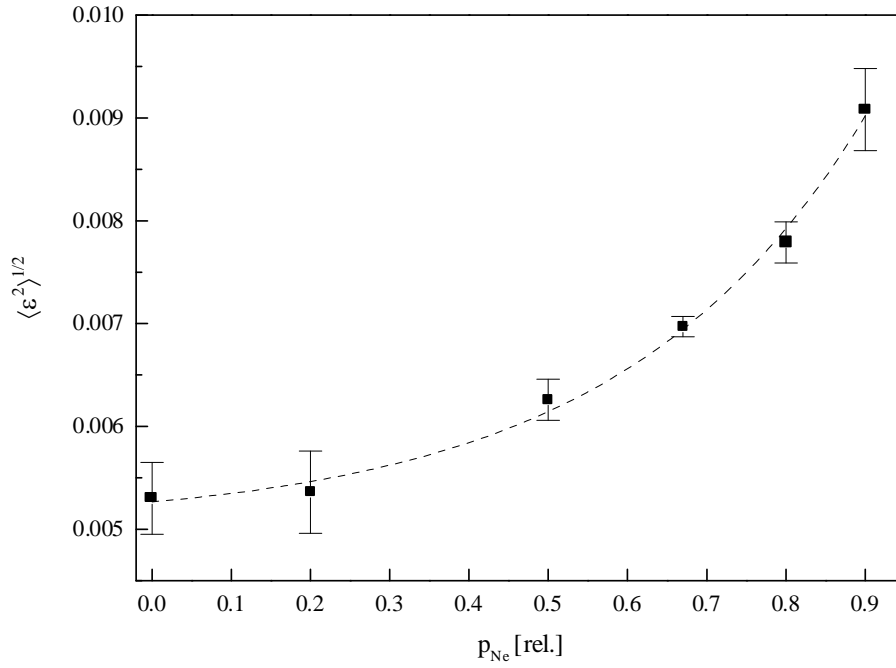


Figure 37. The dependence of the root mean square microstrain in niobium films on the neon partial pressure in the discharge. The latter quantity can directly be related to the neon concentration in the film by means of table 5. The line is an exponential fit to the data, indicating a linear dependence of $\langle \varepsilon^2 \rangle^{0.5}$ on the neon concentration. The point at $p_{Ne} = 0$ represents an average value over different films, grown under same conditions in the sample system with argon as discharge gas. The errors are calculated from the uncertainties on the absolute and integrated intensities of reflections, as determined from a modified Lorentzian peak fit.

8.2 Fourier analysis of diffraction peaks

8.2.1 Theoretical considerations and experimental procedure

To perform the Fourier analysis, all diffraction peaks were corrected to resolve the true shape of the $K\alpha_1$ peak by expressing the observed profile $I(\theta)$ as

$$I(\theta) = I_{\alpha_1}(\theta) + 0.5I_{\alpha_2}(\theta - \Delta), \quad (48)$$

where I_{α_1} and I_{α_2} denote the α_1 and α_2 profile respectively, Δ is the angular doublet separation (taken as a constant on a $\sin\theta$ scale) and the term 0.5 describes the ratio of the intensities of $K\alpha_1$ to $K\alpha_2$. Equation (48) was expressed in terms of the modified Lorentzian function (Eqn. 7) to allow a doublet separation through a global fit to the experimentally observed line profile [34].

The LP corrected $K\alpha_1$ line profile of the specimen, h , is a convolution of the desired structurally broadened profile, f and the standard profile, g , which describes the line broadening owing to the non-ideal geometry of the diffractometer and the wavelength distribution. For evaluation of the g profile, an annealed bulk niobium sample with a grain size of about 100 μ m has been measured and care has been taken to use the same slits as for the measured h profiles. Deconvolution of the h profiles was accomplished by [172],

$$A(n) = \frac{H_r(n)}{G_r(n)} \text{ and } B(n) = \frac{H_i(n)}{G_r(n)}, \quad (49a,b)$$

where $A(n)$ and $B(n)$ are the cosine and sine coefficients of the structural broadening function f and $H_r(n)$, $(H_i(n))$ and $G_r(n)$ are the cosine (sine) coefficients of the profiles h and g , respectively. The sine coefficients, G_i , do not appear in these equations, since the measured g function is symmetrical around $2\theta_p$. Figure 38 shows the measured (220) peak of sample E8.7e and the functional representation of the specimen line profile after doublet separation and LP correction. The measured line profile of a (220) oriented niobium grain (insert, bottom figure) is also shown.

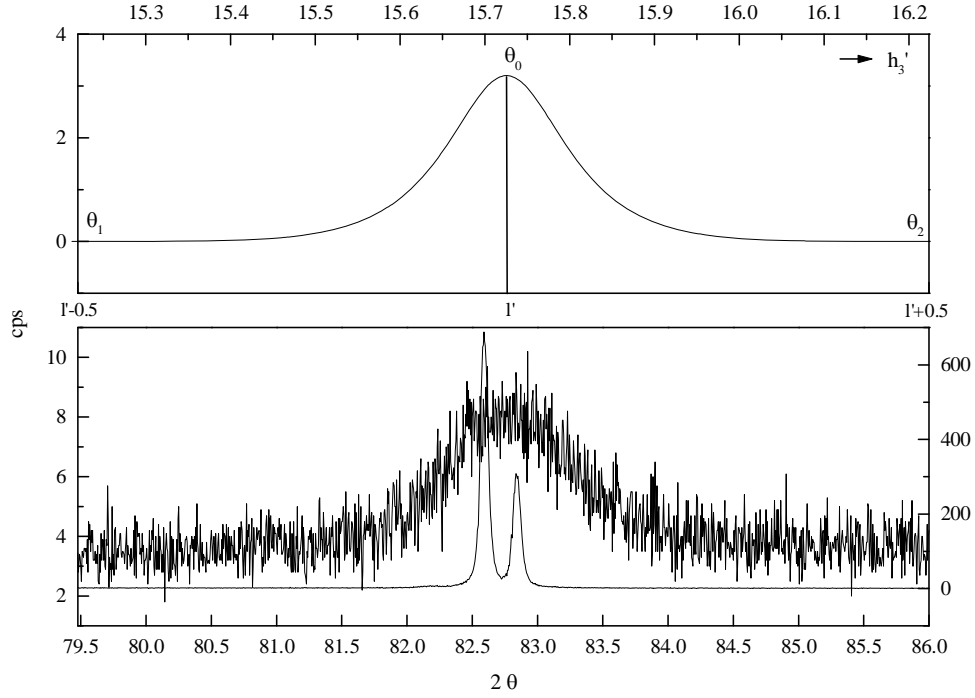


Figure 38. (220) peak from a niobium film deposited on oxidised copper (bottom figure; $\psi = 60^\circ$) and the functional representation of the measured line profile after doublet separation, LP and background correction (top figure; see text). The response of a (220) orientated grain in the annealed niobium standard (measured at $\psi = 0$) is inserted in the bottom figure (ordinate scale on the right axis).

The notations used in figure 38 and in the following part of this chapter follow those given by *Klug and Alexander* [31] in their generalisation of the *Warren-Averbach* theory [164].

In the *Warren-Averbach* theory of separating size-strain broadening, each reflection is considered as a $(00l)$ reflection from a crystal having orthorhombic axis a_1 , a_2 , and a_3 . Regions in the sample, which scatter the X-rays coherently, are designated as domains, and each domain is thought to consist of columns of unit cells normal to $(00l)$ planes. Then it can be shown [173] that, after correction of instrumental effects, the diffracted intensity $P'(2\theta)$, which in fact is the intensity integrated over the number of grains oriented to diffract and the area of the receiving surface, can be written in terms of the corrected coefficients,

$$A(n, l) = \left(\frac{N_n}{N_{h_3'}} \right) \langle \cos 2\pi l z_n \rangle, \quad B(n, l) = - \left(\frac{N_n}{N_{h_3'}} \right) \langle \sin 2\pi l z_n \rangle, \quad (50a, b)$$

where z_n is the difference between the displacements of two unit orthorhombic cells, n cells apart in a column, and l is the order of the reflection. Usually, z_n is replaced by the strain $\varepsilon_n = z_n/n$. N_n is the average number per column of pairs of unit cells a distance n cells apart (the average being over all columns in the region under the beam) and $N(h_3')$ is the average number

of cells in a column perpendicular to the reflecting planes. The averages $\langle \cos 2\pi lz_n \rangle$ and $\langle \sin 2\pi lz_n \rangle$ are averages over pairs that are n th neighbours in all columns of the sample.

Since the sine coefficients are only about a few percent of the cosine coefficients, even when there is a high concentration of twin faults [171, 175], they are not considered in the present analysis.

Proceeding with the analysis of the cosine coefficients, $A(n, l)$, one can write equation (50a) as the product of a ‘size’ coefficient, which depends only on the column length and $\langle \cos 2\pi lz_n \rangle$, which depends only on the local distortion in the crystallite and is thus a ‘distortion’ coefficient,

$$A(n, l) = A^S(n)A^D(n, l), \quad (51)$$

where $A(0, l) = A^S(0) = A^D(0, l) = 1$, as only the shape of the peak is important. The ‘size’ Fourier coefficient⁽¹⁾, $A^S(n)$, is real and independent of the order l of the reflection, in contrast with the ‘distortion’ coefficient $A^D(n, l)$. Under the condition that l and n are sufficiently small, so that the product lz_n is also small, one can approximate $A^D(n, l) = \langle \cos 2\pi lz_n \rangle$ by a power series expansion, neglecting terms in higher orders of l^2 . Substitution of the power series expansion in equation (50a) and making the substitution $z_n/n = \varepsilon_n$, yields,

$$A(n, l) \cong \left(\frac{N_n}{N_{h_3'}} \right) - \left(\frac{N_n}{N_{h_3'}} \right) 2\pi^2 l^2 n^2 \langle \varepsilon_n^2 \rangle. \quad (52)$$

Equation (52) is the fundamental expression in the theory of *Warren and Averbach* and allows a separation of the effective size and the mean square value of the strain components of peak broadening by plotting $A(n, l)$ against l^2 .

For the determination of the Fourier coefficients, the profiles were converted to an h_3' axis, which is along the normal of the diffracting planes,

$$h_3' = 2a_3' \frac{\sin \theta}{\lambda} \quad (53)$$

where a_3' is a fictitious quantity of the lattice constant of the orthorhombic cell, normal to the diffracting planes. In practice, a_3' is determined for each peak from the point, where the tails reach the background. Hence, the Fourier series representing a $(00l')$ peak, is in terms of a period, which is the inverse of the fictitious cell parameter a_3' . In general, coefficients for different peaks are compared for the same value of $na_3' = L$ rather than for the same harmonic number n . L is the true, undistorted distance between the pair of cells in a column perpendicular to the diffracting planes. Distortion changes this distance by $\Delta L = a_3' z_n$ and the calculated strain is $\Delta L/L$ in the a_3' direction averaged over the distance L .

At the peak position, θ_p , $h_3' = l'$. An interval in h_3' extending from $l' - 0.5$ to $l' + 0.5$ is then selected, large enough to span the entire observable line profile. With the angles θ_1 and θ_2 corresponding, respectively, to the limits $l' - 0.5$ and $l' + 0.5$ (Fig. 38) and substituting these limits into equation (53), one gets,

$$\frac{l}{2} = \frac{2a_3'}{\lambda} (\sin \theta_2 - \sin \theta_0). \quad (54)$$

The fictitious cell edge, a_3' , is accordingly calculated from the high and low angle positions of a $(00l')$ peak, rather than from the distance between orders. Having determined the normalised Fourier coefficients for at least two orders of a reflection, a separation of size and strain

⁽¹⁾The term size means in fact effective size, which comprises contributions from domain length and faulting.

broadening based on equation (52) can be performed. The present analysis is restricted to the reflection pair (110)-(220), which is the only set of multiple orders available. The normalised Fourier cosine coefficients $A(n,l)$, derived from the corrected line profile of the (110) and (220) peaks of sample E8.7e and E10.4e, are plotted in figure 39 as a function of a distance L along a column, perpendicular to the reflecting planes. In addition, the coefficients of the standard are also shown. Since the latter are close to unity for small values of L (for the given slit geometry), the correction for instrumental broadening, according to equation (49a), does not change the sample coefficients significantly.

In the experimental $A(n,l)$ and $A^S(n)$ curves, a small bend near $n = 0$ is observed (Figure 39). This so-called ‘Hook’ effect is often attributed to an overestimation of the background⁽¹⁾ [179, 180] and to the truncation of the line profile, which necessarily occurs, because the range of the observations is finite (a profile of inherently infinite extent is truncated at arbitrary points, which are scaled to have coordinates -0.5 and $+0.5$). It has been suggested by several authors [180-182] to renormalise the $A(n,l)$ data by extrapolation of the straight portion of the curve (values from beyond $n = 2-4$), to obtain a good estimate of the true $A(0,l)$.

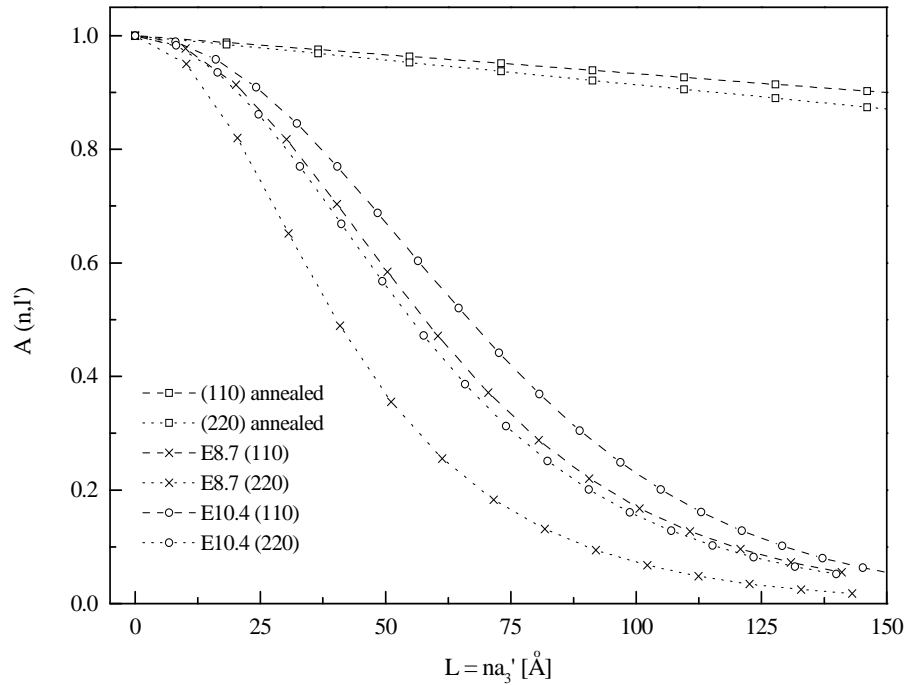


Figure 39. Fourier cosine coefficients from niobium films and from an annealed niobium standard.

Whereas a ‘Hook’ effect in the $A^S(n)$ vs. L curve is indeed impossible⁽²⁾ and should be corrected for, the same effect in the $A(n,l)$ data need not necessarily be the result of an experimental error and can be due to the strain present in the sample. Figure 41 illustrates the effect of the ‘Hook’ correction on the obtained values of the mean square strain.

Since $d = a_3/l = a_3'/l'$, where d is the interplanar spacing of reflecting planes, equation (52) can be transformed for cubic crystals to the form,

$$A(n,l) \cong \left(\frac{N_n}{N_{h_3'}} \right) - \left(\frac{N_n}{N_{h_3'}} \right) 2\pi^2 (h^2 + k^2 + l^2) \frac{a_3'^2 n^2}{a_0^2} \langle \varepsilon_n^2 \rangle. \quad (55)$$

⁽¹⁾The truncation of the series expansion after the term l^2 can also introduce a small error in the $A^S(n)$ curve, as discussed by *M. Wilkens* [178].

⁽²⁾Differentiation of equation (57a) (section 8.3) gives $p(n)/N(h_3')$, which can never be negative.

Therefore, a plot of $A(n,l)$ vs. $(h^2+k^2+l^2)$ for a fixed value of n (or L) is a convenient way to perform the separation of $A(n,l)$ into the effective particle size coefficients $A^S(n)$ and the distortion coefficients $A^D(n,l)$. In figure 40, such a plot is presented, using the data for the (110) and (220) peak at $\psi = 60^\circ$ of sample E10.4. The mean square values of the strain, $\langle \varepsilon_{(L)}^2 \rangle$, averaged over distances in the [110] direction, are calculated from the slope of the curves, and the $l^2 = 0$ intercepts define $N_n/N(h_3')$. Measurements were performed with the crystallographic planes inclined at 60° and 0° with respect to the surface of the substrate.

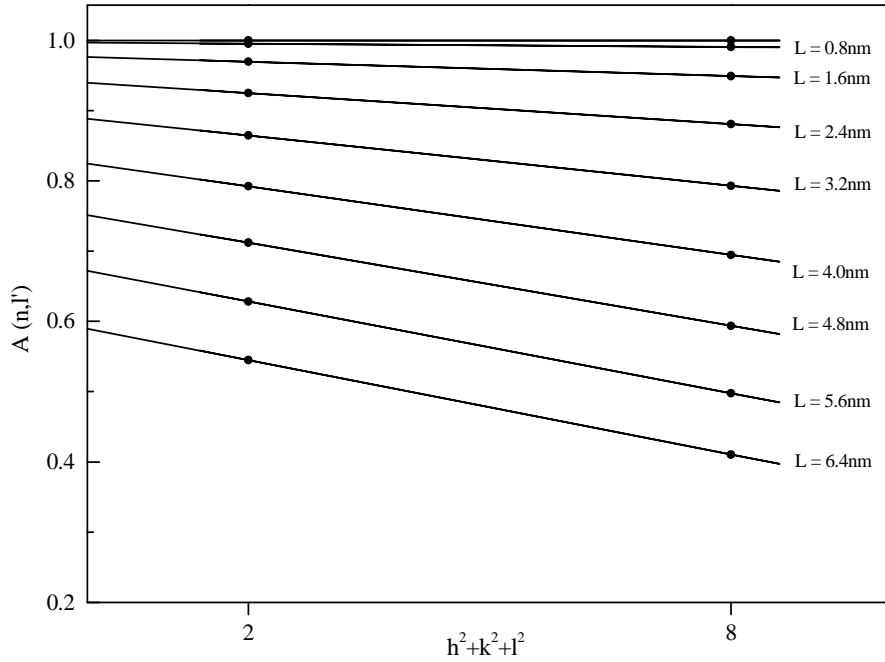


Figure 40. Plot for separating the effective crystallite size and the distortion effects for the (110)-(220) multiple of sample E10.4e, recorded at $\psi = 60^\circ$. The data, which are shown here were not corrected for the 'Hooke' effect.

8.2.2 Analysis of microstrain

Figure 41a and 41b show the strain $\langle \varepsilon_{(L)}^2 \rangle^{1/2}$ vs. the averaging distance, L , for niobium films grown on oxidised and non-oxidised copper substrates, corresponding to sample E8.7e and E10.4e, respectively. The values of the 'Hook' corrected mean square strains at small L distances are highly sensitive to slight changes in the Fourier coefficients, indicating that the distortions are inhomogeneous and possibly greater in the smaller domains. On the contrary, the not corrected strains do not slope as steeply, but indicate the same effect to be significantly present for sample E8.7e. This behaviour will be analysed in detail below. Not too much emphasis should be put upon the magnitudes of the strains averaged over distances smaller than 20\AA , since the errors involved in these data are high. For L larger than $\sim 30\text{\AA}$, the 'Hook' corrected values agree within a few percent with the strain obtained from the non-corrected data. Table 17 summarises the results of strain calculations averaged over 30, 60, 90 and 120\AA , respectively. Results obtained from studies performed by Vion [114] on magnetron sputtered niobium films, grown on flat copper substrates in the sample system, are included in table 17.

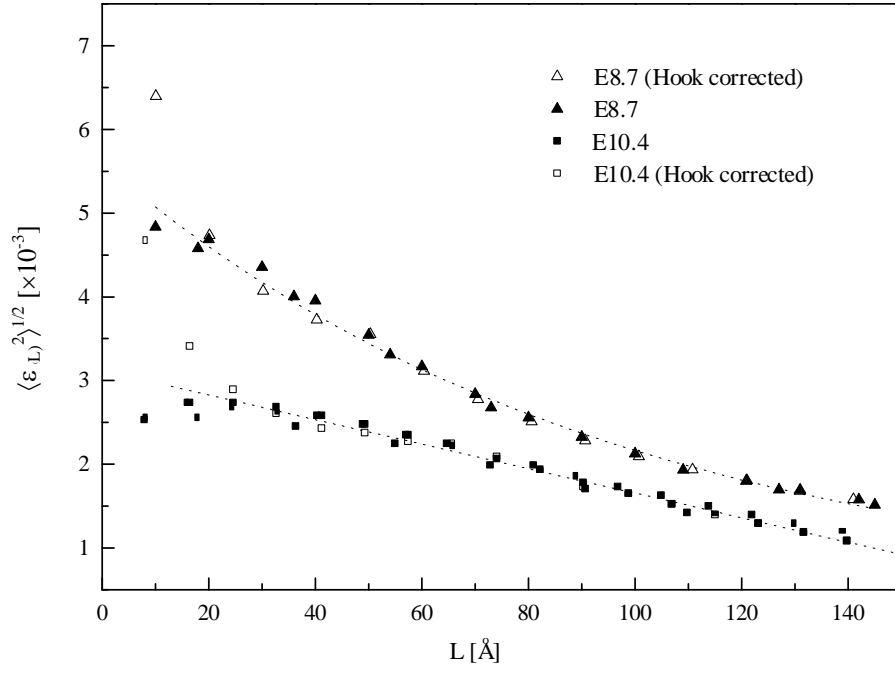


Figure 41a. The variation of $\langle \varepsilon_{(L)}^2 \rangle^{1/2}$ as a function of L along [110] inclined at 60° from the surface normal (the lines are drawn to guide the eye).

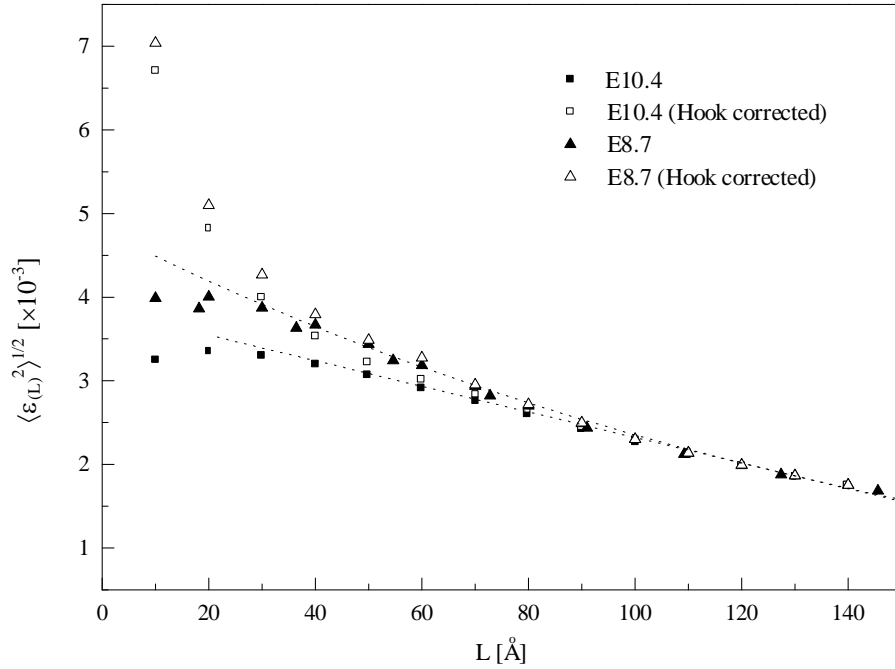


Figure 41b. The variation of $\langle \varepsilon_{(L)}^2 \rangle^{1/2}$ as a function of L along [110] perpendicular to the surface.

The feature, that strains rise sharply as L approaches zero, may in general indicate the presence of point defects with sizes of the order of a few \AA , like embedded atoms or vacancies, and gives evidence for a non-uniform and localised nature of the strain in the films [164].

Measurements on filings of many bcc materials [183] have shown that the mean square strains are generally inversely proportional to the distance L in the range over 20 to 100\AA . In these cold-work distorted materials, where $\langle \varepsilon_{(L)}^2 \rangle$ comes mainly from correlated atomic displacements, resulting from strain fields around dislocations, $\langle \varepsilon_{(L)}^2 \rangle^{1/2} \cong G_{(hkl)} L^{-k}$, with $k = 0.5$ has theoretically been justified [183, 184] and experimental data on Ta, W, Nb, Cr and Mo

filings [185] and on electroplated Ag [186] have proven k to take an average value of 0.46 ± 0.09 .

Sample	ψ [°]	$\langle \epsilon_{(30)}^2 \rangle^{1/2}$	$\langle \epsilon_{(60)}^2 \rangle^{1/2}$	$\langle \epsilon_{(90)}^2 \rangle^{1/2}$	$\langle \epsilon_{(120)}^2 \rangle^{1/2}$
E10.4e	60	2.63 ± 0.09	2.32 ± 0.04	1.76 ± 0.06	1.31 ± 0.05
E10.4e	0	3.65 ± 0.08	2.96 ± 0.04	2.44 ± 0.02	1.98 ± 0.01
E10.4e $_{350^\circ\text{C}}$	60	2.67 ± 0.22	2.33 ± 0.06	1.77 ± 0.03	1.32 ± 0.02
E10.4e $_{350^\circ\text{C}}$	0	3.44 ± 0.21	2.79 ± 0.03	2.29 ± 0.02	1.89 ± 0.01
E8.7e	60	4.21 ± 0.14	3.14 ± 0.03	2.30 ± 0.02	1.80 ± 0.01
E8.7e	0	3.94 ± 0.24	3.22 ± 0.04	2.47 ± 0.03	2.00 ± 0.02
E8.7e $_{350^\circ\text{C}}$	60	3.80 ± 0.05	2.86 ± 0.02	2.09 ± 0.02	1.60 ± 0.01
E8.7e $_{350^\circ\text{C}}$	0	3.73 ± 0.35	3.06 ± 0.08	2.38 ± 0.03	1.91 ± 0.01
Ref. [114]*	0	3.5	3.1	2.7	---
Ref. [114]	0	3.8	3.1	2.7	---

Table 17. Mean square microstrain calculations (values $\times 10^{-3}$). Data from [114] marked with * are obtained after UHV heat treatment of the Cu substrate at 800°C before sputtering. The given errors are due to the scattering in the data. The strain $\langle \epsilon_{(L)}^2 \rangle^{1/2}$ is a relative displacement between unit cells in a column, averaged over a length L .

It should be mentioned again that in this representation of strain, one considers each diffracting grain to be made up of columns of cells, arranged perpendicular to the reflecting planes and therefore, $\langle \epsilon_{(L)}^2 \rangle^{1/2}$ represents the rms strain between all n th neighbours cells ($na_3' = L$), averaged over all columns. Due to long-range interactions of the stresses around a dislocation, the balance of positive and negative stresses will produce an asymptotic strain value. Therefore, at some average distance L away from the source of the stress, $\langle \epsilon_{(L)}^2 \rangle$ will level off to a constant value.

A fit of the form

$$\langle \epsilon_{(L)}^2 \rangle^{1/2} = G_{(hkl)} L^{-k}, \quad (56)$$

as shown in figure 42 was found to describe well the $\psi = 60^\circ$ data for values of L ranging from 20 to ~ 50 (65) Å and the $\psi = 0^\circ$ data in the range from 30 to 80 Å. The ‘Hook’ corrected data are included in the analysis, since they do not differ significantly from the non-corrected values in the explored range. If k values, obtained from sputter deposited niobium films, are compared with those obtained from niobium filings, one finds the film values to be significantly lower than the values reported for mean root square strains from filings (Table 18). This results in a much smaller initial fall off of strain with distance in the films.

Adler and Houska [185] discussed the limiting profile shapes $k = 0, 1/2, 1$. If $k = 0$, each column of cells undergoes either uniform positive or negative strain with $\langle \epsilon_{(L)}^2 \rangle^{1/2} = G_{(hkl)}$ for adjacent pairs of cells. The pure strain profile is Gaussian, and this type of long-range strain exists, if a distribution of column strains occurs due to the presence of point defects. The pure strain profile due to nonuniform strains in the limiting case, $k = 0.5$, is Cauchy-like, having a slowly decreasing tail that may not completely go to zero. The obtained values of k (table 18) are clearly intermediate between the discussed limiting cases, but in agreement with the value 0.27, describing the strain distribution obtained from the (110) and (220) reflection pairs of sputter deposited Mo films [185]. The first neighbour strain $G_{\{110\}}$ was reported to be 0.012, which is also very close to the values found in the present study. In sputter deposited films, the formation of dislocations and statistical fluctuations in the strain, produced by embedded point effects, cause long-range nonuniform strains, which are manifested as local variations in the

strain about an uniform component of column strain, with $k = 0$. The steeper decrease at 50 and 65Å for sample E8.7 and E10.4, respectively, should mostly be due to dislocations. Similar results have been obtained by *Hecq et al.* [187] on sputtered deposited platinum films. *Huang et al.* [188] found, in accordance with the present data, that in ion bombarded silver films, the mean square strain at $L \geq 50\text{\AA}$ is mainly attributed to dislocations, but no further discussion of the results was given.

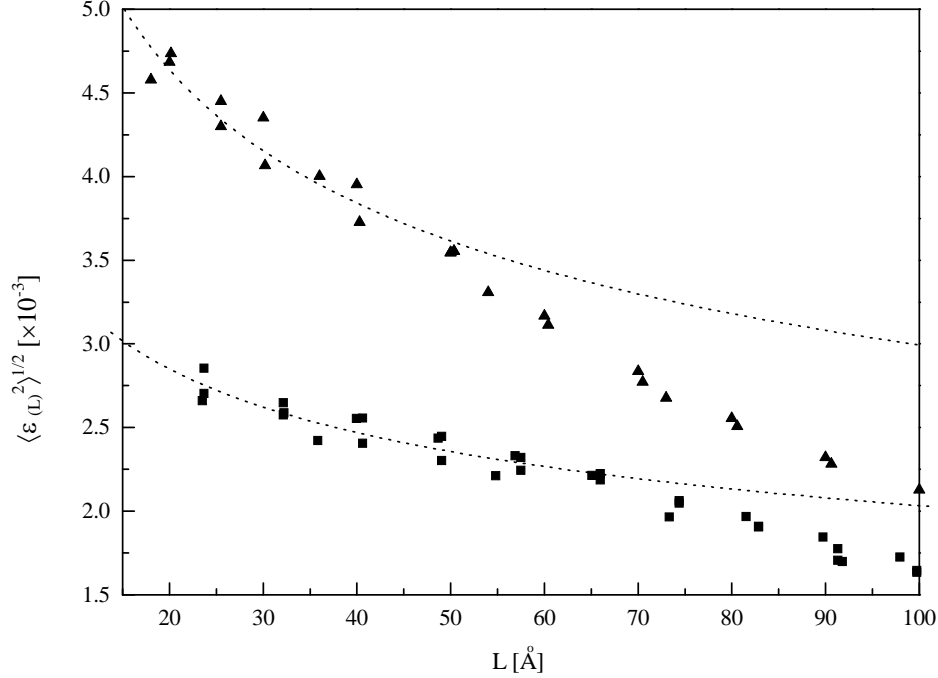


Figure 42. The root mean square strain of a niobium film grown on oxidised copper (triangles) and on sputter-cleaned copper (squares), as a function of the averaging distance L . The dotted lines correspond to a form, as given by relation (56).

It is appropriate at this stage to summarise the effect of the substrate and of annealing on the microstrain evolution in niobium films.

As can be seen from the values of $\langle \varepsilon_{(L)}^2 \rangle^{1/2}$ in table 18, measured at $\psi = 0$ and 60° , respectively, a significant microstructural inhomogeneity of the film E10.4e, i.e. a dependence of the grain microstructure on its orientation with respect to the film surface, is observed. This effect causes microstrain fluctuations of the order of 30% between differently oriented grains and indicates a lower overall defect density for the in-plane oriented grains. This seems mainly to be correlated with a lower amount of in-plane dislocations, as indicated by the lower k values when tilting the sample 60° from the surface normal. For films grown on an oxidised substrate, structural inhomogeneities seem also to be present, but they are less important. The $\psi = 0$ data show that the number of dislocations in growth direction is approximately the same for both types of films, since the values for $\langle \varepsilon_{(L)}^2 \rangle^{1/2}$ coincide for both samples at approximately 65Å (Fig. 41b). The overall point defect density, however, is certainly smaller in the case of coating E10.4e, as expected from the lower argon content and confirmed by the significantly lower first neighbour strain calculated for this film. It is interesting to comment on the ratio of $G_{(E10.4)}/G_{(E8.7)}$ at $\psi = 0$, where an equal dislocation density can be assumed from the data. The value of 0.67 ± 0.14 perfectly represents the measured ratio of the argon concentration in those films, which is 0.66 ± 0.18 (chapter II/4). Consequently, the root mean square microstrains, averaged over columns of grains with a length L between 10 and 60Å perpendicular to the reflecting $\{110\}$ planes, are lower in sample E10.4e. The large difference between $\langle \varepsilon^2 \rangle^{1/2}_{E10.4}$ and $\langle \varepsilon^2 \rangle^{1/2}_{E8.7}$, when averaged over columns of grains inclined at 60° from the surface normal, suggests that

the higher density of in-plane dislocations contributes a large additional fraction of strain in films grown on oxidised copper.

Sample	ψ°	$G_{\{110\}} [\times 10^{-3}]$	k	Range of fit [\AA]
E10.4e	60	5.67 ± 0.41	0.22 ± 0.02	20-65
E10.4e $_{350^\circ\text{C}}$	60	6.78 ± 1.28	0.26 ± 0.04	20-60
E8.7e	60	10.49 ± 0.96	0.27 ± 0.03	20-50
E8.7e $_{350^\circ\text{C}}$	60	9.06 ± 0.94	0.26 ± 0.03	20-50
E10.4e	0	10.27 ± 1.8	0.31 ± 0.04	30-80
E10.4e $_{350^\circ\text{C}}$	0	10.76 ± 1.4	0.33 ± 0.03	30-80
E8.7e	0	15.34 ± 1.7	0.39 ± 0.03	30-80
E8.7e $_{350^\circ\text{C}}$	0	12.76 ± 3.1	0.35 ± 0.06	30-80

Table 18. The parameters G and k , relating the line-shape results to the distribution of defects.

Also included in tables 17 and 18 are data obtained on heat treated films. The results may be of interest, since any microstructural annealing could have implications on the mobility of diffusive hydrogen in niobium (see chapter I/5). The films are not very responsive to annealing at 350°C and significant microstructural changes, in particular annealing out of dislocations, are therefore not expected upon UHV heating the samples to this temperature. Only a small decrease of the rms strains by $\sim 5\text{-}10\%$ with annealing may occur in the films, which in case of sample E10.4e, seems to be restricted to out-of-plane oriented grains. The reason is that at moderate temperatures, dislocation annihilation occurs presumably by glide [189]. Since point like defects, which promote pinning of dislocations, are present in the films, dislocation movement and glide become a very slow process, exclusively controlled by the diffusion of impurities.

8.3. The determination of the effective grain size

To interpret the size coefficients, $A^S(n)$, for different values of n , as obtained from the intercepts on the plot of $A(n, l)$ vs. l^2 (Fig. 40), *Bertraut* [190] expressed these coefficients in terms of the fraction of the columns of length i cells, $p(i)$. Then, $A^S(n)$ becomes

$$A_n^S = \frac{N_n}{N_{h_3}'} = \frac{I}{N_{h_3}'} \int_{i=n}^{\infty} (i-n)p(i)di \quad \text{and} \quad \left(\frac{dA_n^S}{dn} \right)_{n \downarrow 0} = -\frac{I}{N_{h_3}'}. \quad (57a, b)$$

The initial slope of the $A^S(n)$ vs. n curve is given by $-I/N(h_3')$, and $N(h_3')$ is just the intercept of the initial slope on the axis of abscissa. If the values of $A^S(n)$ are plotted vs. L , the initial slope is $-1/(N(h_3')a_3')$. Since $N(h_3')a_3'$ is an average column length perpendicular to the (00 l) planes, the average domain dimension, D_{eff} , is obtained, provided that the intercept at $L = 0$ is normalised to unity. When the $A^S(n)$ curve shows a ‘Hook’ effect at small n , the initial slope has no significance. An approximate correction is to use the slope of the straight portion at small n values, disregarding the $A^S(0)$ point (this correction is possible only, when the straight portion of the data extends over several n values). Correcting the ‘Hook’ effect in this way, one finds that the missing peak area involved in an attempted measurement of $A^S(0)$ may be as much as 10-15%.

Figure 43 shows the $A^S(n)$ vs. L curves and the intercepts of the initial slope for the (110)-(220) reflections. The values of D_{eff} are listed in table 20.

The intercept, D_{eff} , involves both a true domain dimension, D_{coh} and a contribution from faulting, which acts like a particle size effect,

$$-\left(\frac{dA_L^S}{dL}\right)_{L \rightarrow 0} = \frac{1}{D_{eff}} = \frac{1}{D_{coh}} + \sum_T \frac{1.5\alpha_T + \beta_T}{a_0} V_T(hkl), \quad (58)$$

where the coefficient $V_{(hkl)}$ has a numerical value depending on the lattice type, the type of fault T and the crystallographic direction [171, 191, 192]⁽¹⁾. The deformation fault probability, α , represents the probability, that in going from one layer to the next, a deformation fault is encountered and, if the faults occur at random, $1/\alpha$ is the average number of layers between faults. In the case of bcc metals, the growth fault probability, β , or the average number of layers between growth faults, $1/\beta$, cannot be determined separately from α [191]. However, the occurrence of deformation faults in thin fcc films has been reported to be negligible [187], and only the growth (twin) faults, β , need to be considered.

From the value of D_{eff} for any reflection, one obtains only a combination of the average mosaic size, D_{coh} and a faulting probability term, $(1.5\alpha + \beta)$. In principle, making use of the (hkl) dependence of D_{eff} , a separation of the two quantities can be obtained, provided that D_{coh} is independent of the order of the reflection. The latter condition is only satisfied, if the distribution of dislocations and embedded atoms does not depend on the crystallographic direction.

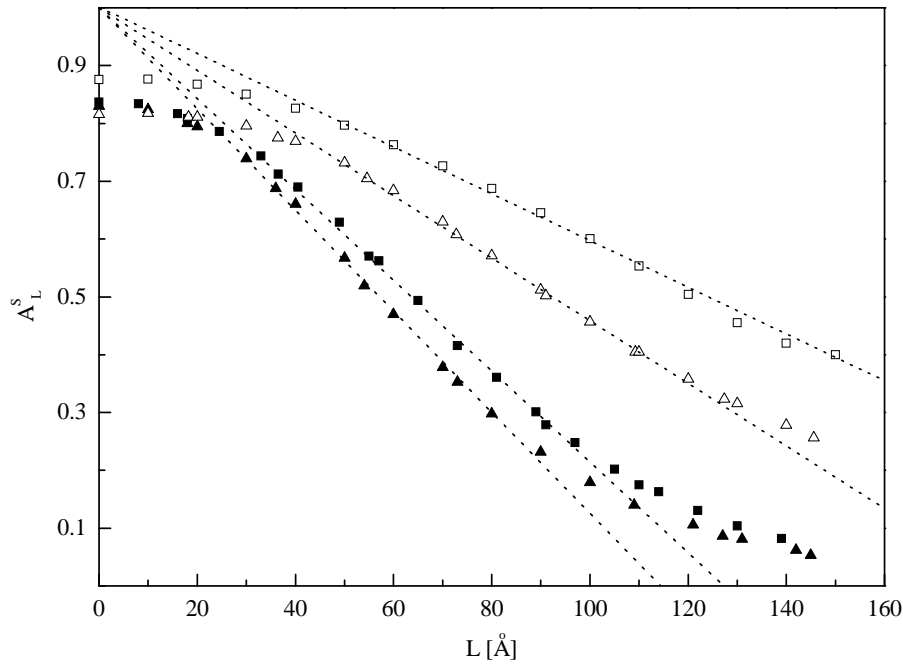


Figure 43. The determination of the effective domain size. The figure includes data of a niobium film, grown on oxidised copper (triangles) and a film, grown on a sputter cleaned substrate (squares). Data obtained at $\psi = 60^\circ$ are labelled with full symbols and open symbols represent data from the measurement in the Bragg-Brentano configuration ($\psi = 0^\circ$). The curves were re-normalised to obtain a linear fit to the straight portion of the data, which intersects at $A_L^S(L) = 1$ (see text).

When studying the effect of faulting on the diffraction pattern by means of the *Warren-Averbach* method, it is often considered that deformation and twin faulting in bcc metals is only possible on $\{211\}$ (see i.e. [171, 191]). Investigations on bcc bulk materials by transmission

⁽¹⁾The contribution to D_{eff} from the fractional change of interplanar spacing at the fault is not considered in equation (58).

electron microscopy indeed showed that faulting occurs preferentially on {211}. However, it is known that the slip system in the bcc structure is not unique and a possibility of faulting on other planes, especially on {110}, exists [169, 183]. The latter should be important for films, which show a strong texture in (110).

The ratio $D_{eff(110)} / D_{eff(211)}$ is a useful parameter for the importance of faulting. If the size broadening is completely due to faulting on (211), this ratio has the maximum value of $\sqrt{3}$ [171, 193]. Unfortunately, the present study is restricted to an analysis of the (110)-(220) pair, since other multiple order reflections are absent. Therefore, a separation of D_{eff} into the compound fault probability and the true grain size cannot be performed in a straightforward manner. In obtaining size and strain parameters from a single line, various single-line methods in real space have been proposed [194, 195]. Since extreme differences are observed to exist among size parameters determined by different methods [31], it has been decided to avoid a single line analysis in real space in the present work.

Another method proposes a Fourier single-line method, using the relation $\langle \varepsilon_L \rangle^2 \gamma^{1/2} \cong G'_{(hkl)} L^{-0.5}$ (see above), as it applies in deformed and vapour deposited materials [181]. With

$$A^S(L) = 1 - \frac{L}{D_{eff}} \quad \text{and} \quad A^D(L, hkl) = 1 - \frac{2\pi^2(h^2 + k^2 + l^2)LG'^2}{a_0^2}, \quad (59a, b)$$

where the substitution $\langle \varepsilon_L \rangle^2 \gamma^{1/2} \cong G'_{(hkl)} L^{-0.5}$ was made, Eqn. (52) can be written as

$$\ln A(L, 211) = -L \left(\frac{1}{D_{eff}} + \frac{2\pi^2(h^2 + k^2 + l^2)G'^2(211)}{a_0^2} \right). \quad (60)$$

The approximation $1-x \approx \exp(-x)$ was used in writing Eqn. (60). Accordingly, a single line analysis can be performed, when knowing the directional variation of the strain. If the stress distribution is isotropic for the crystallographic directions explored, then the ratio of the microstrains in different directions will be inversely proportional to the ratio of the *Young's* modulus in these directions [196, 197]. Since the ratio E_{110}/E_{211} is 1 (chapter II/6), $G'_{(211)}$ is equal to $G'_{(110)}$, and the effective grain size along (211) can be obtained. A possible variation of the mean square microstrain due to a different amount of embedded atoms along different crystallographic directions cannot be accounted for in these considerations. For sample E10.4e, which has a (211) texture normal to the surface plane and therefore a certain probability of (211) faulting, an approximate value of $D_{eff(211)}$ has been obtained, according to the approach described above. To estimate $G'_{(110)}$, a global fit to the $\psi = 0$ data, with k forced to 0.5 was applied over the whole range up to $L = 120\text{\AA}$, ignoring the data at $n = 1-3$. The estimated value of $G'_{(110)}$ is 0.023 ± 0.004 ; values for niobium filings given in literature vary between 0.011 and 0.035 [183]. For an evaluation of the grain size in the (211) direction, only the coefficients calculated for $L = 30$ to 60 were used to minimise the error coming from the approximation in Eqn. (60). The resulting value, $D_{eff(211)} = 154 \pm 18\text{\AA}$, suggests a major contribution from faulting on the particle size broadening, as indicated by the ratio $D_{eff(110)} / D_{eff(211)} = 1.51 \pm 0.18$. Using equation (58) and taking the coefficients $V_{(110-220)}$ and $V_{(211)}$ from [169] or [191] for planar faulting on the (211) planes (0.471 and 0.817, respectively), one obtains the value of the faulting probability term $(1.5\alpha + \beta)$ of sample E10.4. The results are summarised in table 19.

$D_{eff(110-220)} [\text{\AA}]$	$D_{eff(211)} [\text{\AA}]$	$(1.5\alpha + \beta)$
---------------------------------	-----------------------------	-----------------------

233 ± 10	154 ± 21	0.021±0.006
----------	----------	-------------

Table 19. The particle size anisotropy and the calculated compound fault probability on the (211) planes of sample E10.4.

Excluding the possibility of finding deformation faults in sputtered films, the compound fault probability, $(1.5\alpha + \beta)$, leads directly to the growth fault density, which is one every 50 planes for films sputter deposited on oxide-free copper. As a result, growth faults do contribute to line broadening in sputter-deposited films, although dislocation broadening is dominant. It is interesting to refer to the growth fault probability, β , obtained from peak asymmetry analysis of thin platinum films [187], which is given to be 0.020, in excellent agreement with the result presented above.

The lack of sufficiently intense reflections other than {110} prevents a reliable separation of the faulting term from the measured values of D_{eff} in sample E8.7e. Preliminary results, however, indicated that the particle size anisotropy obtained in sample E8.7e cannot be explained by stacking faults on (211) planes alone. A detailed discussion of this effect is certainly beyond the scope of this work, also because of difficulties to get a reliable estimate of the Fourier cosines from very weak diffraction lines.

In table 20, the effective domain sizes of the films are compared. If the coherent domain size is large enough to make $1/D_{coh}$ negligible, the data give a good estimate of the importance of faulting. The value of D_{coh} , which was calculated for sample E10.4e, indeed indicates the latter condition to be approximately satisfied, since the estimated size is about 70nm. Unfortunately, the errors involved in this value are enormous. In addition, as already mentioned above, D_{coh} , as defined in equation (58) is still not a measure of the grain size in the films, since the effect of stacking faults is to add a term T , the domain size in the faulting plane, to D_{coh} . [198]. If stacking faults were completely extended across a coherent domain dimension, D , T and D would be approximately equal and D_{coh} , when measured at $\psi = 0^\circ$, would be of the order of several hundreds of nm, reflecting the length of a columnar grain.

Sample	$D_{eff(110-220)} [\text{\AA}]$ ($\psi = 0^\circ$)	$D_{eff(110-220)} [\text{\AA}]$ ($\psi = 60^\circ$)
E10.4e	233 ± 10	130 ± 5
E10.4e (350°C)	232 ± 8	125 ± 4
E8.7e	190 ± 6	113 ± 4
E8.7e (350°C)	226 ± 5	118 ± 5

Table 20. The values of the effective particle size, D_{eff} , along {110}, essentially made up of a true particle size independent of (hkl) and a fictitious size due to faulting.

The data in table 20 indicate a dependence of the growth fault probability on the nature of the substrate. Films grown on oxidised copper substrates seem to suffer from an increased number of stacking faults. This statement, however, may not be strictly valid, since diffraction effects due to 110-type stacking faults are different from the considered [111](211)-type.

Annealing at low temperatures does not seem to alter the effective grain size and therefore the fault probability significantly, although in case of the film grown on an oxidised copper substrate, an positive effect of annealing is observed, as indicated by the increased value of D_{eff} measured at $\psi = 0$.

9. The low temperature resistivity of niobium films

This chapter describes the measurements of the residual resistivity on the various kinds of film discussed in the preceding chapters. The motivation for this study was to compare the values of the mean free path deduced from the penetration depth data with those obtained from the normal state resistivity. Both sets of data were found to be in very good agreement (see also figure 21 in chapter II/5).

The method to determine the residual resistivity ratio, RRR , of the films is based on a measurement of the DC electrical resistance, R , at room temperature and at a single temperature just above the transition to the normal conducting state and is applicable only after having removed the underlying copper substrate. The experimental method of sample preparation is outlined in figure 44. Resistivity measurements were carried out by the dc four-point probe technique using a digital multimeter. The temperature was stabilised by a computer controlled heating resistor and measured by a Lakeshore™ semiconductor diode thermometer, having an accuracy of $\pm 0.05\text{K}$. In order to avoid heating of the sample, the measuring current was kept low ($10\mu\text{A}$).

The residual resistivity ratio of a niobium film is an approximate indicator of the sample purity and does not depend on sample geometry. It is defined as

$$RRR = \frac{R_{300\text{K}}}{R_{10\text{K}}} = \frac{\rho_{phon.,300\text{K}} + \rho_{defects}}{\rho_{phon.,10\text{K}} + \rho_{defects}}, \quad (61)$$

where $\rho_{phon.}$ is the resistivity caused by thermal motions of the lattice, and $\rho_{def.}$ is the resistivity caused by scattering of the electron waves by lattice imperfections. The electrical resistivity, ρ , is defined by

$$\rho = \frac{m}{ne^2\tau}. \quad (62)$$

The resistivity is inversely proportional to the charge density ne and the factor m/e enters because the acceleration in a given electric field is proportional to the charge e and inversely proportional to the mass m . The time τ describes the time during which the electric field driving the transport current acts on the carrier and enters in the definition of the mean free path l of a conduction electron, $l = v_F\tau$, where v_F is the electron velocity at the *Fermi* surface. Replacing τ in equation (62) for l/v_F , one can see that the product ρl is constant for a given metal. In the case of niobium this constant is $3.75 \pm 0.05 \times 10^{-16} \Omega\text{m}^2$. The net resistivity, $\rho = \rho_{phon.}(T) + \rho_{def.}$ is dominated at 300K by collisions of the conduction electrons with lattice phonons and at 10K by collisions with impurity atoms and imperfections that disturb the periodicity of the lattice. The experimental observation that $\rho_{def.}$ is independent of temperature and $\rho_{phon.}$ is independent of the defect density is known as *Matthiessen's rule*.

The measured resistivity ratio, RRR , was used to calculate the resistivity at 10K, ρ_{10} , which is dominated by the contribution from $\rho_{def.}$, and the mean free path, l . The latter has been calculated under the assumption that the product ρl will remain unchanged upon adding noble gas impurities [199].

The value of $\rho_{phon.}(T)$ at 300K, $1.45 \pm 0.05 \times 10^{-7} \Omega\text{m}$ has been interpolated from a collection of experimental data summarised in [200]. The value at 10K, $3.66 \pm 0.1 \times 10^{-12} \Omega\text{m}$ has been taken from reference [161], measured on a niobium single crystal with a RRR of 16500. A direct calculation of the resistivity was avoided, because of the limited precision in the determination of the contact geometry. This would contribute, along with some uncertainties in the average

film thickness, to large errors in the form factor (length/cross sectional area) and consequently in the absolute values of ρ_{10} .

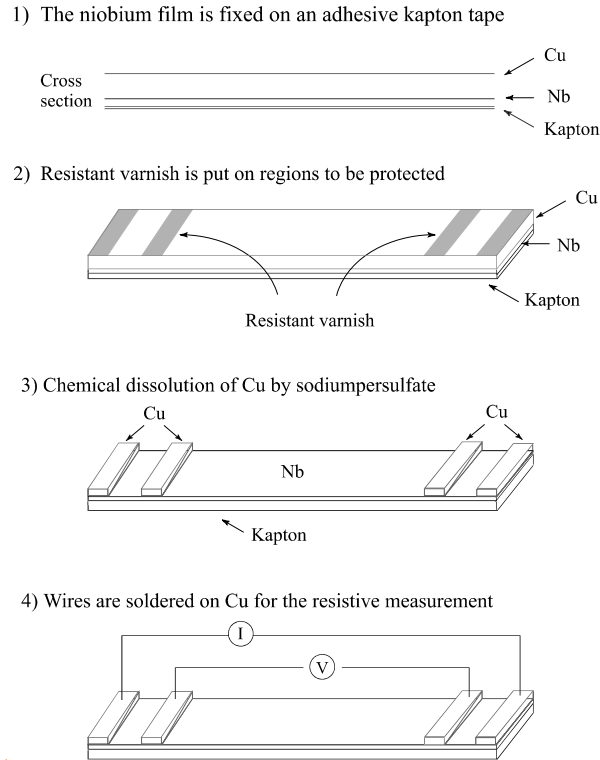


Figure 44. Experimental procedure to prepare the samples for measurements of the residual resistivity ratio, RRR .

The accuracy of the temperature dependence of the resistance, R , was limited only by the accuracy of the voltage and current measurements. Possible deviations of R_{300} from the set point temperature were corrected. The measured RRR and the calculated residual resistivity and mean free path of films, deposited with different discharge gases on flat copper and quartz substrates, which are placed at diametrically opposite points along the equatorial plane inside the 500MHz cavity ('sample system', see chapter II/1), are summarised in table 22. The insulating quartz substrates do not require the film to be detached prior to the measurements. This is advantageous for films, which contain more than 1at-% neon, since these films are very brittle and not available in the free-standing form. Data from films, which have directly been cut and detached from 1.5GHz copper resonators, can be found in table 21.

The most important information, which can be extracted from table 21, is the significant difference in the low temperature resistivity, ρ_{10} , between sample E10.4e and E8.7e. The difference of $0.87 \pm 0.02 \mu\Omega\text{cm}$ cannot be explained solely by an impurity effect, since the differences in the argon content and probably also in the hydrogen content are not sufficient to account for the observed increase of ρ_{10} in the film grown on oxidised copper. Vion [114] found a similar difference in the values of RRR between films grown on annealed and non-annealed copper substrates. Based on the results of a TEM analysis, showing a higher density of grain boundaries per unit surface in standard films, he suggested enhanced grain boundary scattering to be responsible for the increased normal state resistivity in those films. This was a sensible conclusion, since contrary to the results obtained in the present work, the microstructural parameters, the macrostresses and the argon content were reported to be absolutely the same in both kinds of film.

Sample	RRR	$\rho_{(10)} [10^{-9}\Omega\text{m}]$	$l [\text{nm}]$
E8.7e	11.49±0.06	13.8±0.1	27.2±0.2
E8.7i (1)	10.92±0.03	14.6±0.5	25.8±1.0
E8.7i (2)	10.40±0.08	15.4±0.6	24.3±0.9
E10.4e	28.92±0.92	5.1±0.2	74.5±2.6
E10.4i (1)	21.83±0.26	7.0±0.3	53.9±2.1
E10.4i (2)	17.66±0.35	8.7±0.4	43.3±1.9
E9.6e	12.34±0.06	12.8±0.3	29.6±0.7
E9.6i (1)	15.67±0.14	9.9±0.4	38.0±1.5
E9.6i (2)	10.60±0.09	15.1±0.5	24.8±1.0
E8.7e (350°C)	6.50±0.02	26.4±0.9	14.2±0.5
E10.4e (350°C)	21.67±0.09	7.0±0.2	53.5±2.0

Table 21. Experimental results of the low temperature resistivity and the mean free path obtained for various samples cut from 1.5GHz copper-niobium resonators. Values given for sample E10.4e and E8.7e represent a mean value, obtained from several measurements along the cavity equator and the errors include the dispersion of the measured values from the mean.

Sample	RRR	$\rho_{(10)} [10^{-9}\Omega\text{m}]$	$l [\text{nm}]$
A1 (0.07)	9.80±0.04	16.5±0.6	22.9±0.9
A3 (0.59)	5.61±0.04	31.4±0.8	12.0±0.3
A4 (0.95)	4.76±0.06	38.5±1.4	9.7±0.4
A1-Quartz (0.07)	14.75±0.12	10.5±0.4	35.8±1.4
A2-Quartz (0.32)	12.96±0.10	12.1±0.4	31.1±1.2
A3-Quartz (0.59)	10.04±0.04	16.0±0.6	23.5±0.9
A4-Quartz (0.95)	8.78±0.04	18.6±0.6	20.2±0.8
A5-Quartz (1.9)	5.95±0.03	29.2±1.0	12.8±0.5
A6-Quartz (4.2)	3.02±0.02	71.8±2.5	5.2±0.2

Table 22. Experimental results obtained on films, sputter-deposited in the ‘sample system’ under different discharge gas compositions (table 5 in chapter 4) on quartz and copper substrates. The numbers in parenthesis refer to the measured neon content in at-%.

It is known that in polycrystalline thin films, other scattering mechanism have to be taken into account in addition to the usual lattice and defect scattering. Scattering at the film surfaces (external size effect) as described by the *Fuchs-Sondheimer* theory [201, 202] and, even more important, at grain boundaries [203, 204] significantly contributes to the resistivity, especially when the intrinsic electron mean free path due to defect scattering, l_i , is large compared to the distance between grain boundaries, D . Since size effects give a limited contribution to the reduction of the *RRR* at a film thickness, $d = 1.5\mu\text{m}$, an applicable method to separate experimentally the contribution of grain boundary scattering from the total measured resistivity, ρ_{10} , is based on the power law description of the dc resistivity of polycrystalline pure metal films [204],

$$\rho = \frac{m\nu_F}{ne^2l_i} T^{-\frac{l_i}{D}}. \quad (63)$$

The mechanism of grain growth was studied theoretically by *Srolovitz* [205], who obtained a simple relation between grain size and film thickness,

$$D = ad^b. \quad (64)$$

The values of the coefficient a , which depends on the film and substrate nature and on the sputtering parameters, and the exponent b were determined experimentally for niobium films sputter deposited on copper substrates at 200°C in the ‘sample system’ [1] and are found to be ~ 0.08 and 0.35 ± 0.05 , respectively. Taking these data to calculate the grain size at $d = 1.5 \mu\text{m}$, one finds $D = 95 \pm 11 \text{ nm}$, a value which is in good agreement with the grain size of 110 nm for sample E8.7e, obtained from a TEM analysis [206]. *Benvenuti et al.* [1] calculated the defect mean free path, l_i , by fitting equation (63) to the observed thickness dependence of the resistivity of niobium films and found the transmission probability, T , to be $T = 0.67$. This value, which describes the probability for an electron to pass a single grain boundary, is in perfect agreement with $T = 0.7 \pm 0.1$ given for other polycrystalline metal films [204]. Using the data given above for a rough estimation of l_i by means of equation (63), one finds that grain boundary scattering still accounts for a significant fraction of the observed resistivity⁽¹⁾, ρ_{10} , but the main contribution comes from other lattice defects (see also [1]). The latter have already qualitatively been evaluated by an analysis of microstrain and coherent domain size (chapter II/8). TEM analysis of the films E8.7e and E10.4e has shown that the grain size is significantly larger in film E10.4, which explains partly the observed difference in the low temperature resistivity between both films. Taking l_i to be identical in both films, as assumed by *Vion*, it is not solely the difference in grain size, which accounts for the observed change in RRR , but rather a significant difference in the transmission probability, T . *Vion* indeed explained the lower resistivity in epitaxial films by an epitaxial ordering effect, leading to less resistive boundaries between heteroepitaxial grains. However, to explain the observed increase of ρ_{10} in film E8.7e on the basis of resistive grain boundaries requires T to be as low as ~ 0.35 . This is in sharp disagreement with the experimental results reported above, which were obtained for non-epitaxial pure metal films. A value of $T \cong 0.3$ was only found for granular films composed of a transition metal and a non-metallic compound [204, 207], but this does by far not apply to the niobium films described in this work.

It should be noted that in the *Reiss* description as given by equation (63), a possible small variation of T with the film thickness, d , is not accounted for. A more detailed analysis on niobium sputtered thin films on glass substrates [208] has shown that for d between 250 and 1000 nm, the transmission probability at the grain boundaries varies from 0.5 to 0.9 (a RRR of 8 at 1000 nm was reported). This behaviour was attributed to the observed variation of microstructure with thickness, modifying the potential between grains.

In conclusion from the discussion given above, it is strongly believed that differences in the microstructure, as they have been worked out in the preceding chapters, are the predominant reason for the different RRR between the two families of films, represented by cavity E8.7 and E10.4, respectively. This argumentation is supported by further experimental results on polycrystalline niobium films [209], which have shown that the residual resistivity, ρ_{10} , tends to increase when increasing the microstrain.

As can be seen from table 21, the RRR at the cavity equator is somewhat higher than those measured close to the iris of a cavity. This effect is small for standard films and probably related to the higher concentration of implanted argon, which has been measured on samples cut from the iris. This is a consequence of the entrapment mechanism discussed in chapter II/4, the cell geometry and the fact that the average energy of the reflected energetic argon atoms

⁽¹⁾This means that increasing the thickness of the coatings still provides higher RRR values.

increases with decreasing scattering angle (Eqn. 12). The large discrepancy between the resistivity ratio measured at different positions in cavity E10.4 cannot be explained by a different argon concentration only, but is supposed to be indirectly related to the asymmetry of the plasma supporting magnetic field as already reported previously. This field inhomogeneity was found to increase the mean square microstrain at the iris of the cavity. Figure 45 relates $\langle \varepsilon^2 \rangle^{1/2}$, measured at the upper and lower iris and at the equator of cavity E10.4 and E8.7, respectively, to RRR as listed in table 21. In addition, two films coated in an argon/neon discharge gas mixture are also included in figure 45. It can be seen that the residual resistivity ratio of polycrystalline films has the tendency to decrease with increasing microstrain.

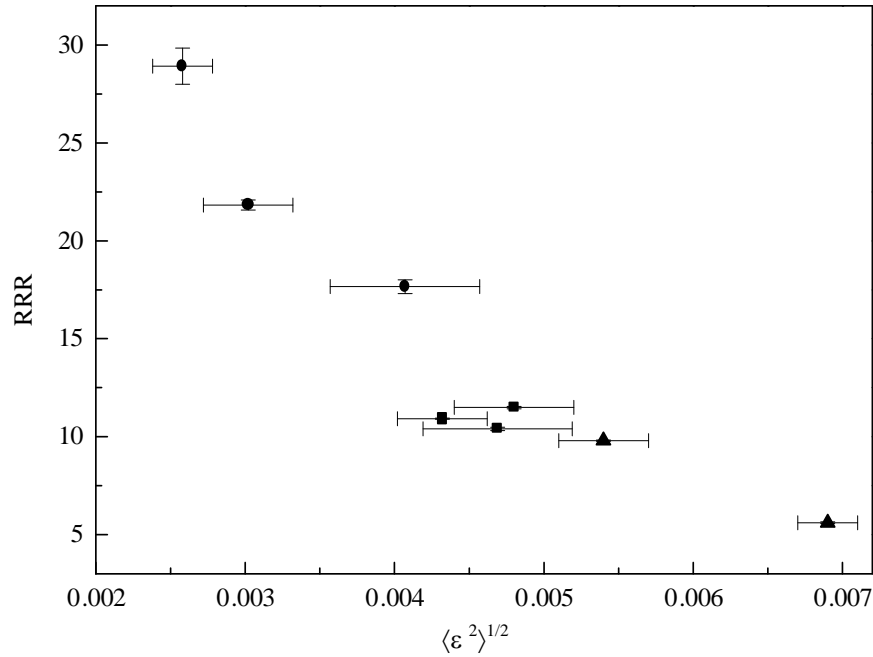


Figure 45. RRR as a function of the estimated strain for films cut from cavity E10.4 (circles), E8.7 (squares) and for neon implanted films (triangles). The strain has been determined from a *Williamson Hall* plot and was found to vary considerably when measured at different locations in the cell of cavity E10.4.

From this analysis it seems that the universal parameter $\langle \varepsilon^2 \rangle^{1/2}$, which is a measure of the local strain field in the sample, can indeed explain the gross features of the data, provided that the concentration of reactive impurities in the film is comparable and small.

As already discussed in previous chapters, annealing the films at temperatures above 300°C is known to release oxygen into the film, but to conserve the strain present in those films. On condition that interstitial oxygen is homogeneously dissolved into the lattice, the latter has been reported to modify significantly the resistivity of niobium in the normal state. A linear increase of $5.1 \pm 0.1 \mu\Omega\text{cm}$ per at-% oxygen was calculated by taking the data tabulated in [17, 18]. This value can explain the observed increase of ρ_{10} by $1.26 \pm 0.08 \mu\Omega\text{cm}$, which was obtained after UHV annealing of film E8.7e. Since for films grown on oxidised copper substrates, oxygen will not only diffuse from the surface into the film, but also from the interface by reduction of the copper oxide, oxygen contamination may indeed be significant over the whole film thickness. The effect of low temperature annealing on the residual resistivity of niobium foils was also investigated by other authors [79] and similar results were obtained. To improve the residual resistance of niobium by degassing and to anneal out mechanical stress, elevated temperatures and an effective getter pump are needed [210].

The relatively small increase of ρ_{10} by only $0.2\mu\Omega\text{cm}$ in a film grown on non-oxidised copper (E10.4e), however, is not well understood. One might argue that oxygen is not homogeneously dissolved into the film after the heat treatment, since free oxygen, produced at the surface might diffuse only a limited range into the material. The measured resistance, R , would then be determined by two resistances in parallel, consisting of an oxygen free film close to the interface and a region of increased impurity content closer to the surface. This argument, however, is not supported by measurements of the critical temperature, which was found to decrease approximately by the same amount in both films after heat treatment.

For cavity E9.6, it could be expected to measure values of ρ_{10} very similar to those obtained for cavity E10.4. From the data given in table 21, it can however be seen that the low temperature resistivity determined from this cavity is significantly lower than the value quoted for sample E10.4 after annealing.

Cavity E9.6 was coated in the same way as cavity E10.4, but has thereafter undergone several post treatments. It was loaded with hydrogen before venting to air to determine the effects of hydrogen on the rf superconducting properties (chapter I/5). After the rf measurements, the cavity was again mounted on the sputtering system and annealed to 320°C in order to degas H_2 . Since the effect of H_2 on the transition temperature and on the low temperature resistivity of niobium is well studied and known to be reversible [160], loading with hydrogen and subsequent unloading should not affect the RRR . However, the annealing-outgassing treatment of cavity E9.6 was not performed in an UHV furnace, as in the case of the heat treated samples E8.7e and E10.4e, but on the sputtering system itself and the cavity outside was exposed to ambient air during heating. This may continuously release contaminants into the film, which diffuse through the copper to the film-substrate interface. The fact that the thickest film E9.6i (1) shows the highest RRR among the three samples measured from this cavity may support this hypothesis.

Figure 46 shows that incorporated neon also increases the residual resistivity, ρ_{10} , linearly, but only by $1\mu\Omega\text{cm/at}\%$. The film grown in a pure neon discharge is not shown in this figure, but has a higher value of ρ_{10} than described by the simple linear dependence of the resistivity on the impurity concentration. This behaviour is attributed to changes in the microstructure of this film. The XRD pattern has a ‘quasiamorphous’ appearance, i.e. very small absolute reflection intensities associated with an enormous peak broadening.

As may be seen from the values quoted in table 22, the resistivity of niobium films deposited on quartz is lower than that of films deposited on copper substrates. This effect was also observed for standard coatings, but no further investigations to explain this difference was performed.

A comparison of available values of the relative increase of ρ_{10} by dissolved impurities in niobium like argon, $(4.1\pm 0.3\mu\Omega\text{cm/at}\%)$ [15], nitrogen $(2.7\mu\Omega\text{cm/at}\%)$ [211] and oxygen reveals that the residual resistivity is changed much more appreciably by these impurities than by neon. Hydrogen however, is reported to increase the resistivity only at a rate of about $0.6\mu\Omega\text{cm/at}\%$ at low concentration [160].

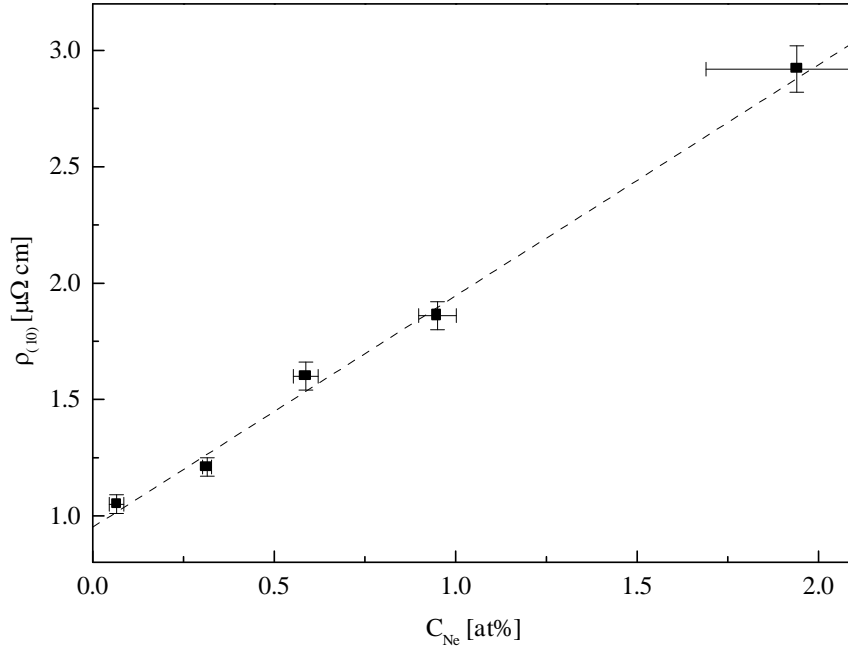


Figure 46. Low temperature resistivity of niobium films as a function of neon content, C_{Ne} . Films were deposited at 150°C on quartz substrates at deposition rates as given in table 5. The dashed line represents a linear fit to the data with a slope of $0.99 \pm 0.06 \mu\Omega\text{cm/at\%}$. The point at 4.2at% neon concentration (sputter deposition in pure neon) lies significantly above this line and is not shown here (see text).

Finally, it may be interesting to estimate approximate values of the dimensionless *Ginzburg-Landau* parameter, $\kappa(l, T = T_c)$, which is defined as the ratio of the penetration depth, λ , of the magnetic field and the Ginzburg-Landau coherence length, ξ^{GL} , denoting the distance along which the superconducting order parameter, Ψ , changes significantly. In principle, κ can be determined from the residual resistivity by using *Gor'kov's* prediction of a mean-free-path dependence of κ [212], which led to the formulation of the *Gor'kov-Goodman* relation [213],

$$\kappa = \kappa_0 + 2.37 \times 10^{-6} \sqrt{\gamma} \rho_{10}. \quad (65)$$

In this relation, which was shown to describe experimental data on niobium within the theoretical accuracy of 6% [211], κ_0 is the clean limit ($\rho_{10} \sim 0$) value of κ , and γ is the coefficient of the electronic specific heat per unit volume. The latter was determined for niobium from calorimetric measurements and found to be $701 \pm 18 \text{ JK}^{-2} \text{ m}^{-3}$ [211]. Experimental results on niobium with varying impurity content, correlating the *Ginzburg-Landau* parameters, κ , with the normal state resistivity data are also available in reference [211]. These data were extrapolated to the clean limit by a weighted linear regression to obtain the value $\kappa_0 = 0.715 \pm 0.004$. Applying the *Gor'kov-Goodman* relation and taking the values quoted above gives values of the *Ginzburg-Landau* parameter, $\kappa = 1.581 \pm 0.013$ for a niobium film sputter deposited on an oxidised copper substrate and $\kappa = 1.035 \pm 0.014$ for a film sputter deposited on non-oxidised copper.

10. Measurements of the critical fields

10.1. The upper critical field

Magnetisation measurements to determine the upper and lower critical fields of magnetron sputtered niobium films were performed at the Technical University of Vienna. The main motivation for this study is the lack of reliable data on the upper critical field of niobium films in the existing literature. In reference [129], an upper critical field at 4.2K of approximately 2T was measured for niobium films with $RRR \sim 10$. This value is much higher, than the values on bulk niobium with a similar RRR , reported by *Koch et al.* [17]. These authors showed that H_{c2} increases by a factor 1.5 (resp. 2.2), when the RRR value is reduced from above 1000 to 17.6 (resp. 6.3) by the presence of interstitial oxygen in the niobium lattice. Accurate measurements of H_{c2} on pure niobium are available in [67, 211, 225]. To a good approximation, $H_{c2}(0) = 0.4T$. Quantitatively, the H_{c2} vs. l relation may, of course, depend on the detailed mechanism, responsible for the reduction of l and the results on bulk niobium may not be easily extended to films, where the low values of the RRR are mainly caused by the residual microstrain. The measurements discussed in the present chapter are aimed to clarify this question and to investigate the importance of macrostresses on H_{c2} .

A Quantum Design™ high-sensitivity superconducting quantum interference device (SQUID) magnetometer has been used. The measurements were carried out in fields, $\mu_0 H_a$, up to 1T and in the temperature range from 1.8 to 11K [214]. The samples, having a size of $1 \times 0.5 \text{ cm}^2$, were placed into the interior of a quartz tube and fixed with vacuum grease to ensure free contraction during cool down, but sufficient rigidity to keep the film surface parallel to the applied magnetic field. In this case and because of this narrow plate geometry, the demagnetisation factor D is zero and the field at the surface of the film is equal to the applied field, H_a .

For a type-II superconductor, as niobium, the parameter κ entering the phenomenological *Ginzburg-Landau* theory is greater than $1/\sqrt{2}$. *Ginzburg* and *Landau* [215] showed that for this type of superconductor, superconductivity is maintained at fields greater than the thermodynamic critical field, H_c , for which an equilibrium could exist between the normal and superconducting states. *Abrikosov* [216] solved, under some assumptions on the values of H_a and κ , the linear *Ginzburg-Landau* equations analytically and showed that the superconductor enters into a special state, the so-called mixed state, which is bounded by two field strengths, H_{c1} and H_{c2} . At the lower critical field H_{c1} , magnetic flux starts to penetrate a superconducting sample in the form of a lattice⁽¹⁾ of quantised flux lines. The mixed state continues up to some value of the upper critical field $H_{c2} = \kappa\sqrt{2}H_c$, at which the superconductor undergoes a second order phase-transition to the normal state [218].

In the present work, the upper critical field was mainly determined from the temperature dependence of the field-cooled (FC) magnetisation. These measurements rely on the fact that $H_{c2}(T)$ is defined as the field at which the diamagnetic moment vanishes at a certain temperature T . The measurement is done at constant field, and the magnetisation is measured as a function of temperature as the temperature is decreased from well above the transition temperature. The external magnetic field, $\mu_0 H_a$ ($0.05T \leq \mu_0 H_a \leq 1T$), was applied at 15K. The sample was then cooled down in H_a and, starting from 11K, the magnetic moment of the sample was measured in steps of 0.3K. An example of such a measurement and the evaluation procedure of $T_c(H)$ from the experimental data are shown in figure 47. The upper critical field

⁽¹⁾Later, *Kleiner et al.* [217] showed that *Abrikosov's* square-lattice solution had a higher free energy and is therefore unstable compared with an equilateral triangular lattice structure, which could be confirmed by a variety of experiments in the meanwhile.

for the temperature $T = T_c(H)$ is equal to the applied external field, $H_{c2} = H_a$. The uncertainty in determining the transition temperature was normally less than 0.15K; in cases when a peak was observed just below $T_c(H)$, the uncertainty may have reached 0.4K (see figure 47, insert). Independent measurements of $H_{c2}(T)$ were obtained from magnetisation curves performed at constant temperature by varying the external field, H_a , from 0 to values greater than H_{c2} . As the field approaches H_{c2} , the field profile in the interior of the sample becomes flat and equal to the applied field, H_a [219, 220].

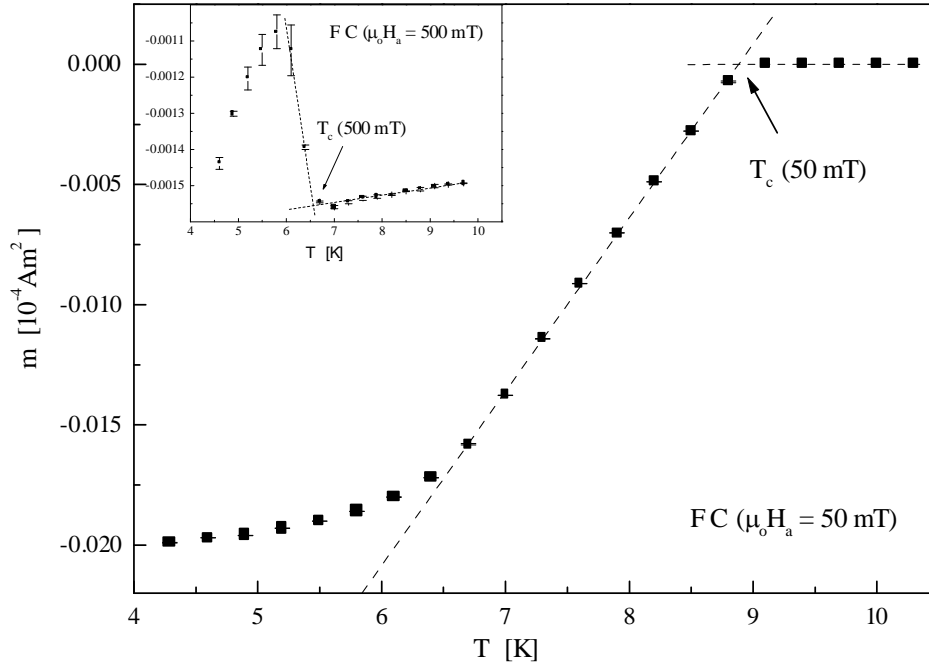


Figure 47. Magnetic moment vs. temperature of a niobium film in an applied field (FC-curve). At higher applied fields, $\mu_0 H_a$, a hump at the transition is frequently observed (see insert). Field inhomogeneities together with strong surface pinning may lead to this behaviour, which does not seriously affect the result [235]. In each case, the transition temperature was estimated from the intersection between a linear extrapolation of the magnetisation in the superconducting state and the diamagnetic signal in the normal state.

The dependence of H_{c2} on the reduced temperature, $t = T/T_c$, is shown for sample E8.7e and E10.4e in figures 48 and 49, respectively. *Abrikosov* [216] finds in his theory of type-II superconductors in the mixed state,

$$H_{c2} = \sqrt{2\kappa} H_c. \quad (66)$$

Writing κ as [215, 216, 221],

$$\kappa = 2\pi\mu_0 \sqrt{2} \left(\frac{2e}{h} \right) \lambda^2(T) H_c(T), \quad (67)$$

and substituting the flux quantum, φ_0 (2.067×10^{-15} Wb) for $h/2e$, leads to an expression of $H_{c2}(T)$ as a function of the penetration depth, $\lambda(T)$ and the thermodynamic critical field, $H_c(T)$,

$$H_{c2}(T) = \frac{4\pi\mu_0 \lambda^2(T) H_c^2(T)}{\varphi_0}. \quad (68)$$

This solution of the temperature dependence of the upper critical field, H_{c2} , which results from the *Ginzburg-Landau-Abrikosov-Gor'kov* (GLAG) theory, is, although applicable for all mean free paths, l , restricted to temperatures in the immediate vicinity of the zero field transition

temperature, T_c , where $\kappa = \kappa_1(T) = \kappa_2(T)$ [222, 223]. The generalised *Ginzburg-Landau* parameters, $\kappa_1(T)$ and $\kappa_2(T)$ were introduced by *Maki* [222] to extend *Abrikosov's* theory of the mixed state to temperatures $T < T_c$.

In order to facilitate comparison with experiment, the temperature dependence of $\lambda(T)$ and $H_c(T)$ is often approximated by the *Gorter-Casimir* two-fluid expressions [224],

$$\lambda(T) = \lambda(0) \frac{1}{\sqrt{(1-t^4)}} \text{ and } H_c(T) = H_c(0)(1-t^2). \quad (69ab)$$

Substituting equations (69ab) for λ and H_c in equation (68) leads to an approximate expression for the temperature dependence of H_{c2} , derived for the limiting case $T_c - T \ll T_c$,

$$H_{c2}(T) = \frac{4\pi\mu_0 H_c^2(0) \lambda^2(0) (1-t^2)}{\varphi_0 (1+t^2)}. \quad (70)$$

Experimental values of $H_{c2}(T)$ for pure niobium [225, 226] and for very thin films [227] were shown to agree reasonably well with the *Gorter-Casimir* temperature dependence, $(1-t^2)/(1+t^2)$. However, at $T \rightarrow 0$, the measured data were found to lie significantly below the predicted dependence, and the two-fluid expression gives a too high value of $H_{c2}(0)$. In order to find a better approximation as t approaches zero, the experimental data were compared with numerical results of the theoretical temperature dependence of the upper critical field derived by *Helfand* and *Werthamer* [228, 229]. Their calculations are based on a linearisation of the *Gor'kov* equations [221, 230] for small values of the position-dependent pair wave function in an applied magnetic field. This approach leads to an integral equation, whose lowest eigenvalue is related to the critical field. Exact solutions were given by *Maki* [222] in the dirty limit, by *Gor'kov* [230] at $T = 0$ in the pure limit and by *Helfand* and *Werthamer* for all T and l . The calculations were simplified by the assumption that the magnetic field only interacts with the orbital motion of electrons and ignoring any effects arising from the electron spin. The Fermi surface is taken as a sphere and the interaction between electrons is described by the simple instantaneous short-range BCS potential, i.e. anisotropy and strong coupling are not taken into account.

Under these assumptions and in the clean limit, the theoretical temperature dependence of $H_{c2}(T)$ can best be approximated by the function

$$H_{c2}(T) = H_{c2}(0) (1-t^{1.5}). \quad (71)$$

The shape of this function depends only very little on the actual value of l . It can be seen from figures 48 and 49 that for $t < 0.7$, the data follow closely the theoretical dependence for weakly coupled superconductors. The fitted values of $\mu_0 H_{c2}(0)$ are 1150 ± 25 and 770 ± 10 mT for sample E8.7e and E10.4e, respectively. The observed ratio $\mu_0 H_{c2}(0)_{E10.4} / \mu_0 H_{c2}(0)_{E8.7} = 0.67 \pm 0.02$ is surprisingly close to the theoretical value 0.69, as calculated from the tabulated values of the reduced temperature dependent *Ginzburg-Landau* parameter κ^* [222] at $T = 0$, for impurity parameters, $\alpha = 0.5$ (E10.4e) and 1.2 (E8.7e), respectively⁽¹⁾ [223, 228]. However, the absolute values of the upper critical field calculated by *Helfand* and *Werthamer* lie significantly below the measured values for bulk niobium given in the literature [211, 225].

⁽¹⁾The impurity parameter α was calculated taking $\xi_0 = 36$ nm and a mean free path as given in table 21 (chapter II/9).

The measurements of the upper critical field were repeated for the film E8.7e after the removal of the substrate, i.e. in the stress-free state. The results are included in figure 49 and show that H_{c2} is not sensitive to macrostresses build up in the films.

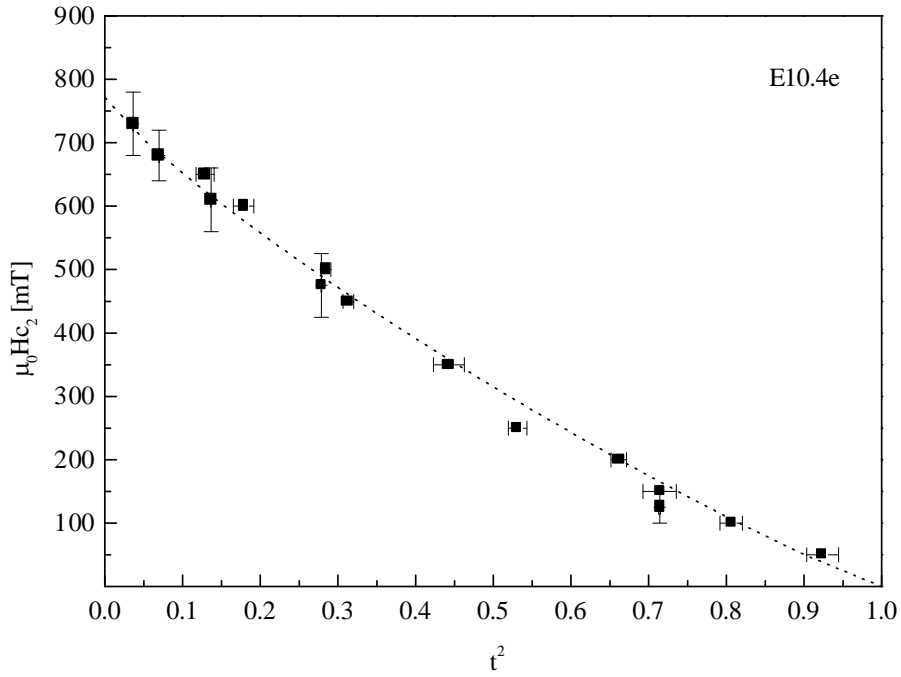


Figure 48. Temperature dependence of the upper critical field, H_{c2} , of film E10.4e determined from magnetisation measurements at constant field and constant temperature, respectively. The dotted line corresponds to the theoretical dependence as approximated by relation (71).

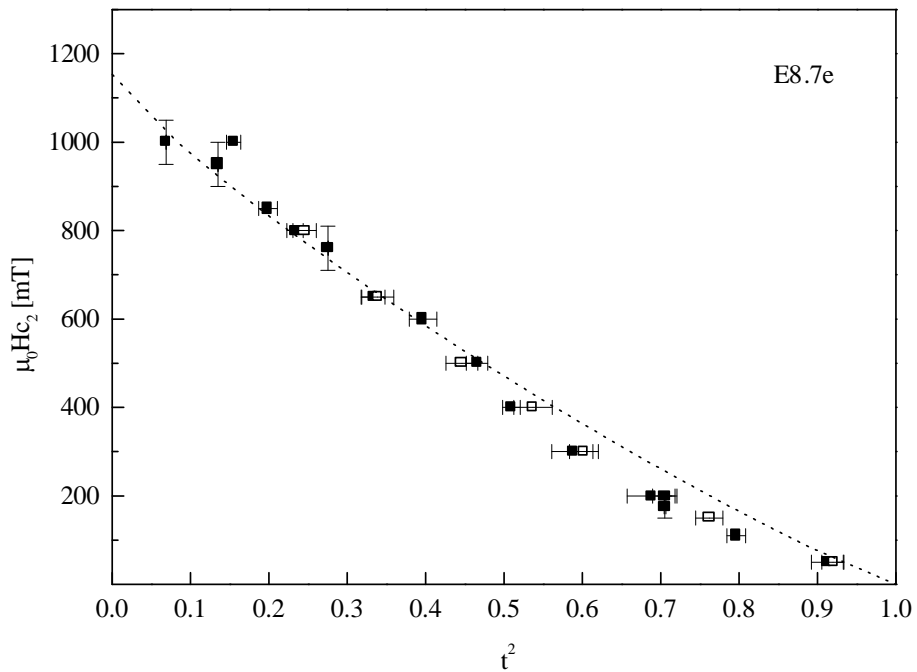


Figure 49. Temperature dependence of the upper critical field, H_{c2} , of film E8.7e. Measurements of the same film after dissolution of the copper substrate (open squares) are included in this plot. The dotted line has the same meaning as in figure 48.

10.2. The lower critical field

The lower critical magnetic field, H_{c1} , has been determined for two different values of T (1.8, 5K) from a magnetisation curve in the external field range $0 \leq H_a < H^*$, where $H^* \sim J_c d$ is the field at which the flux penetrates the sample completely [220]. As the field is increased from zero to H_{c1} , the magnetisation of the sample will increase as H_a , illustrating perfect diamagnetism. In this experiment, the lower critical field H_{c1} is evaluated as the field, at which a deviation from a linear $m(H)$ dependence first appeared (method of ‘first deviation’ from the diamagnetic response). Since for type-II superconductors with strong pinning, $m(H)$ has a smooth positive curvature close to H_{c1} , it is extremely difficult to obtain the point of the first deviation from linearity, since the deviations themselves are very small [231, 232]. The criterion, which was chosen to determine H_{c1} , is to reject all observations from a linear model, which have studentised residuals greater than 2 in absolute value. Provided that perfect linearity of $m(H)$ below H_{c1} is observed, this method should be sensitive to determine the point of first deviation (Figure 50a).

Another possibility to determine H_{c1} , which is considered to give most accurate results [232, 233, 234], was proposed by *Moshchalkov et. al.* [233] and is known as the ‘trapped flux’ method. This method was also applied to determine H_{c1} at 1.8K. Measurements of the trapped magnetic moment, m_t , were made according to the following scheme. The sample is cooled down from $T > T_c$ to 1.8K in zero field and after temperature stabilisation, the magnetic moment, m_1 , is measured. Then an external field, H_a , is applied. After having again set the field to zero, the magnetic moment, m_2 , of the sample is measured again. Warming up the sample above T_c completes the first measurement cycle and the trapped magnetic moment $m_t(H_a) = m_2 - m_1$ can be calculated. These cycles are repeated and each time the applied field is increased by 5mT. The field dependence of m_t is shown in figure 50b for sample E10.4e. For values of the external field $H_a < H_{c1}$, magnetic fields do not penetrate the sample and the magnetic moment measured before and after the application of the external field is the same. The trapped magnetic moment m_t , may have some background value, which is independent of H_a . The situation changes as soon as H_a exceeds H_{c1} . Now m_2 should be smaller than m_1 due to some trapped magnetic flux, which is pinned in the sample and makes $-m_t > 0$.

From figure 50, it becomes clear that the values of H_{c1} obtained by both techniques differ significantly from each other.

A rather simple analysis of penetration of magnetic field in a strong pinning type-II superconductor in terms of an extended Bean model, which includes the reversible magnetisation, predicts [233],

$$m_t = \frac{(H_a - H_{c1})^2}{4 (H^* - H_{c1})}, \quad (72)$$

where H^* is the value of H_a , which corresponds to the onset of full magnetic field penetration into the sample. The formula has been derived for a slab with thickness d and is valid at large values of H^* .

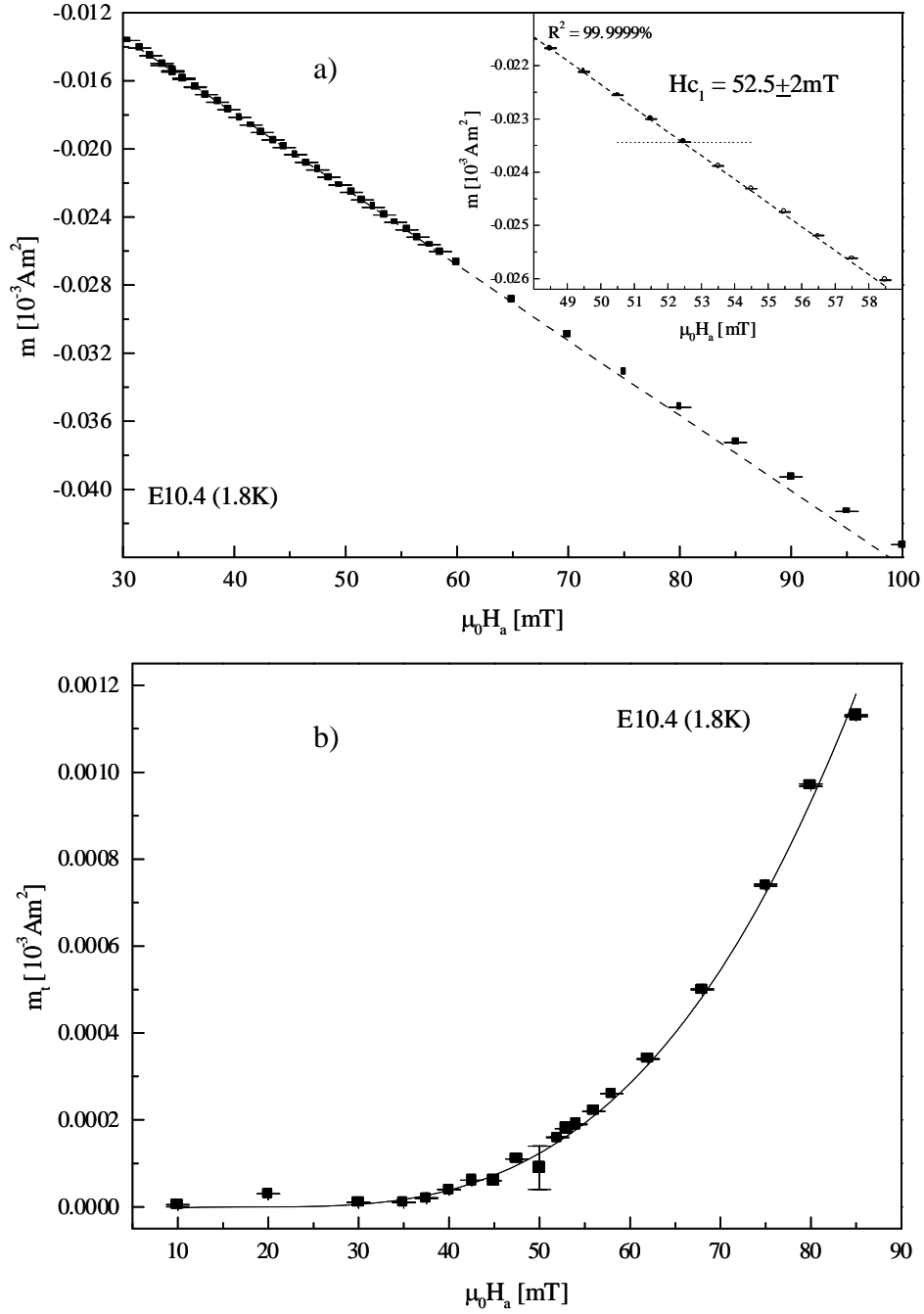


Figure 50ab. Field dependence of the magnetic moment (top) and of the trapped magnetic moment (bottom). The full line in the bottom figure represents a fit of the trapped magnetic moment data to the equation $m_t = A (H_a - H_{c1})^2$ with $H_{c1} = 31 \pm 3 \text{ mT}$.

Equation (72) was found to give a good fit to the data, in particular the smooth behaviour in the vicinity of H_{c1} . The value of $31 \pm 3 \text{ mT}$ is significantly lower than that obtained from the method of ‘first deviation’. It is obvious that the determination of H_{c1} from magnetisation data depends strongly on the method employed. *Böhmer et al.* [232] discussed the various methods for the determination of H_{c1} and concluded that the trapped flux method gives most accurate results. The reason for the higher value of $\mu_0 H_{c1}$, when determined from the method of ‘first deviation’, is that flux pinning by material defects or the existence of surface barriers makes an exact detection of the lower critical field extremely difficult. The $m_t^{0.5} \rightarrow 0$ extrapolation as illustrated in figure 50b (full line), seems to work quite well for the films under study and

should be considered as the most appropriate method for a determination of the lower critical field of superconducting films with strong pinning.

Measurements of the trapped magnetic moment at 1.8K in the field range $0 \leq H_a < H^*$ was performed for the films E8.7e and E10.4e. The results on H_{c1} (T) obtained with this method is summarised in table 23 together with the experimental values of H_{c2} (T).

Sample	T [K]	$\mu_0 H_{c1}$ [mT]	$\mu_0 H_{c2}$ [mT]
E10.4e	1.8	31 ± 3	730 ± 50
E8.7e	1.8	85 ± 5	1150 ± 100

Table 23. The upper and the lower critical fields for niobium films sputter deposited on non-oxidised copper (E10.4e) and on oxidised copper (E8.7e) at 1.8K. The lower critical field H_{c1} was determined from the field dependence of the trapped magnetisation, as described by the modified *Bean* model [233].

11. Summary

The present work was aimed at the optimisation of the rf performance of superconducting niobium film cavities, as used in the LEP2 circular particle collider at CERN. As a final goal, the results should allow a clear assessment of the applicability of the film technology in future linear accelerators, where the superconducting cavities must reach accelerating gradients in excess of 20MV/m at very low resistances. To this end, a thorough study was started, aimed at the understanding of the influence of the film structure on the surface resistance and other superconducting properties of 1.5GHz niobium-copper resonators.

Niobium films were deposited onto the inner walls of copper resonators by the magnetron sputter technique, using argon, krypton, xenon, and argon-neon discharge gases. The amount of gas implanted in a growing film depends on its atomic mass. Therefore, using different discharge gases offers the possibility of changing the electron mean free path in the films without introducing reactive impurities or structural damage. Niobium films were grown on oxidised copper, on oxide free copper and on sputter deposited pre-layers, such as titanium and copper, to study the influence of the substrate on the rf performance of the deposited film. Optimised sputtering parameters, giving compact films with the lowest possible values of the residual resistivity, have already been obtained in previous studies carried out at CERN and were adopted in the present work. Two sputtering systems were used for the production of the cavities, a single cathode system and a two electrode system. The latter allows the deposition of an underlayer or the removal of the naturally grown oxide layer on the copper substrate by reverse sputtering prior to niobium film deposition. Chemical and electrochemical polishing were used as surface treatment techniques for the copper resonators. The latter method was developed in the present work.

The value of the rf surface resistance as a function of the temperature and the electron mean free path is predicted by the BCS theory. The theoretical mean free path dependence of the BCS resistance at 4.2K and 1.5GHz was computed, taking material parameters of relevance for the present films. A comparison with the experimental results gave excellent agreement, and the data presented in this work are the first for a pure metal, which were compared in detail with theoretical predictions. The predicted minimum of the BCS resistance, $R_{BCS} > 400\text{n}\Omega$ just below $l = \xi_0$, as obtained for cavities sputter deposited in krypton on oxidised copper, was experimentally verified. This value is approximately 2.5 times lower than the resistance of high purity bulk niobium cavities at 4.2K.

Recording the temperature dependence of the cavity resonant frequency close to T_c allows the determination of the penetration depth. For bulk niobium cavities, a clean limit value of 30.5nm was obtained, by fitting the BCS temperature dependence of the penetration depth to the data. This value increases by a factor of 1.5 in films sputter deposited on oxidised copper or on titanium in an argon discharge, which corresponds to a mean free path, $l > 30\text{nm}$. An independent estimation of the electron mean free path was obtained from measurements of the low temperature resistivity of films, cut from the cavities. Both sets of data practically overlap. Films, which were grown in the two-electrode system after sputter cleaning the copper substrate had a significantly larger mean free path ($l > 70\text{nm}$), than the films grown in the standard system. This is not the result of a lower concentration of reactive impurities or the existence of less resistive grain boundaries, but related to the grain size and the microstructural defects present in the films. The tendency that the residual resistivity ratio of polycrystalline films decreases with increasing microstrain was unequivocally confirmed by the experimental data. Films grown on oxidised copper have a 30% higher density of point-like defects, caused by implanted noble gas and in part by a higher density of dislocations, as deduced from a Fourier analysis of X-ray diffraction peak broadening. The first of these observations could be

confirmed by thermal desorption measurements of the noble gas content, but a direct observation of dislocations by TEM analysis could not be performed. Whereas about 450ppm argon are trapped in standard films, grown on oxidised copper in the single cathode system, only about 300ppm are found in films grown on oxide-free copper. In order to understand this difference, the influence of the nature of the copper substrate on the film growth had to be analysed. Valuable information was obtained from measurements of the texture and the stresses present in the films. X-ray diffraction analysis in the θ - 2θ Bragg-Brentano configuration on samples, which were cut from different regions along the meridian of superconducting niobium-copper cavities, revealed a strong difference in texture between the two types of film. Films grown on oxidised copper have a strong fibre texture with the most widely spaced (110) plane parallel to the sample surface. This type of texture is typical for films sputter deposited on amorphous substrates and can develop if there are no constraints imposed by the substrate on the alignment of the sputtered atoms.

Niobium films grown on oxide-free copper display a texture, which is governed by the alignment of the copper grains parallel to the surface of the substrate. This was quantitatively analysed by means of texture indices introduced for the film and the substrate, describing the relative amount of grains oriented in a certain crystallographic direction with respect to a randomly oriented material. In addition to the known heteroepitaxial relationships between copper and niobium, Nb(110)7Cu(111)(100) and Nb(100)7Cu(110), a third orientation relationship, Nb(211)7Cu(311) was found, which is not described in the literature. The higher concentration of trapped argon in films sputter deposited on oxidised copper can be explained by the preferred (110) orientation, which are the widest spaced planes and therefore capable to accommodate a larger number of argon atoms. In addition, one can conclude from the different thermal desorption behaviour observed for films grown in pure neon and argon discharges, respectively, that argon and the heavier noble gases cluster in bubbles, mainly along (110), whereas neon is trapped substitutionally.

The energy gap was derived from the observed temperature dependence of the surface resistance and found to be insensitive to the presence of noble gas impurities up to ~2at% in the film. The coupling parameter, $\alpha = 1.87 \pm 0.01$ is in agreement with other types of measurement on bulk niobium. The critical temperature, however, is significantly higher than that of bulk niobium. The values are 9.54K for standard films and 9.45K for films grown on oxide-free copper in an argon discharge. This increase is directly related to the film stresses and compares favourably with measurements reported in the literature on niobium subjected to a non-hydrostatic pressure. A biaxial compressive in-plane stress of -700MPa was measured in the case of a standard film, whereas for heteroepitaxial films, a value of approximately -500MPa was obtained. Consequently, the observed increase of the critical temperature is smaller in films grown on oxide-free copper because of the lower stress state. When the film is removed from its substrate, the stresses relax and the critical temperature reaches its nominal value, 9.3K. Small amounts of implanted neon also lead to a slight increase of T_c , probably because of the change of the effective atomic volume, induced by substitutionally dissolved neon. This effect, however, is very small, when compared to the increase of T_c caused by the macrostresses present in the films.

The film stresses were calculated from the strains, measured by X-ray diffraction, by means of experimentally determined elastic constants. The *Young's* modulus, E , was determined from nanoindentation measurements and the *Poisson's* ratio, ν , was calculated from the strain data themselves, assuming a biaxial stress state in the films. The latter condition could be verified by the measurement of the complete stress tensor for the films. The measured *Poisson's* ratio, $\nu > 0.45$ is significantly higher than the value for isotropic niobium given in the literature. A

comparison of the experimentally determined elastic constants with the theoretical values for anisotropic niobium, however, showed satisfactory agreement.

Stresses build up in the growing film because of the continuous bombardment with noble gas atoms. The thermal stresses, which evolve during cool down of a niobium-copper cavity from deposition to room temperature, also give an important contribution to the observed total stress and were calculated from the thermal expansion coefficients of niobium and copper. Both kinds of stress are compressive in the plane of the film and relax after removal of the copper substrate. The sputter deposition of a niobium film on a niobium substrate also allowed a direct estimation of the thermal stresses. The obtained value, $\sigma = -300\text{MPa}$ is in good agreement with the calculated one.

Because of the heteroepitaxial film growth, misfit or coherency strains build up in the films, which are sputter deposited on oxide-free copper. These stresses are tensile in the plane of the film and consequently lower the total amount of strain. The net result is the lower stress state observed in those films.

Films sputter deposited on titanium were observed to behave exactly as films grown on oxidised copper, in particular they have the same electron mean free path, the same BCS resistance, and the same critical temperature. This observation reconciles with the results reported above, since, contrary to the system niobium-copper, heteroepitaxial film growth is impossible for a niobium film grown on a titanium substrate.

Another important result of this study is the observed increase of the BCS resistance with the amplitude of the rf magnetic field, H_S . An increase of R_{BCS} at 4.2K with H_S by 50% between 0 and $H_S \sim 35\text{mT}$ was measured. This feature, which is independent of the mean free path, is not specific to films and a similar increase is observed in bulk niobium. The limitation to the lowest order in the field of the perturbative expansion, used in the calculations available in the literature, prevents a precise comparison of these data with theory.

Measurements of the upper critical field have been compared with numerical results of the theoretical temperature dependence of H_{c2} , derived in the framework of the GLAG theory. The estimated values of the upper critical field at zero temperature are 770 and 1150mT for films grown on oxide-free and oxidised copper, respectively, and are in agreement with the expectations from the mean free path dependence of H_{c2} . These values were shown to be independent of the amount of stresses present in the films.

At $T = 1.8\text{K}$, the BCS resistance is practically negligible, and the residual resistance is the only term, which subsists at zero temperature. It was often observed to increase dramatically with H_S , first linearly, and then, beyond some field emission threshold, exponentially. Whereas field emission is a common problem of both the film and the bulk technology, the dependence of R_{res} on the magnetic field is specific to films. In this study, no significant correlation between the residual resistances and the other measured variables (T_c , α , R_{BCS} , l) was obtained. As the most important result of the present work, it was shown for the first time that the residual resistance of the film cavities can be maintained at low values over a broad range of the microwave amplitude, similar to those obtained with bulk niobium. This improvement was achieved by electropolishing the copper resonators before sputtering, identifying the roughness of the substrate and macroscopic film defects as the main sources of the residual resistance. A surface resistance at $H_S = 0$ below $10\text{n}\Omega$, increasing with the field by not more than $1\text{n}\Omega/\text{MVm}^{-1}$, was reliably obtained, independent of the kind of the noble gas present in the films. These results contradict earlier doubts about the possibility to produce film cavities and demonstrate that they could become competitive to bulk niobium resonators.

An important consequence of the present work is its implication for the large scale production of radiofrequency superconducting cavities for particle accelerators. The present results have proven the reliability of the film technology for the production of such cavities. Considering the numerous assets of this technology, which were discussed in this work, it is clear that the film technology should be preferred over the more conventional and commonly accepted bulk technology.

12. References

- [1] C. Benvenuti, S. Calatroni and G. Orlandi, *Physica B*, 197, 72, (1994)
- [2] L.D. Landau and E.M. Lifshitz in *Course of Theoretical Physics Vol. 8: "Electrodynamics of Continuous Media"*, Pergamon press, New York, Sect. 45, (1960)
- [3] V.B. Geshkenbein, V.M. Vinokur and R. Fehrenbacher, *Phys. Rev. B* 43, 4, 3748, (1991)
- [4] H. Kuepfer, I. Apfelstedt, R. Fluekiger, C. Keller, R. Meier-Hirmer, B. Runtsch, A. Turowski, U. Wiech and T. Wolf, *Cryogenics* 28, 650, (1988)
- [5] V. Buntar, *Physica C* 309, 98, (1998)
- [6] V.V. Struzhkin, Y.A. Timofeev, R.J. Hemley and H. Mao, *Phys. Rev. Lett.* 79, 21, 4262, (1997) and references therein
- [7] T.F. Smith, *Phys. Lett.* 33A, 7, 465, (1970)
- [8] W.E. Gardner and T.F. Smith, *Phys. Rev.* 144, 1, 253, (1966)
- [9] W. Gey, *Z. Physik* 229, 85, (1969) and W. Buckel and W. Gey, *Z. Physik* 176, 336, (1963)
- [10] D. Köhnlein, *Z. Physik* 208, 142, (1968)
- [11] G. Heim and E. Kay, *J. Appl. Phys.* 46, 4006, (1975)
- [12] J. Bardeen, L. Cooper and J. Schrieffer, *Phys. Rev.* 108, 1175, (1957)
- [13] V.G. Bar'yakhtar and V.I. Makarov, *Sov. Phys.-JETP* 22, 1320, (1966)
- [14] Y. Nakagawa and M. Umeda, *Cryogenics* 36, 579, (1996) and references therein
- [15] M. Zakirov, V.P. Kuznetsov and T.D. Shermergor, *Sov. J. Low. Temp. Phys.* 6, 11, (1980) and references therein
- [16] J.C. Schwanebek, R.H. Buitrago and L.E. Toth, *J. Appl. Phys.* 49, 848, (1978)
- [17] C.C. Koch, J.O. Scarbrough and D.M. Kroeger, *Phys. Rev. B* 3, 9, 888, (1973)
- [18] DeSorbo, *Phys. Rev.* 132, 107, (1963)
- [19] A.B. Pippard, *Phys. Chem. Solids* 3, 175, (1957)
- [20] P.W. Anderson, *J. Phys. Chem. Solids* 11, 26, (1959)
- [21] D. Markowitz and L. P. Kadanoff, *Phys. Rev.* 131, 2, 563, (1963)
- [22] P. Crozat and R. Adde, *Physics* 108B, 1251, (1981)
- [23] W.L. McMillan, *Phys. Rev.* 167, 331, (1968)
- [24] C.T. Wu, *Thin Solid Films* 64, 103, (1979)
- [25] N. Ya. Fogel, A.A. Moshenskii, I.M. Dmitrenko, L.P. Tishchenko, T.I. Peregon and Ya. M. Fogel, *Sov. Phys.-JETP*, 39, 2, (1974)
- [26] A.M. Toxen, *Phys. Rev.* 123, 442, (1961)
- [27] B.G. Lazarev, L.S. Lazareva and V.I. Makarov, *Sov. Phys.-JETP* 43, 2311, (1962)
- [28] V.G. Lazarev, E.V. Semenenko and V.M. Kuzmenko, *FMM* 25, 26, (1968)
- [29] N.V. Zavaritskii, *Sov. Phys.-JETP* 30, 412, (1970)
- [30] H.W. Weber, E. Seidl, M. Botlo, C. Laa, H.P. Wiesinger and J. Rammer, *Physica C* 161, 287, (1989)
- [31] H.P. Klug and L.E. Alexander, *'X-Ray Diffraction Procedures'*, 2nd ed., Wiley Interscience, New York, (1974)
- [32] F. C. Blake, *Rev. Mod. Phys.* 5, 169, (1933)
- [33] A. Taylor and H. Sinclair, *Proc. Phys. Soc. (London)*, 57, 160, (1945)
- [33] J. B. Nelson and D. P. Riley, *Proc. Phys. Soc. (London)*, 57, 126, (1945)
- [34] J. Mignot and D. Rondot, *J. Appl. Cryst.* 9, 460, (1976)
- [35] C.T. Wu, *Thin Solid Films*, 64, 103, (1979)
- [36] C.N.J. Wagner in *'Local Atomic Arrangements Studied by X-Ray Diffraction'*, J.B. Cohen and J.E. Hilliard eds., Gordon and Breach, New York, (1966)
- [37] J.A. Thornton and D.W. Hoffman, *J. Vac. Sci. Technol.* 18, 2, (1981)

- [38] G.W. Greenwood and M.V. Speight, J. Nucl. Mat. 10, 140, (1963)
- [39] D.W. Hoffman and J.A. Thornton, Thin Solid Films 40, 355, (1977) and J. Vac. Sci. Technol. 17, 380, (1980)
- [40] H.D. Hagstrum, Phys. Rev. 123, 758, (1961) and Phys. Rev. 96, 335, (1954)
- [41] B.V. Panin, Sov. Phys.-JETP 15, 2, 215, (1962)
- [42] C.T. Wu, R.T. Kampwirth and J.W. Hafstrom, J. Vac. Sci. Technol. 14, 1, 134, (1977)
- [43] G. Carter and J.S. Colligon in '*Ion Bombardment of Solids*', Chap. 7, Elsevier, New York, (1968)
- [44] W.A. Jesser and D. Kuhlmann-Wilsdorf, Phys. Status Solidi 19, 95, (1967)
- [45] D.W. Hoffman and J.A. Thornton, Thin Solid Films 45, 387, (1977)
- [46] J.A. Thornton, Annu. Rev. Mater. Sci. 7, 239, (1977) and J. Vac. Sci. Technol. 11, 4, 666, (1974)
- [47] J.H. Thornton and D.W. Hoffman, J. Vac. Sci. Technol. A3, 576, (1985) and references therein
- [48] B.A. Movchan and A.V. Demchishin, Fiz. Met. Metalloved. 28, 653, (1969)
- [49] D. Henderson, M.H. Brodsky and P. Chaudhari, Appl. Phys. Lett. 25, 641, (1974)
- [50] Natl. Bur. Stand. (U.S.), Monogr. 25, 19, 67, (1982)
- [51] A. Pialoux, M. L. Joyeux and G. Cizeron, J. Less-Common Metals, 87,1, (1982)
- [52] B.M. Varyutinshiy, G.N. Kartmazov, Y.M. Smirnov and V.A. Finkel, Phys. of Metals and Metallography, 21(4), 134, (1966)
- [53] R. Roberge, J. Less-common Metals, 40, 161, (1975)
- [54] E. Gebhardt and R. Rothenbacher, Z. Metallk. 54, 443, (1963)
- [55] D.P. Smith, J. Appl. Phys. 38, 1, 340, (1967)
- [56] R.C. Sun, T.C. Tisone and P.D. Cruzan, J. Appl. Phys. 44, 3, 1009, (1973)
- [57] D.S. Rickerby, J. Vac. Sci. Technol. A4, 6, 2809, (1986)
- [58] D.S. Rickerby, G. Eckold, K.T. Scott and I.M. Buckley-Golder, Thin Solid Films, 154, 125, (1987)
- [59] D.S. Rickerby and P.J. Burnett, Thin Solid Films 157, 195, (1988)
- [60] C. Benvenuti, S. Calatroni and G. Orlandi, Physica B 197, 72, (1994)
- [61] A.J. Perry, V. Valvoda, D. Rafaja, D.L. Williamson and B.D. Sartwell, Surf. Coat. Technol. 54/55, 180, (1992)
- [62] D.S. Rickerby, A.M. Jones and A.J. Perry, Surf. Coat. Technol. 36, 631, (1988)
- [63] D.S. Rickerby, A.M. Jones and B.A. Bellamy, Surf. Coat. Technol. 37, 111, (1989)
- [64] B. Window, J. Vac. Sci. Technol. A11, 1522, (1993)
- [65] H.F. Winters and E. Kay, J. Appl. Phys. 38, 3928, (1967)
- [66] B. Window and G.L. Harding, J. Vac. Sci. Technol. A11, 1447, (1993) and references therein
- [67] J. Auer and H. Ullmaier, Phys. Rev. B7, 136, (1973)
- [68] C. Benvenuti, S. Calatroni, P. Chiggiato, M. Marino and R. Russo, Proceedings of the 7th workshop of superconductivity, 2, 473, (1995)
- [69] B. Window, Surf. Coat. Technol. 71, 93, (1995)
- [70] J.P. Biersack and L.G. Haggmark, Nucl. Instrum. Methods 174, 257, (1980)
- [71] L. Hultman, G. Hakansson, U. Wahlström, J.E. Sundgren, I. Petrov, F. Adibi and J.E. Greene, Thin Solid Films 205, 153, (1991)
- [72] C. Carter, D.G. Armour, S.E. Donnelly, D.C. Ingram and R.P. Webb, Radiat. Eff. 53, 143, (1980)
- [73] R.S. Barnes, J. Nucl. Mater. 11, 135, (1964)
- [74] L. Hultman, B.O. Johansson, J.E. Sundgren, L.C. Markert and J.E. Greene, Appl. Phys. Lett. 53, 1175, (1988)
- [75] L. Hultman, J.E. Sundgren, L.C. Markert and J.E. Greene, J. Vac. Sci. Technol. A7, 1187, (1989)

- [76] A. Prymboom, P. Berghuis and P.H. Kes, *Appl. Phys. Lett.* 50, 23, 1645, (1987)
- [77] J.H. Evans, A. Van Veen and L.M. Caspers, *Scripta Metall.* 15, 323, (1981)
- [78] D.E. Rimmer and A.H. Cottrell, *Phil. Mag.* 2, 1345, (1957)
- [79] M.P. Volkov, Yu. N. Sokurskii, S.I. Tsypkin, V.I. Chuev and V.N. Shishov, *Sov. Phys. Solid State*, 28, 2, 302, (1986) and *Phys. Met. Metall.* 59, 6, 58, (1985)
- [80] J. Th. De Hosson, *Phys. Stat. Sol. (a)*, 40, 293, (1977)
- [81] A. vom Felde, J. Fink, Th. Müller-Heinzerling, J. Pflüger, B. Scheerer and G. Linker, *Phys. Rev. Lett.* 53, 922, (1984)
- [82] J.H. Evans and D. J. Mazey, *J. Phys. F* 15, L1, (1985) and *Scripta metall.* 19, 621, (1985)
- [83] C. Templier, H. Garem and J.P. Riviere, *Phil. Mag. A*, 53, 5, 667, (1986)
- [84] R.C. Birtcher and W. Jäger, *Ultramicrosc.* 22, 267, (1987) and references therein
- [85] P. Ehrhart, A. Gaber, A.A. Gadalla, W. Jäger and N. Tsukuda, *Nucl. Instrum. Methods Phys. Res. B*, 19/20, 180, (1987)
- [86] W. Jäger, P. Ehrhart and W. Schilling, *Rad. Eff. Def. Solids* 113, 201, (1990)
- [87] R. Kelly and H.J. Matzke, *J. Nucl. Materials* 17, 179, (1965)
- [88] R. Kelly and E. Ruedl, *The 3rd European Conference on Electron Microscopy*, Prague, (1964) and *Phys. Status Solidi* 13, 55, (1966)
- [89] C.W. Tucker and F.J. Norton, *J. Nucl. Mater.* 2, 4, 329, (1960)
- [90] R.S. Barnes and D.J. Mazey, *Proc. Roy. Soc. A*, 275, 47, (1963)
- [91] M. Doerner, D.S. Gardner and W.D. Nix, *J. Mater. Res.* 1, 845, (1986)
- [92] B. Window, F. Sharples and N. Savvides, *J. Vac. Sci. Technol. A*6, 2333, (1988)
- [93] P.B. Johnson and D.J. Mazey, *J. Nucl. Mater.* 218, 273, (1995)
- [94] L.P. Tishchenko, T.I. Peregon and A.G. Koval, *Phys. Chem. Mech. Surf.* 4, 870, (1986)
- [95] A. Van Veen, L.M. Caspers, E.V. Kornelsen, R. Fastenau, A. Van Gorkum and A. Warnaar, *Phys. Stat. Sol.* 40, 235, (1977)
- [96] T. Slimani, N.B. Thoft and A. Naudon, *J. Physique IV*, 3, 303, (1993)
- [97] A. Luukainen, J. Keinonen and M. Erola, *Phys. Rev. B*32, 4814, (1985)
- [98] H.H. Andersen J. Bohr, A. Johansen, L. Sarholt-Kristensen and V. Surganov, *Phys. Rev. Lett.* 59, 14, 1589, (1987)
- [99] O.G. Peterson, D.N. Batchelder and R.O. Simmons, *Phys. Rev.* 150, 2, 703, (1966)
- [100] G.B. Harris, *Phil. Mag.* 43, 113, (1952)
- [101] V. Valvoda and M. Järvinen, *Powder Diffraction* 5, 4, 200, (1990)
- [102] *Natl. Bur. Stand. (U.S.), Monogr.* 25, 19, 67, (1982)
- [103] W.A. Rachinger, *J.Sci. Instrum.* 25, 254, (1948)
- [104] H. Ji, G.S. Was, J.W. Jones and N.R. Moody, *J. Appl. Phys.* 81, 10, 6754, (1997)
- [105] L.S. Yu, J.M.E. Harper, J. J. Cuomo and D.A. Smith, *J. Vac. Sci. Technol. A*4, 443, (1986) and *Appl. Phys. Letters*, 47, 932, (1985)
- [106] A. Van der Drift, *Philips Res. Rep.* 22, 267, (1967)
- [107] F. Ying, R.W. Smith and D.J. Srolovitz, *Phys. Lett.* 69, 20, 3007, (1996)
- [108] V. Matolin, Charles University, Prague, unpublished results of collaborative studies (1998)
- [109] R. Bruinsma and A. Zangwill, *J. Phys. (Paris)* 47, 2055, (1986)
- [110] E. Bauer and J.H. van der Merwe, *Phys. Rev. B* 33, 6, 3657, (1986)
- [111] R. Ramirez, A. Rahman and I.K. Schuller, *Phys. Rev. B*30, 10, 6208, (1984)
- [112] C.S.L. Chun, G.G. Zheng, J.L. Vicent and I.K. Schuller, *Phys. Rev. B*29, 9, 4915, (1984)
- [113] I.K. Schuller, *Phys. Rev. Lett.* 44, 1597, (1980)
- [114] D. Vion, Ph.D. thesis (93 ISAL 0065), Lyon University, France, (1993), unpublished
- [115] H.J. Wallbaum, *Z. Metallk.* 42, 207, (1951)

- [116] V. Valvoda, R. Cerný, R. Kuzel and L. Dobiasova, *Crys. Res. Technol.* 22, 1301, (1987)
- [117] S.M. Durbin, J.E. Cunningham, M.E. Mochel and C.P. Flynn, *J. Phys. F* 11, L223, (1981)
- [118] R. Kuzel, R. Cerný, V. Valvoda, M. Blomberg, M. Merisalo and S. Kadlec, *Thin Solid Films*, 268, 72, (1995)
- [119] J.H. Souk, A. Segmüller and J. Angilello, *J. Appl. Phys.* 62, 509, (1987)
- [120] L.M.M. Stals, C. Quaeyhaegens and M. Van Stappen, *Surf. Coat. Technol.* 54/55, 121, (1992)
- [121] M. Field and M.E. Merchant, *J. Appl. Phys.* 20, 741, (1949)
- [122] R.H. Bragg and C.M. Packer, *J. Appl. Phys.* 35, 1322, (1964)
- [123] J.L. Loubet, Ph.D thesis, Lyon University, France (1986), unpublished.
- [124] M.F. Doerner and W.D. Nix, *J. Mater. Res.* 1, 601 (1986)
- [125] W.C. Oliver and G.M. Pharr, *J. Mater. Res.* 7, 1564 (1992)
- [126] S.I. Bulychiev and V.P. Alekhin, *Zavod. Lab.* 53, 76 (1987) and references therein
- [127] I.N. Sneddon, *Int. J. Eng. Sci.* 3, 47 (1965)
- [128] A. Karimi, EPFL, private communications (1998)
- [129] D. Bloess, C. Durand, E. Mahner, H. Nakai, W. Weingarten, P. Bosland, J. Mayer and L. van Loyen, *IEEE Trans. Appl. Supercond.* 7, 1776 (1997) and references therein
- [130] P.J. Burnett and D.S. Rickerby, *Thin Solid Films* 154, 403, (1987)
- [131] J. Woirgard and J.C. Dargentton, *J. Mater. Res.* 12, 9, (1997)
- [132] ASM Metals Handbook, 10th ed., vol. 2, (1990)
- [133] R.W. Hertzberg, *'Deformation and Fracture Mechanics of Engineering Materials'*, Wiley, New York, p.13f, (1976)
- [134] J.F. Nye, *'Physical Properties of Crystals'*, Oxford University Press, Oxford, GB, (1976)
- [135] S.P. Timoshenko and N.J. Goodier, *'Theory of Elasticity'*, 3rd ed., McGraw-Hill, New York, (1970)
- [136] H. Dölle and J. B. Cohen, *Metallurgical Trans. A.* 11A, 831, (1980)
- [137] H. Dölle, *J. Appl. Cryst.* 12, 489, (1979)
- [138] R. Glocker, *Z. Techn. Phys.* 19, 289, (1938)
- [139] F. Bollenrath, V. Hauk and E.H. Muller, *Z. Metallk.* 58, 76, (1967)
- [140] R. Russo and S. Sgobba, *Part. Accel.* 60, 135, (1998)
- [141] J.A. Thornton and D.W. Hoffman, *Thin Solid Films*, 171, 5, (1989)
- [142] H. Dölle and V. Hauk, *Z. Metallk.* 68, 128, (1977)
- [143] T. Hirsch and P. Mayr, *Surf. Coat. Technol.* 36, 729, (1988)
- [144] R.H. Marion and J.B. Cohen, *Adv. X-ray Anal.* 18, 466, (1975)
- [145] M. Barral, J.L. Lebrun, J.M. Sprauel and G. Mader, *Metall. Trans. A*18, 1229, (1987)
- [146] P. Scardi, P. Polonioli and S. Ferrari, *Thin Solid Films* 253, 349, (1994)
- [147] H. Dölle and V. Hauk, *Z. Metallk.* 69, 410, (1978) and *Z. Metallk.* 69, 766, (1978)
- [148] H. Dölle and J.B. Cohen, *Metall. Trans. A*11, 831, (1980)
- [149] J.M. Sprauel, M. Barral and S. Torbaty, *Adv. X-ray Anal.* 26, 217, (1983)
- [150] J.B. Cohen, *Powder Diffraction* 1, 15, (1986)
- [151] K-N. Tu, J.W. Mayer and L.C. Feldman, *'Electronic Thin Film Science'*, MacMillian Publishing Company, New York, (1988)
- [152] H.P. Kattelus, J.L. Tandon, C. Sala and M.A. Nicolet, *J. Vac. Sci. Technol.* A4, 1850, (1986)
- [153] G. Håkansson, J.E. Sundgren, D. McIntyre, J.E. Greene and W.D. Münz, *Thin Solid Films*, 153, 55, (1987)
- [154] O. Knotek, R. Elsing, G. Krämer and F. Jungblut, *Surf. Coat. Technol.* 46, 265, (1990)
- [155] A. Pan and J.E. Greene, *Thin Solid Films* 78, 25, (1981)

- [156] W. Voigt, *Lehrbuch der Kristallphysik*, Teubner, Leipzig/Berlin, (1928)
- [157] A. Reuss, Z. angew. Math. Mech. 9, 49, (1929)
- [158] E. Kröner, Z. Physik 151, 504, (1948)
- [159] E. Macherauch, Exp. Mech. 6, 140, (1966)
- [160] N.M. Jisrawi, M.W. Ruckman, T.R. Thurston, G. Reisfeld, M. Weinert and M. Strongin, Phys. Rev. B58, 10, 6585, (1998)
- [161] G.W. Webb, Phys. Rev. 181, 3, 1127, (1969)
- [162] M. K. Small and W.D. Nix, J. Mater. Res. 7, 6, 1553, (1992)
- [163] W.D. Nix, Metallurgical Trans. A. 20A, 2217, (1989).
- [164] B.E. Warren and B.L. Averbach, J. Appl. Phys. 21, 595, (1950)
- [165] G.K. Williamson and W.H. Hall, Acta Cryst. 1, 22, (1953)
- [166] R. Kuzel, R. Cerný, V. Valvoda, M. Blomberg and M. Merisalo, Thin Solid Films 247, 64, (1994)
- [167] R. Cerný, R. Kuzel, V. Valvoda, S. Kadlec and J. Musil, Surf. Coat. Technol. 64, 111, (1994)
- [168] A.J. Perry, M. Jagner, W.D. Sproul and P.J. Rudnik, Surf. Coat. Technol. 42, 49, (1990)
- [169] G.P. Mohanty and R.A. Schmidt, J. Appl. Phys. 41, 9, 3573, (1970) and J. Appl. Phys. 41, 9, 3582, (1970)
- [170] C.N.J. Wagner and E.N. Aqua, Adv. X-ray Anal. 7, 46, (1964)
- [171] O.J. Guentert and B.E. Warren, J. Appl. Phys., 29, 1, 40, (1958)
- [172] A.R. Stokes, Proc. Phys. Soc. London 61, 382, (1948)
- [173] B.E. Warren in *Progress in Metal Physics*, 8, 147, Pergamon Press, N.Y. (1959)
- [175] J.B. Cohen and C.N.J. Wagner, J. Appl. Phys. 33, 6, 2073, (1962)
- [176] E.J. Mittemeijer and R. Delhez, J. Appl. Phys. 49, 7, (1978)
- [177] C.N.J. Wagner in *Local Atomic Arrangements Studied by X-Ray Diffraction*, J.B. Cohen and J.E. Hilliard, eds., Addison-Wesley, Reading, Mass, (1966)
- [178] M. Wilkens, J. Appl. Cryst. 12, 119, (1979)
- [179] E.F. Bertaut, Acta Cryst. 5, 117, (1952)
- [180] R.A. Young, R.J. Gerdes and A.J.C. Wilson, Acta Cryst. 22, 155, (1967)
- [181] R.L. Rothman and J.B. Cohen, Adv. X-ray Anal. 12, 208, (1969)
- [182] B.Y. Bines and A.F. Sirenko, Sov. Phys. Cryst. 7, 1, 15, (1962)
- [183] R.L. Rothman and J.B. Cohen, J. Appl. Phys. 42, 3, (1971)
- [184] J. Mering, Acta Crystallogr. 2, 371 (1949)
- [185] T. Adler and C.R. Houska, J. Appl. Phys. 50, 5, (1979) and references therein
- [186] R.W. Hinton, L.H. Schwartz and J.B. Cohen, J. Electrochem. Soc., 110, 103, (1963)
- [187] M. Hecq, A. Hecq and J.I. Langford, J. Appl. Phys. 53, 1, (1982)
- [188] T.C. Huang, G. Lim, F. Parmigiani and E. Kay, J. Vac. Sci. Technol. A3, 6, 2161, (1985)
- [189] A. Gangulee, J. Appl. Phys. 43, 10, 3943, (1972)
- [190] F. Bertaut, C.R. Acad. Sci. Paris 228, 492 (1949)
- [191] B.E. Warren, X-Ray Diffraction, Addison-Wesley, Reading, Massachusetts, (1969)
- [192] H.M. Otte and E. Holland, *Lattice Defects and their Interactions*, R.R. Hasiguti, ed., Gordon and Breach, Science Publishers, New York, (1967)
- [193] P.B. Hirsch and H.M. Otte, Acta Cryst. 10, 447, (1957)
- [194] J.I. Langford, J. Appl. Cryst. 11, 10 (1978)
- [195] R.K. Nandi and S. P. Gupta, J. Appl. Cryst. 11, 6, (1978)
- [196] G.B. Greenough in *Progress in Metal Physics*, 3, 176, Pergamon Press, New York (1959)
- [197] E.N. Aqua and C.N.J. Wagner, Phil. Mag. 9, 565, (1964)
- [198] B.E. Warren, J. Appl. Phys. 32, 2428, (1961)
- [199] R.A. French, Cryogenics 8, 301, (1968)

- [200] Landolt-Börnstein, '*Metals: Electronic Transport Phenomena*', III, 15, Springer Verlag, Heidelberg, (1982)
- [201] K. Fuchs, Proc. Camb. Phil. Soc. 34, 100, (1938)
- [202] E.H. Sondheimer, Adv. Phys. 1, 1 (1952) and Adv. Phys. 36, 1832, (1965)
- [203] A.F. Mayadas and M. Shatzkes, Phys. Rev. B1, 4, 1382, (1970)
- [204] G. Reiss, J. Vancea and H. Hoffmann, Phys. Rev. Lett. 56, 19, 2100, (1986) and Phys. Rev. B35, 12, 6435, (1987) and references therein
- [205] D.J. Srolovitz, J. Vac. Sci. Technol. A4, 2925, (1986)
- [206] Viguier, unpublished results of collaborative studies (1999)
- [207] G. Reiss, J. Vancea and H. Hoffmann, J. Phys. C18, L657, (1985)
- [208] V. Lacquaniti, S. Maggi, E. Monticone and R. Steni, Phys. Stat. Sol. (a) 151, 335, (1995)
- [209] G. Oya, M. Koishi and Y. Sawada, J. Appl. Phys. 60, 4, 1440, (1986)
- [210] S. Isagawa, J. Appl. Phys. 51, 8, 4460, (1980)
- [211] H.W. Weber, E. Seidl, C. Laa, E. Schachinger, M. Prohammer, A. Junod and D. Eckert, Phys. Rev. B44, 14, 7585, (1991)
- [212] L.P. Gor'kov, Sov. Phys.-JETP 10, 998, (1960)
- [213] B.B. Goodman, IBM J. Res. Dev. 6, 63, (1962)
- [214] J.C. Gallop, '*SQUID's, the Josephson Effects and Superconducting Electronics*', IOP Publishing Ltd., Bristol (1991)
- [215] V.L. Ginzburg and L.D. Landau, Zh. Eksperim. i Teor. Fiz. 20, 1064, (1950)
- [216] A.A. Abrikosov, Sov. Phys.-JETP 5, 1174, (1957)
- [217] W.H. Kleiner, L.M. Roth and S.H. Autler, Phys. Rev. 133, 5A, 1226, (1964)
- [218] A.A. Abrikosov, Dokl. Akad. Nauk SSSR 86, 489, (1952)
- [219] W.A. Fietz and W.W. Webb, Phys. Rev. 178, 2, 657, (1969)
- [220] C.P. Bean, Phys. Rev. Lett. 8, 250, (1962)
- [221] L.P. Gor'kov, Sov. Phys.-JETP 9, 1364, (1959)
- [222] K. Maki, Physics 1, 1, 21, (1964)
- [223] G. Eilenberger, Phys. Rev. 153, 2, 584, (1966)
- [224] C.J. Gorter and H.B. Casimir, Z. Phys. 35, 963, (1934)
- [225] D.K. Finnemore, T.F. Stromberg and C.A. Swenson, Phys. Rev. 149, 1, 231, (1966)
- [226] H.R. Kerchner, D.K. Christen and S.T. Sekula, Phys. Rev. B21, 1, 86, (1980)
- [227] M. Tinkham, Phys. Rev. 129, 6, 2413, (1963)
- [228] E. Helfand and N.R. Werthamer, Phys. Rev. Lett. 13, 686, (1964) and Phys. Rev. 147, 1, 288, (1966)
- [229] N.R. Werthamer, E. Helfand and P.C. Hohenberg, Phys. Rev. 147, 1, 295, (1966)
- [230] L.P. Gor'kov, Sov. Phys.-JETP 10, 593, (1960)
- [231] J. Winter and H. Kuzmany, Phys. Rev. B52, 7115, (1995)
- [232] C. Böhmer, G. Brandstätter and H.W. Weber, Supercond. Sci. Technol. 10, A1, (1997)
- [233] V.V. Moshchalkov, J.Y. Henry, C. Marin, J. Rossat-Mignod and J. F. Jacquot, Physica C 175, 407, (1991) and references therein
- [234] V. Buntar, F.M. Sauerzopf and H.W. Weber, Phys. Rev. B54, 14, R9651, (1996)
- [235] F. Sauerzopf, TU Vienna, private communications, (1999)
- [236] H.W. Weber, E. Seidl, M. Botlo, C. Laa, E. Mayerhofer, F.M. Sauerzopf, R.M. Schalk and H.P. Wiesinger, Physica C 161, 272, (1989)

13. Appendix

13.1. The absorption correction to the XRD peak intensities for the finite thickness

If A is the cross-sectional area of the beam at its point of intersection with the sample, the diffracting volume of a layer of specimen of thickness dx at depth x is,

$$dV = \frac{A}{\sin \theta} dx, \quad (73)$$

or, since $x = 0.5s \sin \theta$,

$$dV = \frac{I}{2} Ads. \quad (74)$$

If I_0 is the intensity diffracted at the angle θ by unit volume of the specimen under the hypothetical condition of non-absorption, the intensity diffracted by the element dV is

$$dI = \frac{I}{2} I_0 A e^{-\mu s} ds, \quad (75)$$

where s denotes the absorbing path length and μ the linear absorption coefficient ($0.131 \mu\text{m}^{-1}$ for niobium). The total intensity diffracted at the angle θ by the infinitely thick sample is then

$$I_\infty = \int_{s=0}^{s=\infty} dI = \frac{I_0 A}{2\mu} \quad (76)$$

The intensity diffracted by a finite thickness x is then

$$I_x = \frac{I_0 A}{2\mu} \left[1 - e^{-\frac{2\mu x}{\sin \theta}} \right]. \quad (77)$$

The quantities I and I_0 may denote any desired measure of the reflection intensity, integrated, peak, and so on. The following factor is then applied to convert the observed intensity I_x to the intensity corresponding to a specimen of effectively infinite thickness,

$$\frac{I_\infty}{I_x} (BB) = \left[1 - \exp\left(-\frac{2\mu x}{\sin \theta}\right) \right]^{-1}. \quad (16)$$

This formula may only be applied to a diffractogram recorded in the *Bragg-Brentano* (BB) configuration and considers already the change in irradiated area with θ (the above derivation follows the *ansatz* as given in [31, page 487]).

The signal coming from the substrate is partially shielded by absorption in the outer niobium layer and must also be corrected to obtain the texture indices of the copper substrate (chapter II/5). In the simple case of a diffractogram recorded in the symmetric configuration, the integrated intensity is multiplied by the factor,

$$A(\theta) = \exp\left(-\frac{\sin \theta}{2\mu x}\right). \quad (78)$$

To correct the peak intensities of a XRD pattern recorded at a small angle of incidence, ω , of the incident beam with the sample surface, one can rewrite equation (77) to

$$\frac{I_\infty}{I_x}(\omega) = \left[1 - \exp\left(-\mu x \left(\frac{1}{\sin \omega} + \frac{1}{\sin(2\theta - \omega)} \right) \right) \right]^{-1}, \quad (79)$$

since

$$s = x \left(\frac{1}{\sin \omega} + \frac{1}{\sin(2\theta - \omega)} \right). \quad (80)$$

For the more general case of an inclination $\psi = \theta_{hkl} - \omega$ (as directly realised with the ψ -goniometer), equation (79) reads,

$$\frac{I_\infty}{I_x}(\psi) = \left[1 - \exp \left(-2\mu x \left(\frac{\sin \theta \cos \psi}{\sin^2 \theta - \sin^2 \psi} \right) \right) \right]^{-1} \quad (81)$$

This expression is equal to the left hand side of relation (2) given by *Valvoda et al.* in their review article on X-ray diffraction [116].

13.2. The absorption correction for the ω -goniometer (asymmetric case)

The beam intensity after penetrating the sample by a distance S_1 is

$$I = I_0 e^{-\mu S_1}. \quad (82)$$

For a diffracting element, the diffracting intensity transmitted is

$$dI = I_0 e^{-\mu S_1} A dS_1 e^{-\mu S_2}. \quad (83)$$

S_1 denotes the path length within the sample before diffraction and S_2 the path length within the sample after diffraction. The other notations have their usual meanings. From geometrical considerations (Fig. 51) follows that

$$S_1 = x / \cos(90 - \psi - \theta) \text{ and } S_2 = x / \cos(90 + \psi - \theta) \quad (84a, b)$$

and

$$S_2 = S_1 \frac{\sin(\theta + \psi)}{\sin(\theta - \psi)} = S_1 U. \quad (85)$$

Then, from equation (83) and (85),

$$dI = I_0 A e^{-\mu S_1(1+U)} dS_1. \quad (86)$$

Integrating Eqn. (86) from $S_1 = 0$ to $S_1 = \infty$ to get the total intensity of the diffracted beam leads to

$$I = \frac{I_0 A}{(1+U)\mu} \quad (87)$$

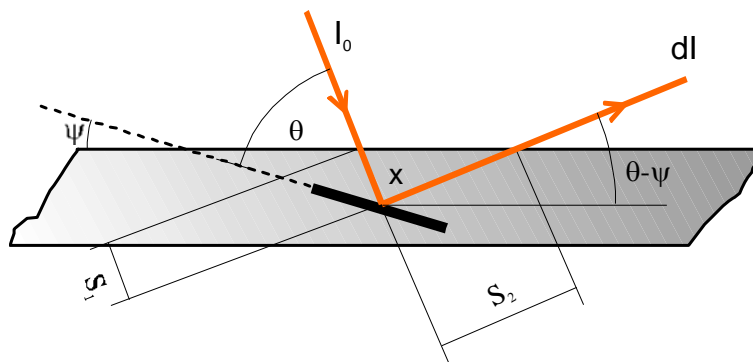


Figure 51. Geometry of the reflection process in the asymmetric configuration.

The specimen can only be considered to be of infinite thickness for penetration by the X-ray beam, when equation (79) is applied to the raw data. In the *Bragg-Brentano* configuration, when $\psi = 0$, $U = 1$ and equation (76) is obtained. Finally, the correction factor to be applied to normalise the measured intensity at any ψ , realised with the ω -goniometer (asymmetric configuration), by the intensity at $\psi = 0$ is obtained:

$$\frac{I_{(\infty, \psi=0)}}{I_{(\infty, \psi)}} = \frac{1}{2} \left(1 + \frac{\sin(\theta + \psi)}{\sin(\theta - \psi)} \right). \quad (88)$$

Curriculum Vitae

<i>Family name:</i>	<i>Peck</i>
<i>First name:</i>	<i>Michael Alexander</i>
<i>Date of birth:</i>	<i>June 5th, 1968</i>
<i>Place of birth:</i>	<i>Vienna</i>
<i>Nationality:</i>	<i>Austria</i>
<i>Marital status:</i>	<i>mar. 1 child</i>

Education

1974-1978	Private Catholic Elementary School, Vienna
1978-1986	Classical Secondary School, Vienna
1986	Final examination
1987	Austrian Military Service
1988-1995	Technical University of Vienna Study of Technical Chemistry
1992-1995	Specialization in Inorganic and Analytical Chemistry
1993	University of Vienna Study of Hungarian Language and Style
1994 - 1995	Institute of Analytical Chemistry Diploma Thesis on "Characterization and Optimization of a Microwave-Induced-Plasma Atomic Emission Detector for Gas Chromatographic Trace Analysis" (Prof. M. Grasserbauer)
June 1995	Graduation in Technical Chemistry (with honors)
June 1995 - Oct. 1995	Research Activities at the University of Dortmund (Prof. J.A.C. Broekaert)
Nov. 1995 - July 1996	Technical University of Vienna Work on publications
Aug. 1996 - Jan. 1999	Europ. Organization for Nuclear Research, CERN Ph.D. Thesis on "Study of the Surface Resistance of Superconducting Nb Films" (Prof. H.W. Weber)
Jan. 1999 – Aug. 1999	Scientific associate at CERN

Professional Experiences

July-Dec. 1986,	Schärdinger Corp. Vienna - Distribution Center
July-Sept. 1988-1990	EMC Computer Corp. - Hardware Configuration
Dec. 1990-March 1991	United Parcel Service Vienna - Import Handling,
Nov. 1995-June 1996	Data Management
Since Sept. 1999	UMS Schweizerische Metallwerke AG -
	Project Management
1993 - 1995	Delegate at the student councils of the Technical
	University of Vienna.

Languages

German (native language)
English (VG)
French (Fair)
Hungarian (Fair)